Ph.D. DISSERTATION

Synthesis of atomically thin transition metal disulfides for photovoltaics and water splitting catalysts

By

Ki Chang Kwon

February 2018

SEOUL NATIONAL UNIVERSITY

COLLEGE OF ENGINEERING

DEPARTMENT OF MATERIALS SCIENCE AND ENGINEERING

Synthesis of atomically thin transition metal disulfides for photovoltaics and water splitting catalysts

Advisor: Prof. Ho Won Jang

by

Ki Chang Kwon

A thesis submitted to the Graduate Faculty of Seoul National University in partial fulfillment of the requirements for the Degree of Doctor of Philosophy

Department of Materials Science and Engineering

December 2017

Approved
by

심사위원장 : 한 승 우

부위원장 : 장 호 원

심사위원 : 김 수 영

심사위원 : 김 진 영

심사위원 : 이 철 호

Abstract

As a new class of material, two-dimensional (2D) atomic crystals have attracted enormous research interest in the last decade that has led to a number of breakthroughs in physics owing to the confined charge, spin and heat transport within the 2D planes. The most outstanding one of these materials is graphene, as its exceptional electronic, optical and mechanical properties may hold great promise for a variety of future applications.

The chapter 3 will cover the application of 2D transition metal disulfide thin films to charge transport layers and p-n junction material with *p*-Si wafer. Transition metal disulfides (MeS_2) such as MoS_2 and WS_2 were used as charge transport layers in organic light-emitting diodes (OLEDs) and organic photovoltaic (OPV) cells in order to enhance the stability in air comparing to poly(3,4-ethylenedioxythiophene):poly(styrenesulfonate) (PEDOT:PSS). MeS_2 layers with a polycrystalline structure were synthesized by a chemical deposition method using uniformly spin-coated $(NH_4)MoS_4$ and $(NH_4)WS_4$ precursor solutions. The ultraviolet-ozone ($UV\text{-}O_3$) treatment on MeS_2 leads to the removal of the surface contaminants produced by the transfer process, resulting in a uniform surface and an increase of the work function.

Furthermore, the strong light absoption of single-layer of MoS_2 could be utilized by light absorption layer in p-type Si-based photovoltaic cells. Specifically, a single semiconducting 0.6-nm-thick MoS_2 can absorb as much sunlight as 50 nm of Si and generate photocurrents as similar as 12-nm-thick GaAs semiconductor. The MoS_2 thin films could be the one of promising light

absorption layer and have potential to make p-n heterojunction photovoltaic cells with p-Si substrate. We synthesize the wafer-scale molybdenum disulfide thin-films by thermolysis of solution precursor based method. After that, the thin films are transferred to p-Si and formed a heterojunction with p-Si. In order to maximize and fully utilize the excellent property of the n-MoS_2, Transparent Au nanomesh electrode (Sheet resistance ≈ 6 Ω/sq. at 90% transmittance) fabricated from UV-O_3 treated polymeric nanofiber templates is integrated to *n*-MoS_2/*p*-Si heterojunction**.** The *n*-MoS_2/*p*-Si heterojunction with Au nanomesh electrodes exhibit a power conversion efficiency of 4.69%. After antireflection coating, the device shows the efficiency of 5.96% at 0.44 cm^2 of the active area.

Hydrogen appears as a next-generation clean energy source to replace fossil fuels. One of the most promising ways to produce hydrogen is photoelectrochemical (PEC) water splitting. However, the existing photoelectrodes such as Si with noble metal catalysts still suffer from low efficiency and poor stability and the extremely high cost of the noble metal catalysts limits the wide use of water splitting photoelectrodes. Therefore, a novel approach is necessary to make a breakthrough for highly efficient PEC water splitting. This thesis contains that the demonstration of wafer-scale, transferable, and transparent thin-film catalysts based on MoS_2, which consists of cheap and earth abundant elements, can provide the low onset potential of 1 mA/cm^2 at 0.17 V versus a reversible hydrogen electrode and the high photocurrent density of 24.6 mA/cm^2 at 0 V for a *p*-type Si photocathode. c-Domains with vertically stacked (100) planes in the transferable 2H-MoS_2 thin

films, which are grown by a thermolysis method, act as active sites for the hydrogen evolution reaction, and photogenerated electrons are efficiently transported through the *n*-MoS_2/*p*-Si heterojunction**.**

Moreover, in chapter 4.3, the anion-engineered MoS_2 thin-films display the higher catalytic activity compared to the partially vertical-aligned MoS_2 thin films, due to its many inherent dangling bonds on their surface and the metallic nature. The transferrable and transparent anion-engineered molybdenum disulfide thin-film catalysts synthesized through simple thermolysis method by using $[(NH_4)_2MoS_4]$ solution and powder precursors with different sulfur/phosphorus weight ratios. The synthesized sulfur-doped molybdenum phosphide (S:MoP) thin film changed from two-dimensional van der Waals structure to three-dimensional hexagonal structure by introduction of phosphorus atoms in the MoS_2 thin film. The S:MoP thin film catalyst, which is composed of cheap and earth abundant elements, could provide the lowest onset potential and the highest photocurrent density for planar *p*-type Si photocathode. The density functional theory calculations indicate that the surface of S:MoP thin film absorb hydrogen better than that of MoS_2 thin film. The structurally engineered thin film catalyst facilitates the easy transfer of photogenerated electrons from *p*-Si light absorber to electrolyte. Anion-engineering of MoS_2 thin film catalyst would be an efficient way to enhance the catalytic activity for photoelectrochemical water splitting.

Student Number: 2014-31048

Ki Chang Kwon

Table of Contents

List of Tables

List of Figures

Chapter 1

Introduction to Transition Metal Dichalcogenides and Its Synthetic Method

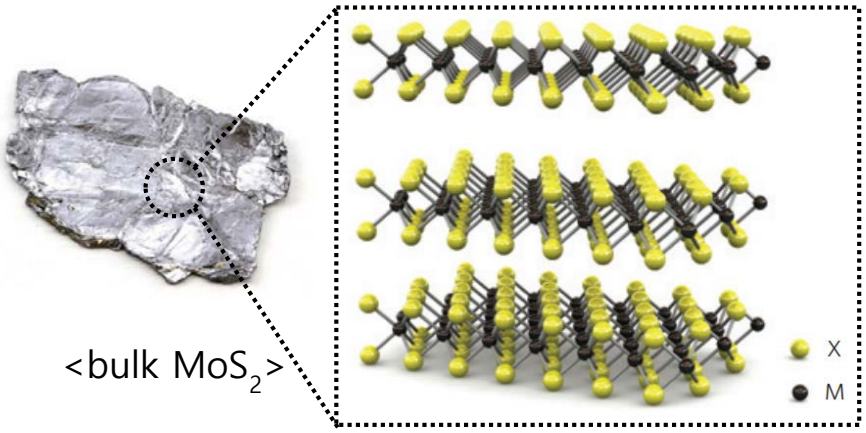

1.1. Scope and objective of the thesis

This thesis focuses on the synthesis of transition metal disulfides (TMD) thin films by using chemical vapor deposition technique for applying to photovoltaic cells and water splitting catalysts. The TMD have been reported as a tremendous potential material because of its unique physical properties such as high absorption coefficient, semiconducting, and flexibility etc. The chemical vapor deposition method is the best way to synthesize the uniform atomically thin TMD films without the pinholes.

The atomically thin TMD films can be one of the possible charge transport layer in optoelectronic devices and the light absorber in Si-based photovoltaic cells. In optoelectronic devices, the synthesized TMDs can act as not only the charge transport layer but also the passivation layer for preventing the diffusion of defective atoms from the transparent conduction electrode. In addition, though the 0.6-nm-thick MoS_2 film could generate the more exitons compared to 50-nm-thick Si, the most of generated exitons are disappeared. The p-n junction between *p*-Si and *n*-MoS_2 can utilize the light absorption property of the MoS_2 and the Au meshed electrode not only make the ohmic contact between n-MoS_2 and Au electrode, but also increase the amount of light absorption compared to the Al-fingered electrode in conventional Si-based photovoltaic cells. The additional anti-reflective coating on the fabricated photovoltaic cell shows the increase of photocurrent density and the power conversion efficiency.

The TMD thin films, especially *n*-type MoS_2 have recently attracted potential electrocatalyst because of its inherent catalytic edge sites, environmentally clean, and low cost. In case of photoelectrochemical water splitting, the Si was widely used as a photocathode due to its high visible light absorption and well-defined technology. However, two main issues such as low stability and high overpotential should be resolved for the industrial application. The surface of *p*-Si was easily degraded under the light illumination with electrolyte. High overpotential originates from the high hydrogen adsorption Gibbs free energy. The *n*-MoS_2/*p*-Si photocathode could provide not only passivation layer and catalytic edge sites for efficiently evolving hydrogen. Furthermore, the band energy diagram of the *n*-MoS_2/*p*-Si clearly shows that the photogenerated electrons can be transported from the p-Si photocathode to n-MoS_2, resulting in the fabricated *n*-MoS_2/*p*-Si could be a candidate for replacing platinum catalysts. Even though the *n*-MoS_2/*p*-Si photocathode shows the enhanced catalytic behavior compared to bare *p*-Si photocathode, it is not comparable to the platinum. The anion-engineering of *n*-MoS_2 could be the one of possible way to enhance the catalytic activity of MoS_2. Many dangling bonds on the sulfur-doped molybdenum phosphide could provide a plenty of sites for absorbing the hydrogen ions and the 2D to 3D structural transition gives the more stability in electrolytes.

From these results, the atomically thin TMD films can utilize into various device applications and the defect-engineering of TMD films could provide the higher device performance.

1.2. Transition Metal Dichalcogenides (TMDs)

As a new class of material, two-dimensional (2D) atomic crystals have attracted enormous research interest in the last decade that has led to a number of breakthroughs in physics owing to the confined charge, spin and heat transport within the 2D planes.[1] The most outstanding one of these materials is graphene, as its exceptional electronic, optical and mechanical properties may hold great promise for a variety of future applications.[2] However, the zero energy gap of graphene greatly impedes its application in logic electronics, creating a very real need for an analogous substitute that can offer a finite bandgap. Furthermore, unlike graphene, many 2D transition metal dichalcogenides (TMDs) are semiconductor in nature and possess huge potential to be made into ultra-small and low power transistors that are more efficient than state-of-the-art silicon based transistors fighting to cope with ever-shrinking devices.[3,4] Besides sharing the similarities of a band gap in the visible-near IR range, high carrier mobility, and on/off ratio with ubiquitous silicon, TMDs can be deposited onto flexible substrates and survive the stress and strain compliance of flexible supports.[5,6]

Graphene, while being fundamentally and technologically interesting for a variety of applications, is chemically inert and can only be made active by functionalization with desired molecules, which in turn results in the loss of some of its exotic properties.[7] In contrast, single-layered 2D TMDs — whose generalized formula is MX_2, where M is a transition metal of groups 4 – 10 and X is a chalcogen (Fig. 1.1.) — exhibit versatile chemistry. This offers

opportunities for fundamental and technological research in a variety of fields including catalysis, energy storage, sensing and electronic devices such as field-effect transistors and logic circuits.

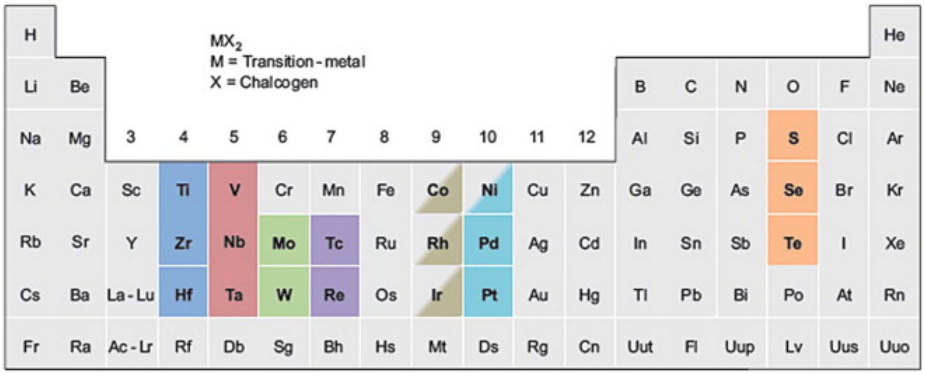

Fig. 1.1. About 40 different layered TMD compounds exist. The transition metals and the three chalcogen elements that predominantly crystallize in those layered structure are highlighted in the periodic table.

Fig. 1.1 depicts the 40 different layered TMD compounds which can exist in MX_2 form. Even though 2D TMDs exhibit a breadth of new properties that are distinct from transition bulk semiconductors or materials, developing such materials into large-scale and defect-free atomic layers with thickness controllability on desired substrates is challenging. This chapter will address the synthesis technique of TMDs and its basic properties. The application of synthesized TMDs from various techniques also be addressed in this chapter.

1.2.1. Crystal structure

Many TMDs crystallize in a graphite-like layered structure that leads to strong anisotropy in their electrical, chemical, mechanical and thermal properties.[8] Group 4–7 TMDs in Fig. 1.1 are predominantly layered, whereas some of group 8–10 TMDs are commonly found in non-layered structures. In layered structures, each layer typically has a thickness of 6~7 Å, which consists of a hexagonally packed layer of metal atoms sandwiched between two layers of chalcogen atoms. The intralayer M–X bonds are predominantly covalent in nature, whereas the sandwich layers are coupled by weak van der Waals forces thus allowing the crystal to readily cleave along the layer surface. The metal atoms provide four electrons to fill the bonding states of TMDs such that the oxidation states of the metal (M) and chalcogen (X) atoms are +4 and –2, respectively. The lone-pair electrons of the chalcogen atoms terminate the surfaces of the layers, and the absence of dangling bonds renders those layers stable against reactions with environmental species. The M – M bond length varies between 3.15 Å and 4.03 Å, depending on the size of the metal and chalcogen ions. These values are 15–25 % greater than the bond lengths found in elemental transition metal solids, indicating limited energetic and spatial overlap of the d orbitals in TMD compounds. The metal coordination of layered TMDs can be either trigonal prismatic or octahedral (typically distorted and sometimes referred to as trigonal-antiprismatic) as shown in Fig.1.2, respectively.

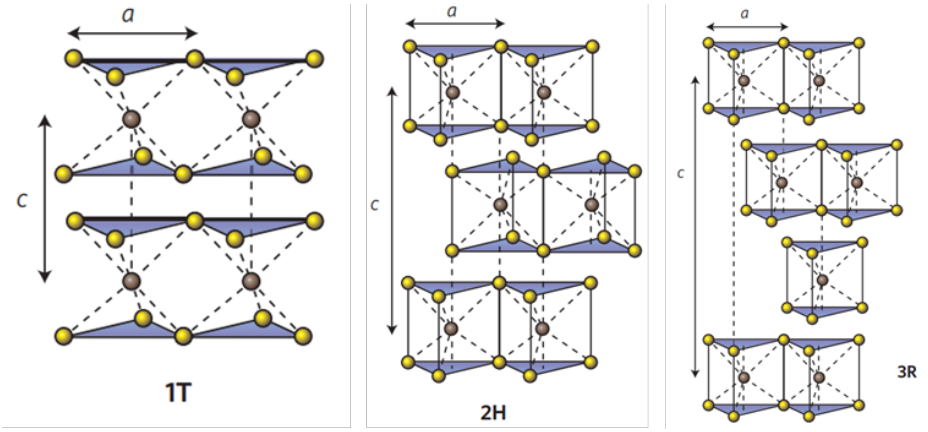

Fig. 1.2. The crystal structure of TMDs according to the coordination of metal and chalcogen atoms. (a) 1T-phase (tetragonal), (b) 2H-phase (hexagonal), and (c) 3R-phase (rhombohedral) TMDs.

Depending on the combination of the metal and chalcogen elements, one of the two coordination modes is thermodynamically preferred. In contrast to graphite, bulk TMDs exhibit a wide variety of polymorphs and stacking polytypes (a specific case of polymorphism) because an individual MX_2 monolayer, which itself contains three layers of atoms (X–M–X), can be in either one of the two phases. Most commonly encountered polymorphs are 1T, 2H and 3R where the letters stand for trigonal, hexagonal and rhombohedral, respectively, and the digit indicates the number of X–M–X units in the unit cell (that is, the number of layers in the stacking sequence). There are three different polytypes (that is, three different stacking sequences) for 2H polymorphs. A single TMD can be found in multiple polymorphs or polytypes, depending on the history of its formation. For example, natural MoS_2 is commonly found in the '2H phase' where the stacking sequence is AbA BaB (The capital and lower case letters denote chalcogen and metal atoms, respectively). Synthetic MoS_2, however, often contains the 3R phase where the stacking sequence is AbA CaC

BcB.[9] In both cases, the metal coordination is trigonal prismatic. Group 4 TMDs such as TiS_2 assume the 1T phase where the stacking sequence is AbC AbC and the coordination of the metal is octahedral. For the sake of simplicity, we will focus our attention on monolayer TMDs in the discussions below. It should be highlighted that monolayer TMDs exhibit only two polymorphs: trigonal prismatic and octahedral phases. The former belongs to the D3h point group whereas the latter belongs to the D3d group. In the following discussion, they are referred to as monolayer 1H (or D3h)- and 1T (or D3d)- MX_2, respectively. Recent studies have shown that due to the lattice match of the 1H and 1T phases of MoS_2 and WS_2, coherent interfaces between domains of the two phases can also form.[10]

1.2.2. Physical properties

2D TMDs exhibit unique electrical and optical properties that evolve from the quantum confinement and surface effects that arise during the transition of an indirect bandgap to a direct bandgap when bulk materials are scaled down to monolayers. This tunable bandgap in TMDs is accompanied by a strong photoluminescence(PL) and large exciton binding energy, making them promising candidate for a variety of opto-electronic devices, including solar cells, photo-detectors, light-emitting diodes, and photo-transistors.[11,12] For example, unique properties of MoS_2 include direct bandgap (1.8 eV), good mobility (700 cm^2 V^{-1} s^{-1}), high current on/off ratio of 10^7 –10^8 , large optical absorption (10^7 m^{-1} in the visible range) and a giant PL arising from the direct bandgap (1.8 eV) in monolayer; thus, it has been studied widely for electronics and optoelectronics applications.[13]

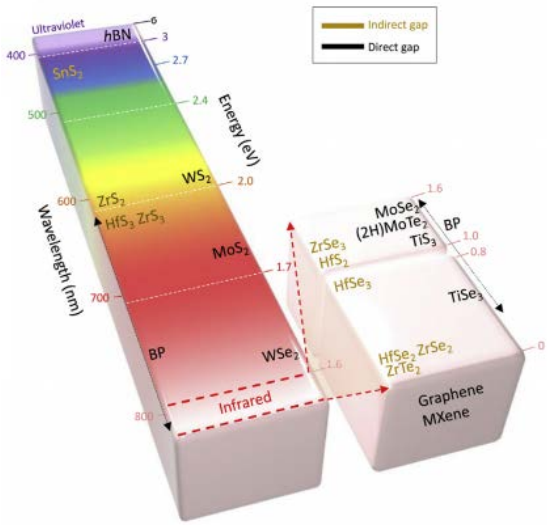

Fig. 1.3. Bandgap of 2D layered materials varying from zero band gap of graphene (white color) to wide bandgap of hBN. The color in the column is presenting the corresponding wavelength of bandgaps of each 2D TMDs.

Despite the extraordinary mobility of electrons (i.e. 15,000 cm^2 V^{-1} s^{-1} at room temperature) in graphene, the lack of a bandgap restricts its use as an active element in FETs.[14] Tremendous efforts to open the bandgap of graphene using nanoribbons, AB-stacked bilayer graphene, and chemical doping have met with marginal success providing the bandgap opening up to 200 meV in most cases.[15,16] This remains a challenging issue and has been a driving force in developing 2D TMDs with a finite bandgap. As listed in Fig. 1.3, the 2D TMDs reveal a wide range of bandgap covering all visible and infrared range with the choice of material.[15] Most semiconducting 2D TMDs reveal direct bandgap in monolayer, whereas they are indirect bandgap in bulk form except few cases of GaSe and ReS_2. For example, monolayer dichalcogenides such as MoS_2 (1.8 eV), $MoSe_2$ (1.5 eV), (2H)-$MoTe_2$ (1.1 eV), WS_2 (2.1 eV) and WSe_2 (1.7 eV) show direct bandgap, whereas bulk phases exhibit indirect gap with smaller energies.[17] Most MX_2 materials have both metallic phase and semiconducting phase.[17] The stable phase of MX_2 material at room temperature is 2H phase, whereas 1T phase can be obtained by Li-intercalation or electron beam irradiation. The chemically exfoliated 1T MoS_2 phase is known to be 107 times more conductive than the semiconducting 2H phase. In case of WTe_2, 1T or $1T^0$ phase is more stable than 2H phase at room temperature. Both 2H and $1T^0$ phase in $MoTe_2$ can be easily modulated into each other because the cohesive energy difference between both phases is similar to each other. Besides, the dichalocogenides of titanium (Ti), chromium (Cr), nickel (Ni), zinc (Zn), vanadium (V), niobium (Nb), and tantalum (Ta) simply exhibit metallic behavior.[18] Besides excellent electrical transport,

TMDs are mechanically flexible and strong similar to graphene. An exceptionally high Young's modulus (E) of 0.33 - 0.07 TPa has been reported in suspended few-layer MoS_2 nanosheets, as shown in Fig. 1.4.[19] The Young's modulus of monolayer MoS_2 outperforms the stainless steel (204 GPa) and graphene oxide (207 GPa), which are attributed to the absence of stacking faults, high crystallinity and defect-free nature of the atomically thin TMDs.[19].

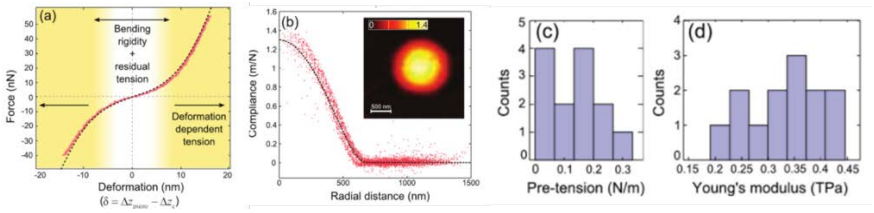

Fig. 1.4. (a) Force versus deformation traces obtained on a flake 8 layers thick suspended over a hole 1.1 μm in diameter. (b) Force–volume measurement showing a colormap of the compliance (inset) and its radially-averaged profile of the sheet as (a). (c), (d) Histogram of the Young's modulus obtained from fitting F(d) curves.

Although the various TMDs have been revealed its excellent optical, electrical, mechanical properties with its high crystallinity, defect-free, and atomically thin films, the development of its synthetic techniques is still challenging to make the higher quality of TMDs for applying these materials to industry. The synthetic techniques of TMDs by using mechanical and liquid exfoliation, chemical vapor deposition, etc.

1.3. Synthetic methods

Considerable efforts have been devoted to the synthesis of controllable, large-scale, and uniform atomic layers of diverse 2D TMDs using various top-down and bottom-up approaches, including mechanical exfoliation, chemical exfoliation, and chemical vapor deposition (CVD). Most of the reported data and theory on the fundamental physics and devices on 2D TMDs have largely relied on the exfoliation method due to its high quality. However, the critical limitations of the flake size and film uniformity have dragged its development beyond the fundamental studies. On the contrary, the CVD process has been studied for scalable and reliable production of large area 2D TMDs. Nevertheless, CVD grown TMDs show poor quality as compared to their exfoliated counterparts. Very recently, many attempts have been made to obtain high quality TMDs with thickness controllability and wafer-scale uniformity using atomic layer deposition (ALD), metal-organic-CVD (MOCVD), and direct deposition methods (sputtering, pulsed laser deposition (PLD), e-beam). The 2D materials forming chemical reactions generally use either thermal energy from a heated substrate or non-thermal energy such as microwave or photon energy into the reaction process and the 2D materials forming process depends on lattice parameter of substrates, temperatures, and atomic gas flux. Here, the following chapters are focused on the 2D TMDs growth by mechanical exfoliation, liquid exfoliation, chemical vapor deposition methods.

1.3.1. Mechanical exfoliation

In 2004, Novoselov et al. successfully produced various single-layer 2D crystals from bulk materials, such as graphite, hBN, MoS_2, $NbSe_2$, etc.[20] Atomically thin flakes including the graphite, various TMDs can be peel from bulk material by micromechanical exfoliation using adhesive tape, such as graphene. As layered materials, MoS_2 can be cleavage as graphene using the same technique.

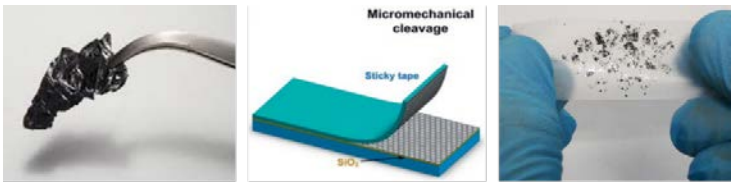

Fig. 1.5. The photographic images and schematic illustration of mechanical exfoliation of bulk MoS_2 by using scotch tape method.

Fig. 1.5 shows the photographic images and schematic illustration of mechanical exfoliation of bulk MoS_2 by using scotch tape method. This method is typically adopted to prepare single-layer TMDs samples. The single crystal TMDs samples prepared by the mechanical exfoliation method are of good quality, and can be used for studying their basic properties by optical microscopy, atomic force microscopy (AFM), scanning tunneling microscopy (STM), transmission electron microscopy (TEM) and so on.[21-23]

The sample made by this method has high purity and cleanliness that is ideal for demonstration of high-performance devices and condensed-matter phenomena. However, micromechanical exfoliation method has inevitable shortcomings, that is the thickness and size of samples is not controllable.

1.3.2. Liquid exfoliation

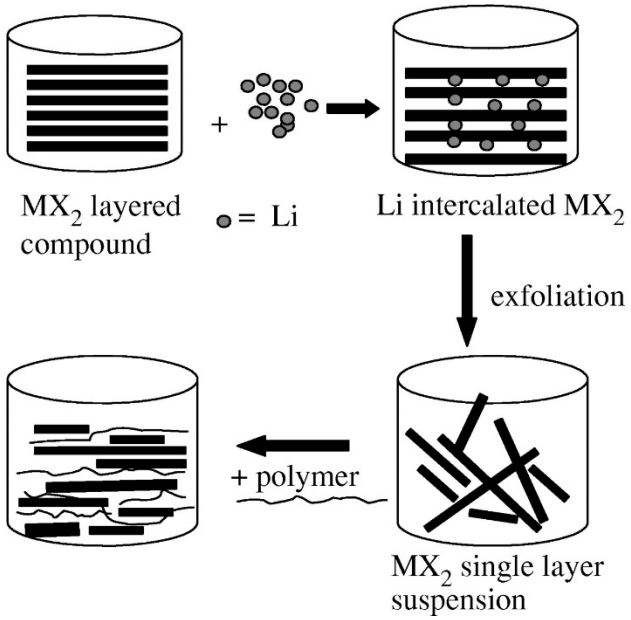

Fig. 1.6. The schematic illustration of lithium (Li) intercalation of bulk MX_2 layered compounds. The polymer was used to prevent the aggregation of exfoliated nanosheets.

Compared with the mechanical exfoliation method, the intercalation method can obtain a large number of nanosheets, which allows layered materials to be exfoliated in liquid by certain ions.[24,25] The basic principle is that a lithium-containing compound such as n-butyllithium (n-BuLi) is embedded in bulk molybdenum disulfide power in solution, and form Li_xMoS_2 ($x \geq 1$), The protic solvent (usually water, also can choose dilute acid or low boiling point of alcohol) reacts vigorously with intercalation compounds between the layers to evolve H_2 gas, which rapidly separates the layers, multi-layer and single-layer MoS_2 is obtained at last.

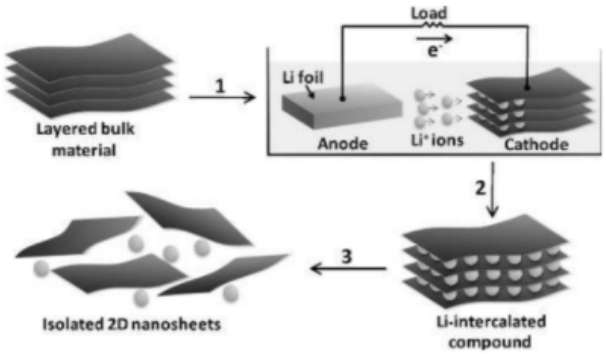

Fig. 1.7. Electrochemical lithiation process for the fabrication of 2D nanosheets from the layered bulk materials.

Compared with more than a day for the n-BuLi method, there is a new method of lithiation which require only several hours for Li intercalation uses an electrochemical cell with a lithium foil anode and MoS_2 cathode (Fig. 1.7).[26] The intercalation will occur while a galvanic discharge is occurring in the electrochemical cell, and the degree of lithiation can be monitored and controlled. The electrochemical lithiation method can be easily conducted at room temperature within 6h, compared to the lithium intercalation method. Furthermore, the n-BuLi is relatively expensive method and ineffective way to obtain nanosheets due to its high cost and fast aggregation of exfoliated nanosheets.

Another method is liquid exfoliation which uses the appropriate solvent and high-power sonication. In recent studies, the liquid exfoliation method has been performed on MoS_2.[27] MoS_2 powder was dispersed in solution which is water and surfactant or organic solvent such as N-methyl-2-pyrrolidone (NMP), 1-ethyl-2-pyrrolidinone (EP), dimethylcarbinol (DMC), dimethyl sulfoxide (DMSO), and so on. Then, the suspensions were ultrasonic, centrifuged, dried.

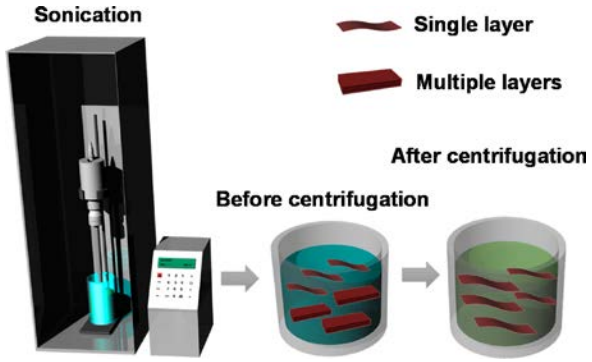

Fig. 1.8. Synthetic scheme of TMD nanosheets via liquid exfoliation with ultrasonication.

The key parameters were material concentration, surfactant concentration, sonication method, duration, and centrifuge speed. Different concentrations of surfactant solutions and material suspensions were mixed, these suspensions were dispersed by sonication method for different time, and then the suspension was centrifuged for different time with different speeds. It is evident that the optimized parameters were 3 mg/ml surfactant concentration, 3 mg/ml material concentration, and a RPM speed of 500 for 60 minutes. It is attractive that liquid exfoliation can product a mass of layered MoS_2 in spite of lower stripping degree and the stripping efficiency.

The liquid exfoliation is one of promising approaches to obtain nanosheet form of TMDs with mass production. However, the quality of synthesized TMDs from this method is relatively lower than mechanical exfoliation, that is to say, it is not appropriate for the sensitive electronic devices such as memory or field-effect transistors. The following chemical vapor deposition technique is the most potential candidate for synthesizing the large-scale thin film growth and the higher quality of TMD thin films for resolving these issues.

1.3.3. Chemical vapor deposition

The CVD is one of the most effective methods to achieve large area growth of atomically thin 2D TMDs for the successful device applications. The simplest form of CVD to grow 2D TMDs is the co-evaporation of metal oxides and chalcogen precursors that lead to vapor phase reaction followed by the formation of a stable 2D TMD over a suitable substrate. The growth mechanism of CVD method differs in each synthesis process as the materials forming process also depends on (1) properties of substrate, (2) temperature and (3) atomic gas flux as briefly discussed in the following section.

(1) Properties of substrate: the atomic layer of 2D materials is influenced by nanoscale surface morphology and terminating atomic planes of substrates as well as lattice mismatching.

(2) Temperature: the reaction process is limited by the growth temperature. Normally, if the growth temperature is high, that is, the surface diffusion is fast enough, a randomly deposited adatoms will move to the energetically most favorable places and results in a 3D island growth. On the other hand, if the substrate temperature is too low, an amorphous or polycrystalline film will form since adatoms will not have enough kinetic energy to diffuse and find the lowest potential energy site.[28]

(3) Atomic gas flux: atomic gas flux is another important parameter to achieve high quality 2D materials growth. Only a sufficient high vapor pressure enables mixing of atomic gases and transport the atomic species to the substrate. The stability of vaporized atoms is required to prevent unnecessary reaction

during vaporized atom transport to the substrate. The vaporized atoms are transported by a carrier gas to the substrate and the flow rate of vapored atom is governed by the Clausius– Clapeyron equation. Lee et al. reported large-scale MoS_2 layers by chemical vapor reaction of molybdenum trioxide (MoO_3) and sulfur powder at elevated temperatures (650 °C).[29] MoO_3 is initially reduced into a sub-oxide MoO_{3-x}, which reacts with vaporized sulfur further to form a 2D layered MoS_2 film. This simple process is capable of producing large-scale MS_2; however, it often results in the formation of randomly distributed flakes rather than a continuous film. The inhibition of the growth of MoS_2 was attributed to the presence of interfacial oxide layer as a significant obstacle. In a similar approach, Najmaei et al. synthesized MoS_2 atomic layers on SiO_2/Si substrates by using the vapor-phase reaction of MoO_3 and S powders and reported the formation of MoS_2 monolayer triangular flakes on the substrates rather than the formation of a continuous MoS_2 layer.[13,84,30] Wang et al. found an interesting shape evolution in CVD grown MoS_2 domains from triangular to hexagonal geometries depending upon the spatial location of the silicon substrate as shown in Fig. 1.9.[31]

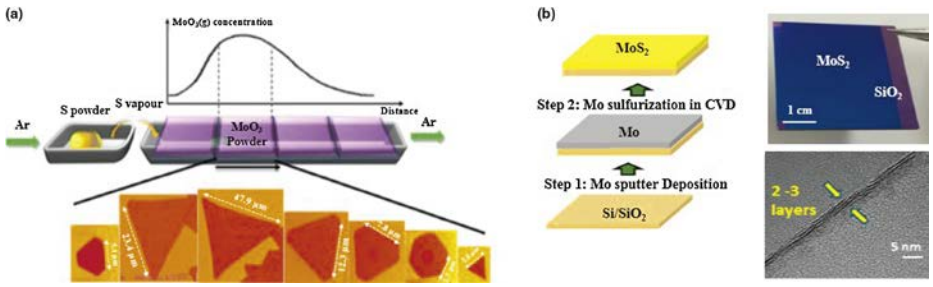

Fig. 1.9. (a) Schematic diagram of CVD process and AFM images showing shape evolution of MoS2 crsytals from triangular to hexagonal depending on the spatial location of silicon substrate. (b) Large area growth of 2 – 3 layers of MoS2 using Mo seed layer sulfurized in a CVD furnace.

Another facile method for growing large area and continuous TMDs is using the ‘two-step method, depositing transition metal thin film (e.g. Mo, W, Nb, etc.) on substrate (usually Si/SiO2) followed by thermal reaction with chalcogen (S, Se, Te) vapor. The following reaction occurs to form a stable 2D TMD during the CVD process at high temperatures (300 – 700 °C) and inert atmosphere. This ‘two-step method’ has demonstrated wafer scale fabrication (2 inches) and successful thickness modulation of MoS_2 layers (multilayer to monolayer) on SiO_2/Si substrates (Fig. 1.9).[32] After metal deposition (Mo, W) with controlled thickness, the metal-coated substrate and sulfur powder were placed inside the CVD furnace, and the reaction environment was kept inert under a constant flow of 200 sccm Ar at 600 °C for 90 min. In addition to metal film approach, direct sulfurization/selenization of various metal oxide and chloride precursors such as $(NH_4)_2MoS_4$, MoO_3, and WO_3 have been widely employed to grow TMDs.

The metal-organic chemical vapor deposition (MOCVD) is similar to a conventional CVD except that metal-organic or organic compound precursor are used as the source materials.[33] In MOCVD reaction, the desired atoms are combined with complex organic molecules and flown over a substrate where the molecules are decomposed by heat and the target atoms are deposited on the substrate atom by atom. The quality of films can be engineered by varying the composition of atoms at atomic scale, which results in the desired thin film with high crystallinity.

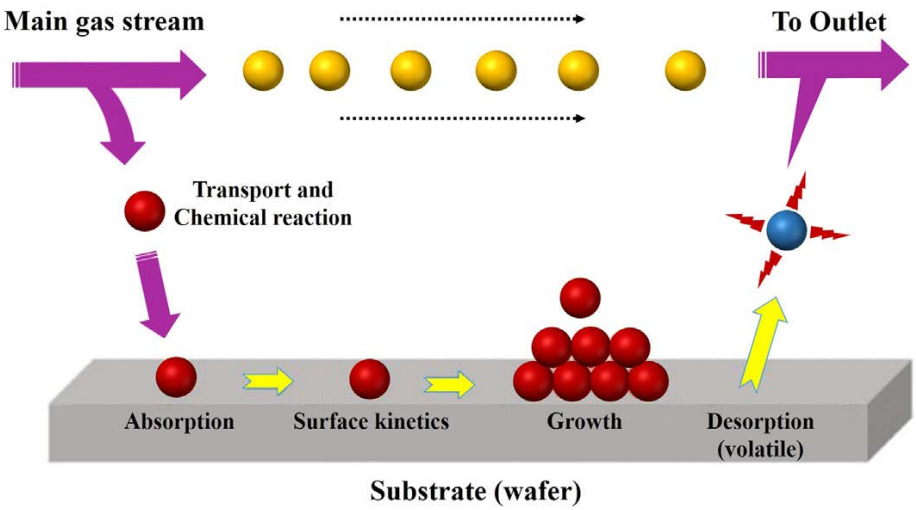

Fig. 1.10. Deposition process on the substrate and surface processes in MOCVD while growing active layers on the substrate. The gaseous precursors are thermally decomposed and adsorbed on the substrate followed by surface diffusion kinetics to form quality thin films.

Fig. 1.10 is the representative schematic of the MOCVD method showing various steps involved during the syn-thesis of 2D materials. A series of surface reactions occur during MOCVD process including adsorption of precursor molecules followed by surface kinetics (i.e. surface diffusion), nucleation and growth of desired material with the desorption of the volatile product molecules. MOCVD has been used to grow 2D TMDs only very recently. The advantages of MOCVD in 2D TMDs growth are: (i) it can achieve large-scale and uniform growth of 2D TMDs, (ii) it provides a precise control over both metal and chalcogen precursors and thereby controls the composition and morphology of 2D TMDs. Kang et al. synthesized wafer-scale (4-in.) mono-layer and few layers MoS_2 and WS_2 films on SiO_2 substrates by using molybdenum hexacarbonyl ($Mo(CO)_6$), tungsten hexacarbonyl ($W(CO)_6$), ethylene disulfide ($((C_2H_5)2_S$), and H_2 gas-phase precursors with Ar carrier gas.[34]

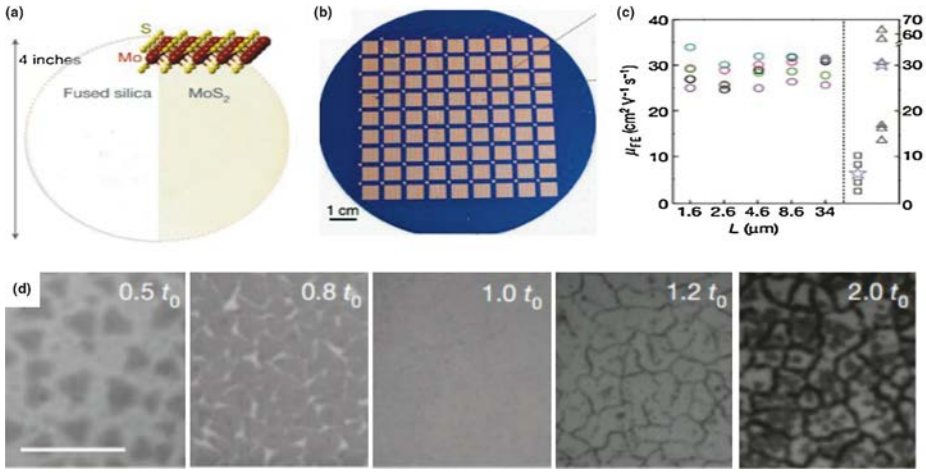

Fig. 1.11. Large scale MOCVD growth of continuous (a) MoS_2 monolayers on fused silica using all-gas phase precursors. (b) The scalable growth enables mass production of ~ 8000 of FET devices. (c) Field effect mobility (μ_{FE}) measured from five FET devices with different length scales. A consistent mobility of ~ 30 $cm^2V^{-1}s^{-1}$ was observed. (d) Optical images of MoS_2 films at different growth times, where t0 is the optimal growth time for full monolayer coverage (scale bar: 10 mm).

They show large-scale MoS_2 and WS_2 films on 4-inch fused silica substrates (Fig. 1.11a), and about 8000 MoS_2 FET devices fabricated by a standard photolithography process (Fig. 1.11b). The MoS2-FETs showed high electron mobility of ~ 30 $cm^2V^{-1}s^{-1}$ at room temperature and 114 $cm^2V^{-1}s^{-1}$ at 90 K (Fig. 1.11c). Fig. 1.11d is the time evolution of the monolayer coverage over the entire substrate as a function of critical time (t0).

From these results, the chemical vapor deposition method is one of promising way to synthesize the atmonically thin TMDs with defect-free, high crystallinity. The CVD grown TMDs are relatively expensive way, but the quality of synthesized thin films shows the better compared to other previously mentioned two techniques.

1.4. References

[1] K. S. Novoselov, D. Jiang, F. Schedin, T. J. Booth, V. V. Khotkevich, S. V. Morozov and A. K. Geim, *Proc. Natl. Acad. Sci. U. S. A.*, **2005**, *102*, 10451.

[2] K. S. Novoselov, A. K. Geim, S. V. Morozov, D. Jiang, M. I. Katsnelson, I. V. Grigorieva, S. V. Dubonos and A. A. Firsov, *Nature*, **2005**, *438*, 197.

[3] X.-R. Wang, Y. Shi, Z. Rong, *Chin. Phys. B*, **2013**, *22*, 098505.

[4] S. Das, J. A. Ronbinson, M. Dubey, H. Terrones, M. Terrones, *Annu. Rev. Mater. Res.*, **2015**, *45*, 1.

[5] R. Cheng, S. Jiang, Y. Chen, Y. Liu, N. Weiss, H.-C. Cheng, H. Wu, Y. Huang, X. Duan, *Nat. Commun.*, **2014**, *5*, 5143.

[6] D. Akinwande, N. Petrone, J. Hone, *Nat. Commun.*, **2014**, *5*, 5678.

[7] K. P. Loh, Q. L. Bao, G. Eda, M. Chhowalla, *Nat. Chem.*, **2010**, *2*, 1015.

[8] J. A. Wilson, F. J. di Salvo, S. Mahajan, *Adv. Phys.*, **1975**, *24***,** 117.

[9] J. A. Wilson, A. D. Yoffe, *Adv. Phys.*, **1969**, *18***,** 193.

[10] G. Eda, T. Fujita, H. Yamaguchi, D. Voiry, M. W. Chen, M. Chhowalla, *ACS Nano*, **2012**, *6***,** 7311.

[11] W. Bao, X. Cai, D. Kim, K. Sridhara, M. S. Fuhrer, *Appl. Phys. Lett.*, **2013**, *102*, 042104.

[12] G. Frey, S. Elani, M. Homyonfer, Y. Feldman, R. Tenne, *Phys. Rev. B*, **1998**, *57*, 6666.

[13] M.S. Fuhrer, J. Hone, *Nat. Nanotechnol.*, **2013**, *8*, 146.

[14] K. Novoselov, A. K. Geim, S. V. Morozov, D. Jiang, M. I. Katsnelson, I. V. Grigorieva, S. V. Dubonos, A. A. Firsov, *Nature*, **2005**, *438*, 197.

[15] S.Y. Lee, D. L. Duong, Q. A. Vu, Y. Jin, P. Kim, Y. H. Lee, *ACS Nano*, **2015**, *9*, 9034.

[16] M.Y. Han, et al. Phys. Rev. Lett. 98 (2007) 206805.

[17] W. Choi, N. Choudhary, G. H. Han, J. Park, D. Akinwande, Y. H. Lee, *Mater. Today*, **2017**, *20*, 116.

[18] Q.H. Wang, K. Kalantar-Zadeh, A. Kis, J. N. Coleman, M. S. Strano, *Nat. Nanotechnol.*, **2012**, *7*, 699.

[19] A. Gastellanos-Gomez, M. Poot, G. A. Steele, H. S. J. van der Zant, N. Agrait, G. Rubio-Bollinger, *Adv. Mater.*, **2012**, *24*, 772.

[20] S.Z. Butler, et al. *ACS Nano*, **2013**, *7*, 2898.

[21] J. Lee, P. Dak, Y. Lee, H. Park, W. Choi, M. A. Alam, S. Kim, *Sci. Rep.*, **2014**, *4*, 7352.

[22] C.-H. Lee, G.-H. Lee, A. M. van der Zande, W. Chen, Y. Li, M. Han, X. Cui, G. Arefe, C. Nuckolls, T. F. Heinz, J. Guo, J. Hone, P. Kim, *Nat. Nanotechnol.*, **2014**, *9*, 676.

[23] X. Zhou, J. Cheng, Y. Zhou, T. Cao, H. Hong, Z. Liao, S. Wu, H. Peng, K. Liu, D. Yu, *J. Am. Chem. Soc.*, **2015**, *137*, 7994.

[24] D. Sarkar, W. Liu, X. Xie, A. C. Anselmo, S. Mitraqotri, K. Banerjee, *ACS Nano*, **2014**, *8*, 3992.

[25] G.Z. Madga, J. Peto, G. Dobrik, C. Hwang, L. P. Biro, L. Tapaszto, *Sci. Rep.*, **2015**, *5*, 14714.

[26] X. Zhou, J. Cheng, Y. Zhou, T. Cao, H. Hong, Z. Liao, S. Wu, H. Peng, K. Liu, D. Yu, *J. Am. Chem. Soc.*, **2015**, *137*, 7994.

[27] A. Gastellanos-Gomez, M. Poot, G. A. Steele, H. S. J. van der Zant, N. Agrait, G. Rubio-Bollinger, *Adv. Mater.*, **2012**, *24*, 772.

[28] A. Mzerd, D. Sayah, J. C. Tedenac, A. Boyer, *J. Cryst. Growth*, **1994**, *140*, 365.

[29] Y.H. Lee, X.-Q. Zhang, W. Zhang, M-T. Chang, C.-T. Lin, K.-D. Chang, Y.-C. Yu, J. T.-W. Wang, C.-S. Chang, L.-J. Li, T.-W. Lin, *Adv. Mater.*, **2012**, *24*, 2320.

[30] S. Najmaei, Z. Liu, W. Zhou, X. Zou, G. Shi, S. Lei, B. I. Yakobson, J.-C. Idrobo, P. M. Ajayan, J. Lou, *Nat. Mater.*, **2013**, *12*, 754.

[31] S. Wang, Y. Rong, Y. Fan, M. Pacios, H. Bhaskaran, K. He, J. H. Warner, *Chem. Mater.*, **2014**, *26*, 6371.

[32] J. Park, N. Choudhary, J. Smith, G. Lee, M. Kim, W. Choi, *Appl. Phys. Lett.*, **2015**, *106*, 012104.

[33] H.M. Manasevit, *Appl. Phys. Lett.*, **1968**, *12*, 156.

[34] K. Kang, S. Xie, L. Huang, Y. Han, P. Y. Huang, K. F. Mak, C.-J. Kim, D. Muller, J. Park, *Nature*, **2015**, *520*, 656.

Application of synthetic TMDs to various devices

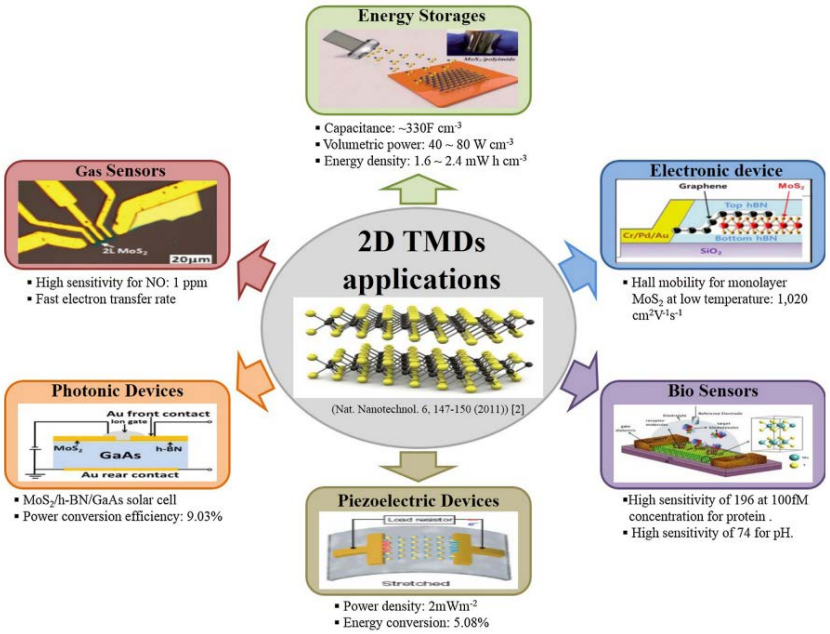

2. Application to various devices

2D TMD materials are considered attractive for diverse applications including electronics, photonics, sensing, and energy devices. These applications are inspired by the unique properties of layered materials such as thin atomic profile that represents the ideal conditions for maximum electrostatic efficiency, mechanical strength, tunable electronic structure, optical transparency, and sensor sensitivity. Of particular interest for applications is flexible nanotechnology, which is considered for potentially ubiquitous electronics and energy devices that can benefit from the range of outstanding properties afforded by 2D materials. Flexible technology comprises a wide array of scalable large-area devices including thin film transistors (TFTs), displays, sensors, transducers, solar cells and energy storage on mechanically compliant substrates.

2.1. Application to electronic devices

The scaling limits of conventional silicon-based technology over the last decades suggest that atomically thin semiconductors such as TMDs might be applicable for future generation large-scale electronics, provided manufacturing and integration challenges can be resolved.[1] Indeed, the first consumer product featuring graphene touch panel displays in smart-phones was released in China in 2014, after only ten years of global graphene research, a relatively short time in the innovation cycle. Moreover, in this timeframe, several articles have reviewed breakthroughs and perceived applications of 2D materials.[2]

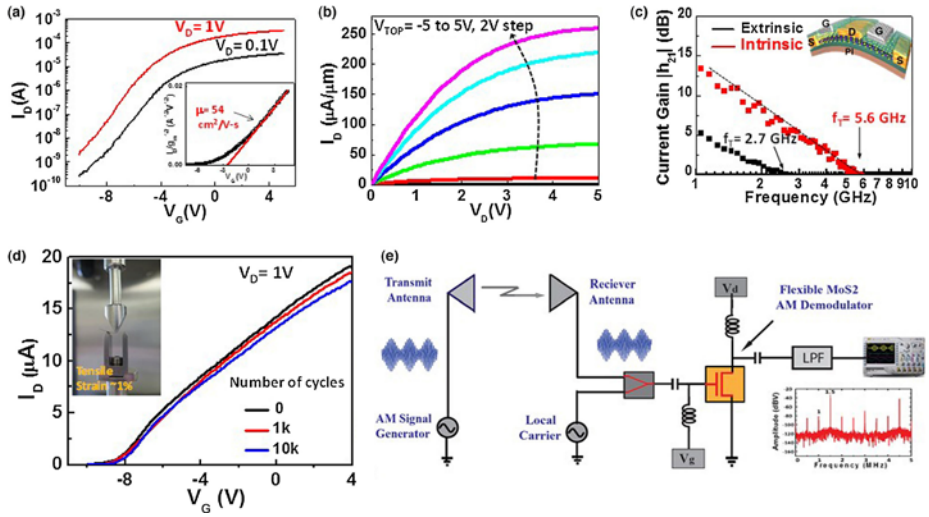

Fig. 2.1. Representative CVD-grown MoS_2 FET (L = 1 mm, W = 2.6 mm) on 280 nm SiO_2/Si. (a) Electrical transfer characteristics. The insert shows the low-field mobility ~54 $cm^2V^{-1}s^{-1}$, which is at the high-end for monolayer MoS_2. (b) I_D–V_D characteristics featuring linear-saturation profile expected for well-behaved semiconducting FETs. (c) Extracted cut-off frequency for flexible MoS_2 transistors with intrinsic f_T ~ 5.6 GHz (L = 0.5 mm). Inset is an illustration of the device structure. (d) Multi-cycle bending tests showing that the flexible MoS_2 afford strong electrical stability after 10,000 cycles of bending at 1% tensile strain. (e) Schematic of flexible MoS_2 RF transistor used as an AM demodulator within a wireless AM receiver system (AM radio band 0.54–1.6 MHz).

After several years of active research and development, the high-performance 2D TFTs based on synthesized MoS_2 have now been achieved. These TFTs operating at room temperature feature the characteristic high on/off current ratio and current saturation expected from high-quality TMDs (Fig. 2.1.). In particular, electron mobility ~ 50 $cm^2V^{-1}s^{-1}$ and current density ~ 250 mA/cm^2 have been observed, which is very encouraging for high-performance TFTs. Importantly, cut-off frequencies exceeding 5 GHz have been realized on flexible plastic substrates at a channel length of 0.5 mm (Fig. 2.1c). At first, this was rather surprising given the relatively low mobility of MoS_2; however, at the high fields needed for maximum high frequency operation, transport is determined by the saturation velocity (V_{sat}) that turns out to be sufficiently reasonable (2×10^6 cm/s) to achieve GHz speeds at sub-micron channel lengths.[3] In addition, flexible monolayer MoS_2 TFTs offer robust electronic performance to 1000 s of cycles of mechan-ical bending (Fig. 2.1d). Altogether, the combined high on/off ratio, saturation velocity and mechanical strength make MoS_2 and related TMDs very attractive for low-power RF TFTs for advanced flexible Internet of Things (IoT) and wearable connected nanosystems. Toward this end, a simple wireless flexible radio receiver system has been demonstrated using monolayer CVD MoS_2 for demodulation of the received signal, the central signal processing function of wireless receivers (Fig. 2.1e).

From these previous reports, the MoS_2 and TMDs could be one of the potential candidate for logic devices as a channel, replacing the Si-based logic

devices. The semiconducting properties of TMDs could be useful replacement which can resolve not only the limitation of device size and dimension, but also the lower on/off ratio and mobility of previous devices.

2.2. Application to water splitting catalysts

Photocatalytic water splitting, using solar energy to produce H_2, is considered as a promising technology to address environmental crises and energy shortages.[4,5] Solar water splitting based on inorganic semiconductors as a means of converting solar energy to chemical energy in the form of fuels has been drawn much attention since the 1970s.[6,7] Typically, the photocatalytic ability of a semiconductor depends on the absolute positions of the valence band (E_{VB}) and conduction band (E_{CB}) edges. If its E_{CB} is located more negative than that of hydrogen ($E_{H2/H+}$) and the E_{VB} is more positive than that of oxygen ($E_{O2/H2O}$), it is possible to split the water molecule into H_2 and O_2 under light. A proper band gap is therefore of primary importance for photocatalytic reactions.[4] Furthermore, the composite photocatalysts, including hybrids with other semiconductors, carbon materials and noble metals, are extensively studied due to improved carrier diffusion and efficient absorption of the solar spectrum.[8] The TMDs, especially MoS^2 and WS_2 could be lowered the activation energy barrier as a role of cocatalysts in photoelectrochemical water splitting, as shown in Fig. 2.2.

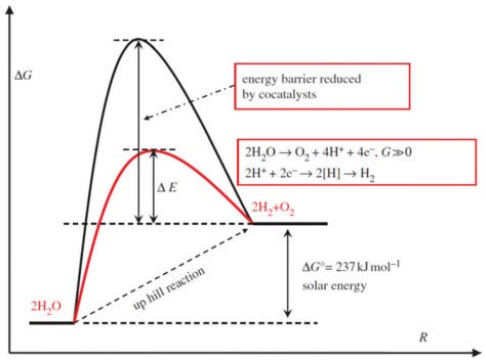

Fig. 2.2. Schematic description of energy diagram for photocatalytic water splitting.

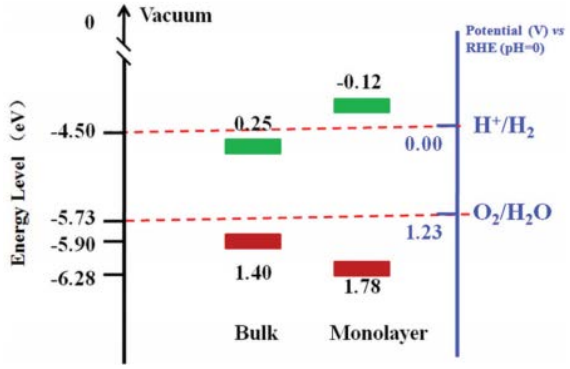

Fig. 2.3. Energy diagrams of the VB and CB edge potentials in bulk and monolayer MoS_2.

The conduction band position of bulk-form of MoS_2 cannot be adaptable for H+/H2 redox reaction.[9] However, the that of monolayer of MoS_2 could be one of effective catalysts due to its elevation of conduction band position from the reduce of its thicknesses. Furthermore, the TMDs, especially Mo and W based ones, have been used as photoelectrodes for water splitting due to the following advantages: (i) their band gaps ranges from 1.0 to 1.6 eV, which are well matched with the solar spectrum. (ii) These semiconductors should be quite stable towards to photodissolution because of *d–d* optical transitions and involving nonbonding electrons. For example, the stability of the MoS_2 photoelectrode has been associated with the fact that the electronic excitation does not involve a transition having $S^{2-} \rightarrow$ Mo(IV) charge-transfer character. (iii) They are earth-abundant and composed of non-precious materials. However, TMD nanostructures are usually utilized as cocatalysts for photocatalytic H_2 generation, presently, because their conduction band position is inadaptable to reduce H^+ to H_2 under light illumination.

The photocatalytic properties of both single component and composite TMD based on very commonly used MoS_2 and WS_2 materials. In particular, monolayer MoS_2 and the heterostructures, in which MoS_2 and WS_2 act as cocatalysts, are highlighted in recent reports. In addition, the other TMDs have been recently reported its excellence in role of water splitting catalyst both hydrogen and oxygen productions. The water splitting catalyst is one of the promising application of TMD-based materials for replacing the noble metal catalysts.

2.3. Application to gas sensors

The huge demand for developing highly sensitive, selective, low power consuming, reliable and portable sensors has stimulated extensive research on new sensing materials based on 2D allotropes of TMDs and phosphorous after the great success made by their 2D carbon analog, that is, 'graphene'. The high surface to volume ratio in 2D TMDs offers huge potential for the detection of large amounts of target analysts per unit area as well as rapid response and recovery with low power consumptions.[10] Moreover, the recent demonstration of scalable synthesis of 2D TMDs has shown the potential to fabricate cost-effective sensors.

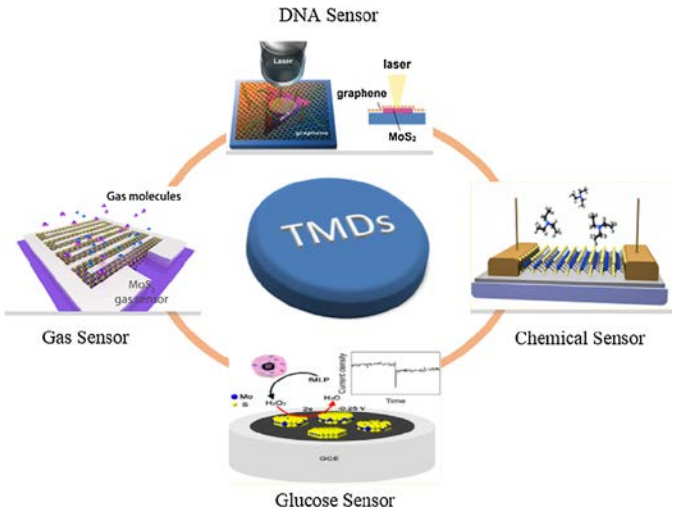

Fig. 2.4. Various gas-, chemical- and bio-sensors constructed using 2D TMDs materials like MoS_2, WS_2, etc.

Fig. 2.4 shows the use of 2D TMDs such as MoS_2, WS_2, etc. for various sensing applications including gas, chemical, and biosensors. As expected, most of the reported 2D TMDs based sensors have been realized using mechanically exfoliated or liquid phase exfoliated MoS_2 flakes.[11] For example,

Li et al. fabricated MoS_2-FET sensor device using mechanically exfoliated single and few layer MoS_2 films to detect nitric oxide (NO).[12] It was observed that MoS_2 films exhibited a very high sensitivity to NO with a low detection limit of 0.8 parts per million (ppm). A chemically exfoliated MoS_2 flakes-based sensor by Donarelli et al. out-performs similar sensors, with a measured detection limit of 20 parts per billion (ppb) when exposed to nitrogen dioxide (NO_2) gas.[13] The potential mechanism for the p-type behavior of the sensing material (MoS_2) toward NO_2 is the N substitutional doping of S vacancies in the MoS_2 surface. This detection limit is the lowest ever measured to NO_2 for MoS_2-based sensors and is com-parable or better than ZnO-, graphene oxide-, and CNT-based sensors. BP and its single atomic layer (phosphorene) have shown great possibility to be effectively employed for gas detection similar to other 2D materials like graphene, MoS_2, etc.[14]

Based on these results, the TMDs-based gas sensor which shows the excellent stability and can operate at room temperature can replace the oxide-based ones, however, the low sensitivity compared to the oxide-based gas sensors are still challenging. The nanostructured TMDs would be one of the solution to resolve the low sensitivity at room temperature. Furthermore, the only NO_2 detective issue is one of the potential barrier to apply the TMDs as sensing materials. The defect-engineering and doping with a foreign atom are one of the solution to settle these issues.

2.4. Reference

[1] G. Fiori, F. Bonaccorso, G. Iannaccone, T. Palacios, D. Neumaier, A. Seabaugh, S. K. Banerjee, L. Colombo, *Nat. Nanotechnol.*, **2014**, *9*, 768.

[2] G.R. Bhimanapati, et al. *ACS Nano*, **2015**, *9*, 11509.

[3] H.-Y. Chang, M. N. Yogeesh, R. Ghosh, A. Rai, A. Sanne, S. Yang, N. Lu, S. K. Banerjee, D. Akinwande, *Adv. Mater.*, **2015**, *28*, 1818.

[4] S. Y. Reece, J. A. Hamel, K. Sung, T. D. Jarvi, A. J. Esswein, J. J. Pijpers and D. G. Nocera, *Science*, **2011**, *334*, 645.

[5] A. Fujishima, *Nature*, **1972**, *238*, 37.

[6] K. Maeda, K. Teramura, D. Lu, T. Takata, N. Saito, Y. Inoue and K. Domen, *Nature*, **2006**, *440*, 295.

[7] F. E. Osterloh, *Chem. Mater.*, **2008**, *20*, 35.

[8] W. Ho, J. C. Yu, J. Lin, J. Yu, P. Li, *Langmuir*, **2004**, *20*, 5865.

[9] N. Singh, G. Jabbour, U. Schwingenschlögl, *Eur. Phys. J. B*, **2012**, *85*, 1.

[10] F. Schedin, A. K. Geim, S. V. Morozov, E. W. Hill, P. Blake, M. I. Katsnelson, K. S. Novoselov, *Nat. Mater.*, **2007**, *6*, 652.

[11] D.J. Late, Y.-K. Huang, B. Liu, J. Acharya, S. N. Shirodkar, J. Luo, A. Yan, D. Charles, U. V. Waghmare, V. P. Dravid, C. N. R. Rao, *ACS Nano*, **2013**, *7*, 4879.

[12] H. Li, Z. Yin, Q. He, H. Li, X. Huang, G. Lu, D. W. H. Fam, A. I. Y. Tok, Q. Zang, H. Zhang, *Small*, **2012**, *8*, 63.

[13] M. Donarelli, S. Prezioso, F. Perrozzi, F. Bisti, M. Nardone, L. Giancaterini, C. Cantalini, L. Ottaviaon, *Sens. Actuators B: Chem.*, **2015**, *207* 602.

[14] F. Xia, H. Wang, Y. Jia, *Nat. Commun.*, **2014**, *5*, 4458.

Chapter 3

Application to Photovoltaic Cells

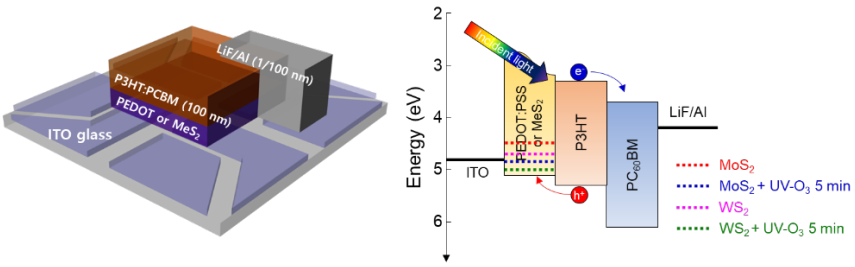

ACS Nano **2015**, *9*, 4146

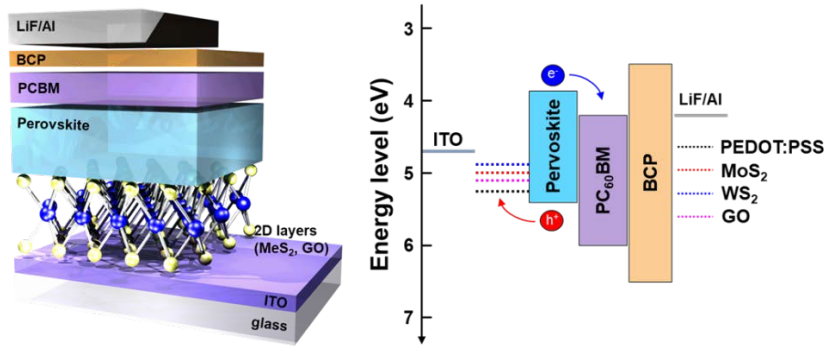

J. Power Sources **2016**, *319*, 1

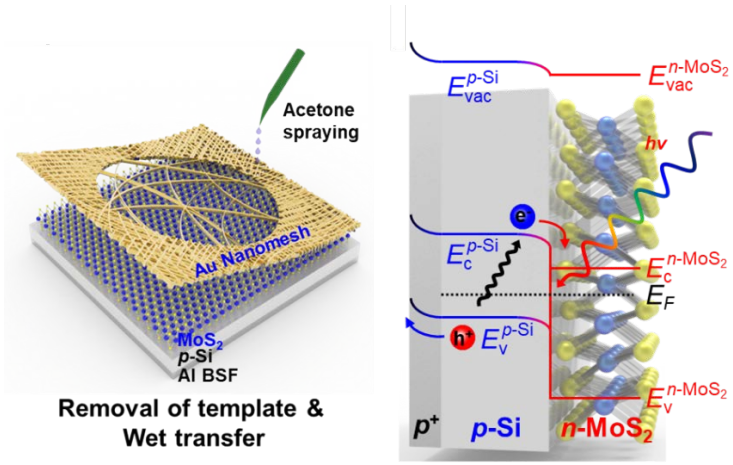

In preparation

3.1. Charge transport layers in organic-based optoelectronics

3.1.1. Introduction

Transition metal dichalcogenides (TMDCs) have attracted increasing attention because of their great potential as catalysts of hydrogen evolution reactions as well as their application in energy storage, memory and logic devices, and optoelectronic devices, because of their high on/off current ratio, high carrier mobility, and semiconducting properties.[1-6] TMDCs with transition metals from groups IV–VII of the periodic table are predominantly layered, whereas some of the TMDCs with metals from the groups VIII–X of the periodic table are commonly found in non-layered structures. The graphite-like layered structure of the TMDCs leads to a strong anisotropy in the electrical, chemical, mechanical, and thermal properties of the TMDCs. Theoretical and experimental studies reported several advantages of isolated monolayers of TMDCs.[7-10] First, the lone-pair electrons of the chalcogen atoms in the isolated monolayer structure enable ballistic transport, indicating that the carrier mobility can be improved.[7] Second, the indirect-to-direct band gap transition from bulk to monolayer material induces quantum confinement effects. Therefore, the photoluminescence properties of MoS_2 and WS_2 monolayers are strongly enhanced, whereas only weak emission is observed in the multilayered form.[8-9] Lastly, the typical band gap of the monolayer is approximately 50% larger than that of the bulk form.[10]

Owing to the advantages of monolayer TMDCs, many researchers try to exfoliate bulk TMDCs to a monolayer and synthesize monolayers of TMDCs using precursor materials. Liquid exfoliation and alkali metal complex intercalations have been widely used to exfoliate each layer of the TMDCs.[11-12] However, the products obtained by these methods tend to assume zero-(fullerene-like nanoparticles) or one-dimensional (nanotube structures) structures.[13] Furthermore, the quality of the TMDC products is not good enough compared with that of those obtained by a mechanical exfoliation method, albeit the solution process has the potential for mass production. For these reasons, the chemical vapor deposition (CVD) method with sulfur powder and precursors is introduced to synthesize TMDCs with high quality and on a large scale.[13-17] However, to enable the wide application of TMDCs, the growth technique of TMDCs with few layers still needs to be improved in relation to the domain size, crystal quality, and thickness control.[18]

The well-known poly(3,4-ethylenedioxythiophene):poly(styrenesulfonate) (PEDOT:PSS), widely used as a hole injection layer (HIL) or hole extraction layer (HEL), has several disadvantages such as hygroscopic properties (damages to organic layers) and a highly acidic suspension ($pH \approx 1$; corrosion of indium-tin oxide (ITO)), which result in a poor stability in air.[19] Metal oxides (MeO_3) such as molybdenum oxide (MoO_3) and tungsten oxide (WO_3) were also used as HIL or HEL for enhancing the stability of the optoelectronic devices. However, the thermal deposition of MoO_3 and WO_3 produced a partially amorphous region, inducing the dangling bonds which facilitate the reaction of the organic materials and deteriorating the device performance.[20-21]

In TMDCs, the oxidation state of the Mo and W atoms is +4 and that of the S atom is -2, meaning that MeS_2 (Me = Mo or W) is terminated with S atoms on the upper and lower side. The lone-pair electrons on the surfaces and the absence of dangling bonds in MoS_2 and WS_2 layers enhance the stability against reactions with other chemical species. As a result, MoS_2 and WS_2 are expected to be quite good candidates as HILs or HELs in optoelectronic devices such as organic light-emitting diodes (OLEDs) and organic photovoltaic (OPV) cells.

In this work, we introduced ultraviolet-ozone (UV-O_3) treated MoS_2 and WS_2 in OLEDs and OPV cells as a HIL and HEL to enhance the stability in air comparting to PEDOT:PSS. MoS_2 and WS_2 were synthesized on a SiO_2/Si substrate using spin-coated $(NH_4)_2MoS_4$ and $(NH_4)_2WS_4$ precursors. To investigate the effect of UV-O_3-exposed TMDCs on the performance of OLEDs and OPV cells, the core levels of Mo 3*d*, W 4*f*, and S 2*p* were obtained using synchrotron radiation photoemission spectroscopy (SRPES). Ultraviolet photoemission spectroscopy (UPS) and Raman spectroscopy were performed as well. Field-emission scanning electron microscopy (FE-SEM), energy dispersive spectroscopy (EDS), and atomic force microscopy (AFM) were carried out to analyze the surface morphology of the synthesized MoS_2 and WS_2 layers. The atomic structure was revealed using high-energy transmission electron microscopy (HR-TEM) and selected area electron diffraction (SAED) patterns. The use of UV-O_3-treated MoS_2 and WS_2 in OLEDs and OPV cells is discussed on the basis of the obtained experimental results and measurements.

3.1.2. Experimental procedures

Synthesis of MoS_2 and WS_2. The insulating substrates, SiO_2 (300 nm)/Si wafer, were prepared with a standard piranha solution and conventional cleaning procedures based on acetone, isopropyl alcohol, and DI water bath sonication. The precursor solution was prepared with a 5 mM concentration of $(NH_4)_2MoS_4$ and $(NH_4)_2WS_4$ in ethylene glycol. For the optimized precursor coating conditions, the cleaned substrates were subjected to O_2 plasma and UV-O_3 surface treatment for 15 min. The substrates were spin coated with the precursor solutions at 3500 rpm for 60 s. For the thermolysis of the precursor films, a thermal CVD system involving high purity hydrogen (H_2) and nitrogen (N_2) gas was used. First, the temperature of the CVD furnace was set to 500 °C for 30 min, under H_2 and N_2 gas flow at 1 Torr pressure. The H_2 and N_2 flow rate were controlled by mass flow controllers for a rate of 40 (H_2) and 200 (N_2) cm^3/min. Then, the thermolysis was slowly initiated under H_2 gas at a relatively high temperature. After the preheating step, the temperature was dramatically increased to approximately 950 °C. When the CVD furnace temperature reached 950 °C, the samples were placed on the heating zone for 1 h, and the heating zone with sulfur powder was turned on to initiate the sulfur sublimation. After 60 min of thermolysis, the furnace was cooled to room temperature at a rate of 10–15 °C/min under 40 and 200 sccm of H_2 and N_2 flow, respectively. The poly[methyl methacrylate] (PMMA) was then spin coated on the synthesized MoS_2 and WS_2 layers. For a fast separation between MeS_2 and the substrate, the edge of the substrate was scratched with a razor blade, and then

immersed into a hydrogen fluoride and aluminum fluoride (1:1) bath at room temperature for 1 h to etch away the SiO_2 layers. After that the remaining MoS_2 and WS_2 layers were carefully dipped into a DI water bath for 7–9 times to remove any residual etchant, the MoS_2 and WS_2 sheets were transferred to an arbitrary substrate. PMMA was removed by an acetone bath at 50 °C for 30 min after that the PMMA/MeS_2 layer had completely adhered to the target substrate.

Fabrication of the OLED. ITO glass was used as the starting substrate; its surface was cleaned in sequence with acetone, isopropyl alcohol, and DI water, and then dried with high purity nitrogen gas. After cleaning of substrate, the PEDOT:PSS or MeO_3 or MeS_2 layer were formed at the active area. The samples were treated with UV-O_3 for 3, 5, 7, and 9 min. Subsequently, they were loaded into the thermal evaporator where 40 nm of NPB was deposited. In a continuous process, Alq_3 (30 nm) doped with fluorescent dye 10-(2-benzothiazolyl)-2,3,6,7-tetrahydro-1,1,7,7-tetramethyl-1H,5H,11H-(1)-benzopyropyrano(6,7-8-i,j)quinolizin-11one (C545T) (1%), BCP (30 nm), LiF (1 nm), and Al (100 nm) layers were deposited in sequence. During the deposition, the base pressure of the chamber was maintained as low as 10^{-6} Torr. The active area of the device was 0.3×0.3 cm^2.

Fabrication of the OPV. The substrate preparation step was the same as that for the OLED fabrication procedure. After the HIL preparation step, the samples were treated with UV-O_3 and then loaded into a N_2-filled glove box (<0.1 ppm O_2 and H_2O). Regioregular P3HT (purchased from Rieke Metals and used as received) was first dissolved in 1,2-dichlorobenzene to make a 30

mg/mL solution, followed by blending with [6,6]-phenyl C_{61} butyric acid methyl ester ($PC_{61}BM$) (Nano-C, used as received) in a 3:2 weight ratio. The blend was stirred for approximately 12 h in a glove box before being spin coated (700 rpm, 30 s) on top of the prepared substrate. The thickness of the active layer was approximately 160 nm, as measured by a surface profiler. The devices were annealed on a hot plate in a glove box at 130 °C for 10 min. The cathode consisted of LiF (1 nm) and Al (100 nm) and was deposited at a base pressure of 1×10^{-6} Torr using a thermal evaporation method. The active device area was 0.3×0.3 cm^2.

Characterization. Raman spectra of synthesized MoS_2 and WS_2 were obtained with a Lab RAM HR (Horiba JobinYvon, Japan) at an excitation wavelength of 532 nm. SRPES experiments were performed in an ultra-high vacuum chamber (base pressure of ca. 10^{-10} Torr) with a 4D beam line, equipped with an electron analyzer and heating element, at the Pohang Acceleration Laboratory. The onset of photoemission, corresponding to the vacuum level at the surface of the MoS_2 and WS_2 layers, was measured using the incident photon energy of 350 eV with a negative bias on the sample. The results were corrected for charging effects by using Au 4*f* as an internal reference. The current density-voltage and luminescence-voltage characteristics of the OLEDs and OPV cells were measured with a Keithley 2400 semiconductor parameter analyzer under ambient air conditions. The photocurrent of the OPV cells was measured under AM 1.5G 100 mW/cm^2 illumination with an Oriel 150 W solar simulator.

3.1.3. Results and Discussion

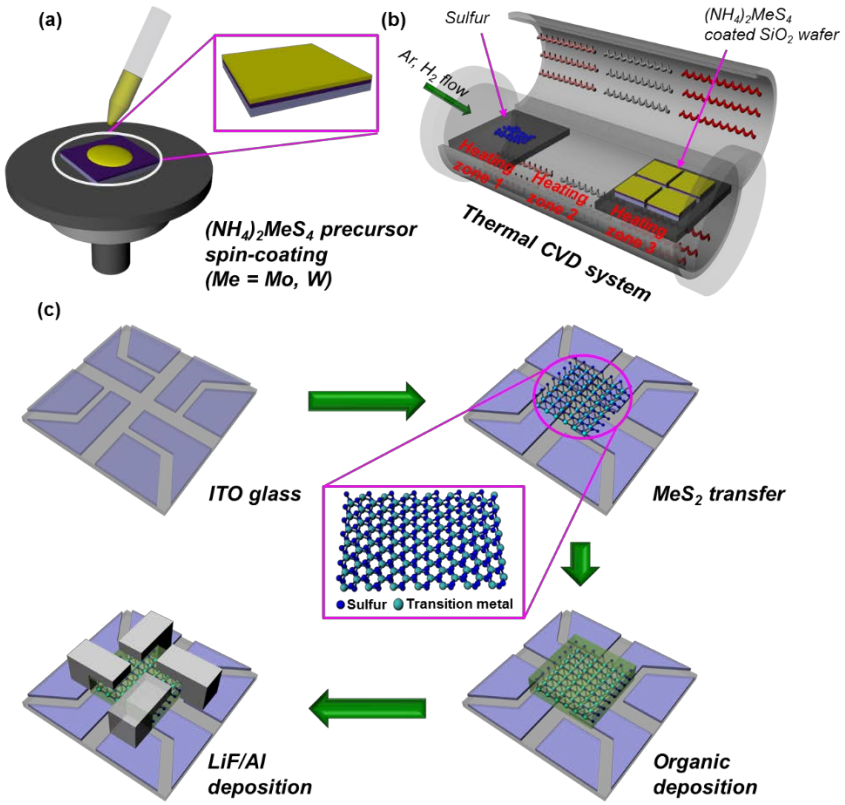

Fig. 3.1. Schematic illustration of the synthesis of MoS_2 and WS_2, and their application to optoelectronic devices. (a) The preparation of the substrate using $(NH_4)_2MoS_4$ and $(NH_4)_2WS_4$ precursors. (b) Synthesis of MoS_2 and WS_2 layers by using a thermal CVD system. (c) Fabrication procedure of OLED and OPV devices with MeS_2 HIL or HEL.

The TMDCs were synthesized using $(NH_4)_2MoS_4$ or $(NH_4)_2WS_4$ as a precursor. The thermolysis at 500 °C under N_2 atmospheric conditions converted the precursors to MoS_x and WS_x thin layers. The conversion of MoS_x and WS_x thin layers to MoS_2 and WS_2 thin films occurred at a temperature above 900 °C in the presence of H_2 gas, as described by the following equations.[22-23]

$$(NH_4)_2MeS_4 + H_2 \rightarrow 2\ NH_3 + H_2S + MeS_3 \text{ (below 500 °C)} \qquad (1)$$

$MeS_3 + H_2 \rightarrow MeS_2 + H_2S$ (above 900 °C) (2)

We have investigated the thermolysis of a series of ammonium thio-transition metal complexes by using a thermal CVD system. Figs. 3.1(a) and 3.1(b) show how to synthesize the MoS_2 and WS_2 thin layers by using our CVD thermolysis method. Highly pure $(NH_4)_2MeS_4$ (Me = Mo, W, purchased from Sigma-Aldrich, purity of 99.99%) was dissolved in ethylene glycol with a concentration equal to 5 mM. The selection of a well-coordinated solvent is important to obtain uniform precursor layers that are converted to TMDCs layers. The solution was sonicated for 10 min before spin coating on a 300-nm-thick SiO_2/Si substrate. The SiO_2/Si substrate was cleaned with a piranha solution (H_2SO_4/H_2O_2 = 1:1), acetone, isopropyl alcohol, and de-ionized (DI) water for 10 min in regular sequence. Then, the substrate was blown with N_2 gas and baked on a hot plate at 120 °C for 10 min. To obtain a uniform layer of the precursor solution, the substrate was treated with O_2 plasma and UV-O_3 for 15 min. The surface of starting substrate should be hydrophilic for the uniform coating of precursor solution. Figs. 3.2(a)-(c) shows the effect of surface treatment and using oxygen plasma and ultraviolet-ozone (UV-O_3) treatment. The UV-O_3 surface and O_2 plasma can transform the surface of substrate temporarily to hydrophilic state. The coordination between solvent and solution is one of the important factors to make the uniform precursor layer by using spin-coating method as shown in Figs. 3.2(d)-(g). The ethylene glycol shows the best spin-coating property among the used solvents due to its nature viscosity.

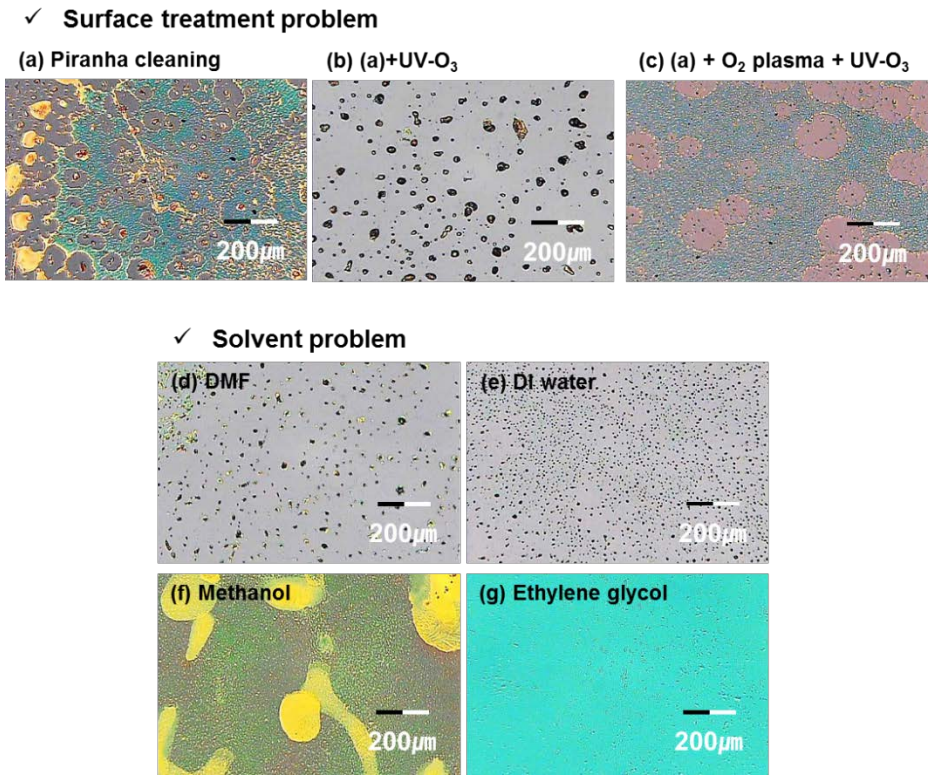

Fig. 3.2. Identification of the degree of spin-coating with respect to the surface treatment and coordinating solvent. Optical microscopic images of each different substrate after surface treatment: (a) standard piranha cleaning, (b) (a) + 15 min UV-O_3 treatment, (c) (b) + 15 min O_2 plasma treatment. Type (c) shows the best degree of spin-coating even when using *N*,*N*-Dimethylformamide (DMF). The solution comprised 20 mM $(NH_4)MoS_4$ as a precursor in DMF solvent. Optical microscopic images for the different solvents: (d) (DMF), (e) de-ionized (DI) water, (f) methanol, and (g) ethylene glycol. The ethylene glycol shows the best spin-coating property among the used solvents.

The thermal annealing process was performed in three different parts of the hot zone of the CVD system. The small amounts of sulfur powder and the SiO_2 wafers spin-coated with the precursors were located at the heating zones 1 and 3 in Fig. 3.1(b), respectively. Further synthesis and transfer techniques are discussed in the experimental procedure section. The fabrication sequence of MeS_2 HIL/HEL based OLED/OPV devices is shown in Fig. 3.1(c): (i) cleaning of the ITO electrode with acetone, isopropyl alcohol, and DI water; (ii) MeS_2

transfer (Me = Mo, W); (iii) deposition of the organic layer; (iv) deposition of the LiF/Al electrode. After the fabrication, the optoelectronic device properties were measured and the devices were put under atmospheric conditions to perform the stability measurements.

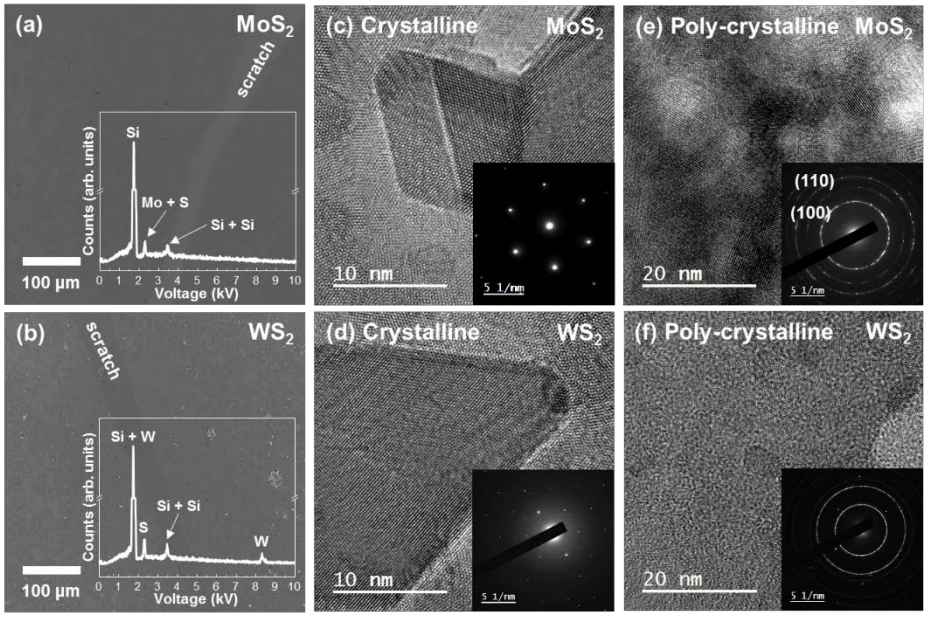

Fig. 3.3. Microscopic analysis of synthesized MoS_2 and WS_2 layers. FE-SEM images and EDS spectra of (a) MoS_2 and (b) WS_2 layers. The EDS spectra show the presence of specific metal and sulfur atoms on the synthesized MoS_2 and WS_2 layers. HR-TEM images and SAED patterns are shown for (c) crystalline-MoS_2, (d) crystalline-WS_2 layer, (e) poly-crystalline region of MoS_2, and (f) poly-crystalline region of the WS_2 sheet.

The FE-SEM images of MoS_2 and WS_2 are shown in Figs. 3.3(a) and 3.3(b). Scratches are intentionally made to confirm the presence of MeS_2. The surface of MeS_2 is smooth. The EDS spectra show the specific peaks of molybdenum, tungsten, and sulfur, confirming that the synthesized films are MoS_2 and WS_2. Figs. 3.3(c)–(f) show the HR-TEM images of MoS_2 and WS_2. The periodic atomic arrangements of the MeS_2 films are shown in Figs. 3.3(c) and 3.3(d). Furthermore, the SAED patterns reveal a hexagonal structure. These results

indicate that single-crystalline MeS_2 layers were synthesized.[24] However, a non-periodic atomic arrangement in the HR-TEM images and ring motifs in the SAED patterns are also found, as shown in Figs. 3.3(e) and 3.3(f), indicating the presence of polycrystalline areas in the synthesized MoS_2 and WS_2 layers. These data are consistent with previous reports that discussed the lower crystalline properties of MoS_2 and WS_2 synthesized on a SiO_2/Si wafer compared with MeS_2 synthesized on a sapphire substrate.[25] Therefore, MoS_2 and WS_2 with few layers and polycrystalline structure were synthesized by using uniformly spin-coated $(NH_4)MoS_4$ and $(NH_4)WS_4$ precursor solutions.

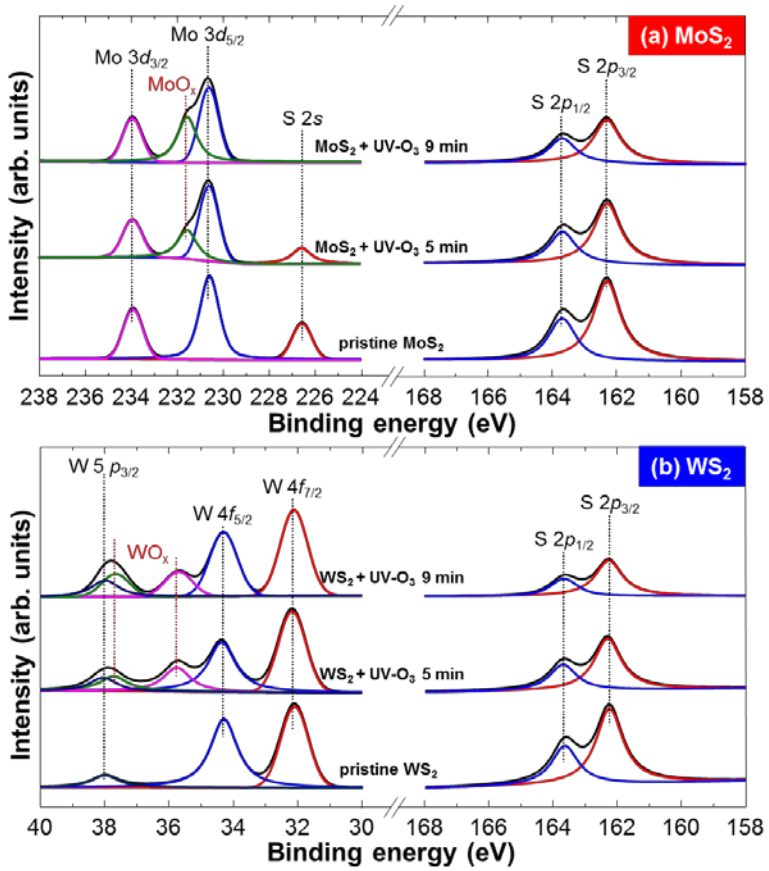

Fig. 3.4. SRPES analysis of pristine and UV-O_3-exposed MoS_2 and WS_2. SRPES core level spectra of (a) Mo 3*d*, S 2*p*, and (b) W 4*f*, S 2*p*. After the UV-O_3 oxidation, the transition metal oxide peak appeared and the intensity of the sulfur peak decreased.

Figs. 3.4(a) and 3.4(b) show the Mo 3*d*, W 4*f*, and S 2*p* SRPES spectra of the MoS_2 and WS_2 layers as a function of the UV-O_3 treatment time. Five peaks appear at 162.3, 163.8, 226.5, 230.5, and 234.0 eV in the MoS_2 sample, which are assigned to S $2p_{3/2}$, S $2p_{1/2}$, S 2*s*, Mo $3d_{5/2}$, and Mo $3d_{3/2}$, respectively. In the case of the WS_2 sample, the W-related peaks of W $4f_{7/2}$, W $4f_{5/2}$, and W $5p_{3/2}$ are shown at 32.0, 34.4, and 38.0 eV, respectively. These results are consistent with the findings of previous reports on MoS_2 and WS_2 crystals.[26-27] As the UV-O_3 treatment time increased, the peak intensity of S 2*s* in the MoS_2 layer progressively decreased until the peak finally disappeared. Furthermore, the Mo–O and W–O bonds were observed, and their intensities increased as a function of the UV-O_3 treatment time. The intensities of the S 2*p* peaks also decreased after the UV-O_3 treatment.

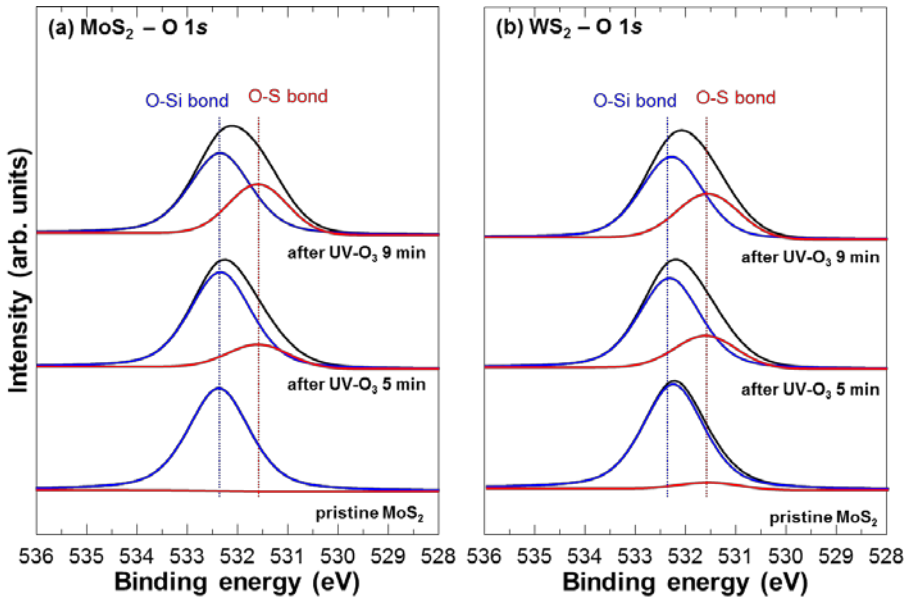

Fig. 3.5. The O 1*s* core level spectra of pristine and UV-O_3-exposed MeS_2 layers. The O–S peak increased as a function of the UV-O_3 exposure time.

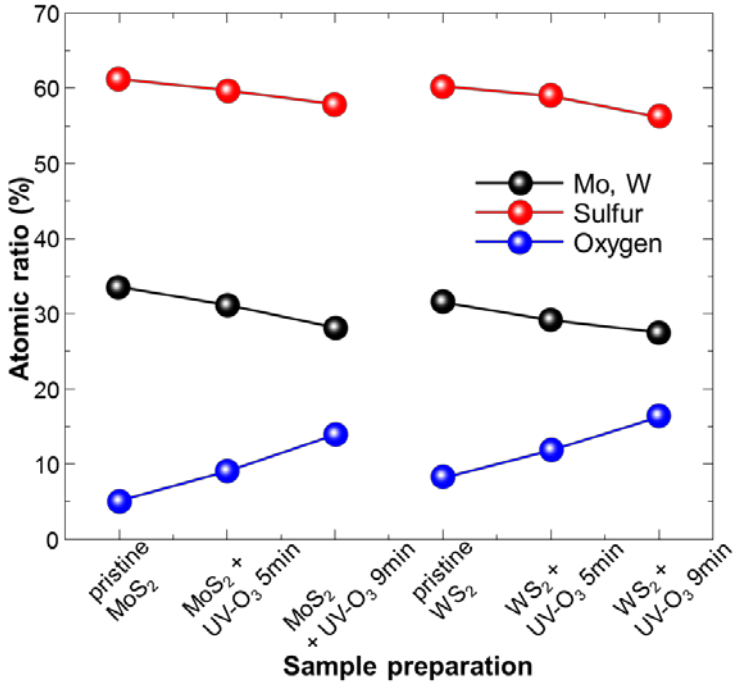

Fig. 3.6. Atomic ratio of the MeS_2 layers with respect to the UV-O_3 exposure times. The oxygen ratio gradually increased from ca. 5% to ca. 12% after UV-O_3 treatment. Conversely, the molybdenum, tungsten, and sulfur ratios decreased after UV-O_3 treatment.

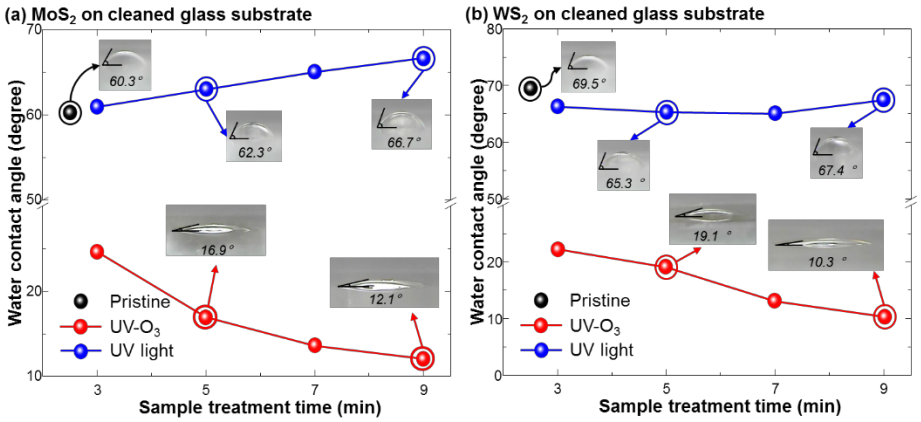

Fig. 3.7. Variation of the water contact angle of MoS_2 and WS_2 as a function of the UV-O_3 treatment time. The water contact angle of MoS_2 decreased from 60.3° to 12.1° after UV-O_3 exposure for 9 min. Similarly, in the case of WS_2, the water contact angle decreased from 69.5° to 10.3° after UV-O_3 exposure for 9 min.

The O 1*s* peak was depicted in Fig. 3.5. In the case of the MoS_2 layers, the intensity ratio of the O–S bond to the O–Si bond increased from 0 to 0.12 and 0.19 after 5 min and 9 min of UV-O_3 treatment, respectively. Similarly, in the case of the WS_2 layers, the ratio increased from 0.05 to 0.13 and 0.21 after 5 min and 9 min of UV-O_3 treatment, respectively. The atomic percentages of Mo, W, and S slightly decreased from 33.6%, 31.6%, and 61.3% to 28.2%, 27.6%, and 57.9%, respectively, after 9 min of UV-O_3 treatment as shown in Fig. 3.6. However, the atomic concentration of O 1s dramatically increased from 5.2% and 8.2% to 14.0% and 16.3% for MoS_2 and WS_2, respectively, after the UV-O_3 surface treatment. These data indicate that some portions of the MeS_2 surface changed from sulfide to oxide. The decrease of the water contact angle after the UV-O_3 treatment supports this assumption, as shown in Fig. 3.7.

Figs. 3.8(a) and 3.8(b) show the Raman spectra of pristine and UV-O_3-treated MoS_2 and WS_2 layers. The Raman spectra of the TMDCs appear to contain two predominant peaks: (i) the out-of-plane (A_{1g}) mode where the top and bottom chalcogen atoms are moving out of the plane in opposite directions while the transition metal is stationary; (ii) the in-plane (E^1_{2g}) mode where both the transition metal and chalcogen atoms are moving in-plane in opposite directions.[28-30] The in-plane and out-of-plane mode of the TMDCs are drawn in the inset of Figs. 3.8(a) and 3.8(b). The E^1_{2g} peak of pristine MoS_2 was revealed at 383.3 cm^{-1} and blue-shifted to 383.5, 384.7, 385.1, and 385.4 cm^{-1} after UV-O_3 treatment for 3, 5, 7, and 9 min, respectively. The A_{1g} peak of pristine MoS_2 was revealed at 405.4 cm^{-1} and red-shifted to 404.6, 403.9, 403.2,

and 402.8 cm^{-1} after the same UV-O_3 treatments, respectively. A similar tendency of peak shift was observed in the case of WS_2.

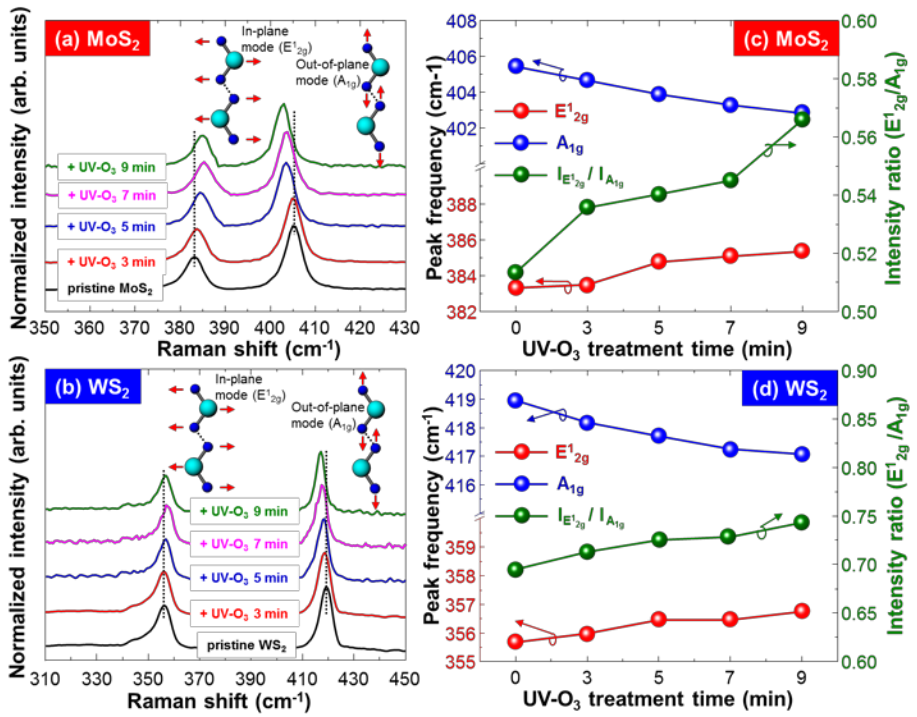

Fig. 3.8. Raman spectroscopy analysis of pristine and UV-O_3-treated MoS_2 and WS_2. Raman spectra of pristine MeS_2: (a) MoS_2 and (b) WS_2, at different UV-O_3 surface treatment times. For both MoS_2 and WS_2, the peak position of E^1_{2g} and A_{1g} shifted to higher and lower wave numbers, respectively, as a function of the UV-O_3 exposure time. The shifted peak position and intensity ratio of E^1_{2g} to A_{1g} are shown in (c) MoS_2, and (d) WS_2.

The peak shift data and the change of the intensity ratio of E^1_{2g} and A_{1g} are summarized in Figs. 3.8(c) and 3.8(d). Both the peak positions of E^1_{2g} and A_{1g} shifted to a higher and lower wavenumber, and the E^1_{2g} to A_{1g} peak intensity ratio increased after the UV-O_3 treatment on the MeS_2 layers. It has been reported that the addition of extra layers on TMDC leads to the stiffening of the out-of-plane phonon modes and relaxation of the in-plane bonding, resulting in a blue-shift of the A_{1g} mode and red-shift of the E^1_{2g} mode.[28] Therefore, the

decrease in distance between E^1_{2g} and A_{1g} suggests the removal of surface contaminants, resulting in the thinning and flattening of the MeS_2 layer. Furthermore, it has been reported that the E^1_{2g} to A_{1g} peak intensity ratio value decreases as the number of TMDC layers increases.[29-30] Thus, the increase of the E^1_{2g} to A_{1g} peak intensity ratio shown in Figs. 3.8(c) and 3.8(d) suggests that the thickness of the MeS_2 layer decreased with the UV-O_3 treatment. According to the AFM analysis shown in supporting information, Fig 3.9, the thickness of MoS_2 and WS_2 decreased from 2.0 and 1.8 nm to 1.5 and 1.2 nm, respectively, after UV-O_3 treatment for 5 min. Therefore, the UV-O_3 treatment on MeS_2 leads to the removal of the surface contaminants induced by the transfer process, producing a uniform surface.

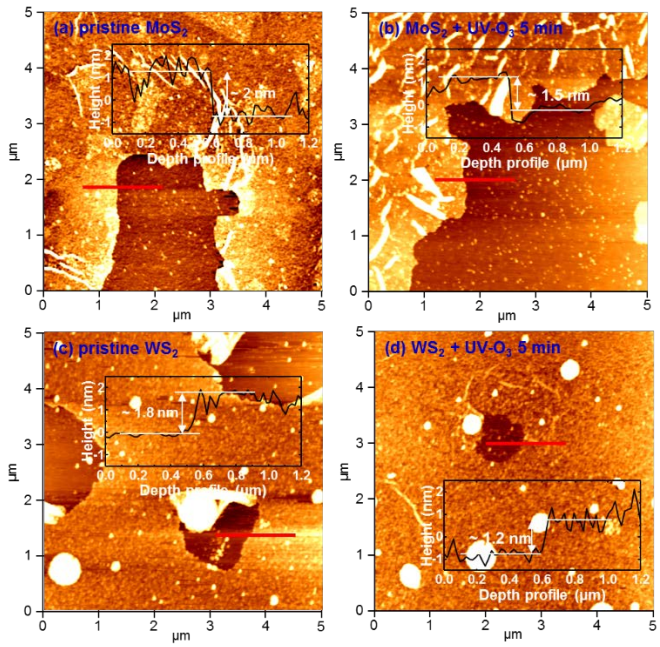

Fig. 3.9. Atomic force microscopy (AFM) analysis of pristine and UV-O_3-exposed (5 min) MeS_2 layers on Si/SiO_2 wafer. The thicknesses of the synthesized MoS_2 and WS_2 layers are measured to be approximately equal to 2 nm and 1.8 nm, respectively, which indicates the presence of two or three layers. The thickness decreased from 2 to 1.5 nm for the MoS_2 sheet and from 1.8 to 1.2 nm for the WS_2 sheet after UV-O_3 surface treatment for 5 min.

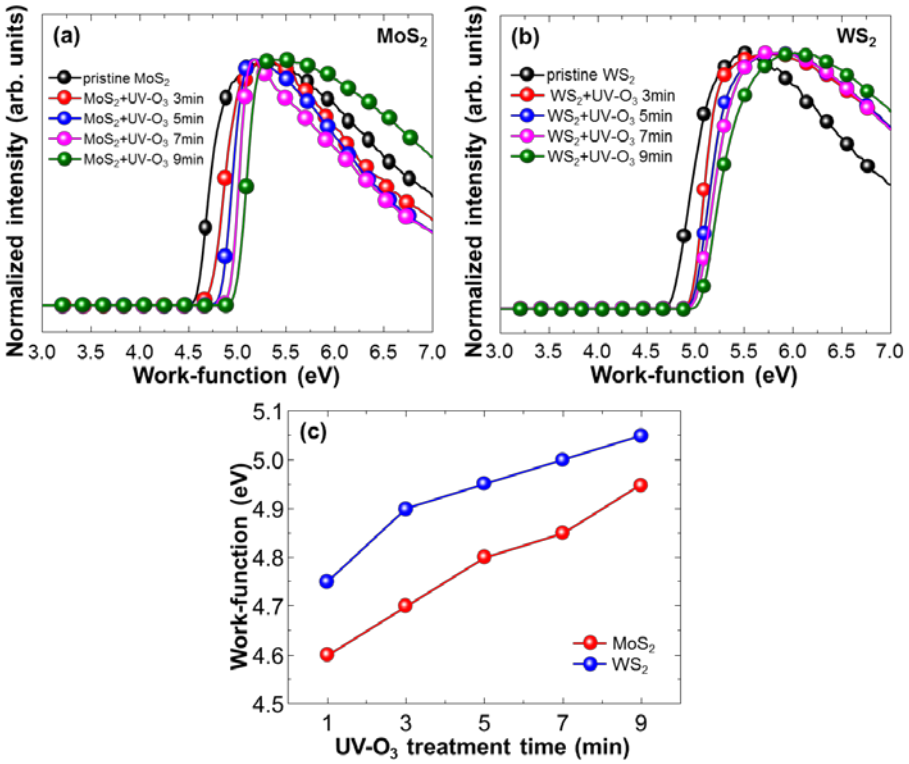

Fig. 3.10. Ultraviolet photoemission spectroscopy (UPS) data of the MeS_2 layers as a function of the UV-O_3 treatment time. The secondary electron threshold curves are shown for (a) MoS_2 and (b) WS_2. The UPS spectra show the tendency of the work function to increase with increasing the UV-O_3 exposure time. The summarized values of the work function are shown in (c).

The structure of the OLED with MeS_2 HIL and the schematic band diagram are depicted in Fig. 3.11(a). The energy levels of ITO, PEDOT:PSS, (*N,N*′-Di(1-naphthyl)-*N,N*′-diphenyl-(1,1′-biphenyl)-4,4′-diamine) (NPB), (Tris-(8-hydroxyquinoline)aluminum) (Alq_3), 2,3,6,7-tetrahydro-1,1,7,7,-tetramethyl-1H,5H,11H-10-(2-benzothiazolyl) quinolizine-[9,9a,1gh] (C545T), bathocurione (BCP), and LiF/Al were obtained from the literature.[31] The values of the work function of MoS_2 and WS_2 were measured by UPS, as shown in supporting information, Fig. 3.10. The work functions increased from 4.6 and 4.75 eV to 4.8 and 4.95 eV for MoS_2 and WS_2, respectively, after UV-O_3

treatment for 5 min. This means that, among all the samples, the lowest hole injection barrier belongs to UV-O_3-treated WS_2.

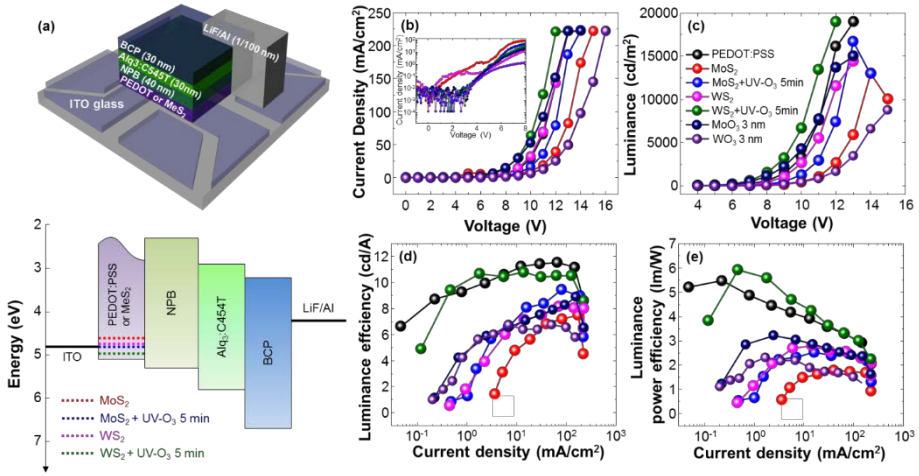

Fig. 3.11. Device characteristics of pristine MeS_2, UV-O_3 treated MeS_2, and MeO_3-based OLEDs. (a) The illustration of OLED device structure of MoS_2 and WS_2 HIL with UV-O_3 exposure. Schematic energy band diagram is also shown. (b) Current density-voltage, (c) luminance-voltage, (d) luminance efficiency-current density, and (e) luminance power efficiency-current density characteristics of OLEDs. The current density-voltage curve at low voltage region is magnified in the inset figure of (b).

Figs. 3.11(b)–(e) show the current density-voltage, luminance-voltage, luminance efficiency-current density, and power efficiency-current density characteristics of the OLEDs with PEDOT:PSS, pristine MeS_2, UV-O_3-exposed MeS_2 and MeO_3. The thickness of MeO_3 is fixed at 3 nm following to the thickness of MeS_2. The OLED with UV-O_3-treated MeS_2 performs better than that with pristine MeS_2 and MeO_3. The inset graph of Fig. 3.11(b) shows the log-scaled leakage current at low voltage region. The leakage current shown in OLEDs based on pristine MeS_2 disappeared in OLEDs based on UV-O_3 treated MeS_2. It is considered that decrease of surface roughness and removal of contaminant on pristine MeS_2 layers after UV-O_3 treatment got rid of leakage

current. The optimized UV-O_3 treatment lasted for 5 min because of the surface damage induced from UV-O_3, as following Figs. 3.12–3.14.

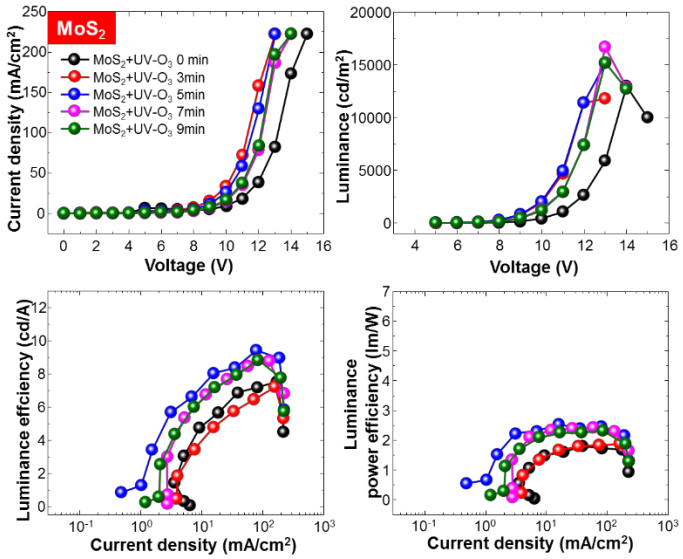

Fig. 3.12. Characteristics of the MoS_2 hole injection layer (HIL) based organic light-emitting diode (OLED) device without PEDOT:PSS-based devices. The device exposed to UV-O_3 for 5 min shows the lowest turn-on voltage and the highest device efficiencies.

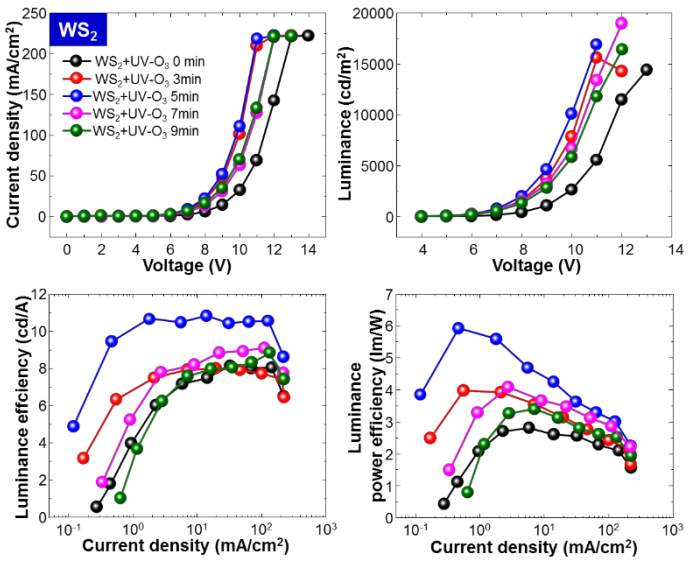

Fig. 3.13. Characteristics of the WS_2 hole injection layer (HIL) based organic light-emitting diode (OLED) device without PEDOT:PSS-based devices**.** The device exposed to UV-O_3 for 5 min shows the lowest turn-on voltage and the highest device efficiencies.

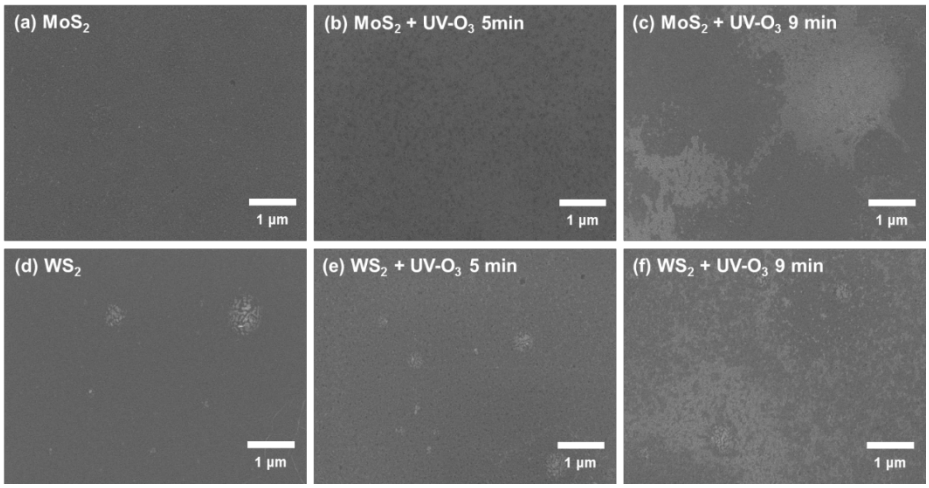

Fig. 3.14. Field-emission scanning electron microscopy (FE-SEM) images of pristine and UV-O_3-treated MeS_2 surfaces. The surface is roughened by the UV-O_3 exposure in both cases. The scale bar is 1 μm. After 9 min of UV-O_3 exposure, the surface of the MeS_2 layers is damaged by ozone molecules so intensely that the island-type defects can be significantly measured.

Table 3.1. Summary of the device characteristics of pristine MeS_2, UV-O_3-treated MeS_2, and MeO_3 HIL based OLEDs.

HIL	Turn-on voltage [a] (V)	Luminance $_{max}$ (cd/m^2)	Luminance Eff$_{max}$ (cd/A)	Power Eff$_{max}$ (lm/W)	CIE1931 Coordinates[b] (x,y)
PEDOT:PSS	4.4	19000	11.42	5.48	(0.32,0.65)
pristine MoS_2	6.4	13000	7.51	1.8	(0.32,0.65)
MoS_2 + UV-O_3 5min	5.65	16700	9.44	2.53	(0.32,0.64)
pristine WS_2	5.1	14400	8.14	2.81	(0.33,0.64)
WS_2 + UV-O_3 5min	4.1	19000	10.82	5.92	(0.33,0.64)
MoO_3 3 nm	4.25	15000	9.03	3.21	(0.31, 0.65)
WO_3 3 nm	5.4	8810	6.99	2.31	(0.33, 0.63)

[a] measured at 10 cd/m^2.
[b] recorded at maximum luminance.

The OLED with UV-O_3-exposed WS_2 shows the lowest turn-on voltage, 4.1 V, and the brightest luminance value, 19000 cd/m^2; these values are comparable with those obtained from the PEDOT:PSS-based device (4.4 V and 19000 cd/m^2) and better than MeO_3-based device (4.25 V and 15000 cd/m^2 for MoO_3, 5.4 V and 8810 cd/m^2 for WO_3). The best luminance efficiency and power efficiency of the OLEDs based on UV-O_3-treated WS_2 are approximately equal to 95% and 109% than those obtained from of the OLEDs based on PEDOT:PSS. The detailed OLED characteristics are summarized in Table 3.1.

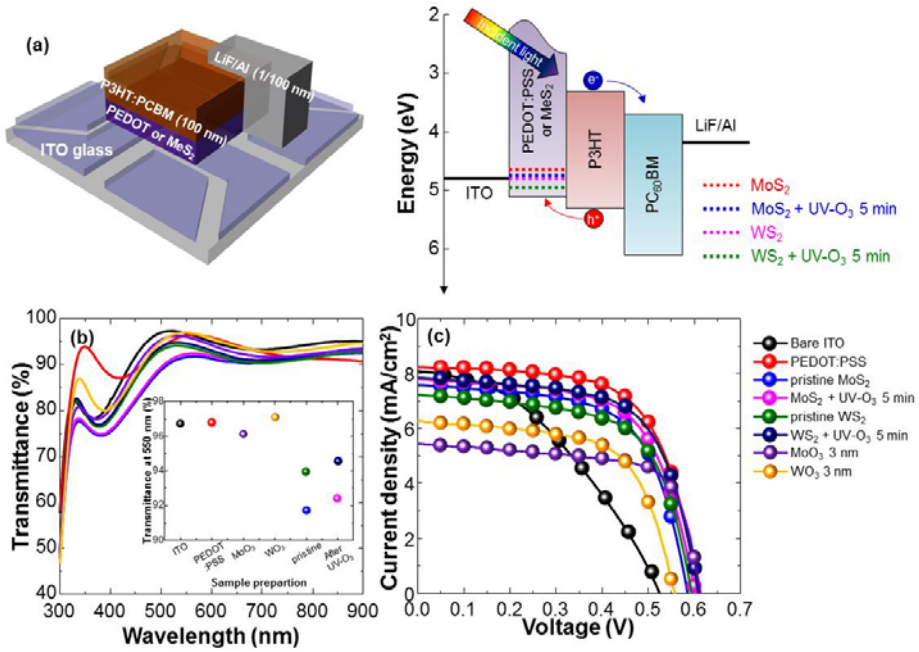

Fig. 3.15. Device characteristics of pristine MeS_2, UV-O_3 treated MeS_2, and MeO_3-based OPVs. (a) Illustration of the OPV device structure of MoS_2 and WS_2 HEL with UV-O_3 exposure. Schematic energy band diagram is also shown. (b) The transmittance spectra of bare ITO, PEDOT:PSS, pristine MeS_2, UV-O_3-treated MeS_2, and MeO_3 layers. The transmittance values at 550 nm are shown in the inset graph of (b). (c) Current density-voltage curves of OPV devices. The OPV based on UV-O_3-exposed WS_2 sample shows the best performance among all the samples.

MeS_2 was used in OPV cells as HEL, as shown in Fig 3.15. Fig. 3.15(a) shows the device structure and energy band diagram. The energy levels of ITO, PEDOT:PSS, poly(3-hexylthiophene) (P3HT), [6,6]-phenyl C_{61} butyric acid methyl ester ($PC_{60}BM$), and LiF/Al were obtained from the literature.[32] The transmittance of each sample was measured by using UV-visible spectra as shown in Fig. 3.15(b). The transmittance at 550 nm of MeS_2 layers slightly elevated from 91.7 % to 94.0 % for MoS_2, and from 92.4 % to 94.6 % for WS_2 after UV-O_3 treatment for 5 min. The device current density-voltage characteristics are shown in Fig. 3.15(c). The open-circuit voltage (V_{oc}), short-circuit current (J_{sc}), fill factor (*FF*), and power conversion efficiency (*PCE*) of the reference (PEDOT:PSS) are 0.61 V, 8.27 mA/cm^2, 64.2, and 3.23%, respectively. The efficiency of the UV-O_3-treated MeS_2-based devices varied from 2.72% to 2.96% for MoS_2 HEL, and from 2.79% to 3.08% for WS_2 HEL at different UV-O_3 exposure times, as shown in Fig. 3.16.

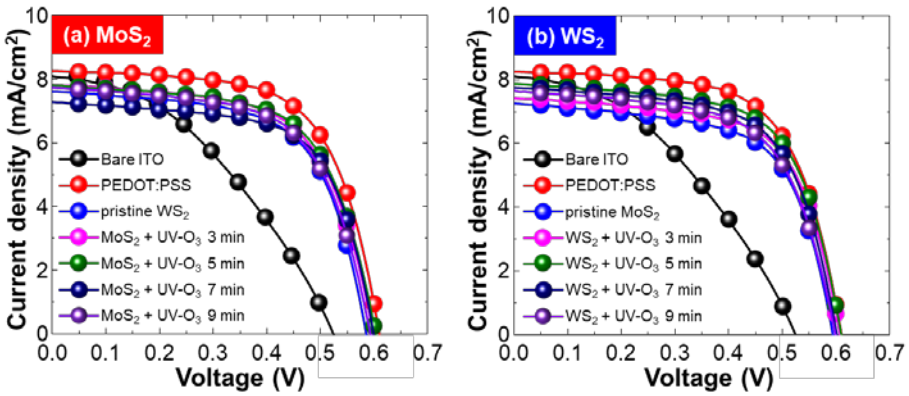

Fig. 3.16. Summary of the organic photovoltaic (OPV) device data of pristine and UV-O_3-exposed MeS_2 layers. Current density-voltage characteristics of (a) MoS_2-hole transport layer (HTL) based and (b) WS_2-HTL based OPV devices with different UV-O_3 exposure times.

Table 3.2. Summary of the device characteristics of pristine MeS_2, UV-O_3-exposed MeS_2, and MeO_3 HEL based OPV cells.

HEL	J_{sc} (mA/cm^2)	V_{oc} (V)	FF	PCE (%)	R_{sh} (Ω cm^2)
Bare ITO	8.10	0.52	0.40	1.70	12725.67
PEDOT:PSS	8.27	0.61	0.64	3.23	36543.93
pristine MoS_2	7.24	0.59	0.63	2.72	21689.53
MoS_2 + UV-O_3 5min	7.81	0.60	0.63	2.96	40068.85
pristine WS_2	7.61	0.59	0.63	2.79	23866.64
WS_2 + UV-O_3 5min	7.87	0.61	0.64	3.08	36149.29
MoO_3 3 nm	6.29	0.61	0.68	2.29	18251.37
WO_3 3 nm	5.45	0.56	0.63	2.20	16589.19

R_{sh}: shunt resistance.

The devices with MeS_2 treated by UV-O_3 for 5 min show the best efficiency: V_{oc} = 0.60 V, J_{sc} = 7.81 mA/cm^2, FF = 63.6, and PCE = 2.96% for MoS_2; V_{oc} = 0.61 V, J_{sc} = 7.87 mA/cm^2, FF = 64.1, and PCE = 3.08% for WS_2. The changes of J_{sc} and PCE were attributed to the increase of transmittance, variation of the work function, and the removal of the surface contamination from the MeS_2 layer by UV-O_3 treatment. The decrease of the device performance for UV-O_3 exposure times longer than 5 min is due to the surface damage. The detailed OPV characteristics are summarized in Table 3.2. These data suggest that the MeS_2 layer may be used as HIL or HEL in organic devices instead of PEDOT:PSS.

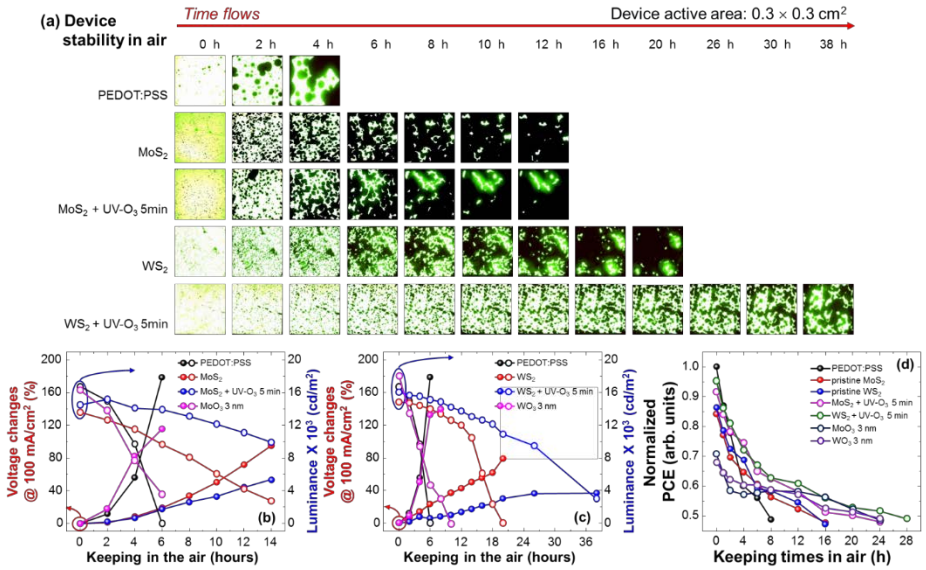

Fig. 3.17 Device stability test results of pristine and UV-O_3-exposed MoS_2 and WS_2 HIL based OLEDs and OPV cells. (a) Illumination images of several types of samples including PEDOT:PSS, pristine MoS_2 and WS_2, UV-O_3 treated MoS_2 and WS_2 HIL. The device illumination size is 0.3 × 0.3 cm^2. Comparison between a PEDOT:PSS device and (b) MoS_2- and MoO_3-based cells and (c) WS_2- and WO_3-based cells; the variation of voltage changes at 100 mA/cm^2 (left column, red, closed circle) and luminance value (right column, blue, open circle) as a function of the time in air ambient. (d) The change of normalized PCE values as a function of keeping time in air ambient for the different sample types.

In order to investigate the stability of OLED and OPV devices with UV-O_3-treated MeS_2, the lifetimes were evaluated in air conditions at 25 °C and 50% humidity. Fig. 3.17(a) shows the illumination images of each different OLED device as a function of the keeping time. The illumination images were captured at the applied current density of 100 mA/cm^2. All the samples progressively degrade because of the moisture. In the case of the PEDOT:PSS-based OLED, the illumination dramatically decreased after exposure for 4 h and the device ceased operating after 6 h. However, the OLEDs based on pristine and UV-O_3-treated MeS_2 layers are shown to be operative even after 6 h under the same conditions. Thus, the device stability of OLEDs based on MeS_2 is superior to

that of the OLEDs based on PEDOT:PSS. The voltage changes of the OLEDs as a function of the keeping time in air are shown in Fig. 3.17(b) for MoS_2 and Fig. 3.17(c) for WS_2. The voltage changes at 100 mA/cm^2 dramatically increased to 180% in the PEDOT:PSS-based OLED after 6 h. However, the voltage change of the OLED based on MeS_2 is lower than that of the OLED based on PEDOT:PSS. Notably, OLEDs with UV-O_3-treated MeS_2 show a smaller voltage variation than the OLEDs with pristine MeS_2. The effect of the MeS_2 layers on the air stability of the OPV cells is shown in Fig. 3.17(d). The PCE value is normalized with respect to the PEDOT:PSS-based OPV cell. The time required to reach half of the PCE value is equal to 8, 16, 21, 16, 28, 24, 24 h for PEDOT:PSS, MoS_2, UV-O_3-treated MoS_2, WS_2, and UV-O_3-treated WS_2, MoO_3 and WO_3-based OPV cells, respectively. Although the PCE values of the MeS_2-based OPV cells are lower than those of the PEDOT:PSS-based cells, the stability is significantly improved. Furthermore, it is shown that the properties of OLEDs and OPVs based on UV-O_3-treated MeS_2 HIL are comparable to, or even better than, those of the OLEDs and OPVs based on MeO_3, which is reported as a good HIL. Hence, the MeS_2 layers are suitable for replacing the PEDOT:PSS layer, which is an acidic material and presents a high reactivity with the ITO layer.

3.1.4. Conclusion

The hole injection and extraction properties of UV-O_3-treated MoS_2 and WS_2 in OLED and OPV devices were investigated in relation to the extended air stability. The MoS_2 and WS_2 layers were synthesized by thermolysis of a $[(NH_4)_2MoS_4)]$ and $[(NH_4)_2WS_4)]$ precursor solution with a two-step annealing process. The synthesized MoS_2 and WS_2 show a polycrystalline structure. According to SRPES and Raman spectra analyses, the UV-O_3 exposure modulated the work-function of MoS_2 and WS_2, as well as removed the surface contaminants. The maximum luminance efficiencies of OLEDs with UV-O_3-treated MoS_2 and WS_2 were 9.44 and 10.82 cd/A, respectively. The PCE values of UV-O_3-treated MoS_2 and WS_2-based OPV cells were 2.96% and 3.08%, respectively. These values correspond to over 95% of those obtained from PEDOT:PSS-based devices. Owing to the removal of surface contaminants and the increased work function, the device performance was significantly enhanced after UV-O_3 exposure of MeS_2. Furthermore, the device stability in air significantly improved because of its non-acidic and chemically stable properties, which can be achieved by replacing conventional PEDOT:PSS with UV-O_3-exposed MoS_2 and WS_2 layers. Therefore, these results show that UV-O_3-treated MoS_2 and WS_2 under optimized conditions may replace the conventional PEDOT:PSS layer, enhancing the overall device reliability.

3.1.5. References

[1] Q. H. Wang, K. Kalantar-Zadeh, A. Kis, J. N. Coleman, S. M. Strano, *Nat. Nanotechnol.* **2012**, *7*, 699.

[2] M. Chhowalla, H. S. Shin, G. Eda, L.-J. Li, K. P, Loh, H. Zhang, *Nat. Chem.* **2013**, *5*, 263.

[3] Y.-H. Chang, C.-T. Lin, T.-Y. Chen, C.-L. Hsu, Y.-H. Lee, W. Zhang, K.-H. Wei, L.-J. Li, *Adv. Mater.* **2013**, *25*, 756.

[4] R. Bhandavt, L. David, G. Singh, *J. Phys. Chem. Lett.* **2012**, *3*, 1523.

[5] S. Kim, A. Konar, W.-S. Hwang, J. H. Lee, J. Lee. J. Yang, C. Jung, H. Kim, J.-B. Yoo, J.-Y. Choi, *Nat. Comm.* **2012**, *3*, 1011.

[6] Barga, D.; Lezama, I. G.; Berger, H.; Morpurgo, A. F. *Nano Lett.* **2012**, *12*, 5218.

[7] Chang, J.; Register, L. F.; Banerjee, S. K. *Appl. Phys. Lett.* **2013**, *103*, 223509.

[8] Tongay, S.; Zhou, J.; Ataca, C.; Lo, K.; Mattews, T. S.; Li, J.; Grossman, J. C.; Wu, J. *Nano Lett.* **2012**, *12*, 5576.

[9] Zhao, W.; Ghorannevis, Z.; Chu, L.; Toh, M.; Kloc, C.; Tan, P.-H.; Eda, G. *ACS nano* **2013**, *7*, 791-797.

[10] Xiao, D.; Liu, G.-B.; Feng, W.; Xu, X.; Yao, W. *Phys. Rev. Lett.* **2012**, *108*, 196802.

[11] Zeng, Z.; Yin, Z.; Huang, X.; Li, H.; He, Q.; Lu, G.; Boey, F.; Zhang, H. *Angew. Chem. Int. Ed.* **2011**, *50*, 11093.

[12] Coleman, J. N.; Lotya, M.; O'neill, A.; Bergin, S. D.; King. P. J.; Khan, U.; Young, K.; Gaucher, A.; De, S.; Smith, R. J., *Science*, **2011**, *331*, 568.

[13] Seayad, A. M; and Antonelli, D. M. *Adv. Mater.* **2004**, *16*, 765.

[14] Lee. Y.-H.; Zhang, X.-Q.; Zhang, W.; Chang, M.-T.; Lin, C.-T.; Chang, K.-D.; Yu, Y.-C.; Wang, J. T.-W.; Chang, C.-S.; Li, L.-J., *Adv. Mater.* **2012**, *24*, 2320.

[15] Zhang, Y.; Zhang, Y.; Ji, Q.; Ju, J.; Yuan, H.; Shi, J.; Gao, T.; Ma, D.; Liu, M.; Chen, Y., *ACS nano* **2013**, *7*, 8963.

[16] Najmaei, S.; Liu, Z.; Zhou, W.; Zou, X.; Shi, G.; Lei, S.; Yakobson, B. I.; Idrobo, J.-C.; Ajayan, P. M.; Lou, J. *Nat. Mater.* **2013**, *12*, 754.

[17] Liu, K.-K.; Zhang, W.; Lee, Y.-H.; Lin, Y.-C.; Chang, M.-T.; Su, C.-Y.; Chang, C.-S.; Li, H.; Shi, Y.; Zhang, H., *Nano Lett.* **2012**, *12*, 1538-1544.

[18] Butler, S. Z.; Hollen, S. M.; Cao, L.; Cui, Y.; Gupta, J. A.; Gutiérrez, H. R.; Heinz, T. F.; Hong, S. S.; Huang, J.; Ismach, A. F., *ACS nano* **2013**, *7*, 2898.

[19] Jørgensen, M. Norrman; K. Krebs F. C., *Sol. Energy Mater. Sol. Clles* **2008**, *92*, 686.

[20] Tokarz-Sobieraj, R.; Hermann, K.; Witko, M.; Blume, A.; Mestl, G.; Scholögl, R. *Surf. Sci.* **2001**, *489*, 107.

[21] Anwar, M.; Hogarth, C. A.; Lott, K. A. K. *Phys. Status Solidi A* **1989**, *114*, 225.

[22] Elías, A. L.; Perea-López, N.; Castro-Beltrán, A.; Berkdemir, A.; Lv, R.; Feng, S.; Long, A. D.; Hyashi, T.; Kim, Y. A.; Endo, M., *ACS nano* **2013**, *7*, 5235.

[23] Brito, J. L., Ilija, M., Hernández, P. *Thermochimica Acta*, **1995**, *256*, 325.

[24] van der Zande, A. M.; Huang, P. Y.; Chenet, D. A.; Berkelbach, T. C.; You. YM; Lee, G.-H.; Heinz, T. F.; Reichman, D. R.; Muller, D. A.; Hone, J. C., *Nat. Mater.* **2013**, *12*, 554.

[25] Yu. Y.; Li, C.; Liu, Y.; Su, L.; Zhang, Y.; Cao, L. *Sci. Rep.* **2013**, *3*, 1866.

[26] Mak, K. F., Lee, C., Hone, J., Shan, J. Heinz, T. F. *Phys. Rev. Lett.* **2010**, *105*, 136805.

[27] Yang, J.; Voriy, D.; Ahn, S. J.; Kang, D.; Kim, A. Y.; Chhowalla, M.; Shin, H. S., *Angew. Chem. Int. Ed.* **2013**, *52*, 13751.

28. Lee, C.; Yan, H.; Brus, L. E.; Heinz, T. F.; Hone, J.; Ryu, S., *ACS nano* **2010**, *4*, 2695.

[29] Li, H.; Zhang, Q.; Yap, C. C. R.; Tay, B. K.; Edwin, T. H. T.; Oliver, A.; Baillargeat, D., *Adv. Funct. Mater.* **2012**, *22*, 1385.

[30] Berkdemir, A.; Gutiérrez, H. R.; Botello-Méndez, A. R.; Perea-López, N.; Elías, A. L.; Chia, C.-I.; Wang, B.; Crespi, V. H.; López-Urías, F.; Charlier, J.-C., *Sci. Rep.* **2013**, *3*, 1755.

[31] K. C. Kwon, S. Kim, C. Kim, J.-L. Lee, S. Y. Kim., *Org. Elec.* **2014**, *15*, 3154.

[32] Q. V. Le, T. P. Nguyen, H. W. Jang, S. Y. Kim. *Phys. Chem. Chem. Phys.* **2014**, *16*, 13123

3.2. Charge transport layers in perovskite-based organic photovoltaic cells

3.2.1. Introduction

Organic photovoltaic (OPV) cells have attracted considerable attention because of their low cost, light weight, flexibility, and ease of enlargement through the roll-to-roll coating process.[1–3] Although a power conversion efficiency (PCE) of over 10% has been achieved by the OPV cells using a comprehensive material design for appropriate materials, structure optimization, and molecule engineering, it is difficult to find a breakthrough for further increasing the PCE value.[4–6] In order to overcome this difficulty, organolead halide perovskite has emerged as an exciting material in the photovoltaic research field because of its large light absorption coefficient, high carrier mobility, and long carrier diffusion length.[7–9] The organolead halide-based photovoltaic cell was first introduced in 2009 as a sensitizer for dye-sensitized solar cells.[10] The structure of the perovskite solar cells (PSCs) has progressed from a perovskite dot deposited on TiO_2 with a PCE of 9.7% to a planar p-n junction with a PCE of 15.4%, via the meso-superstructured scaffold Al_2O_3 concept with a PCE of 10.9% and perovskite-infiltrated nanocomposite with a PCE of 15%.[11] Through the progress of the structure and the materials, the PCE value has increased to 20.1% using formamidinium lead iodide and methylammonium lead iodide as active materials for the PSCs with a planar *p-i-n* junction structure.[12]

Electron and hole conductors are important in PSCs with a planar p-n

junction structure to achieve outstanding device performance. The $CH_3NH_3PbI_2Cl$ or $CH_3NH_3PbI_3$ films have been reported as active materials for the PSCs owing to their long electron–hole diffusion lengths exceeding 1 μm and 100 nm, respectively.[8] Phenyl-C_{61}-butyric acid methyl ester (PCBM) and poly(3,4-ethylenedioxythiophene): poly(styrenesulfonate) (PEDOT:PSS) are conventionally used as the *p*- and *n*-type semiconductors in the *p*-*n* junction PSCs, where holes are collected at the transparent conductive anode and electrons are collected at the metal cathode. Although PEDOT:PSS is one of the best *p*-type semiconductors because of its adequate energy level and excellent carrier mobility, it has been reported that PEDOT:PSS is not suitable for practical applications owing to its hygroscopic effect and high acidic property, which causes fast degradation of organic layers.[13] Furthermore, the organolead halide perovskites layer results in the dissociation of the crystal structures upon contact with the moisture in the air.[14] Therefore, the development of a hole extraction layer (HEL) instead of PEDOT:PSS is required to fabricated PSCs with high PCE and long-term stability.

Graphene oxide (GO) was used as the HEL in the OPV cells due to its high work function after surface treatment, simple fabrication process, and relative stability when exposed to air as compared with PEDOT:PSS.[15] Because of the excellent charge transport properties of the transition metal dichalcogenides (TMDs) such as MoS_2, WS_2, TaS_2, and TiS_2, two-dimensional TMDs were used as both hole and electron transport layers in the OPV cells.[16] The lone-pair electrons of the carbon and chalcogen atoms in the isolated monolayer structure of GO and TMDs enable ballistic transport, indicating improved carrier

mobility.[17] Furthermore, the energy levels of the GO and TMD layers can be modulated by chemical doping and simple surface treatment. Therefore, it is assumed that the GO and TMD layers can be used as the HELs in the PSCs instead of PEDOT:PSS.

Here, we demonstrate that GO, MoS_2, and WS_2 can be used as the HELs in the PSCs instead of PEDOT:PSS. The GO layer was synthesized through the Hummers' method and the TMD layers such as MoS_2 and WS_2 layers were obtained by the chemical vapor deposition (CVD) method. It is shown that the perovskite structure was well-formed on the GO and TMD layers. Therefore, the performance of the PSCs based on the GO and TMD layers was comparable with that of the PEDOT:PSS-based ones. From these results, the working principle of the GO and TMD layers as the HELs in the PSCs is investigated.

3.2.2. Experimental procedures

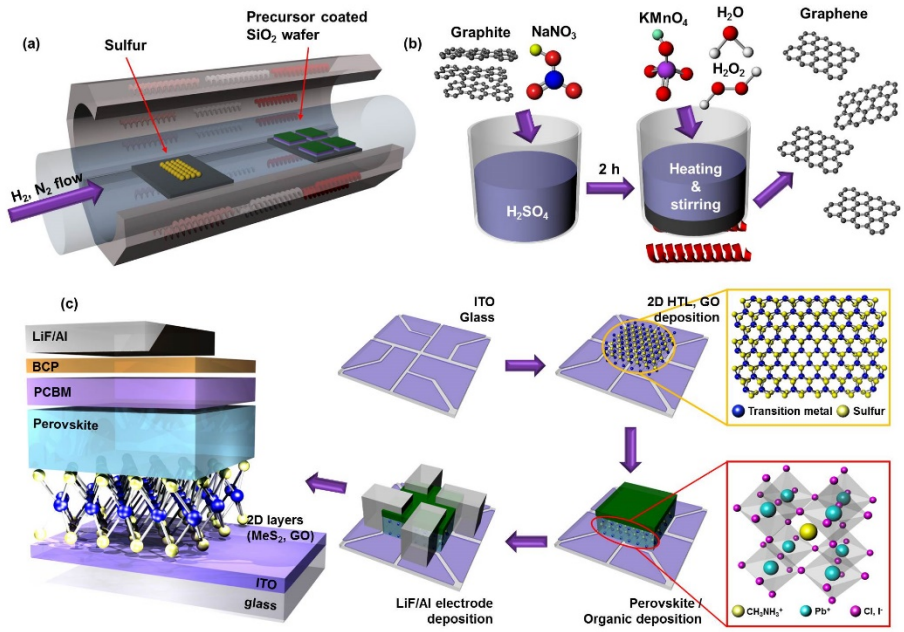

Fig. 2.18. (a) Schematic of chemical vapor deposition (CVD) synthesis for MoS_2 and WS_2 layers. (b) Synthesis of graphene oxide (GO) layers. (c) Schematic of PSC fabrication procedure and device structure.

Synthesis of MoS_2 and WS_2. The insulating substrate, SiO_2 (300 nm)/Si wafer, was prepared using a standard piranha solution and conventional cleaning procedures based on acetone, isopropyl alcohol, and de-ionized (DI) water bath sonication. Two precursor solutions were prepared with a 5 mM concentration of each $(NH_4)_2MoS_4$ and $(NH_4)_2WS_4$ in ethylene glycol. For the optimized precursor coating conditions, the cleaned substrates were subjected to the O_2 plasma and the UV-O_3 surface treatment for 15 min. The substrates were spin-coated with the precursor solution at 3500 rpm for 60 s. A thermal CVD system involving high purity hydrogen (H_2) and nitrogen (N_2) gas was used for the thermolysis of the precursor films. First, the temperature of the

CVD furnace was set to 500 °C for 30 min, under H_2 and N_2 gas flow at 1 Torr pressure. The H_2 and N_2 flow rates were controlled by the mass flow controllers at a rate of 40 cm^3/min for H_2 and 200 cm^3/min for N_2. Then, the thermolysis was gradually initiated under the H_2 gas at a relatively high temperature. After the preheating step, the temperature was significantly increased to approximately 950 °C. When the CVD furnace temperature reached 950 °C, the samples were placed on the heating zone for 1 h, and another heating zone with sulfur powder was turned on to initiate sulfur sublimation. After 60 min of thermolysis, the furnace was cooled to room temperature at a rate of 10–15 °C/min under 40 sccm and 200 sccm of H_2 and N_2 flow, respectively. A schematic illustration of MoS_2 and WS_2 synthesis is shown in Fig. 3.18(a). Poly[methyl methacrylate] (PMMA) was then spin-coated on the synthesized MoS_2 and WS_2 layers. Then, the substrate was immersed into a hydrogen fluoride and aluminum fluoride (1:1) bath at room temperature for 1 h to etch away the SiO_2 layers. Subsequently, the remaining MoS_2 and WS_2 layers were carefully dipped into a DI water bath 7−9 times to remove any residual etchant. The MoS_2 and WS_2 sheets were then transferred onto an indium tin oxide (ITO) substrate. Finally, the PMMA membrane was removed by an acetone bath at 50 ^oC for 30 min after which the PMMA/MoS_2 (or WS_2) layer had completely adhered to the target substrate.

Synthesis of graphene oxide (GO). GO was synthesized by the oxidation of natural graphite powder according to the Hummers' method with $NaNO_3$. Briefly, 1 g natural graphite powder (universal grade, 200 mesh, 99.9995%; Alfa Aesar) and 1 g $NaNO_3$ were stirred in 46 mL concentrated H_2SO_4 for 4 h

in an ice bath. After stirring, 6 g $KMnO_4$ was added gradually, taking care not to increase the temperature of the solution more than 20 °C. After $KMnO_4$ and the solution were mixed, the suspension was heated at 35 °C and stirred for 2 h. Next, 92 mL of DI water was added, and the solution was stirred for 15 min at 98 °C. By adding 200 mL of DI water and 14 mL H_2O_2 (30%) slowly, the color of the solution changed from black to orange. The solution was separated through centrifugation at 8000 rpm and removed except for the GO precipitation. This GO precipitation was washed with 900 mL of 1:8 HCl aqueous solution. The centrifugation at 8000 rpm for 10 min and the washing steps were repeated at least three times to remove any metal ions. After that, the cleaning using only the DI water was repeated about seven times. Finally, the GO was dried at 50 °C for 12 h in a vacuum oven. The schematic illustration of the GO synthesis is shown in Fig. 3.18(b).

Synthesis of perovskite precursor. Hydroiodic acid (10 mL, 57 wt% in water, Aldrich) and methylamine (22 mL, 33% in ethanol, Aldrich) were stirred in the ice bath for 3 h. Next, the solution was evaporated at 90 °C using a rotary evaporator to remove the ethanol and DI water. Then, the dissolution of the precipitate into anhydrous ethanol and recrystallization with diethyl ether were performed three times forming methylammonium iodide (CH_3NH_3I). To prepare a perovskite precursor, CH_3NH_3I, lead (II) chloride ($PbCl_2$, Aldrich), and lead (II) iodide (PbI_2, Aldrich) with 4:1:1 molar ratio were dissolved in anhydrous N,N-dimethyl formamide (DMF, Aldrich).

Fabrication of PSCs. An ITO glass was used as the starting substrate; its surface was cleaned in sequence with acetone, isopropyl alcohol, and DI water, and then dried with high purity nitrogen gas. The samples were treated with UV/ozone (UVO) for 15 min. After the treatment of the substrate, the PEDOT:PSS, MoS_2, WS_2, or GO layer were formed at the active area and then the substrates were loaded into a N_2-filled glove-box (< 0.1 ppm of O_2 and H_2O). The thickness of the PEDOT:PSS layer was 50 nm and that of the MoS_2, WS_2, and GO layers was approximately 2 nm. For preparing the $CH_3NH_3PbI_{3-x}Cl_x$ layer, 40 wt% (4:1:1 molar ratio) solution of perovskite precursor in DMF was spin-coated at 4000 rpm for 30 s to prepare the perovskite films. The substrates were subsequently heated at 100 °C on a hot plate under dry conditions for 60 min. The color of the film changed from transparent light yellow to transparent dark brown via opaque black. The PCBM (Nano-C, used as received) was dissolved in chlorobenzene to prepare a 40 mg/mL solution. The PCBM solution was stirred for approximately 24 h in a glove box before being spin-coated (700 rpm, 15 s, 40 nm) on top of the $CH_3NH_3PbI_{3-x}Cl_x$ active layer. The cathode consisted of bathocuproine (BCP, 3 nm), LiF (1 nm), and Al (100 nm) deposited at a base pressure of 1×10^{-6} Torr using a thermal evaporator. The BCP layer was used as the hole blocking layer. The active device area was 0.2 $\times$ 0.2 cm^2 and the scan rate was 0.1 V/s. The voltage was swept from 0 V to 1 V at intervals of 100 steps. The schematic fabrication procedure and the device structure are shown in Fig. 3.18(c).

Characterizations. Field-emission scanning electron microscopy (FE-SEM) images were taken to measure the thickness of each layer and the surface state.

Raman spectra were obtained using a Lab RAMHR (Horiba JobinYvon, Japan) at an excitation wavelength of 532 nm. The X-ray diffraction (XRD) pattern (D8-Advance/Bruker-AXS) and the transmission electron microscope (TEM, JEOL-2100F, Japan) images were obtained to measure the structures and the sizes of the perovskite materials, MoS_2, WS_2, and GO. Contact-mode atomic force microscopy (AFM, XE-100/PSIA) was used to measure the surface root-mean-square (RMS) roughness. Synchrotron radiation photoemission spectroscopy (SRPES) experiments were performed in an ultra-high vacuum chamber (base pressure of ca. 10^{-10} Torr) with a 4D beam line equipped with an electron analyzer and a heating element at the Pohang Acceleration Laboratory. The onset of the photoemission spectra, corresponding to the vacuum levels at the surface of the samples, was measured using incident photon energy of 350 eV with a negative bias on the sample. The results were corrected for the charging effects using Au 4f as an internal reference. The current density-voltage characteristics of the PSCs were measured with a Keithley 2400 semiconductor parameter analyzer. The photocurrent of the PSCs was measured under AM 1.5G 100 mW/cm^2 illumination using an Oriel 150 W solar simulator.

3.2.3. Results and Discussion

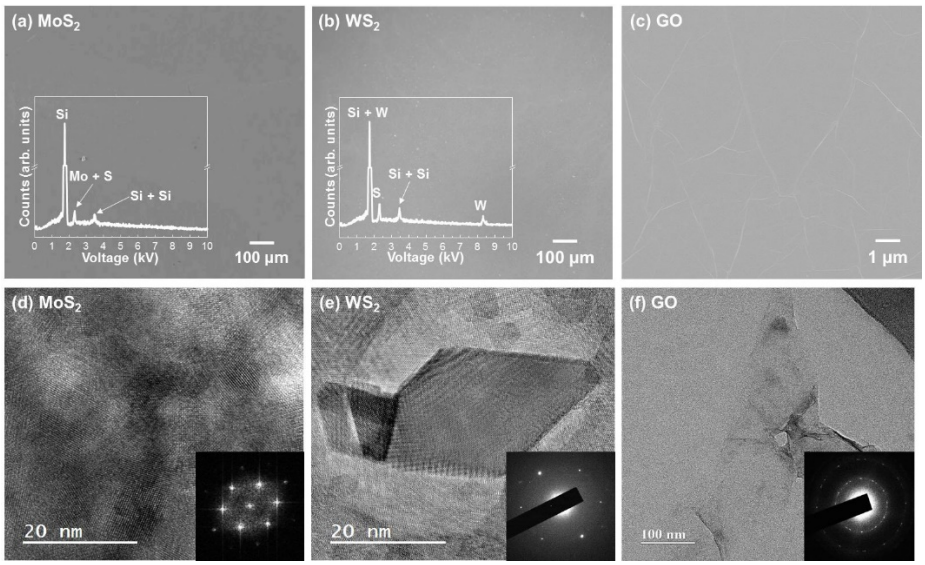

Fig. 3.19. Top view of FE-SEM) images of synthesized (a) MoS_2, (b) WS_2, and (c) GO layers. The scale bar is 100 µm for MoS_2 and WS_2 layers and 1 µm for GO layer. The high resolution TEM images of synthesized (d) MoS_2, (e) WS_2, and (f) GO layers. SAED patterns show the hexagonal atomic distribution of each differently synthesized HELs in the inset of (d)–(f).

Figs. 3.19(a)–(c) show the top view of the FE-SEM images of MoS_2, WS_2, and GO. The surfaces of MoS_2, WS_2, and GO are smooth. The energy dispersive spectra show the specific peaks of molybdenum, tungsten, and sulfur, confirming that the synthesized films are MoS_2 and WS_2. It is shown that the lateral dimensions of the GO flakes range from 1−5 µm. The degree of coverage increased with increasing GO concentration. It was demonstrated that 0.4 mg/mL of GO was sufficient to cover the entire surface. Figs. 3.19(d)–(f) show the TEM images of MoS_2, WS_2, and GO. The periodic atomic arrangements of the MoS_2 and WS_2 films are shown in the insets of Figs. 3.19(d) and (f). The selected area electron diffraction (SAED) patterns reveal a hexagonal structure, indicating that single-crystalline MoS_2 and WS_2 layers were synthesized.[18]

However, a non-periodic atomic arrangement in the TEM images and the ring motifs in the SAED patterns were also found in other areas, indicating the presence of polycrystalline areas in the synthesized MoS_2 and WS_2 layers. In the case of GO, the ring motifs in the SAED patterns shown in Fig. 3.19(f) suggest that GO has a polycrystalline structure.

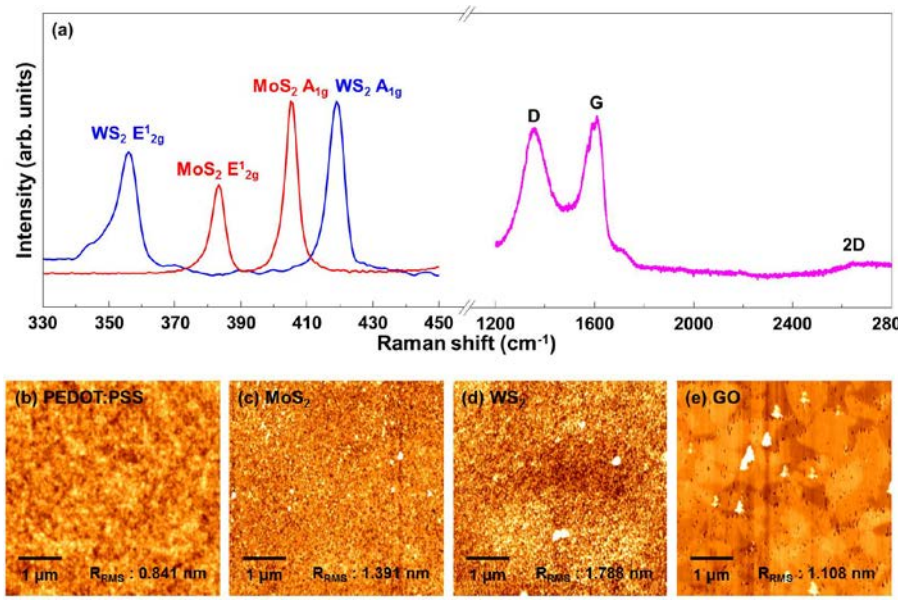

Fig. 3.20. (a) Raman spectra of MoS_2, WS_2 and GO layers ranging from 330 cm^{-1} to 2800 cm^{-1}. AFM images of (b) PEDOT:PSS, (c) MoS_2, (d) WS_2, and (e) GO layers. The RMS roughness values of PEDOT:PSS, MoS_2, WS_2, and GO layers are 0.841 nm, 1.391 nm, 1.788 nm, and 1.108 nm, respectively.

Fig. 3.20(a) shows the Raman spectra of the MoS_2, WS_2, and GO layers. The Raman spectra of the MoS_2 and WS_2 layers appear to contain two predominant peaks: (i) the out-of-plane (A_{1g}) mode where the top and bottom chalcogen atoms move out of the plane in opposite directions while the transition metal is stationary and (ii) the in-plane (E^1_{2g}) mode where both the transition metal and chalcogen atoms move in the plane in opposite directions.[19–21] The peaks at 383.3 cm^{-1} and 405.4 cm^{-1} in the MoS_2 layer correspond to E^1_{2g} and A_{1g} modes

of MoS_2, and the peaks at 357 cm^{-1} and 419 cm^{-1} in the WS_2 layer mean E^1_{2g} and A_{1g} modes of WS_2.[22] This implies that the $(NH_4)_2MoS_4$ and $(NH_4)_2WS_4$ precursors transformed well into the MoS_2 and WS_2 thin layers by the CVD system. The Raman spectrum of the GO thin film contains two characteristic peaks. One peak located at 1350 cm^{-1} (D peak) originated from the structural imperfections produced by the attachment of the hydroxyl and epoxide groups. The other peak located at 1592 cm^{-1} (G peak) was generated by the sp^2 graphitic materials.[23] Therefore, it is considered that the GO film was well synthesized from the graphite powder. The AFM images of PEDOT:PSS, MoS_2, WS_2, and GO are shown in Figs. 3.20(b)–(e). The RMS roughness values of PEDOT:PSS, MoS_2, WS_2, and GO were measured to be 0.841 nm, 1.391 nm, 1.778 nm, and 1.108 nm, respectively. Although the roughness of WS_2 is the highest, the roughness values of all the materials are low enough to spin-coat the perovskite layer on the HEL.

Fig. 3.21 shows the (a) Mo 3*d* and S 2*p* of the synthesized MoS_2, (b) W 4*f* and S 2*p* of the synthesized WS_2, and (c) C 1*s* and O 1*s* of the exfoliated GO SRPES spectra. The five peaks appear at 162.3 eV, 163.8 eV, 226.5 eV, 230.5 eV, and 234.0 eV in the MoS_2 sample, which are assigned to S $2p_{3/2}$, S $2p_{1/2}$, S 2*s*, Mo $3d_{5/2}$, and Mo $3d_{3/2}$, respectively. In the case of the WS_2 sample, the W-related peaks of W $4f_{7/2}$, W $4f_{5/2}$, and W $5p_{3/2}$ are shown at 32.0 eV, 34.4 eV, and 38.0 eV, respectively. These results are consistent with the findings in the previous reports on the MoS_2 and WS_2 crystals.[22] In the case of GO, the spectral line shapes of C 1*s* and O 1*s* were simulated using a suitable combination of Gaussian and Lorentzian functions in order to separate the

chemical bonding states.[24] For all fitting multiplets, the full width at half maximum were fixed accordingly. The C 1s peak was deconvoluted into four components: sp^2 carbon (C=C) at 284.3 eV, sp^3 carbon (C-C) at 285.4 eV, C-O bond at 286.8eV, and a carbonyl group (C=O) near 287.9 eV.[25] The O 1s peak was deconvoluted to two peaks at 530.4 eV and 532.1 eV, which correspond to the O=C and O-C, respectively.[16]

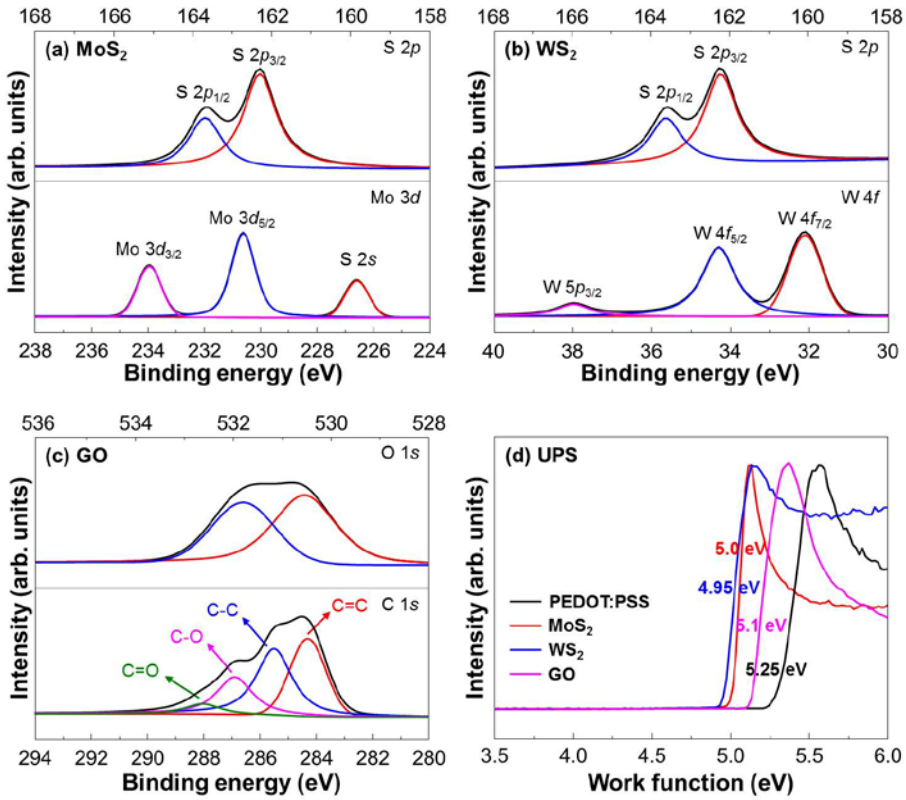

Fig. 3.21. Synchrotron radiation photoemission spectroscopy (SRPES) core level spectra of (a) MoS_2, (b) WS_2, and (c) GO layers. (d) Work functions of PEDOT:PSS, MoS_2, WS_2, and GO layers are 5.25 eV, 5.0 eV, 4.95 eV, and 5.1 eV, respectively. The work function of each different HEL was calculated by extrapolating the ultraviolet photoelectron spectra.

For the MoS_2 and WS_2 layers, the atomic ratio of Mo to S was constant at 38:62 and that of W to S was constant at 32:68. For the synthesized GO film,

the atomic ratio of C to O was constant at 13:87, which is in good agreement with the previous reports.[22, 23] These results indicate that MoS_2 and WS_2 were well synthesized and GO was exfoliated properly through the sonication method. The work functions of PEDOT:PSS, GO, MoS_2, and WS_2 are depicted in Fig. 3.21(d). The onset of the secondary electron was determined by extrapolating the two solid lines from the background and straight onset in the spectra.[26] The work functions of PEDOT:PSS, GO, MoS_2, and WS_2 are measured to be 5.25 eV, 5.1 eV, 5.0 eV, and 4.95 eV, respectively. These values are higher than the work function of O_2 plasma or UV/ozone treated ITO, which is 4.9 eV.[27] Therefore, it is considered that PEDOT:PSS, GO, MoS_2, and WS_2 are adequate to be used as HELs in PSCs from the view point of energy level alignment.

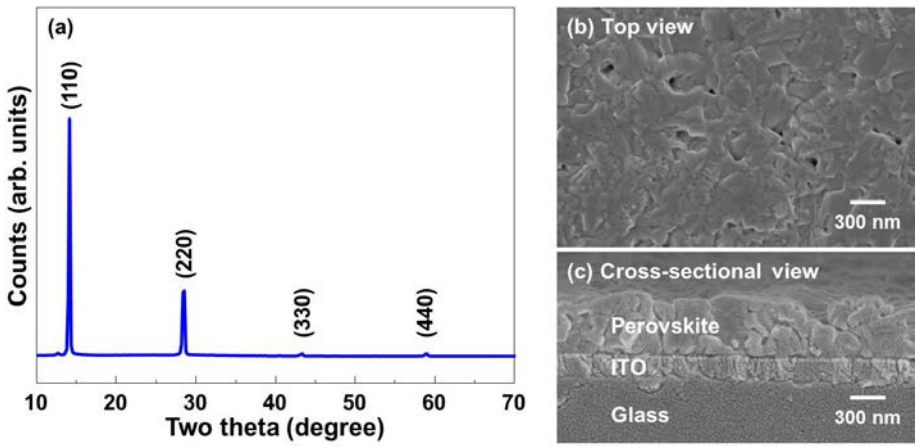

Fig. 3.22. (a) XRD analysis of spin-coated $CH_3NH_3PbCl_{3-x}I_x$ layer. FE-SEM images of $CH_3NH_3PbCl_{3-x}I_x$ layer for (b) top-view and (c) cross-sectional view. The thickness of spin-coated $CH_3NH_3PbCl_{3-x}I_x$ layer is approximately 330 nm.

Fig. 3.22(a) shows the XRD peak of $CH_3NH_3PbI_{3-x}Cl_x$ perovskite layer formed by directly depositing the mixture of CH_3NH_3I, $PbCl_2$, and PbI_2 (4:1:1 molar ratio) in a DMF solution onto the ITO substrates. After annealing the

substrate at 100 °C on a hot plate under dark conditions (< 0.1 ppm of O_2 and H_2O) for 60 min, two intense peaks located at 14.1° and 28.3° and two weak peaks located at 43.2° and 58.8° appeared, indicating the existence of the $CH_3NH_3PbI_3$ and/or $CH_3NH_3PbI_{3-x}Cl_x$ phase.[28,29] Another weak peak appeared at 12.2°, indicating PbI_2. The peak of the intermediate phase at 7.48° was not visible in the XRD spectra, indicating the removal of DMF in the film upon sufficient heating.[30] Furthermore, the absence of any $PbCl_2$ phase is possibly as a result of ion exchange between I^- and Cl^- in the solution or the rapid intercalation reaction that forms the perovskite phase during deposition. The $CH_3NH_3PbCl_3$ peak is reported to be located at 15.57°. However, no strong $CH_3NH_3PbCl_3$ phase was observed in the XRD spectra and the final $CH_3NH_3PbI_{3-x}Cl_x$ film was formed predominantly. This is consistent with the conversion from $CH_3NH_3PbCl_3$ to $CH_3NH_3PbI_3$ in the presence of excess CH_3NH_3I during the film growth under dry conditions. It is reported that the $CH_3NH_3PbCl_3$ phase shows relatively lower thermal stability as compared with $CH_3NH_3PbI_3$.[31,32] The decomposition of the $CH_3NH_3PbCl_3$ phase may release CH_3NH_3Cl, which is replaced by the excess CH_3NH_3I to form $CH_3NH_3PbI_3$ and/or $CH_3NH_3PbI_{3-x}Cl_x$. These results suggest that the perovskite layer formed in this experiment is $CH_3NH_3PbI_{3-x}Cl_x$. Fig. 3.22(b) displays the top view of the FE-SEM images of the $CH_3NH_3PbI_{3-x}Cl_x$ layer. The film shows nearly uniform contrast and grain size across the entire field of view. No cuboid is formed in our sample due to the high concentration of CH_3NH_3I solution compared to the previous report.[33] According to the cross-sectional view of the FE-SEM image of the $CH_3NH_3PbI_{3-x}Cl_x$ layer shown in Fig. 3.22(c), the thickness of the

$CH_3NH_3PbI_{3-x}Cl_x$ perovskite layer is measured to be around 330 nm, which is similar to the reported value.[34]

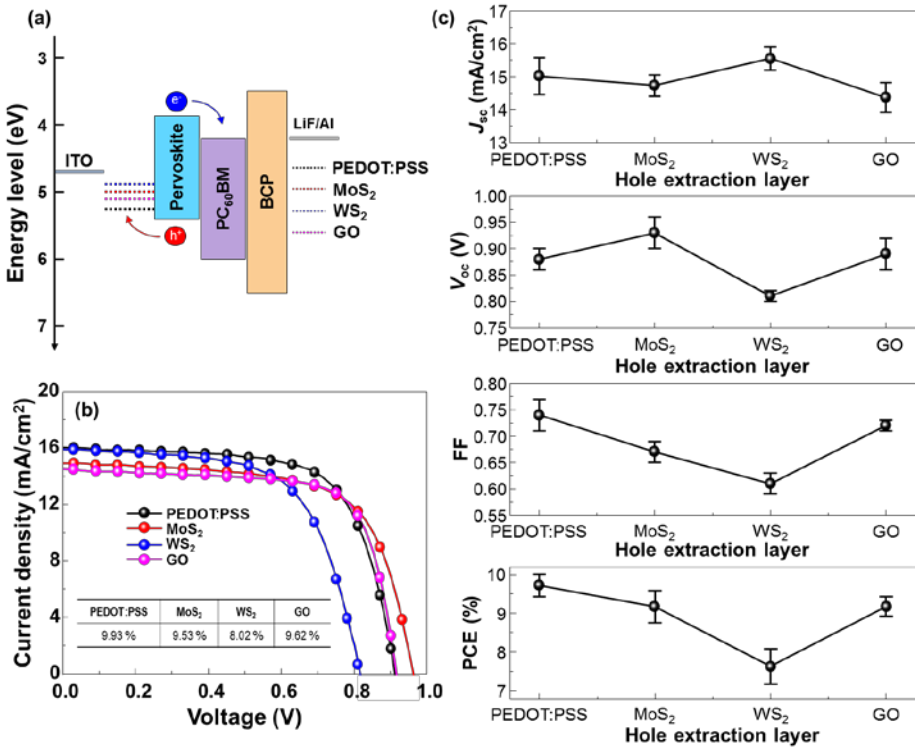

Fig. 3.23. (a) Energy band diagram of fabricated PSCs. (b) Current density–voltage curves of each different HEL-based PSCs. The maximum efficiency of PEDOT:PSS, MoS_2, WS_2, and GO layers are 9.93%, 9.53%, 8.02%, and 9.62%, respectively. (c) The statistical analysis of device characteristics for each different 5 batch fabrications (20 cells).

Fig. 3.23(a) shows the energy band diagram of the PSC with different HELs. The energy levels of ITO, PEDOT:PSS, $CH_3NH_3PbI_xCl_{1-x}$, PCBM, BCP, and LiF/Al were obtained from the literature.[35,36] The energy band diagram suggests that the work functions of GO, MoS_2, and WS_2 are suitable for the HEL in the $CH_3NH_3PbI_xCl_{3-x}$ PSCs as well as the PEDOT:PSS PSCs. The transmittance values of PEDOT:PSS, MoS_2, WS_2, and GO are greater than 90% such that almost no light can reach the $CH_3NH_3PbI_xCl_{1-x}$ active layer through

the ITO/HELs. The device current density-voltage characteristics are shown in Fig. 3.23(b). The open-circuit voltage (V_{oc}), short-circuit current (J_{sc}), fill factor (FF), and power conversion efficiency (PCE) of the PEDOT:PSS based PSCs are 0.91 V, 16.02 mA/cm^2, 0.68, and 9.93%, respectively. The PCEs of MoS_2, WS_2, and GO based PSCs are 9.53%, 8.02%, and 9.62%, respectively. It is interesting to note that the order of the PCE increase is similar to that of the work functions shown in Fig. 3.23(d). It means that work function of the HEL is an important factor in determining the PCE of the PSCs. The detailed characteristics of the PSCs with different HELs are summarized in Table 3.3.

Table 3.3. Summary of the device characteristics of PEDOT:PSS, MoS_2, WS_2 and GO HEL-based PSCs. The statistical analysis of fabricated device was performed with 5 different batch fabrications.

HEL	Work function (eV)	J_{sc} (mA/cm^2)	V_{oc} (V)	FF	PCE (%)	R_{sh}*(Ω cm^2)
PEDOT:PSS	5.25	15.01 ± 0.56	0.88 ± 0.02	0.74 ± 0.03	9.72 ± 0.29	33527.2
MoS_2	5.0	14.73 ± 0.32	0.93 ± 0.03	0.67 ± 0.02	9.17 ± 0.41	40778.9
WS_2	4.95	15.55 ± 0.35	0.81 ± 0.01	0.61 ± 0.02	7.63 ± 0.45	36489.5
GO	5.1	14.36 ± 0.45	0.89 ± 0.03	0.72 ± 0.01	9.17 ± 0.25	10887.7

***R_{sh}: shunt resistance.**

It is important to display the device performance statistics for showing the reproducibility of the fabricated devices. Fig. 3.23(c) shows the statistical analysis of device characteristics (J_{sc}, V_{oc}, FF, and PCE) for each different 5 batch fabrications (20 cells). The standard deviation of each cells are quite reasonable, indicating that the experimental data is reliable and the device fabrication steps are well-established. The lower PCE of the WS_2-based PSC arises from the lower V_{oc} due to the lower work function of WS_2 compared with

the other materials. Although the PCE of WS_2-based PSC was somewhat lower than that of the PEDOT:PSS based one, the PCE of the GO and MoS_2 based solar cells was similar to that of the PEDOT:PSS based one, suggesting that the GO and MoS_2 HELs can be substituted for PEDOT:PSS.

3.2.4. Conclusion

The hole extraction properties of MoS_2, WS_2, and GO in $CH_3NH_3PbI_{3-x}Cl_x$-based PSC devices were investigated. The MoS_2 and WS_2 layers were synthesized by the thermolysis of a $(NH_4)_2MoS_4$) and $(NH_4)_2WS_4$) precursor solution and GO was prepared using the sonication method. The synthesized MoS_2, WS_2, and GO exhibit a polycrystalline structure. According to the FE-SEM and AFM data, the roughness of all the samples was low enough to properly spin-coat the perovskite layer. The core level spectra in the SRPES and the specific peaks in the Raman spectra showed that the MoS_2, WS_2, and GO were well synthesized. The work functions of MoS_2, WS_2, and GO are measured to be 4.95 eV, 5.0 eV, and 5.1 eV, respectively, which are adequate to be used as the HELs in the PSCs from the viewpoint of energy level alignment. Two intense peaks located at 14.1° and 28.3° in the XRD spectrum indicated that the synthesized perovskite material was $CH_3NH_3PbI_{3-x}Cl_x$. The PCE values of the MoS_2, WS_2, and GO-based PSCs were 9.53%, 8.02%, and 9.62%, respectively. The PCE values of the MoS_2 and GO-based PSCs correspond to over 95% of those obtained from the PEDOT:PSS-based devices (PCE of 9.93%). Therefore, these results conclude that MoS_2 and GO can be used as the HELs in the PSCs under optimized conditions.

3.2.5. References

[1] Z. Wu, S. Bai, J. Xiang, Z. Yuan, Y. Yang, W. Cui, X. Gao, Z. Liu, Y. Jin, B. Sun, *Nanoscale*, **2014**, *6*, 10505.

[2] Z. Liu, J. Li, F. Yan, *Adv. Mater.*, **2013**, *25*, 4296.

[3] R. Sondergaard, M. Hosel, D. Angmo, T.T. Larsen-Olsen, F.C. Krebs, *Mater. Today*, **2012**, *15*, 36.

[4] F.-C. Tang, J. Chang, W.-Y. Chou, H.-L. Cheng, S.L.-C. Hsu, J.-S. Chen, H.-S. Sheu, *Phys. Status Solidi A*, **2012**, *2*, 369.

[5] Yang, W. Li, B. Chu, Z. Su, J. Wang, G. Zhang, F. Zhang, *Appl. Phys. Lett.*, **2011**, *99*, 1903301.

[6] X. Zhao, Z. Li, T. Zhu, B. Mi, Z. Gao, W. Huang, *J. Phys. D: Appl. Phys.*, **2013**, *46*, 195105.

[7] S. D. Stranks, G. E. Eperon, G. Grancini, C. Menelaou, M.J.P. Alcocer, T. Leijtens, L. M. Herz, A. petrozza, H. J. Snaith, *Science*, **2013**, *342*, 341.

[8] G. Xing, N. Mathews, S. Sun, S. S. Lim, Y. M. Lam, M. Gratzel, S. Mhaisalkar, T.C. Sum, *Science*, **2013**, *342*, 344.

[9] B. Cai, Y. Xing, Z. Yang, W.-H. Zhang, J. Qiu, *Energy Environ. Sci.*, **2013**, *6*, 1480.

[10] A. Kojima, K. Teshima, Y. Shirai, T. Miyasaka, *J. Am. Chem. Soc.*, **2009**, *131*, 6050.

[11] H.-S. Kim, S.H. Im, N.-G. Park, *J. Phys. Chem. C*, **2014**, *118*, 5615.

[12] W.S. Yang, J.H. Noh, N.J. Jeon, Y.C. Kim, S. Ryu, J. Seo, S.I. Seok, *Science*, **2015**, *348*, 1234.

[13] L.S.C. Pingree, B.A. MacLeod, D.S.Ginger, *J. Phys. Chem. C*, **2008**, *112*, 7922.

[14] H.-S. Kim, C.-R. Lee, J.-H. Im, K.-B. Lee, T. Moehl, A. Marchioro, S.-J. Moon, R. Humphry-baker, J.-H. Yum, J.E. Moser, M. Gratzel, *Sci. Rep.*, **2012**, *2*, 591.

[15] C. Y. Lee, Q. B. Le, C. Kim, S. Y. Kim, *Phys. Chem. Chem. Phys.*, **2015**, *17*, 9369.

[16] Q. V. Le, T. P. Nguyen, K. S. Choi, Y.-H. Cho, Y. J. Hong, S. Y. Kim, *Phys. Chem. Chem. Phys.*, **2014**, *16*, 25468.

[17] J. Chang, L.F. Register, S.K. Banerjee, *Appl. Phys. Lett.*, **2013**, *103*, 223509.

[18] A.M. van der Zande, P.Y. Huang, D.A. Chenet, T.C. berkelbach, Y. You, G.-H. Lee, T.F. Heinz, D.R. Reichman, D.A. Muller, J.C. Hone, *Nat. Mater.*, **2013**, *12*, 554.

[19] C. Lee, H. Yan, L. E. Brus, T. F. Heinz, J. Hone, S. Ryu, *ACS Nano*, **2010**, *4*, 2695.

[20] H. Li, Q. Zhang, C. C. R. Yap, B.K. Tay, T.H.T. Edwin, A. Olivier, D. Baillargeat, *Adv. Funct. Mater.*, **2012**, *22*, 1385.

[21] A. Berkdemir, H.R. Gutierrez, A.R. Botello-Mendez, N. Perea-Lopez, A.L. Elias, C.-I. Chia, B. Wang, V.H. Crespi, F. Lopez-Urias, J.-C. Charlier, H. Terrones, M. Terrones, *Sci. Rep.*, **2013**, *3*, 1755.

[22] K.C. Kwon, C. Kim, Q.V. Le, S. Gim, J.-M. Jeon, J.Y. Ham, J.-L. Lee, H.W. Jang, S.Y. Kim, *ACS Nano*, **2015**, *9*, 4146.

[23] Yang, A. Velamakanni, G. Bozoklu, S. Park, M. Stoller, R.D. Piner, S. Stankovich, I. Jung, D.A. Field, C.A. Ventrice Jr., R.S. Ruoff, *Carbon*, **2009**, *47*, 145.

[24] Choi, Y.-G. Yoon, K. S. Choi, J. H. Kang, Y.-S. Shim, Y. H. Kim, H. J. Chang, J.-H. Lee, C. R. Park, S.Y. Kim, H. W. Jang, *Carbon*, **2015**, *91*, 178.

[25] K. C. Kwon, J. Ham, S. Kim, J.-L. Lee, S. Y. Kim, *Sci. Rep.*, **2014**, *4*, 4830.

[26] A.P. Saxena, M. Deepa, A.G. Joshi, S. Bhandari, A.K. Srivastava, *ACS Appl. Mater. Interfaces*, **2011**, *3*, 1115.

[27] W.J. Dong, G.H. Jung, S.Y. Kim, J.-L. Lee, *Sol. Energ. Mater. Sol. C.*, **2013**, *109*, 240.

[28] S. Dharani, H.A. Dewi, R.R. Prabhakar, T. Baikie, C. Shi, D. Yonghua, N. Mathews, P.P. Boix, S.G. Mhaisalkar, *Nanoscale*, **2014**, *6*, 13854.

[29] A.T. Barrows, A.J. Pearson, C.K. Kwak, A.D.F. Dunbar, A.R. Buckley, D.G. Lidzey, *Energy Environ. Sci.*, **2014**, *7*, 2944.

[30] I. Persson, K. Lyczko, D. Lundberg, L. Eriksson, A. Placzek, *Inorg. Chem.*, **2011**, *50*, 1058.

[31] J. Blazejowski, E. Kowalewska, *Thermochim. Acta*, **1986**, *105*, 257.

[32] P. Dokurno, J. Lubkowski, J. Blaejowski, *Thermochim. Acta*, **1990**,

165, 31.

[33] M. Liu, M.B. Johnston, H.J. Snaith, *Nature*, **2013**, *501*, 395.

[34] J.-H. Im, I.-H. Jang, N. Pellet, M. Gratzel, N.-G. Park, *Nat. Nanotechnol.*, **2014**, *9*, 927.

[35] C. Kim, T.P. Nguyen, Q.V. Le, J.-M. Jeon, H.W. Jang, S.Y. Kim, *Adv. Funct. Mater.*, **2015**, *25*, 4512.

[36] P. Docampo, J.M. Ball, M. Darwich, G.E. Eperon, H.J. Snaith, *Nat. Comm.*, **2013**, *4*, 2761.

3.3. p-n junction photovoltaic layers

3.3.1. Introduction

Two-dimensional transition metal dichalcogenide (TMD) materials have been widely investigated and characterized in the recent years due to their promising potential in future electronics. Devices such as transistors, memories, photodetectors, and hydrogen evolution catalysts based on 2-dimensional (2D) materials have been successfully fabricated and demonstrated.[1-5] Specifically, a single semiconducting 0.6-nm-thick MoS_2 can absorb as much sunlight as 50 nm of Si and generate photocurrents as similar as 12-nm-thick GaAs semiconductor.[6-8] Moreover, the semiconducting MoS_2 is anticipated to offer the additional advantages in serving as photovoltaic active materials, including excellent chemical stability and superior electronic properties for fabricating functional interfaces with other 2D TMDs because they can form the high-quality heterojunction and the interfaces with an extremely low areal density of dangling bonds and charge traps.[9,10]

To enable the TMDs based photovoltaic devices, the growth technique of TMDs needs to be improved in relation to the domain size, crystal quality, and thickness control. A mechanical exfoliation is a facile and cheap method to separate each layer of 2D materials and build heterojunctions.[11] Although the exfoliated nanosheet shows excellent quality, the fabricated nanosheet is too small and hard to apply for various applications in electronic devices. On the other hands, the chemical vapor deposition (CVD) method have been recently spotlighted for synthesizing the TMDs by using precursors and sulfur

powders.[12] The synthesis of MoS_2 by using CVD techniques are mainly subdivided into three methods; (i) thermolysis of solution precursors, (ii) sulfurization of molybdenum oxides (MoO_3), and (iii) vapor deposition of the powder precursors (sulfur (S) and metal chlorides, $MoCl_x$). In the sulfurization of MoO_3 and vapor deposition of the $MoCl_x$ and the S powders, it is difficult to make the uniform and continuous films, however, the thermolysis of solution precursor have been investigated to synthesize the continuous MoS_2 thin films. The reduction reaction of $[(NH_4)_2MoS_4]$ by using CVD technique can provide the continuous and uniform MoS_2 thin film without any treatment.[13,14]

Recently, the exfoliated and CVD-synthesized MoS_2 thin films have been utilized for photovoltaic devices.[15] Although MoS_2 has high potentials and several advantages as a photovoltaic material, the MoS_2-based photovoltaic devices are still suffering from the low photo conversion efficiency (PCE). The only 5 ~ 10 % of light absorption in MoS_2 monolayer is quite lower value to generate electricity, compared to the other photovoltaic materials.[16] Additionally, the MoS_2 has high sheet resistances, which are not appropriate for photovoltaic applications. For these reasons, the MoS_2/graphene- and WS_2/MoS_2-based photovoltaic cells have been reported only 1 ~ 1.5 % efficiency despite their ultrafast charge transfer property.[17] In order to obtain a high-performance MoS_2-based photovoltaic cell, the heterojunctions with existing photovoltaic materials such as Si present new possibilities. A monolayer n-MoS_2/p-Si photovoltaic cell realized an impressive PCE of up to 5.23% with an Al-covered electrode on the top of the monolayer n-MoS_2.[18] Moreover, Hao *et al.* achieved the PCE of 4.5% in bulk-like MoS_2/p-Si solar

cells with a Pd-covered electrode under 15.0 mW cm^{-2} light illumination. On the other hand, the large contact area between the metal electrode and MoS_2 is used for the devices, resulting in a very small active area of the devices (μm^2 scale).[19] Because of the high sheet resistance of MoS_2 it is difficult to transport the photo-generated carriers to electrodes, these approaches could lower the series resistance of the devices and help to collect photo-generated carriers. However, the excellent absorption property of MoS_2 could not be fully utilized due to large area covered metal electrodes that a large number of photons are reflected by the electrodes.[20] For these reasons, it is essential to find the breakthrough for utilizing the advantages of MoS_2 in the photovoltaic applications.

In this work, we demonstrated the Au nanomesh based high transparent (T = ~90 %) electrodes with low electrical resistance (~ 6 Ω/sq.) and it is successfully integrated to thickness controlled, the wafer-scale growth of *n*-MoS_2 thin film / *p*-Si heterojunction solar cells. The ultraviolet-ozone and pre-thermal treatments to polymeric templates for transparent electrodes enable fabrication of transparent electrodes with high figure of merits (F=700). The Au nanomesh electrodes help to effectively collect photo-generated carriers from the junctions while maintaining a high transmittance. Our approach paves a way to utilize the outstanding MoS_2 properties in the practical application to not only the solar cells but also the optoelectronic devices.

3.3.2. Experimental procedures

Synthesis of MoS_2 thin films. The starting substrate, SiO_2 (300 nm)/Si wafer was cleaned with conventional acetone (10 min), isopropyl alcohol (10 min), and de-ionized (DI) water (10 min). Before the spin-coating of ammonium tetrathiomolybdate [$(NH_4)_2MoS_4$] solution precursor, the cleaned substrates were exposed the ultraviolet-ozone (UV-O_3) for 30 min. The precursor-coated substrates were annealed at 50 °C for the evaporation of residual solvent. Then, the substrates were moved into the chemical vapor deposition chamber for the thermolysis process. The thermolysis process subdivided into two-steps. First, the decomposition of precursor thin film to the ammonia and MoS_3 complexes under the 500 °C and N_2/H_2 (1000/100 sccm) flow for 40 min. The transformation of MoS_3 to MoS_2 was occurred when the 900 °C annealing with evaporation of sulfur powder precursors at 330 °C for 1 hour. When the reaction is completed, the temperature of chamber cooled down to room temperature with cooling rate of 5 °C/sec.

Transfer of MoS_2 thin films. The supporting polymer, poly(methyl methacrylate) (PMMA) was spin-coated on the synthesized $MoS_2/SiO_2/Si$ wafer to transfer onto the *p*-Si/Al BSF substrates. The edge of spin-coated substrates was scraped out before the immersing into the buffered oxide etchant/hydrogen fluoride solution (BOE/HF =3/1). The floated PMMA/MoS_2 thin film were rinsed with DI water about 7-9 times for removing the residual etchant solution. The cleaned PMMA/MoS_2 thin film was transferred onto fabricated p-Si/Al BSF substrate by the conventional wet transfer method. The

PMMA layer was removed by using hot acetone bath at 50 °C after the PMMA/MoS_2 layer completed adhered onto the substrate.

Fabrication of Au nanomesh electrodes. The electrospinning was performed by placing 6 ml of solution into a 10 ml plastic syringe tipped with a 26-gauge stainless steel needle and carried out at the needle-to-collector distance of 10 cm with and applied 13 kV. The solution was injected with a feeding rate of 0.5 mL/h. The fabricated nanofibers templates on the metal frame were annealed at 150 °C for 1 hour to connect the nanofibers. Consecutively, ultraviolet-ozone treatment is applied to nanofibers templates before the Au deposition. E – beam evaporator is used to deposit the gold. After deposition of the metal, templates were peeled from the metal frame and transferred to target substrate. Simultaneously, acetone was sprayed about 10 times for removing polymeric template completely, and then it was rinsed by IPA and DI water.

Characterizations of MoS_2 and Au nanomesh electrodes. The Raman spectra of the synthesized thin films were recorded with a Confocal Raman Microscope (RAMANforce, Nanophoton, Japan) at an excitation wavelength of 532 nm. X-ray photoemission spectroscopy (XPS) was carried out of an AXIS Ultra DLD model (KRATOS, U.K.) operating at a base pressure of 5×10^{-10} mbar at 300 K with a monochromatic Al Kα line at 1486.69 eV. Ultraviolet photoemission spectroscopy (UPS) was performed with a He I (21.2 eV) source. The Raman, XPS, and UPS analysis were conducted by in-situ nanosurface analysis system at the Korea Basic Science Institute (KBSI). The non-contact-mode AFM (XE-100, Park Systems) measurements at a scanning rate of 0.5 Hz

were performed to examine the surface morphology and to determine the thickness of the synthesized MoS_2 thin films. The bright-field and high-resolution TEM (JEOL JEM-2100F, 200 kV) images were obtained to investigate the microstructure of the synthesized thin films. The absorption spectra of the synthesized thin films were measured by UV-Visible spectroscopy (JASCO-670). The morphology of Au nanomesh electrode was observed by scanning electron microscopy (Quanta200 FE-SEM, FEI).

3.3.3. Results and Discussion

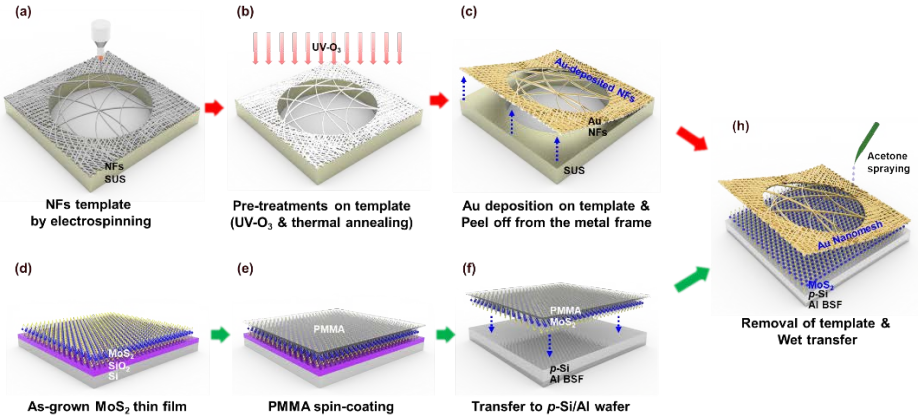

Fig. 3.24. Schematic of device fabrication process for *n*-MoS_2 thin film/*p*-Si heterojunction solar cells.

The fabrication process of *n*-MoS_2/*p*-Si heterojunction solar cells is illustrated in Fig 3.24. The MoS_2 thin films used in this experiment were synthesized by chemical vapor deposition (CVD) method. To prevent the carbon contamination from residual solvent, the two-step thermolysis process was introduced for transforming of $[(NH_4)_2MoS_4]$ to MoS_2 thin film (Fig. 3.24a). By the thermolysis processes, the $[(NH_4)_2MoS_4]$ precursor layers were gradually transformed to MoS_2 thin film according to the following equations;

$$[(NH_4)_2MoS_4] + H_{2(g)} \rightarrow 2NH_{3(g)} + H_{2(g)} + H_2S_{(g)} + MoS_3 \text{ (500 °C)} \quad (1)$$

$$MoS_3 + H_{2(g)} + S_{(g)} \rightarrow MoS_2 + H_2S_{(g)} \quad \text{(900 °C)} \quad (2)$$

To utilize the synthesized MoS_2 thin films, the conventional wet transfer was performed. The poly(methyl metharcrylate) (PMMA) was used as supporting polymer (Fig. 3.24b). The PMMA/MoS_2 layer was transferred onto p-Si/Al back surface field (BSF) substrate by conventional wet transfer method to fabricate the device (Fig. 3.24c). The Au nanomesh electrodes fabricated from

nanofiber templates are utilized as a top electrode. In the first step, the continuous polymeric nanofibers (NFs) are prepared on a circular metal frame collector by electrospinning method. The charged electrospun jet is subjected to the external electric field because a high voltage is applied to the needle. The external field originating from the needle is directed to the metal frame rather than the air gap. Eventually, a lot of electrospun fibers are deposited on metal surfaces while a few fibers are assembled in the circular holes (Fig. 3.24d). In the second step, the fabricated polymeric NF templates are annealed at 150 °C to connect the NF-to-NF junctions. Additionally, ultraviolet-ozone treatment is applied to NF templates before the Au deposition (Fig. 3.24e). Finally, the templates are coated with the Au using electron beam deposition and peeled from the metal frame (Fig 3.24f). Then, the Au coated templates are transferred to MoS_2/p-Si, and spraying acetone to remove polymeric NF templates and laminate the electrodes on the surface of MoS_2/p-Si/Al BSF substrate, simultaneously (Fig. 3.24g). High-density region of Au nanowires is used as a pad to create electrical contacts for measurements, and assembled a few Au nanowires in the center of the fabricated cell are used as transparent nanomesh electrodes.

The bulk form of MoS_2 have an indirect bandgap of 1.3 eV and the direct bandgap of 1.8 eV was revealed as the material approaches a monolayer. It facilitates that the devices fabricated with monolayer of MoS_2 fundamentally different from their bulk from in the point of view of their electrical and optical properties. The thickness of MoS_2 have a significant influence in performance of fabricated devices such as field-effect transistors, photovoltaic cells, and

hydrogen evolution reaction. For these reasons, we have synthesized the MoS_2 thin films by changing the concentration of precursor solutions.

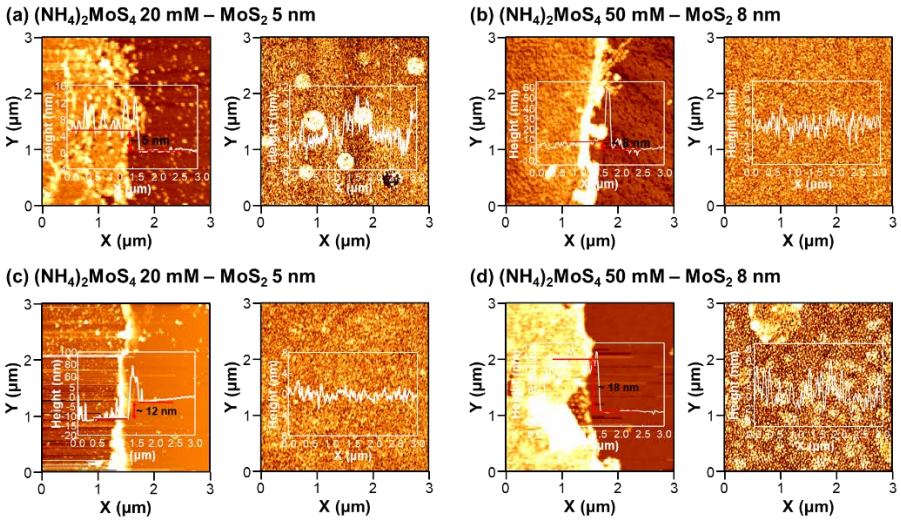

Fig. 3.25. Atomic force microscopy images with edges and morphologies of synthesized MoS_2 thin films with different thicknesses.

The atomic fore microscopy (AFM) was performed to identify the thickness and surface morphology of the synthesized MoS_2 thin films (Fig. 3.25). The thickness of MoS_2 thin films could be tailored to be ranged between 5 nm and 18 nm. The nano-serrated surfaces were observed in the each synthesized MoS_2 thin films, regardless of its thickness. The root-mean-square (RMS) roughness of synthesized MoS_2 thin films is similar to each other.

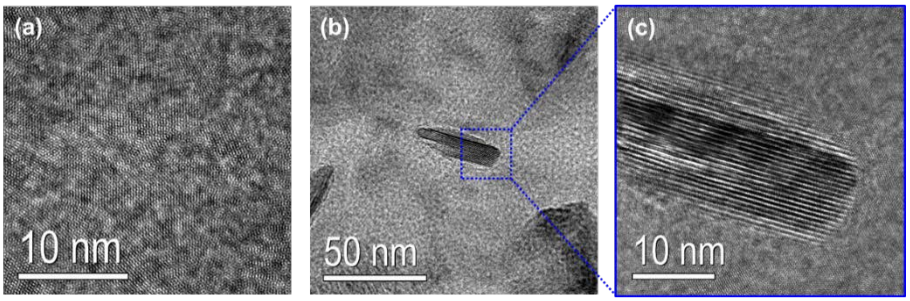

Fig. 3.26. Transmission electron microscopy images of (a) in-plane region and (b) vertically aligned region. (c) The magnified image of (b).

The microstructure of the synthesized 12-nm-thick MoS_2 thin film was studied using transmission electron microscopy (TEM). The high-resolution and the low-magnification TEM images show a pinhole-free 12-nm-thick MoS_2 thin films with some wrinkles on a meshed Cu grid (Fig. 3.26). In recent reports, the charge transport resistance of in-plan orientated 2H-MoS_2 is ~ 200 Ω, which is 4 times higher than the vertically aligned 2H-phase MoS_2 thin films.[21,22] Furthermore, the out-of-plane orientated 2H-MoS_2 have been reported as the better charge transport compared to that of in-plane orientated one.[21] There are two orientations which are grains with the preferred out-of-plane (001) orientation and grains with the preferred in-plane (001) orientation of 2H-MoS_2 phase, as shown in the TEM images (Fig. 3.26). The randomly presence of vertically stacked (001) planes could be helpful in the point view of the charge transport for the MoS_2/*p*-Si heterojunction PV cell.

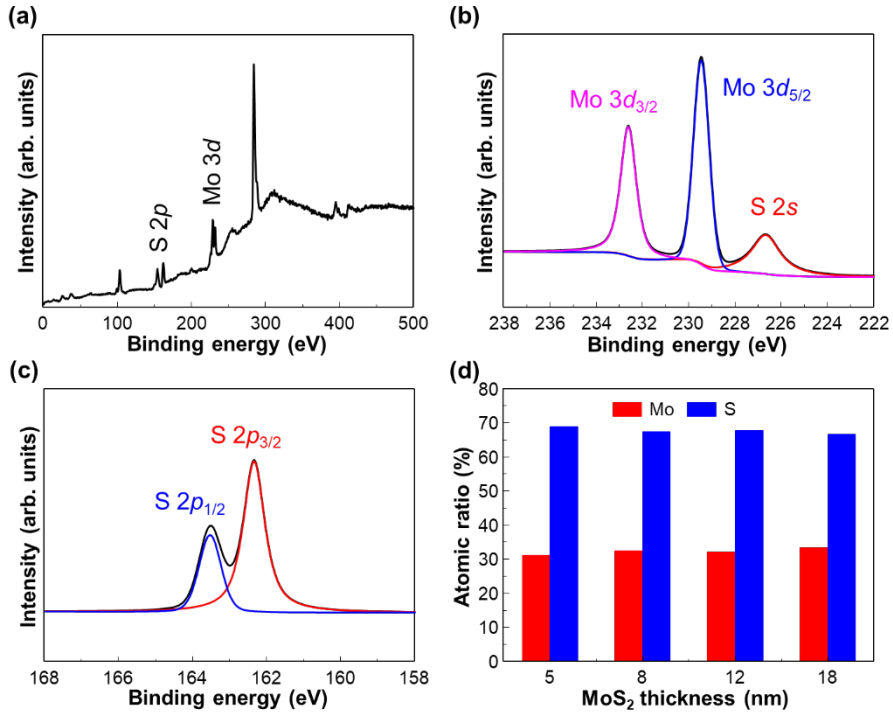

Fig. 3.27. XPS analysis of synthesized MoS_2 thin films. (a) wide scan from 0 to 500 eV. The core level spectra of (b) Mo 3*d* and (c) S 2*p* peak for 12-nm-thick MoS_2 thin film on Si wafer. (d) The Atomic ratio of synthesized MoS_2 thin films with different thicknesses.

To investigate the atomic composition of the synthesized 12-nm-thick MoS_2 thin film, the X-ray photoemission spectroscopy (XPS) was performed (Fig. 3.27). In the core level spectra, the Mo 3*d*, S 2*s*, and, S 2*p* peak was revealed at near 230, 226, and 162 eV, respectively. For synthesized MoS_2 thin films of different thicknesses, the atomic ratio of Mo to S was constant at 62 % to 38 %, consistent with previous reports.[23]

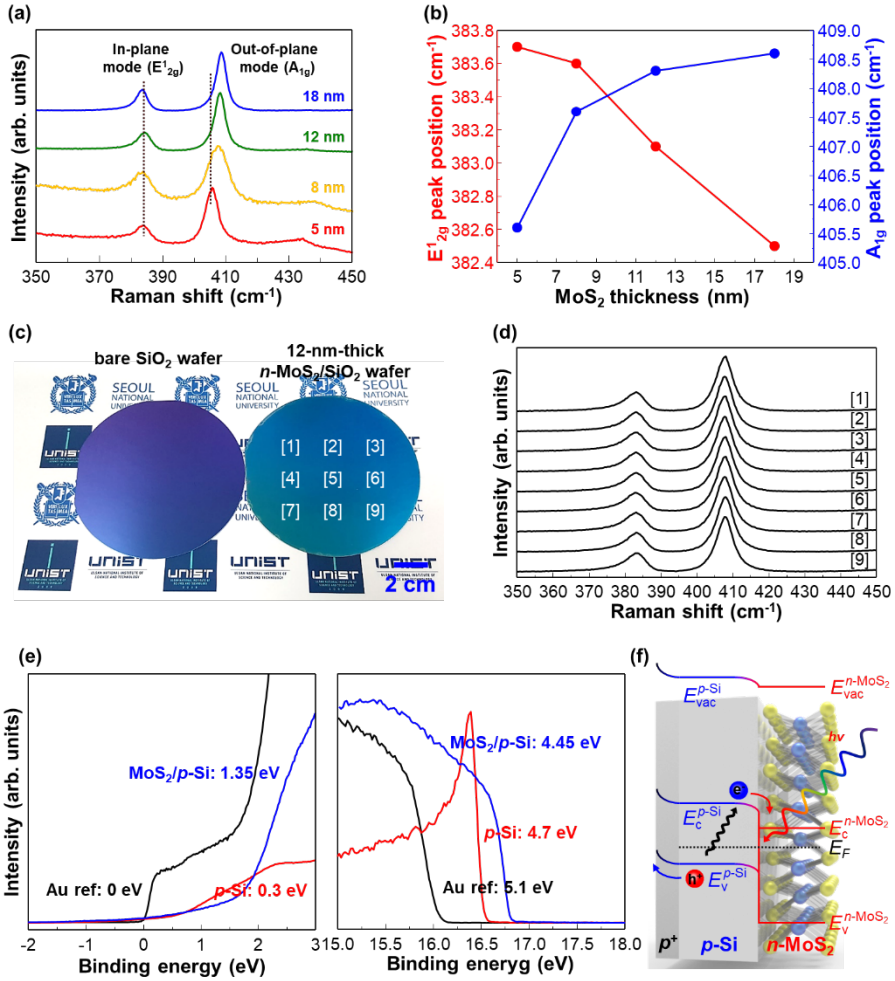

Fig. 3.28. (a) Raman spectroscopy of synthesized MoS_2 with different thicknesses. (b) The peak position of in-plane mode (E^1_{2g}) and out-of-plane mode (A_{1g}). (c) Wafer-scale synthesis of 12-nm-thick MoS_2 thin film on SiO_2 wafer. (d) Raman spectra of wafer-scale MoS_2 with 9 different places. The energy band diagram of fabricated n-MoS_2/p-Si heterojunctions (e) Ultraviolet photoelectron spectroscopy and valence band spectroscopy analysis of 12-nm-thick n-MoS_2/p-Si device. (g) Proposed energy band diagram based on the measurement result in (e).

Raman spectroscopy is widely used for characterizing of synthesized 2D materials such as graphene, MoS_2, and WS_2. In the case of MoS_2 thin film, there are two main peaks in their Raman spectrum which are in-plane mode (E^1_{2g}) and out-of-plane mode (A_{1g}). The Raman spectra of MoS2 thin films with different thicknesses are displayed in Fig. 3.28(a). With increasing of film

thicknesses, the peak gap between E^1_{2g} and A_{1g} vibrational mode becomes wider. This originates from the stiffening of the out-of-plane mode and the relaxation of the in-plane mode, which decreases the peak intensity ratio of the E^1_{2g} mode to A_{1g} mode. To identify the uniformity of the wafer-scale synthesized MoS_2 thin film on the 4-inch SiO_2 wafer, the photographic image of the wafer-scale synthesized MoS_2 thin film and the Raman spectra with 9 different places was investigated as shown in Fig. 3.28(c) and 3.28(d). The color of SiO_2 wafer changed to greenish-blue after the synthesis of MoS_2 thin film by using thermolysis method and the Raman spectra with 9 different places are almost similar to each other. Based on the measurement the XPS and Raman spectra, the uniform, wafer-scale and high-quality MoS_2 thin film could be synthesized by our simple thermolysis method. Even if the high-quality MoS_2 is synthesized, it is important to be capable to identify the charge transport property at heterojunction with *p*-Si. The photo-generated carriers in *p*-Si should be efficiently transported to the MoS_2/electrode interfaces for high-performance MoS_2/*p*-Si heterojunction PV cell. The band-bending in the MoS_2/*p*-Si heterojunction was investigated using ultraviolet photoemission spectroscopy (UPS) and XPS valence spectra. The XPS valence and secondary electron emission (SEE) spectra of bare *p*-Si, 12-nm-thick MoS_2, and reference Au foil are displayed in Fig. 3.28(e). The work functions of the samples can be estimated by extrapolation from the SEE cutoffs as 4.7 eV and 4.45 eV for bare *p*-Si and MoS_2/*p*-Si, respectively. Based on the XPS valence spectra, the energy difference between the Fermi level and the valence band minimum for 0.3 eV and 1.35 eV for bare *p*-Si and MoS_2/*p*-Si, respectively, which means the

downward band bending is formed. Since the escape depth of photoelectrons from the X-ray is under 5 nm and the optical bandgap energy is 1.6 eV observed in UV-visible spectroscopy (Fig. 3.29), the Fermi level of MoS_2 is determined to be 0.2 eV below the conduction band maximum, indicating that the synthesized MoS_2 is *n*-type semiconductor.

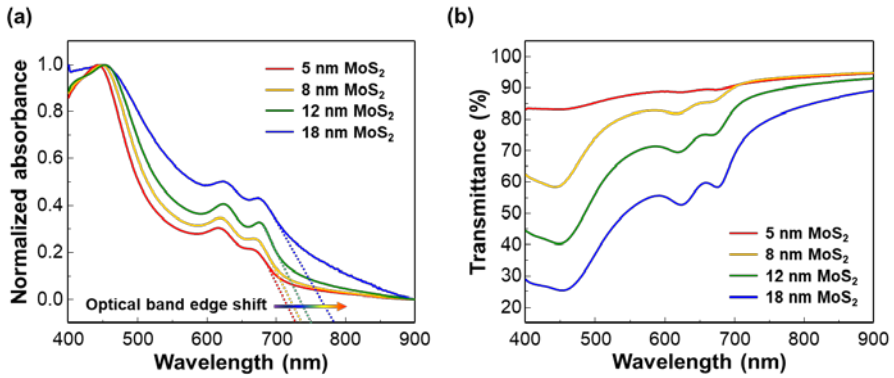

Fig. 3.29. (a) Absorbance spectra and (b) transmittance of the synthesized MoS_2 thin films on glass substrates.

Based on these results, the proposed energy band diagram for the *n*-MoS_2/*p*-Si heterojunction is illustrated in Fig. 3.28(f). The *n*-MoS_2/*p*-Si heterojunction is found to form a type-II junction, resulting in the photo-generated carriers are efficiently transported to the electrode. The band diagram clearly shows that the transport of photo-generated carriers is energetically favorable.

Table 3.4. Sheet resistance of *n*-MoS_2 thin films.

MoS_2 Thickness	Sheet resistance (MΩ/sq.)
5 nm	145.2
8 nm	99.59
12 nm	57.85
18 nm	35.72

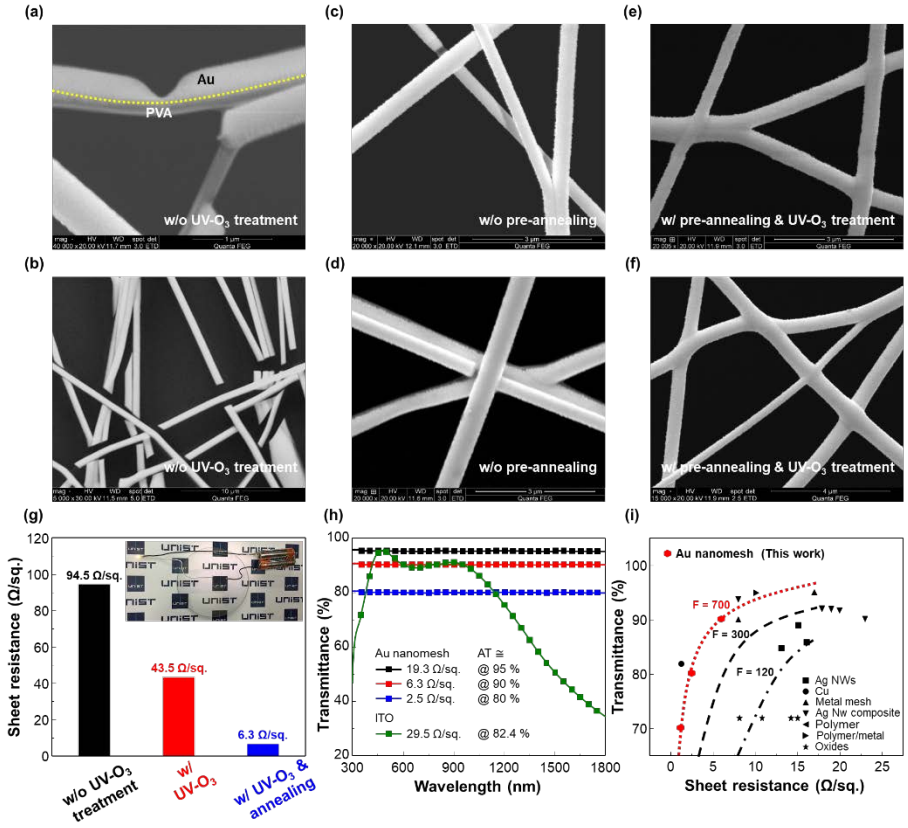

Fig. 3.30. SEM image of Au coated polymeric templates (a) without UV/O_3 treatment, (b) without pre-annealing and (c) with UV/O_3 and pre-annealing treatment. Continuous nanomesh electrodes with UV/O_3 treatment on template. SEM image of Au nanowires after removal of polymeric templates (d) without UV/O_3 treatment, (e) without pre-annealing and (f) with UV/O_3 / pre-annealing treatment (g) The sheet resistance reduction of Au nanomesh with pre-treatments on NFs templets before Au deposition. (h) Optical transmittance as a function of the wavelength from 300 nm to 1800 nm with different density of NFs and ITO. (i) Sheet resistance versus averaged transmission from 400 nm to 800nm for our optimizing Au nanomesh electrodes with previously reported AgNW, Ag composites, CNT, conducting polymers, graphene, PEDOT/PSS@AgNP, and oxide films for comparison.

The high electrical resistance of MoS_2 is main obstacle to achieve high-efficient photovoltaic devices. In a conventional solar cell, the sheet resistance of top semiconducting layer is around 100 Ω/sq and optimal wide spacing (~ mm) of top electrodes is used. The electrical sheet resistances of fabricated MoS_2 thin-films are ranged from 35 MΩ/sq. to 145 MΩ/sq. (Table 3.4), which

is unsuitable for photovoltaic devices and main cause of the high series resistances. Therefore, the Au nanomesh electrodes which can effectively minimize series resistance of the devices and collect the photo generated carriers are utilized as a top electrode. The poly(vinyl alcohol) NF templates are fabricated by electrospinning technique. When the metal is deposited on the templates without any pre-treatment, the Au islands are observed on PVA templates (Fig. 3.30a). Therefore, the broken Au nanowires are observed after the removal of PVA templates by acetone (Fig. 3.30b). The metal films are generally metastable in the as-deposited state and will de-wet to form arrays of islands. This de-wetting effect is due to the low surface energy of substrate. Therefore, the Au is deposited with a large number of grains and coalesced more quickly on polymers with higher surface energy than those on polymers with lower surface energy. The surface energy was estimated from the measured contact angles using the following expression,

$$\gamma_L \cdot (1+\cos\theta) = 2(\gamma^p_s \cdot \gamma^p_L)^{1/2} + 2(\gamma^d_S \cdot \gamma^d_L)^{1/2} \quad (1)$$

where the total surface energy of the film γ_s ($=\gamma_s^p+\gamma_s^d$) is the sum of the polar (γ_s^p) and dispersion components (γ_s^d), and the surface tension of the liquids γ_L ($=\gamma_L^p+\gamma_L^d$) is described as the sum of polar (γ_L^p) and dispersion components (γ_l^d), respectively. These two values can be estimated from contact angles of different test liquids by solving two simultaneous equations. The representative polar solvents H_2O and nonpolar solvents CH_2I_2 are used to measure the contact angles of the pristine and UV-O_3 treated templates. The contact angles of the pristine PVA template and UV-O_3 treated templates are summarized in the following the Fig. 3.31.

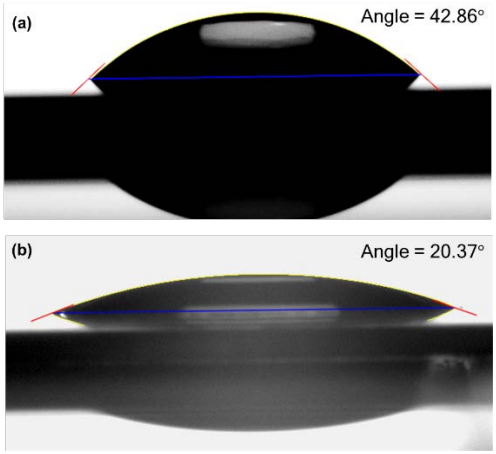

Fig. 3.31. The contact angle of the (a) NFs templets and (b) UV/O_3 treated NFs templets.

As a result, the surface energy of PVA templates without any pre-treatments is 60.8 mN/m^2 while that of the UV-O_3 treated templates exhibits 70.6 mN/m^2, indicating a significantly enhanced the surface energy of templates. The increased surface energy benefits the conformal coating of metal to polymeric templates and reduces the dewetting effect. Accordingly, the Au thin films are uniformly deposited onto PVA templates after the UV-O_3 treatments.

The Au nanomesh electrodes fabricated from UV-O_3 treated templates still exhibit relatively high sheet resistance. The junction between NFs is not perfectly coated due to the shadowing effect originated from poor step coverage of the electron-beam deposition and the gaps between hanged NFs (Fig. 3.30c), resulting in a crack after removal of templates (Fig. 3.30d). Therefore, this shadowing effect is main cause of the junction resistances, leading to high sheet resistance. To minimize the number of wire-to-wire junctions and reduce junction resistances, the PVA templates are annealed at 150 °C for 1 hour. After the annealing process, each polymeric NFs are connected (Fig. 3.32).

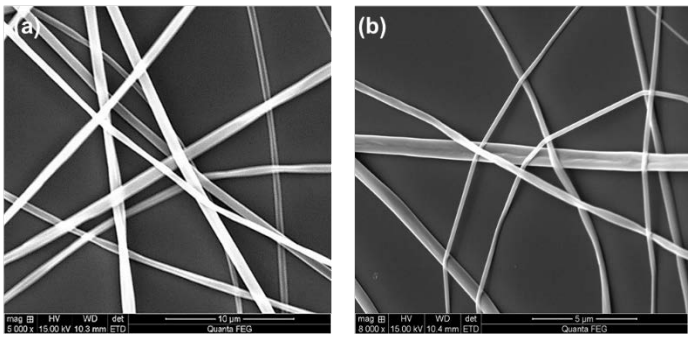

Fig. 3.32. SEM images of the nanofiber templates and nanomesh electrodes. (a) A electrospun nanofibers template. (b) The template after the annealing process.

Subsequently, when the Au is deposited onto both annealed and UV-O_3 treated template, obvious welding at the wire-to-wire junctions is observed (Fig. 3.30e and 3.30f) and the sheet resistance is as low as 7 times that of the nanomesh electrodes without pre-annealing process. Consequently, the sheet resistance of the Au nanomesh electrodes from annealed and UV-O_3 treated templates is 6.3 Ω/sq., while that of the Au nanomesh electrodes from templates without any pre-treatments is 94.5 Ω/sq. (Fig. 3.30g). The Au nanomesh electrodes demonstrated wide band flat transmittance spectra from 300 nm to 1800 nm, which is highly desirable for many optoelectronic devices. On the other hands, conventional transparent electrode, ITO become almost opaque at near-infrared ranges (Fig. 3.30h). As shown in Fig. 3.30i, the Au nanomesh electrode exhibits a much lower sheet resistance and higher optical transparency than the previously reported electrodes, including graphene, polyaniline (PAN), poly(3,4-ethylenedioxythiophene) (PEDOT), conducting oxide. Specifically, our Au nanomesh electrodes have good electro-optical properties, with transmittance ranging from 95% (with 19.3 Ω/sq.) to 70% (with 1.2 Ω/sq.). The figure of merit (F) has been widely used to judge the overall

performance of transparent conductive electrodes. It is related to the transparency (T) and the sheet resistance (R_s) as following equation;

$$T = \left(1 + \frac{188.5}{R_S F}\right) \qquad (2)$$

The figure of merits of the Au nanomesh electrodes is 700, indicating red dotted line in Fig. 3.30i. In comparison with high performance of transparent electrodes that are previously reported, a few electrodes such as polymer/metal, spin-coated silver wire mesh, vacuum filtered Ag NWs, and Ag nano-through have such a high figure of merit.

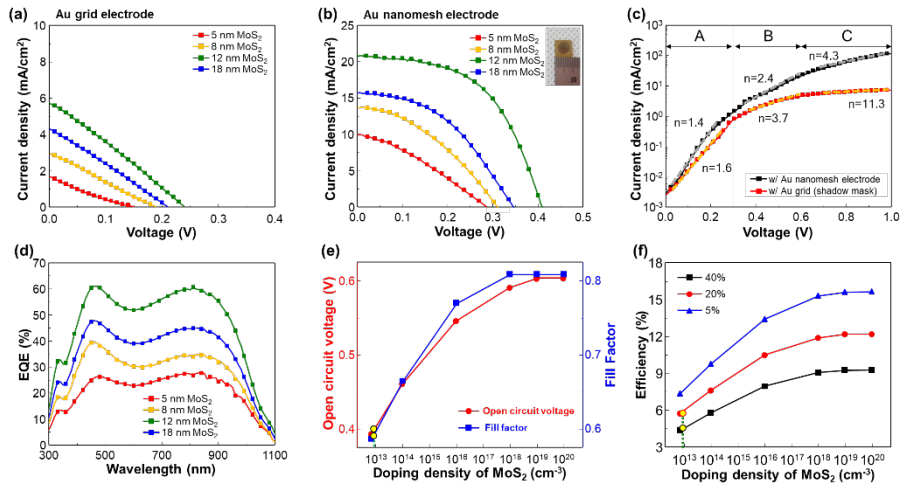

Fig. 3.32. (a) J–V curves for 1-sun-illuminated devices having thicknesses of of 5 nm (red line), 8 nm (yellow line), 12 (blue line) nm and 18 nm (green line) with the Au grid electrodes of a grid width of 50 μm and a grid spacing of 950 μm, and (b) Au nanomesh electrode. (c) Dark J-V characteristics of *n*-MoS_2 thin film/*p*-Si heterojunction solar cell with the Au nanomesh electrode and Au grid electrodes (d) Measured EQE spectra of the *n*-MoS_2 thin film/*p*-Si heterojunction solar cell having thicknesses of 5 nm, 8 nm, 12 nm and 18 nm, respectively, in the wavelength of 300 -1100 nm. (e) Simulated open circuit voltage and fill factor of *n*-MoS_2 thin film/*p*-Si heterojunction solar cell as a function of doping density of MoS_2 (cm^{-3}). (f) The efficiency of *n*-MoS_2 thin film/*p*-Si heterojunction solar cell as a function of doping density of with average reflectance 40% (black, Planar Si), 20% (blue, single ARC coating) MoS_2 and 5% (Textured Si with ARC coating). yellow dots indicate concentration density of fabricated *n*-MoS_2 thin film.

Fig. 3.32a shows the *J–V* curve of *n*-MoS_2/*p*-Si heterojunction photovoltaic cell with 10 % of areal coverage of Au grid electrodes, which are the width of 50 μm and a grid spacing of 950 μm. As expected, the high resistances of MoS_2 lead to very low PCE (summarized in **Table 2**), which originate from the loss of open-circuit voltage (J_{sc}), short-circuit current (V_{oc}), and fill factor (FF).

Table 3.5. *J-V* characteristics of *n*-MoS_2 thin film/*p*-Si heterojunction solar cell with the Au grid electrode.

MoS_2 thickness	**V_{oc} (V)**	**J_{sc} (mA/cm^2)**	**FF (%)**	**Eff. (%)**
5 nm	0.15	1.58	0.20	0.05
8 nm	0.19	2.96	0.25	0.14
12 nm	**0.24**	**5.73**	**0.25**	**0.34**
18 nm	0.21	4.32	0.25	0.22

To realize the high-performance photovoltaic cells using MoS_2 thin films, the study of the relationship between the fractional power losses and electrical sheet resistance in solar cells should be needed. There is a well-established equation to describe the relationship between power loss and electrical resistances as following;

$$p_{loss\%} = \frac{J_{mp}}{12V_{mp}} R_s \cdot S^2 \qquad (3)$$

where J_{MP} and V_{MP} are short-circuit current and open-circuit voltage at maximum power, R_s is sheet resistance of semiconducting layer, and S is the distance between metal grid electrodes, respectively. For example, to have a less than 4 % of power loss in a typical silicon solar cell where R_s = 60 Ω/sq.,

J_{mp} = 30 mA/cm^2, V_{mp} = 450 mV, the finger spacing is less than 3.4 mm. In the same way, to have a less than 4 % of power loss in the *n*-MoS_2/*p*-Si heterojunction solar cell, assuming that the *n*-MoS_2/*p*-Si heterojunction solar cell have J_{mp} = 20 mA/cm^2, V_{mp} = 250 mV, the grid spacing distance is less than 2.4 μm when the sheet resistance of the MoS_2 is about 100 MΩ/sq. This value of spacing is only achievable by Au nanomesh electrodes. As predicted, the *n*-MoS_2/*p*-Si heterojunction solar cells with the Au nanomesh electrodes (T = 90%) show highly improved V_{oc}, J_{sc}, and FF as shown in Fig. 3.32b and Table 3.6.

Table 3.6. J-V characteristics of n-MoS_2 thin film / p-Si heterojunction solar cell with the Au nanomesh electrode.

MoS_2 Thickness	**V_{oc} (V)**	**J_{sc} (mA/cm^2)**	**FF (%)**	**Rs (Ω cm^2)**	**Eff. (%)**
5 nm	0.29	10.15	0.31	22.2	0.91
8 nm	0.31	13.71	0.38	11.6	1.61
12 nm	0.41	20.80	0.55	**6.6**	**4.69**
12 nm + ARC*	0.41	25.54	0.57	-	**5.96**
18 nm	0.34	15.67	0.45	11.2	2.39

*anti reflective coating (ARC).

Particularly, the PCE of the solar cell with 12-nm-thick MoS_2 thin films are dramatically improved from 0.34 to 4.69 %. The series resistances of the device are dramatically reduced due to narrow spacing between Au NWs and the photo-generated carriers are easily transported to the Au nanomesh electrodes, leading to enhancement of V_{oc}, J_{sc} and FF. However, If the spacing of Au NWs is much narrower, the devices with 80 % and 70 % transmittances of Au nanomesh electrodes display the efficiency about 4.14 % and 3.95 %,

respectively (T = 80 % and 2.5 Ω/sq., 70 % and 1.2 Ω/sq.). The 90% transmittance of Au nanomesh electrodes can sufficiently reduce the power loss of *n*-MoS_2/*p*-Si heterojunction solar cells as much as conventional solar cells with a proper distance of grid spacing. Therefore, when the grid spacing is much narrower, the only FF slightly increases while the J_{sc} is decreased due to the reflection of incident light from the electrodes (Fig. 3.33).

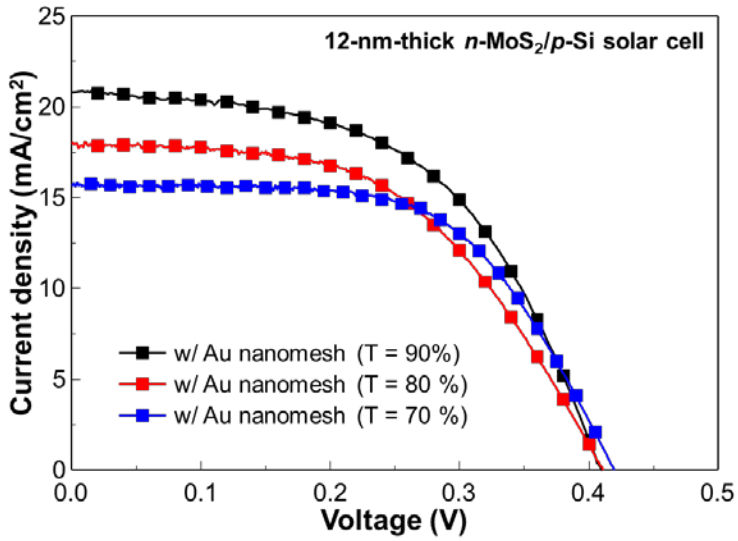

Fig. 3.33. *J-V* curve of *n*-MoS_2/*p*-Si Solar cell with the different density of Au nanomesh.

As shown in Fig. 3.32a and 3.32b, the thickness of *n*-MoS_2 is a critical factor to determine the photovoltaic parameters of *n*-MoS_2/*p*-Si heterojunction solar cells. The 5-nm-thick *n*-MoS_2/*p*-Si heterojunction photovoltaic cell exhibited poor performance with J_{sc} = 10.15 mA/cm^2, V_{oc} = 0.29 V, and FF = 0.31, yielding a PCE of 0.91%. The low J_{sc} and FF originate from the still high series resistances of the device. As the thickness of *n*-MoS_2 gradually increases from 5 nm to 8 nm and 12 nm, the J_{sc} is improved to 13.71 mA/cm^2 at the 8-nm-thick

MoS_2 film and 20.80 mA/cm^2 at the 12-nm-thick MoS_2 film, respectively. Also, the V_{oc} and FF were followed similar trends as summarized in Table 3.6. The relation between open circuit voltage and reverse saturation current density (J_0) give meaningful information to understand the of *n*-MoS_2/*p*-Si heterojunction solar cells.

$$V_{OC} = \frac{nkT}{q} \ln\left(\frac{J_L}{J_0} + 1\right) \quad (4)$$

According to the equation (4) where k is Boltzmann constant, q is electron charge, and T is absolute temperature, reverse saturation current density J_0 is responsible for the increase of V_{oc}. In 5-nm, 8-nm and 12-nm-thick *n*-MoS_2/*p*-Si heterojunction solar cells, the saturation current of the devices decrease until the thickness of MoS_2 reaches at 12 nm. Because the thicker MoS_2 films have been reported that it shows the better mobility than the thinner one, the Shockley-Read-Hall recombinations may be reduced in the thicker film. Furthermore, J_{sc} and FF are improved due to the increased light absorption and intrinsic enhancement of vertical transport in the thicker *n*-MoS_2 film. However, the efficiency of the 18-nm-thick *n*-MoS_2/*p*-Si heterojunction solar cell is decreased to 2.39 %, with J_{sc} = 15.67 mA/cm^2, V_{oc} = 0.34 V, and FF = 0.45. These reduced photovoltaic parameters were attributed to the limited diffusion length of charge carriers and the bulk-like indirect band gap which includes weak light-matter interaction, leading to recombination of the photo generated carriers. Accordingly, the reverse saturation current density is increased in the 18-nm-thick *n*-MoS_2/*p*-Si solar cell and overall photovoltaic parameters are decreased (Fig. 3.33). The absorption coefficient of the MoS_2 is higher than Si or GaAs by one order of magnitude. Therefore, the nanometer-thick MoS_2 films

can absorb the light and contribute to generate photo exited carriers if the excellent absorption property of MoS_2 is fully utilized. Fig. 3.32c shows external quantum efficiency (EQE) spectra of the 5-nm, 8-nm, 12-nm and 18-nm-thick *n*-MoS_2/*p*-Si heterojunction solar cells in the wavelength range from 300 nm to 1100 nm. Interestingly, the EQE spectra below 750 nm is well matched with the absorbance spectra of the MoS_2 layers, indicating that the significant enhancement can be attributed to the MoS_2 thin film. Likewise, in the monolayer or few layers MoS_2 based phototransistors and photodiodes, the photocurrents are maximized around ~ 450 nm. Moreover, the EQE spectra of the bilayer PTB7-MoS_2 heterojunction solar cell, where EQE spectra is similar to the absorbance spectra and maximized at 450 nm, corresponds with our EQE spectra. However, previously reported EQE spectrum of monolayer n-MoS_2/p-Si heterojunction solar cells is similar with transmittances of ultrathin metal films because all area covered metal electrodes are used to compensate poor sheet resistances of MoS_2. On the other hands, a genuine EQE spectra of few-layer *n*-MoS_2/*p*-Si heterojunction solar cells are hard to be obtained without the transparent electrodes that have wide band flat transmittance spectra from 300 nm to 1100 nm.

To reduce the reflection of photons in the devices, the SiN_x 70 nm is coated on the top of the solar cells as the anti-reflection coating. The efficiency of the fabricated ARC/12-nm-thick *n*-MoS_2/*p*-Si heterojunction solar cell is improved to 5.96%, with J_{sc} = 25.54 mA/cm^2, V_{oc} = 0.41 V, and FF = 0.57. For comparing our results to previously reported *n*-MoS_2/*p*-Si based solar cell, the performances of reported solar cells are summarized in Table 3.7.

Table 3.7. Comparison of factors of photovoltaic cells this work and previously reported ones.

Schemes	V_{oc} (V)	J_{sc} (mA/cm^2)	FF (%)	Eff. (%)	Note	Reference
Au/MoS_2	0.59	5.37	48	1.8%	Schottky junction	Nanoscale, **2012**,4, 7399
p-MoS_2/n-MoS_2	0.28	20.9	47	2.8%		ACS nano, **2014**, 8, 5270
Al/MoS_2/p-Si	0.41	22.36	57.26	5.23%	Efficiency of Al/p-Si Solar cell = 4.64%	ACS nano, **2014**, 8, 8317
MoS_2/p-Si	0.14	3.2	42.4	1.3%		Journal of Applied Physics, **2015**, 117, 114502
Pd:MoS_2/p-Si	0.45	15.1	35.3	2.4%		RSC Advance, **2016**, 6, 1346
n-MoS_2/i-SiO_2/p-Si	-	-	-	4.5%	Under 0.2 Sun illumination	Nanoscale **2015**,7, 8304
MoS_2/p-Si	0.39	18	63	4.48%		Solar Energy Materials&SolarCells 144 (2016) 117–127
This work	0.41	20.80	0.55	4.69%		
This work	0.41	25.54	0.57	5.96%	With ARC	

In the previous reports, the most of the top MoS_2 layer is covered by opaque electrodes such as Al, Pd and Cr due to its high sheet resistances. Therefore, active area is quite small (μm^2 scale) or the sun lights are not fully utilized. Although the Al/ monolayer *n*-MoS_2/*p*-Si solar cell with large area (1 cm^2) showed the PCE of 5.23%, the whole area covered aluminum forms a schottky junction with *p*-Si, showing the PCE of 4.64% with J_{sc} = 21.66 mA/cm^2, V_{oc} = 0.38 V, and FF = 0.56. Therefore, the actual contribution of monolayer *n*-MoS_2 to solar cell is very small. In this study, the fabricated *n*-MoS_2/*p*-Si heterojunction solar cell with Au nanomesh electrodes exhibited the highest PCE under the standard AM 1.5 G illumination with the largest active area (0.44 cm^2).

The *n*-MoS_2/*p*-Si heterojunction solar cells have potential to be improved by additional doping on *n*-MoS_2. The electron concentration of our 12-nm-thick MoS_2 thin film is about 1.8 $\times 10^{16}$ cm^{-3}, which is quite reliable value compared with the value of previously reported 10-nm-thick MoS_2 thin film. The fermi

level of the MoS_2 is close to the conduction band minimum after doping process, and as the concentration of electrons in MoS_2 is increased by doping process, the band-bending in the *n*-MoS_2/*p*-Si heterojunction becomes larger and the built-in potential is increased compared to that of undoped MoS_2 and Si (Fig 3.32d). Additionally, the electron doping could lower the sheet resistance of MoS_2, leading to enhance the FF. Therefore, the doping process provide a promising way to obtain the high-performance *n*-MoS_2/*p*-Si heterojunction solar cells. To elucidate the experimental results and predict the photovoltaic parameters of doped MoS_2/p-Si solar cell, we performed a two dimensional model simulation (TCAD, Silvaco). When the electron concentration of MoS_2 thin film is increased to 1×10^{17} cm^{-3}, the V_{oc} and FF are increased to 0.46 V and 0.66, respectively. The V_{oc} and FF could be enhanced to 0.59 V and 0.81 as the electron concentration of MoS_2 thin film is drastically increased to 1×10^{18} cm^{-3} by chemical or electrical doping. (Fig. 3.32e). Planar silicon has a high surface reflection of over 40 %. Therefore, reducing the reflection is the key to obtain high performance solar cell. The reflection is reduced by texturing and by applying anti-reflection coatings. A coating of dielectric thin layer with a specially chosen thickness can encourage the interference effects, leading to reduce the reflectance. However, the interference effect caused by a single ARC layer is not sufficient to make the low reflectance (~ 5 %). Therefore, with SiN_x coating, averaged reflectance is decreased to 16.36 %, which is the relatively low reflectance achievable in the current device structure (planar Si/MoS_2). Based on the simulated and the experimental results about reflectance of planar Si, textured Si with ARC (Fig. 3.34).

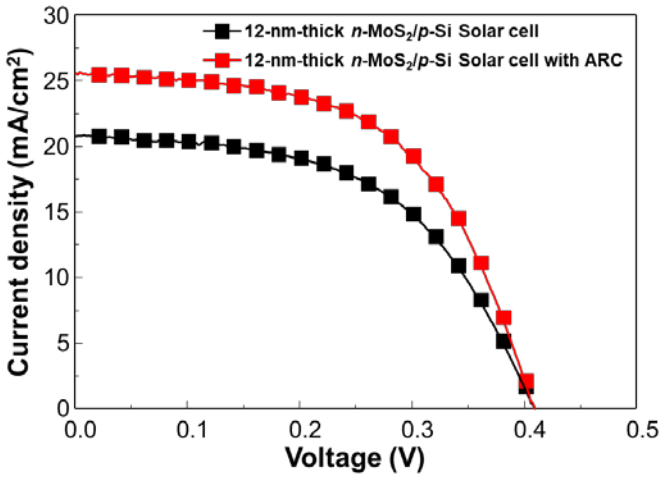

Fig. 3.34. *J-V* curve of *n*-MoS_2/*p*-Si Solar cell with the antireflection coating (SiNx = 70nm).

The efficiency could be improved from 4.5 to 7.5 % when the reflectance is decreased from 40 to 5 %. Under the optimum electron concentration and reflectance, the efficiency of solar cell could be increased to 15 % (Fig. 3.32f). Therefore, further researches that n-MoS_2 thin film is transferred or directly grown to the textured Si are needed to reduce the reflectance below 5%. Then, the J_{sc} of *n*-MoS_2/*p*-Si heterojunction solar cells could be dramatically increased as the reflectance decreases. Finally, through proper doping of MoS_2 and ARC coating on the device, an efficiency of over 15% *n*-MoS_2/*p*-Si heterojunction solar cell can be obtained.

3.3.4. Conclusion

High-quality two-dimensional transition metal dichalcogenides (TMD) are very promising for photovoltaic devices due to their superior light absorption capability and controllable band gap. However, TMD based solar cells are suffering from low photo conversion efficiency with the extremely small active area (μm^2 scale) because TMDs have high sheet resistance which is not appropriate for solar cells and large area growth of the TMD materials is still challenging. Therefore, a breakthrough is needed to obtain the high-performance TMD based solar cells with a large area. Herein, we synthesize wafer-scale molybdenum disulfide thin-films by thermolysis of solution precursor based method. After that, the thin films are transferred to p-Si and formed a heterojunction with p-Si. In order to maximize and fully utilize the excellent property of the n-MoS_2, a transparent Au nanomesh electrode (Sheet resistance ≈ 6 Ω/sq at 90% transmittance) fabricated from UV-O_3 treated polymeric nanofiber templates is integrated to *n*-MoS_2/*p*-Si heterojunction**.** The *n*-MoS_2/*p*-Si heterojunction with Au nanomesh electrodes exhibit a power conversion efficiency of 4.69%. After antireflection coating, the device shows the efficiency of 5.96% at 0.44 cm^2 of the active area. Finally, we suggest and demonstrate the way to obtain over 15% efficiency of *n*-MoS_2/*p*-Si heterojunction based on the light trapping and doping of n-MoS_2 by elucidating finite-difference time-domain (FDTD) simulations.

3.3.5. References

[1] Q. H. Wang, K. Kalantar-Zadeh, A. Kis, J. N. Coleman, S. M. Strano, *Nat. Nanotechnol.* **2012**, *7*, 699.

[2] M. Chhowalla, H. S. Shin, G. Eda, L.-J. Li, K. P, Loh, H. Zhang, *Nat. Chem.* **2013**, *5*, 263.

[3] Y.-H. Chang, C.-T. Lin, T.-Y. Chen, C.-L. Hsu, Y.-H. Lee, W. Zhang, K.-H. Wei, L.-J. Li, *Adv. Mater.* **2013**, *25*, 756.

[4] R. Bhandavt, L. David, G. Singh, *J. Phys. Chem. Lett.* **2012**, *3*, 1523.

[5] S. Kim, A. Konar, W.-S. Hwang, J. H. Lee, J. Lee. J. Yang, C. Jung, H. Kim, J.-B. Yoo, J.-Y. Choi, *Nat. Comm.* **2012**, *3*, 1011.

[6] X. Zhao, Z. Li, T. Zhu, B. Mi, Z. Gao, W. Huang, *J. Phys. D: Appl. Phys.*, **2013**, *46*, 195105.

[7] S. D. Stranks, G. E. Eperon, G. Grancini, C. Menelaou, M.J.P. Alcocer, T. Leijtens, L. M. Herz, A. petrozza, H. J. Snaith, *Science*, **2013**, *342*, 341.

[8] G. Xing, N. Mathews, S. Sun, S. S. Lim, Y. M. Lam, M. Gratzel, S. Mhaisalkar, T.C. Sum, *Science*, **2013**, *342*, 344.

[9] Seayad, A. M; and Antonelli, D. M. *Adv. Mater.* **2004**, *16*, 765.

[10] Lee. Y.-H.; Zhang, X.-Q.; Zhang, W.; Chang, M.-T.; Lin, C.-T.; Chang, K.-D.; Yu, Y.-C.; Wang, J. T.-W.; Chang, C.-S.; Li, L.-J., *Adv. Mater.* **2012**, *24*, 2320.

[11] Zeng, Z.; Yin, Z.; Huang, X.; Li, H.; He, Q.; Lu, G.; Boey, F.; Zhang, H. *Angew. Chem. Int. Ed.* **2011**, *50*, 11093.

[12] Coleman, J. N.; Lotya, M.; O'neill, A.; Bergin, S. D.; King. P. J.; Khan, U.; Young, K.; Gaucher, A.; De, S.; Smith, R. J., *Science*, **2011**, *331*, 568.

[13] Najmaei, S.; Liu, Z.; Zhou, W.; Zou, X.; Shi, G.; Lei, S.; Yakobson, B. I.; Idrobo, J.-C.; Ajayan, P. M.; Lou, J. *Nat. Mater.* **2013**, *12*, 754.

[14] Liu, K.-K.; Zhang, W.; Lee, Y.-H.; Lin, Y.-C.; Chang, M.-T.; Su, C.-Y.; Chang, C.-S.; Li, H.; Shi, Y.; Zhang, H., *Nano Lett.* **2012**, *12*, 1538-1544.

[15] R. Cheng, D. Li, H. Zhou, C. Wang, A. Yin, S. Jiang, Y. Liu, Y. Chen, Y. Huang, X. Duan, *Nano Lett.*, **2014**, *14*, 5590.

[16] M. M. Furchi, A. Pospischil, F. Libisch, J. Burgdorfer, T. Mueller, *Nano Lett.*, **2014**, *14*, 4785.

[17] L. Z. Hao, W. Gao, Y. J. Liu, Z. D. Han, Q. Z. Xue, W. Y. Guo, J. Zhu, Y. R. Li, *Nanoscale*, **2015**, *7*, 8304.

[18] J. Wong, D. Jariwala, G. Tagliabue, K. Tat, A. R. Davoyan, M. C. Sherrott, H. A. Atwater, *ACS Nano*, **2017**, *11*, 7230.

[19] Y. Son, Q. H. Wang, J. A. Paulson, C.-J. Shih, A. G. Rajan, K. Tvrdy, S. Kim, B. Alfeeli, R. D. Braatz, M. S. Strano, *ACS Nano*, **2015**, *9*, 2843.

[20] R. Ganatra, Q. Zhang, *ACS Nano*, **2014**, *8*, 4074.

[21] S. Wi, H. Kim, M. Chen, H. Nam, L. J. Guo, E. Meyhofer, X. Liang, *ACS Nano*, **2014**, *8*, 5270.

[22] Z. Yin, H. Li, H. Li, L. Jiang, Y. Shi, Y. Sun, G. Lu, Q. Zhang, X. Chen, H. Zhang, *ACS Nano*, **2012**, *6*, 74.

[23] S. Lin, X. Li, P. Wang, Z. Xu, S. Zhang, H. Zhong, Z. Wu, W. Xu, H. Chen, *Sci. Rep.*, **2015**, *5*, 15103.

Application to Water Splitting Catalysts

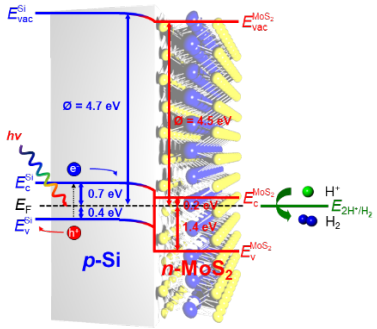

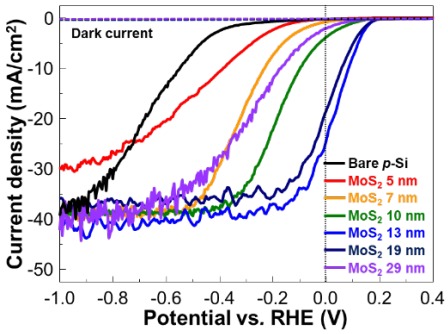

Energy Environ. Sci. 2016, 9, 2240

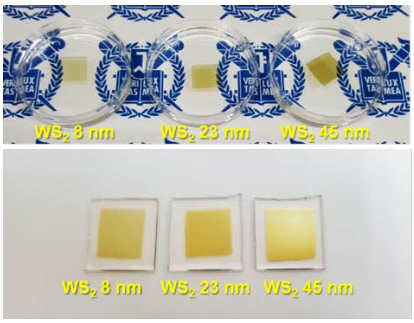

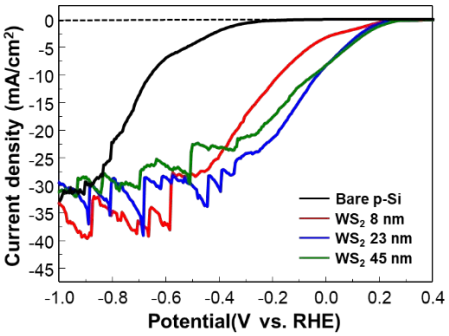

MRS Communications 2017, 7, 272

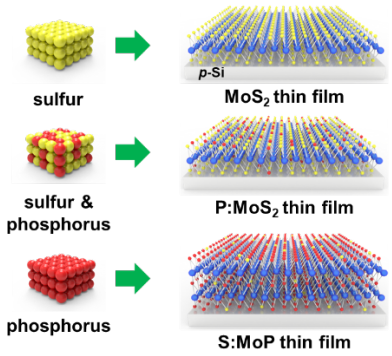

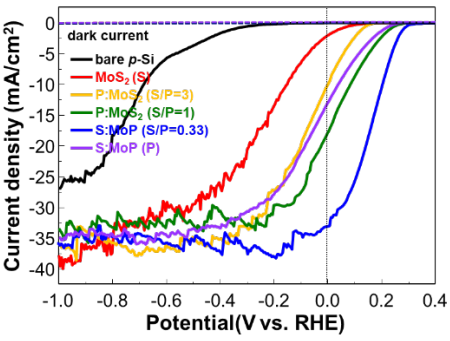

J. Mater. Chem. A 2017, 5, 15534

4.1. Partially vertical-aligned molybdenum disulfides

4.1.1. Introduction

Photoelectrochemical (PEC) water splitting is a promising approach for the efficient and sustainable production of hydrogen as a fuel. In the pursuit of developing efficient and durable photoelectrodes, Si and III-V semiconductors have been extensively studied. These materials absorb wide ranges of the solar spectrum, including near-infrared (NIR) light, and the electrochemical potential for the hydrogen evolution reaction (HER) is within the band edges of the semiconductors.[1-3] *p*-type Si is considered as one of the most promising candidates for photocathode for HER because of its narrow band gap, earth abundance, and well-established production technology with relatively low costs. It also has the appropriate band energies to transport the photogenerated electrons to the hydrogen reduction potential (H^+/H_2). However, the surface of *p*-type Si has poor kinetics for absorbing the hydrogen ions (H^+). To achieve the higher solar-to-hydrogen efficiency, it requires the catalyst which can help the chemisorption or electrosorption of H^+.[4-6] In addition to this overpotential, Si is thermodynamically vulnerable to photoactive dissolution, or photocorrosion.[7] To reduce the overpotential, noble metals such as Pt, Rh, and Ir are widely used as HER catalysts in the form of nanoparticles. Unfortunately, these catalysts are relatively expensive and earth-deficient. Furthermore, the metal nanoparticles cannot prevent photocorrosion in *p*-type Si photocathodes. Although thick layers of noble metals can passivate the photocathodes, those drastically reduce

light transmission through the metal layers, which lowers the photocurrent in the photocathodes, and the pinch-off phenomena of catalysts by which the desired catalytic reactions can be promoted cannot be exploited.[8] Therefore, a novel approach to simultaneously solve the overpotential and stability issues should be developed.

Two-dimensional transition-metal disulfides (2D TMDs) have attracted much attention as promising candidates to replace Pt, because TMD nanoparticles such as MoS_2 and WS_2 have inherently large surface-to-volume ratios and possess high densities of catalytically active edge sites for HER.[9,10] When TMDs are deposited on *p*-type semiconductors, such as *p*-type Si, the induced electrical fields between the TMDs and the *p*-type semiconductors would be very high because of the large difference in work function, which may increase the efficiency of transport of photogenerated electrons from the *p*-type semiconductors via the TMDs to the electrolyte/solid interfaces.

2D TMDs are usually obtained by exfoliation, solution-based synthesis, and chemical vapour deposition (CVD). Exfoliated and solution-processed TMDs nanoparticles have been reported to have many electrochemically active sites. However, as in noble metal particles, fabricating uniform, dense, and thin layers based on 2D TMD nanoparticles on the surface of *p*-type semiconductors is difficult.[11-14] Using CVD, uniform and ultrathin 2D TMD layers can be synthesized using powder precursors, such as MoO_3 and $MoCl_5$, on oxide substrates.[15-17] The surface of CVD-grown TMD layers contains

electrochemically inactive basal planes.[18,19] The direct synthesis of ultrathin 2D TMD layers on *p*-type semiconductors is hindered by the lack of strong adhesion between the *p*-type semiconductors and 2D TMDs. From these reasons, a novel method that overcomes the limitations of nanoparticle-based coating and direct deposition is necessary to fabricate 2D TMD/*p*-type semiconductor heterojunctions.

Here, we demonstrate the wafer-scale fabrication of MoS_2/*p*-Si heterojunctions using a thin-film transfer method for high-performance PEC hydrogen production. Thickness-controlled MoS_2 layers were synthesized by the thermolysis of a solution precursor layer on SiO_2/Si substrates; these layers were transferred to *p*-Si wafers. The synthesized 2H-MoS_2 layers contain a-domains with layer-by-layer stacked (001) planes and c-domains with vertically stacked (100) planes. Since the electrochemically active c-domains act as HER catalytic sites and the *n*-MoS_2/*p*-Si heterojunction efficiently transports photogenerated electrons to the solid/electrolyte interface, the onset potential at a photocurrent of 1 mA/cm^2 is reduced by 0.445 V, which is one of the highest overpotential reduction values yet reported for HER catalysts without noble metals. The transferable MoS_2 thin-film catalyst reduces the overpotential of cathodes comprising *p*-InP, *p*-GaAs, and *p*-GaP as well as *p*-Si.

4.1.2. Experimental procedures

MoS_2 thin film synthesis. SiO_2 (300 nm)/Si wafers were cleaned with a standard piranha solution (3:1 mixture of H_2SO_4 and H_2O_2) and conventional cleaning procedures, followed by ultrasonication in acetone, isopropyl alcohol, and deionized (DI) water. To obtain hydrophilic surfaces on the SiO_2/Si wafers, O_2 plasma and UV-O_3 surface treatment were performed for 15 min. The precursor solution was prepared by dissolving $(NH_4)_2MoS_4$ powder (Sigma-Aldrich, 99.97% purity) in ethylene glycol (Sigma-Aldrich, 99.8% purity, anhydrous) at concentrations of 10, 20, 50, 100, 200, and 500 mM. The precursor solution was spin-coated onto the prepared SiO_2/Si substrate at 3500 rpm for 60 s. High-purity H_2 and N_2 gases were used for the thermolysis process in a thermal CVD system. First, the CVD chamber temperature was increased to 500 °C and maintained at this temperature for 30 min under flowing H_2 and N_2 at 1 Torr. The flow rate of H_2 and N_2 was set to 40 and 200 cm^3/min, respectively, by mass flow controllers. Under a H_2 gas atmosphere at relatively high temperature, the thermolysis process was gradually started. Then, the temperature of the CVD furnace was increased to 950 °C, and maintained for 1 h. Sulfur sublimation was initiated with sulfur powder (Sigma-Aldrich, 99.5% purity) placed in the heating zone, which was set to 300 °C. When the thermolysis process was finished, PMMA was spin-coated onto the CVD-grown MoS_2 thin films. The edges of the synthesized MoS_2 thin films were scratched by a razor blade to promote rapid separation of MoS_2 from the SiO_2/Si substrate. The PMMA/MoS_2/SiO_2/Si substrate was immersed in a buffered oxide etch (BOE, Sigma-Aldrich, NH_4F 40%) to separate the MoS_2 thin film

from the substrate by etching away the SiO_2 layers. The obtained MoS_2 thin films were washed with DI water seven to nine times to remove residual etchant and transferred to an arbitrary substrate of *p*-Si, *p*-InP, *p*-GaAs, or *p*-GaP. After the PMMA/MoS_2 membranes had adhered to the substrates, the PMMA layers were removed using acetone and toluene at 50 °C for 30 min.

PEC measurements. HER measurements (Ivium Technologies, Model: Nstat) were performed with a three-electrode system using a saturated calomel electrode as the reference electrode and a Pt plate as the counter electrode in a 0.5 M H_2SO_4 standard electrolyte solution. The three-electrode system was set up inside a quartz vessel, which protected the samples from UV absorption. A Xe arc lamp was used and calibrated to an output of 100 mW/cm^2 (AM 1.5 G condition). Because the Pt counter electrode was not stable for long-term (several hours) operation in the strong acid electrolytes such as 0.1M H_2SO_4 (pH = 1.5) and 0.5M H_2SO_4 (pH = 1.1), the Pt deposition has been found on the working electrode during chronoamperometry measurements.[1] Thus chronoamperometry measurements were performed for Pt decorated *p*-Si and Pt decorated MoS_2/*p*-Si photocathodes. The Pt decoration was conducted by using electrodeposition method in the H_2PtCl_6 (Sigma-Aldrich, 8 wt% in water) electrolyte. We also measured the chronoamperometry curves of bare *p*-Si and MoS_2/*p*-Si photocathodes using a fritted Pt counter electrode (WonATech Co., Ltd) to eliminate Pt deposition on the working electrode. A scan rate of 10 mV/s was used for the linear sweep. The ICPE was measured with a light source and monochromator. The quantum efficiency was measured with a standard Si photodiode. EIS was conducted by applying a constant potential of -0.7 V

compared to the open-circuit potential. The sweeping frequency was from 250 kHz to 1 Hz with a 10 mV AC dither. The Faradaic efficiency was conducted by using a gas chromatography measurement system (FID-GC, PerkinElmer, NARL8502 Model 4003).

Characterization. The Raman spectra of the synthesized MoS_2 thin films were obtained with a Lab RAM HR (Horiba JobinYvon, Japan) at an excitation wavelength of 532 nm. Non-contact-mode AFM (XE-100, Park Systems) measurements at a scanning rate of 0.5 Hz were performed to identify the surface morphologies and thicknesses of the synthesized MoS_2 thin films. Synchrotron radiation photoelectron spectroscopy experiments were performed in an ultra-high vacuum chamber (base pressure of ca. 10^{-10} Torr) with a 4D beam line, equipped with an electron analyzer and heating element, at the Pohang Acceleration Laboratory. The onset of photoemission, corresponding to the vacuum level at the surface of the MoS_2 thin film, was measured using an incident photon energy of 350 eV with a negative bias on the sample. The results were corrected for charging effects using Au 4*f* as an internal reference. Bright-field and high-resolution TEM (JEOL JEM-2100F) with 200 kV field-emission images were obtained to investigate the microstructures of the synthesized MoS_2 thin films. The transmittance and absorption spectra of the synthesized MoS_2 thin films were measured by UV-Visible spectroscopy (JASCO-670).

4.1.3. Results and Discussion

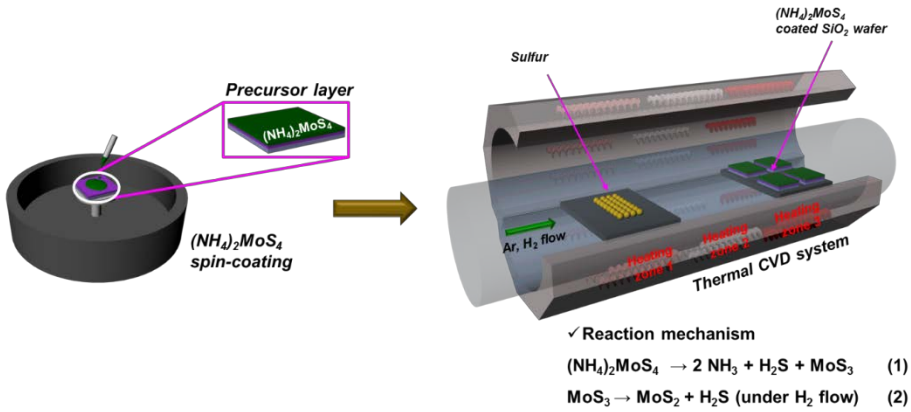

Fig. 4.1. Schematics for the spin-coating and thermolysis of [$(NH_4)_2MoS_4$] precursor solution.

The MoS_2 thin films used in this study were synthesized using a thermolysis system as shown in Fig. 4.1. An ammonium tetramolybdate [$(NH_4)_2MoS_4$] precursor dissolved in ethylene glycol was spin-coated onto a SiO_2/Si substrate. Thermolysis at 500 °C under N_2 and H_2 flow converted the precursor to a MoS_3 layer. Subsequent heating to 900 °C in the reducing ambient atmosphere transformed the MoS_3 layer to a thin film of MoS_2.[20,21] Poly[methyl methacrylate] (PMMA) as a supporting polymer was spin-coated onto the synthesized MoS_2 thin films. The PMMA/MoS_2 thin films were separated from the SiO_2/Si substrates by immersion in a bath of HF and a buffered oxide etchant, and the separated films were transferred onto *p*-Si wafers. The PMMA supporting layer was removed with acetone, creating MoS_2/*p*-Si heterostructures. Backside contacts and epoxy passivation were established to allow PEC measurements. This experimental procedure is illustrated in Fig. 4.2(a).

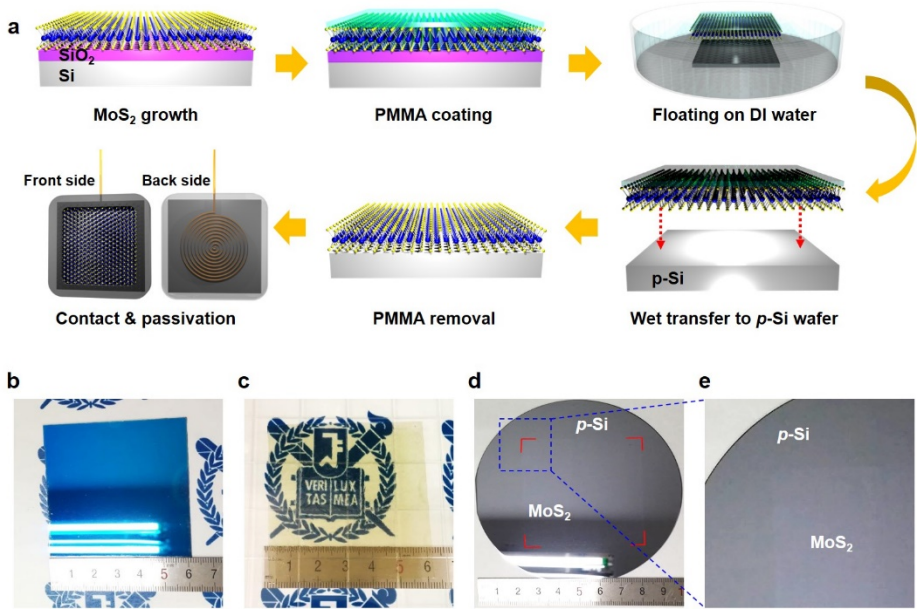

Fig. 4.2. Schematic of experimental procedure and photographic images of large-area synthesis of MoS_2 thin film. (a) Schematic of experimental procedures for fabrication of MoS_2/*p*-Si photocathode. Photographic images of (b) 100 mM $[(NH_4)_2MoS_4]$ spin-coated SiO_2 substrate, (c) synthesized MoS_2 floating in DI water bath, (d) transferred to 4-inch *p*-Si wafer, (e) magnified image from Fig. 4.2(d).

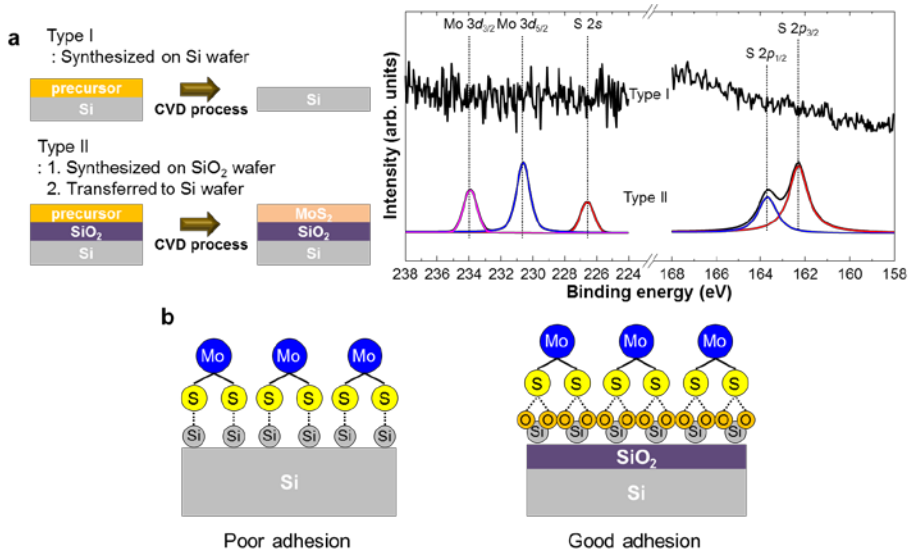

Fig. 4.3. (a) XPS analysis of synthesized MoS_2 thin films on Si and SiO_2 (300 nm)/Si substrates. (b) Schematic of differences in dangling bonds between Si and SiO_2 (300 nm)/Si substrates.

Fig. 4.2(b) shows a photographic image of a 6 cm × 6 cm MoS_2 thin film on a SiO_2/Si substrate. MoS_2 thin films could be grown on oxide substrates, such as SiO_2 and Al_2O_3, using the thermolysis method. The direct growth of MoS_2 thin films on *p*-Si wafers were difficult to achieve because of the poor adhesion between Si and MoS_2, as shown in Fig. 4.3. Since the binding energy of S-O bonds exceeds that of S-Si bonds, MoS_2 could only be grown on oxides, not directly on Si.[22] Photographic images of a PMMA/MoS_2 membrane floating on deionized water and a 6 cm × 6 cm MoS_2 thin film on a 4-inch *p*-Si wafer are displayed in Fig. 4.2(c) and 4.2(d), respectively.

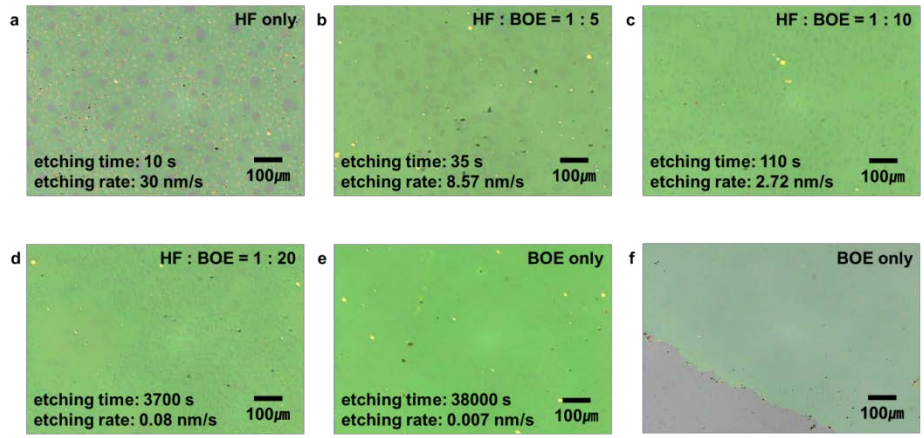

Fig. 4.4. Optical microscopy images of transferred MoS_2 thin films on SiO_2 (300 nm)/Si wafers using different etchant solutions. Pinhole-free MoS_2 thin films are obtained using BOE-only etchant.

To separate the MoS_2 thin films from SiO_2/Si substrates without introducing pinholes, controlling the etch rate of the SiO_2 layer was important (Fig. 4.4). Notably, the areas of the MoS_2 thin films are limited by the chamber size of the thermolysis system.

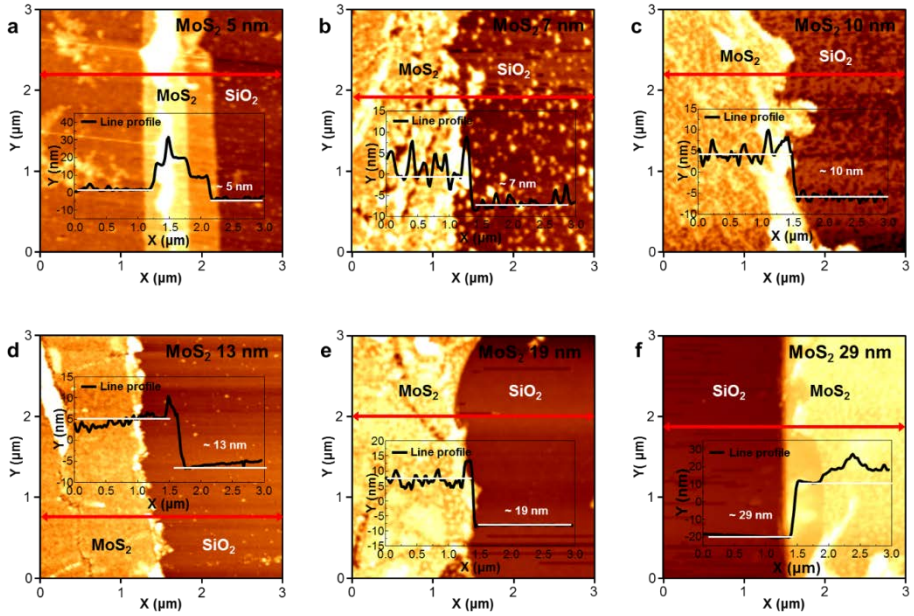

Fig. 4.5. AFM images of synthesized MoS_2 thin films with precursor solutions of different concentrations. Thicker MoS_2 thin films are obtained with higher-concentration precursor solutions. The thicknesses of the MoS_2 thin films are increased with increasing precursor concentrations.

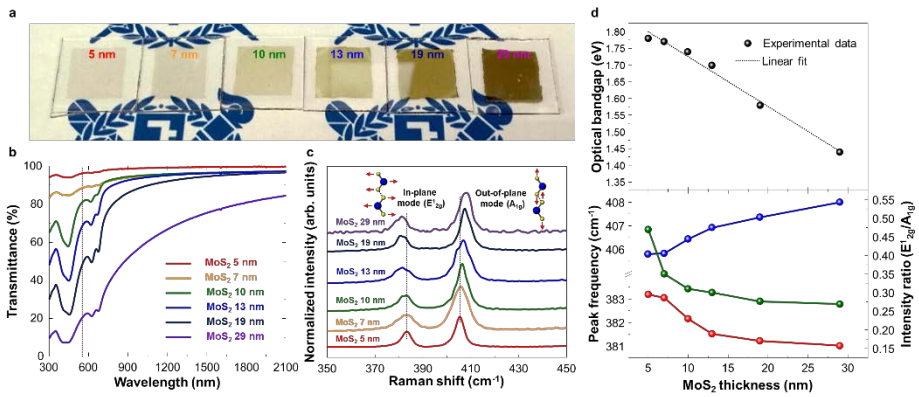

Fig. 4.6. Optical properties of synthesized MoS_2 thin film with various thicknesses. (a) Photographic images of transferred MoS_2 thin films on glass substrates. (b) Transmittance spectra of MoS_2 thin films. (c) Raman spectra of synthesized MoS_2 films at each thickness. (d) The evaluated optical band gap of synthesized MoS_2 thin film and Raman analysis of MoS_2 thin films with different thicknesses. The black dotted line indicates the linear fitting. The peak gap between E^1_{2g} and A_{1g} gradually increases as a function of MoS_2 film thickness. The intensity ratio of E^1_{2g} to A_{1g} is significantly decreased as the MoS_2 thickness is increased.

By changing the concentration of the precursor solution, the thickness of the MoS_2 thin films could be tailored between 5 nm and 29 nm, which were determined by using AFM, as displayed in Fig. 4.5. The transmittances of the MoS_2 thin films were measured by transferring the thin films onto glass substrates as shown in Fig. 4.6(a). The 5-nm-thick MoS_2 thin film is transparent with the high transmittance of ~96 % at 600 nm, while the 29-nm-thick MoS_2 thin film of a dark greenish-yellow color showed a transmittance of ~22 %, as displayed in Fig. 4.6(b). On the *p*-Si substrate, transmittance through the MoS_2 thin films can be increased because the difference of refractive index between *p*-Si substrate (η = 4.298 at 500 nm) and MoS_2 thin films (η = 5.675 at 500 nm) is smaller than between the glass substrate (η = 1.528 at 500 nm) and the MoS_2 thin films.[23-25]

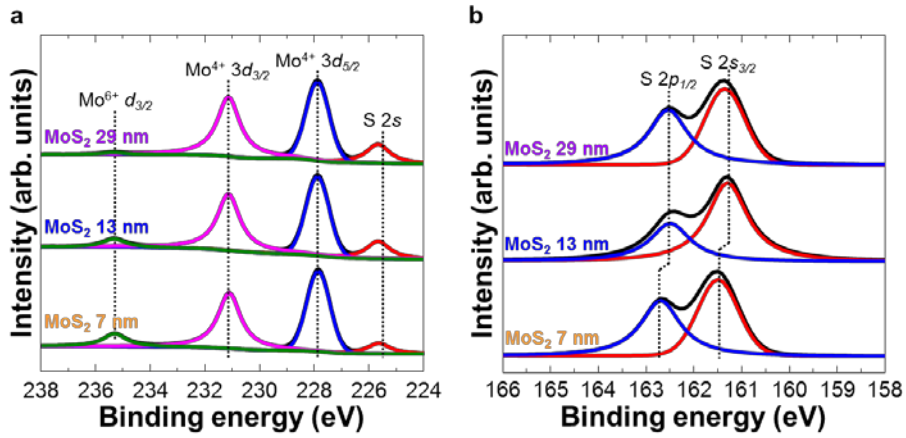

Fig. 4.7. SRPES analysis of synthesized MoS_2 thin films. Peak shapes and atomic compositions of synthesized MoS_2 thin films are similar to each other, regardless of precursor concentrations.

The chemical components and atomic ratios of the synthesized MoS_2 thin films were investigated using XPS. For MoS_2 thin films of different thicknesses, the atomic ratio of Mo to S was constant at 62 % to 38 %, consistent with previous reports (Fig. 4.7).[9,20] The Raman spectra of MoS_2 thin films with different thicknesses are shown in Fig. 4.6(c). As the film thickness increases, the gap between the peaks for in-plane (E^1_{2g}) and out-of-plane (A_{1g}) vibrational modes becomes wider. This originates from the stiffening of the out-of-plane mode and the relaxation of the in-plane mode, which decreases the peak intensity ratio of the E^1_{2g} mode to the A_{1g} mode (Fig. 4.6(d)).[26,27]

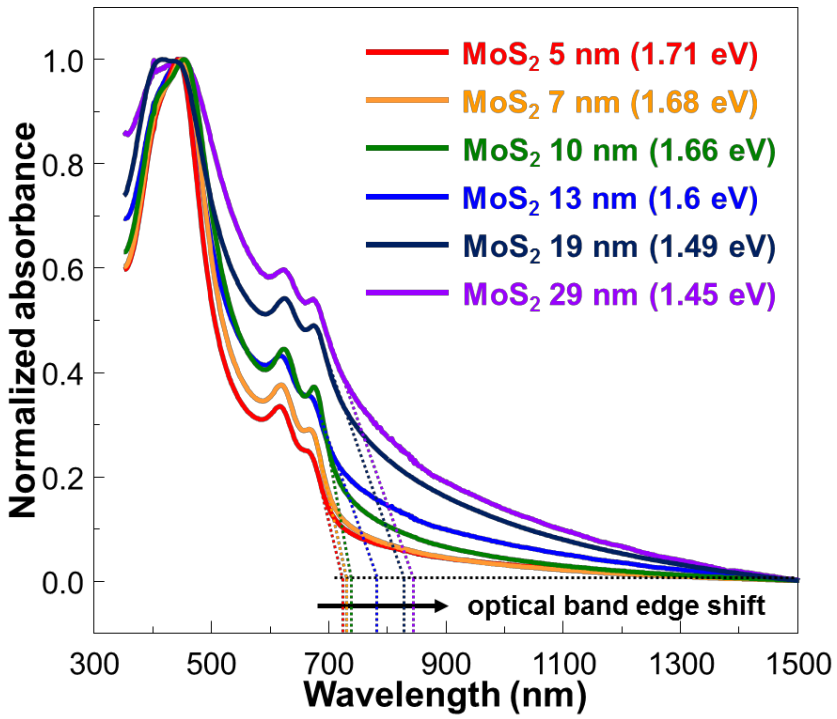

Fig. 4.8. Normalized absorbance spectra of synthesized MoS_2 thin films. The optical band gaps are calculated by extrapolating the initial peaks in the absorption spectra. The optical band edges of MoS_2 thin films are shifted to higher wavelength with respect to thickness of MoS_2 film.

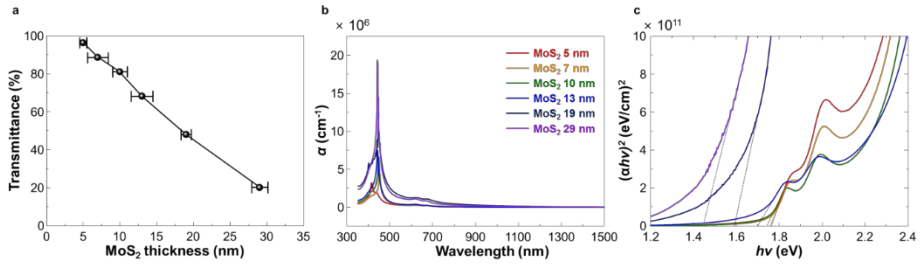

Fig. 4.9. (a) Plotting against the Transmittance at 550 nm to MoS_2 thickness. (b) The absorption coefficient of the MoS_2 thin films with different thicknesses. (c) Plots of $(\alpha h\nu)^2$ versus photon energy of the MoS_2 thin film with different thicknesses.

From the absorption spectra (Fig. 4.8), it was found that the optical band edges of MoS_2 thin films shifts to the longer wavelengths as the film thickness increases. To evaluate the optical band gap energies of the MoS_2 thin films more specifically, we used $(\alpha h\nu)^2$ vs. $h\nu$ plot where α is the absorption coefficient of the film (Fig. 4.9). The obtained band gap energies were plotted in Fig. 4.6(d). The change of band gap energy in our MoS_2 thin films evaluated by transmittance measurements is consistent with the previous report about band gap energies of MoS_2 films on Si substrates evaluated by reflectance measurements and optical properties of mechanically exfoliated MoS_2 layers.[28-30]

PEC measurements with the MoS_2/*p*-Si photocathodes were performed using a standard three-electrode cell with an electrolyte of 0.5 M sulfuric acid. Fig. 4.10(a) shows the photoelectrochemical current densities of the MoS_2/*p*-Si photocathodes plotted as a function of potential vs. reversible hydrogen electrode (RHE). The dark currents are shown as dashed lines. The bare *p*-Si photocathode exhibits a large onset potential of -0.28 V, defined as the potential at the photocurrent density of -1 mA/cm^2.

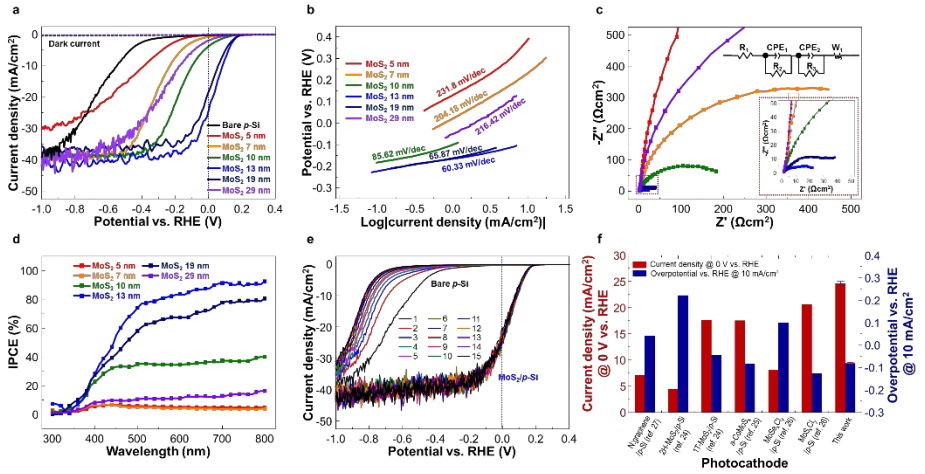

Fig. 4.10. Photoelectrochemical (PEC) and electrochemical impedance spectroscopic (EIS) analyses of MoS_2/*p*-Si heterojunction photocathode system. (a) PEC performances shown as polarization J-V curves of MoS_2 films of different thicknesses. 13-nm-thick MoS_2/*p*-Si photocathode shows 24.6 mA/cm^2 at 0 V and a significant potential value shift at 10 mA/cm^2 from -0.69 V for p-Si to 0.082 V. (b) Tafel slopes of MoS_2 layers plotted as log (j) against potential vs. RHE. 13-nm-thick MoS_2/*p*-Si sample shows the lowest Tafel slope of 60.33 mV/dec. (c) EIS analysis of MoS_2/*p*-Si heterostructures. Inset graph magnifies the 0-to-50 Ω cm^2 results for better comprehension. (d) ICPE measurements of various thicknesses MoS_2/*p*-Si photocathodes. (e) Cyclic test over 15 cycles to compare stabilities of bare *p*-Si and MoS_2/*p*-Si photocathodes. (f) Comparison of PEC performance between our 13-nm-thick MoS_2/*p*-Si photocathode and previously reported state-of-the-art photocathodes using similar materials on planar *p*-Si.

Although *p*-Si is widely used photocathode for solar water splitting because it has a narrow band gap, high crystallinity, and low cost, a large potential must be applied to adsorb hydrogen ions on the surface of the material.[31] All MoS_2/*p*-Si photocathodes exhibit lower onset potentials than the *p*-Si photocathode. The onset potential gradually shifts toward the positive region until the thickness of MoS_2 thin film reaches 13 nm. For the 13-nm-thick MoS_2/*p*-Si photocathode, the onset potential is 0.17 V and the photocurrent density at 0 V is -24.6 mA/cm^2. We emphasize that this value is even higher than the 17.6 mA/cm^2 photocurrent density measured at 0 V for a 1T-MoS_2/*p*-Si heterostructured photocathode, in

which the MoS_2 film was directly synthesized on the p-Si substrate.[31] The curves in Fig. 4.10(a) are from the first scans for each MoS_2/*p*-Si heterojunction photocathodes. The variation of current density in the negative potential regions originates from use of a stirrer for detaching the hydrogen bubbles on the surface of MoS_2/*p*-Si photocathodes. Because of the transferred 13-nm-thick MoS_2 thin film, the potential at the photocurrent density of 10 mA/cm^2 is reduced from 0.69 V to -0.082 V for the fabricated photocathodes. When the MoS_2 thin films exceed 13 nm in thickness, the onset potential is shifted toward the negative region. We also calculated applied-bias photon-to-current efficiency (ABPE) from measurement shown in Fig. 4.10(a). The maximum ABPE and open-circuit voltage are 0.86 % and 0.46 V for 13-nm-thick MoS_2/*p*-Si photocathode, respectively. This result is comparable with the previously reported value for 1T-MoS_2/*p*-Si photocathode (ABPE of ~ 1%).[28]

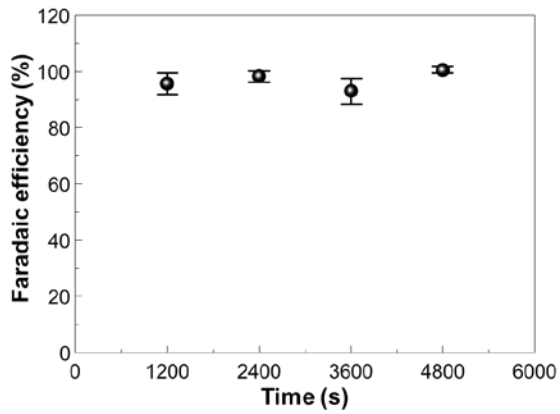

Fig. 4.11. Faradaic efficiency measurements for the 13-nm-thick MoS_2/*p*-Si heterojunction photocathode under continuous illumination at -1.2 V vs. RHE in 0.5 M H_2SO_4 electrolyte, which displays almost 100 % Faradaic efficiency for hydrogen production.

The Faradaic efficiency of the 13-nm-thick MoS_2/*p*-Si heterojunction photocathode was determined by collecting the evolved hydrogen gas. The result reveals that the MoS_2/*p*-Si photocathode gives almost 100 % Faradaic yield during PEC process, which is well-consistent with the previous reports (Fig. 4.11).[32,33]

To understand the catalytic activity of the transferred MoS_2 thin films, the polarization curves in Fig. 4.10(a) were converted to Tafel plots, in which the potentials are plotted as functions of the logarithm of current density. The linear portions of the curves are collected to evaluate the Tafel slopes in Fig. 4.10(b). Catalysts with high HER activities are known to have low Tafel slopes. The 13-nm-thick MoS_2/*p*-Si photocathode with the highest photocurrent at 0 V shows the lowest Tafel slope of 60.33 mV/dec. Interestingly, this value is very close to the Tafel slope of 2H-MoS_2 nanodots, which indicates that the transferred MoS_2 thin film works as an efficient HER catalyst for *p*-Si.[14] Water reduction for the evolution of hydrogen occurs by the accepted three-step mechanism, which includes the Volmer (Tafel slope of 120 mV/dec in an acidic electrolyte), Heyrovsky (40 mV/dec), and Tafel (30 mV/dec) steps. The Tafel slope of 60.33 mV/dec for the 13-nm-thick MoS_2/*p*-Si photocathode indicates that HER most likely occurs by the Volmer-Heyrovsky mechanism with this cathode structure.[14] 5 different samples for each MoS_2/*p*-Si photocathodes showed valuable difference in potential at 10 mA/cm^2, photocurrent densities at 0 V, and Tafel slopes are summarized in Fig. 4.12.

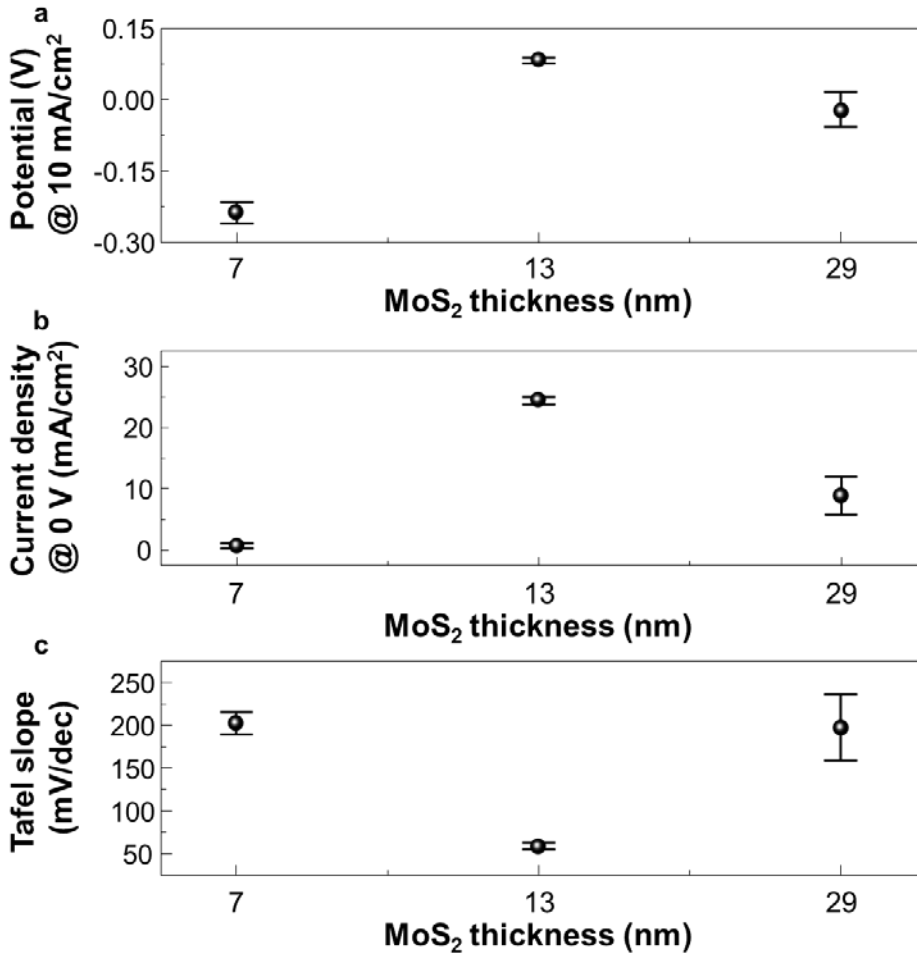

Fig. 4.12. Three key results from 5 different samples for each 7-nm-thick, 13-nm-thick, and 29-nm-thick MoS_2/p-Si heterojunction photocathodes. (a) Potential @ 10 mA/cm^2. (b) Current density @ 0 V. (c) Tafel slope values.

Electrochemical impedance spectroscopy (EIS) measurements were conducted to understand the surface kinetics during HER in the acidic electrolyte. The impedance spectra, measured by applying a small voltage (-0.07 V) near the onset potential, reflect the HER activities of the photocatalysts. A high HER activity is reflected by a small semicircle in the Nyquist plots shown in Fig. 4.10(c). The smallest semicircle, demonstrated by the spectrum for the photocathode with a 13-nm-thick

MoS_2 layer represents the fastest electrode-to-electrolyte shuttling of electrons during HER. An equivalent circuit is composed of constant phase elements (CPE) and charge-transfer resistances (R_{ct}).[31] The variation of R_{ct} at the MoS_2/electrolyte interfaces ($R_{ct,3}$) agrees with that of the photocurrents at 0 V in Fig. 4.10(a), as shown in Table 4.1.

Table. 4.1. Comparison of charge-transfer resistance (R_{ct}) values.

Photocathode	$R_{ct,1}$ (Ω cm^2) contact/*p*-Si	$R_{ct,2}$ (Ω cm^2) *p*-Si/MoS_2	$R_{ct,3}$ (Ω cm^2) MoS_2/EL*
***p*-Si**	**1.17**	**4809.89**[#]	**-**
5 nm MoS_2/*p*-Si	**0.72**	**1066.58**	**2620.42**
7 nm MoS_2/*p*-Si	**1.02**	**455.47**	**520.24**
10 nm MoS_2/*p*-Si	**0.99**	**96.97**	**119.37**
13 nm MoS_2/*p*-Si	**0.90**	**10.43**	**10.56**
19 nm MoS_2/*p*-Si	**0.77**	**13.53**	**15.34**
29 nm MoS_2/*p*-Si	**0.52**	**764.49**	**1063.03**

[#]*p*-Si/electrolyte, *EL: Electrolyte.

The R_{ct} value for the 13-nm-thick MoS_2/*p*-Si photocathode is two orders of magnitude lower than that for the bare *p*-Si, indicating that the transferred 13-nm-thick MoS_2 thin film is critical for charge transfer at the solid/electrolyte interface. The incident-photon-to-current conversion efficiency (IPCE) spectra of the MoS_2/*p*-Si photocathodes, measured at -0.1 V vs. RHE, are displayed in Fig. 4.10(d). Throughout the tested spectrum, the photocathode with the 13-nm-thick MoS_2 layer shows the highest efficiency. Combined with the linear-sweep voltammetry curves, these results clearly show that the PEC properties of the MoS_2/*p*-Si photocathodes depend on the thickness of the MoS_2 thin film and that an optimum MoS_2 thin-film thickness exists.

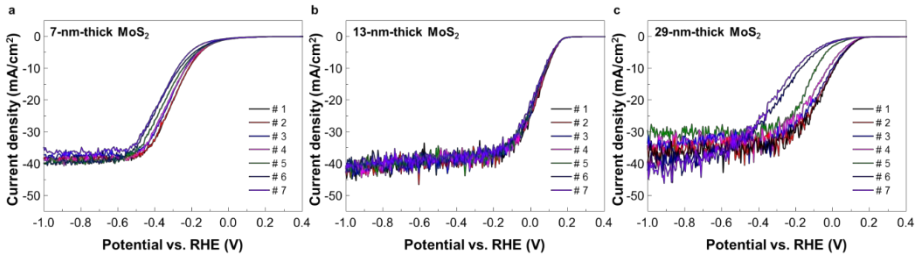

Fig. 4.13. The cyclic test for the MoS_2 thin films with various thicknesses. The 7 times cyclic test shows the thickness dependent stability. The cyclic tests with (a) 7-nm-thick MoS_2/*p*-Si, (b) 13-nm-thick MoS_2/*p*-Si, (c) 29-nm-thick MoS_2/*p*-Si heterojunction photocathode are displayed.

The stability of the 13-nm-thick MoS_2/*p*-Si photocathode was investigated to determine whether the transferred MoS_2 thin-film catalyst could act as a passivation layer. Fig. 4.10(e) shows the linear sweep voltammetry curves of bare *p*-Si and MoS_2/*p*-Si photocathodes for 15 cycles. The bare Si photocathode shows fast degradation, while the MoS_2/*p*-Si photocathode shows significant suppression of shifts toward more negative potentials throughout the measurement cycles. In order to investigate the thickness dependent stability of the fabricated electrodes, cyclic tests were performed for using 7-nm-thick, 13-nm-thick, and 29-nm-thick MoS_2/*p*-Si photocathodes. The stability of the electrodes was different one another (Fig. 4.13). Especially, the lowest stability was found from the 29-nm-thick MoS_2/*p*-Si photocathode, where the top MoS_2 layers would have relatively weaker van der Waals force compared to bottom MoS_2 films which are located at the heterointerface with the *p*-Si.

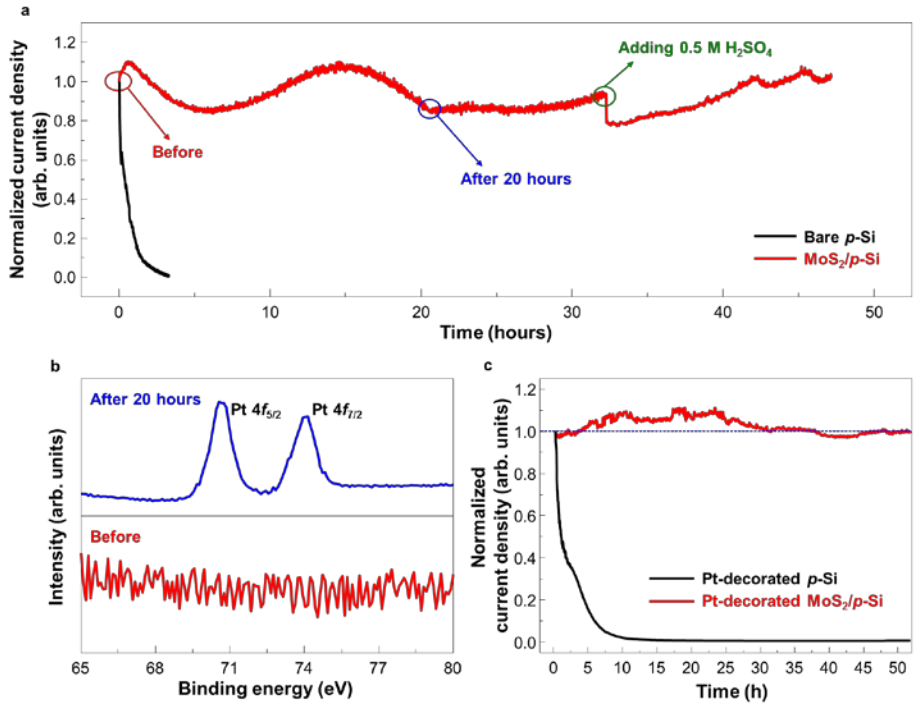

Fig. 4.14. (a) Chronoamperometry measurements of bare *p*-Si and 13-nm-thick MoS_2/*p*-Si photocathodes. (b) The identification of Pt deposition using XPS analysis for before and after 20 hours. The Pt deposition was clearly identified after 20 hours stability measurement. (c) Chronoamperometry measurements of Pt decorated *p*-Si and Pt decorated MoS_2/*p*-Si photocathodes.

The stability enhancement by the transferred MoS_2 thin film was confirmed by chronoamperometry measurements (Fig. 4.14). From the normalized chronoamperometric curves of Pt decorated bare *p*-Si and Pt decorated MoS_2/*p*-Si photocathodes, measured at 0 V vs. RHE, it is observed that the current density of the Pt decorated bare *p*-Si photocathode rapidly decreases during the measurement and retains only 0.1 % of the original current density after 9.6 hours. As aforementioned in the introduction, the photocorrosion of the *p*-Si photocathode cannot be prevented using Pt nanoparticles. Meanwhile, the Pt decorated

MoS_2/*p*-Si photocathode maintain the initial current density even after 50 hours, demonstrating the behavior of the transferred MoS_2 thin film as a passivation layer that prevents the *p*-Si photocathode from experiencing severe photocorrosion.[31]

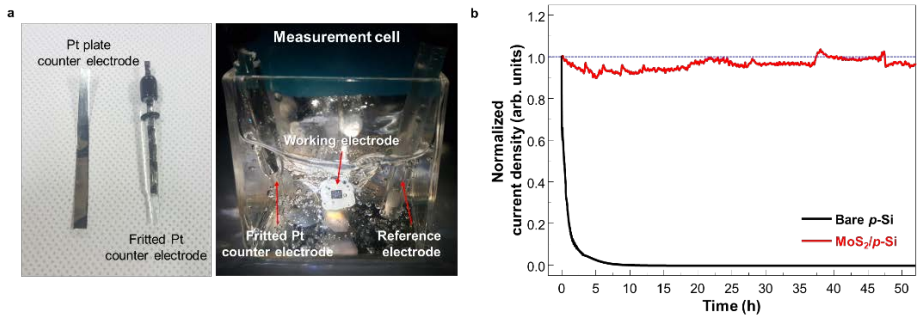

Fig. 4.15. (a) Photographic images of Pt plate, fritted Pt counter electrode (left), and the measurement cell which contains three electrodes i) reference, ii) working, and iii) fritted Pt counter electrode (right). (b)Chronoamperometry measurements of bare *p*-Si and MoS_2/*p*-Si photocathodes by using the fritted Pt counter electrode.

To clarify the passivation effect of the MoS_2 thin film, we have measured the stability of the photocathode using a fritted Pt counter electrode, which is free from dissolving in the strong acid electrolyte (0.5 M H_2SO_4, pH = 1.1) (Fig. 4.15). For the MoS_2/*p*-Si photocathode, the current density was stable after 50 hours without notable degradation, indicating that the transferred MoS_2 thin film acts as not only a catalyst for hydrogen production but also an excellent passivation layer.

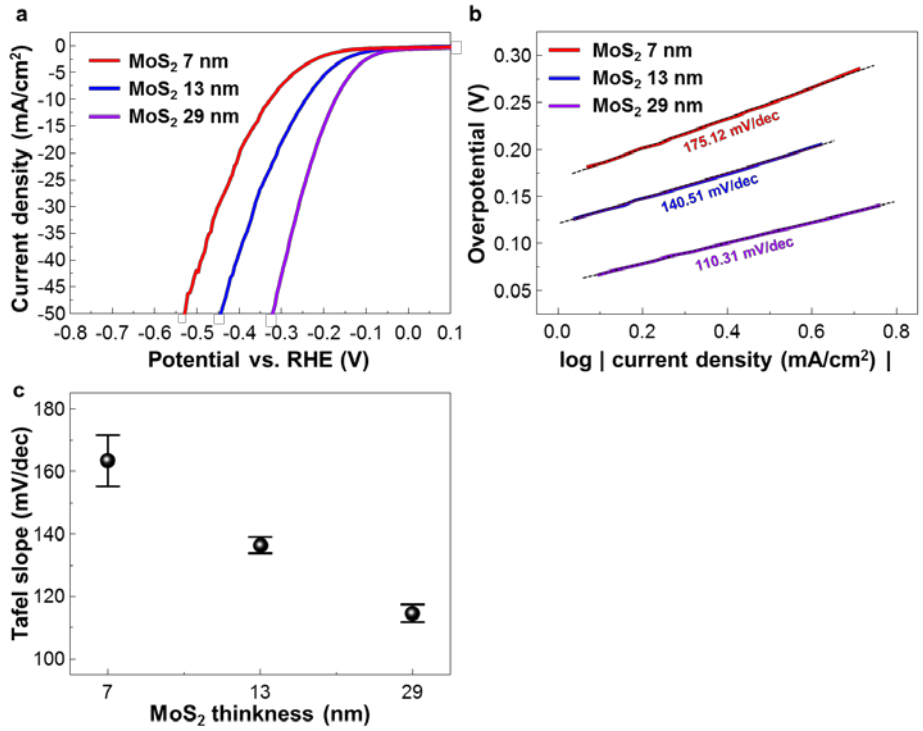

Fig. 4.15. The electrocatalytic HER performance. (a) LSV curves and (b) Tafel slope for MoS_2 thin films on Au plate with various thicknesses.

We have also investigated the electrochemical HER performance of MoS_2 thin films with various thicknesses on Au substrate without iR-correction (Fig. 4.15). The HER performance of our synthesized MoS_2 thin films is comparable to that of the previously reported MoS_2 catalysts.[9-11,13] The slightly lower overpotentials and Tafel slopes of the MoS_2/*p*-Si photocathodes compared with those of the MoS_2 thin films indicate the downward band bending in *p*-Si promotes HER at the soild/electrolyte interface.

In order to compare the PEC performance of the 13-nm-thick MoS_2/*p*-Si photocathode with that of previously reported state-of-the-art photocathodes with similar material systems, photocurrent densities at 0

V vs. RHE and overpotentials vs. RHE at 10 mA/cm^2 for our MoS_2/*p*-Si photocathode and other photocathodes based on TMD material (or graphene)/*p*-Si heterostructures without noble metal catalysts have been plotted in Fig. 4.10(f).[31,34-37] The overpotential at 10 mA/cm^2 of our photocathode is lower than those of other photocathodes including 1T-MoS_2/*p*-Si photocathode and close to that of chlorine-doped MoS_x (MoS_xCl_y)/*p*-Si photocathodes.[31,35] For the photocurrent densities at 0 V vs. RHE, it is clear that our photocathode shows the highest value among the material systems. The details about the material systems and numerical values are summarized in Table 4.2.

Table 4.2. Comparison of the PEC performances between our 13-nm-thick MoS_2/*p*-Si heterojunction photocathode and other similar and state-of-the-art materials on *p*-Si photocathodes.

Ref No.	Materials	Preparation method	Photocathode	Overpotential @10mA/cm^2	Current density @ 0V vs. RHE
1	rGO	Hummer's method	*p*-Si narowires	+ 0.145 V	2.3 mA/cm^2
2	N:graphene	CVD growth (N2 plasma for N doping)	planar *p*-Si	+ 0.041 V	7.1 mA/cm^2
3	1T-MoS_2	Li intercalation	planar *p*-Si	+ 0.055 V	9.6 mA/cm^2
	1T-MoS_2	CVD growth ($MoCl_5$, S)		– 0.045 V	17.6 mA/cm^2
	2H-MoS_2			+ 0.221 V	4.5 mA/cm^2
4	a-MoS_x	Photoassisted deposition	planar *p*-Si	+ 0.065 V	6.0 mA/cm^2
	a-CoMoS_x			– 0.085 V	17.5 mA/cm^2
5	$MoSe_xCl_y$	CVD growth ($MoCl_5$, S, Se)	planar *p*-Si	+ 0.1 V	8.0 mA/cm^2
	MoS_xCl_y			– 0.127 V	20.6 mA/cm^2
6	Ni-Mo[2]	Galvanostatic /potentiostatic deposition	*n*+*p*-Si MW	- 0.09 V	10.35 mA/cm^2
7	W_2C[3]	Reactive ballistic deposition	planar *p*-Si	+ 0.085 V	4.5 mA/cm^2
8	$CoSe_2$ Nanorod[4]	Hydrothermal deposition	planar *p*-Si	+ 0.042 V	8.7 mA/cm^2
Our Work	13-nm 2H-MoS_2	Thermolysis ($[(NH_4)_2MoS_4]$, S)	planar *p*-Si	- 0.082 V	24.6 mA/cm^2

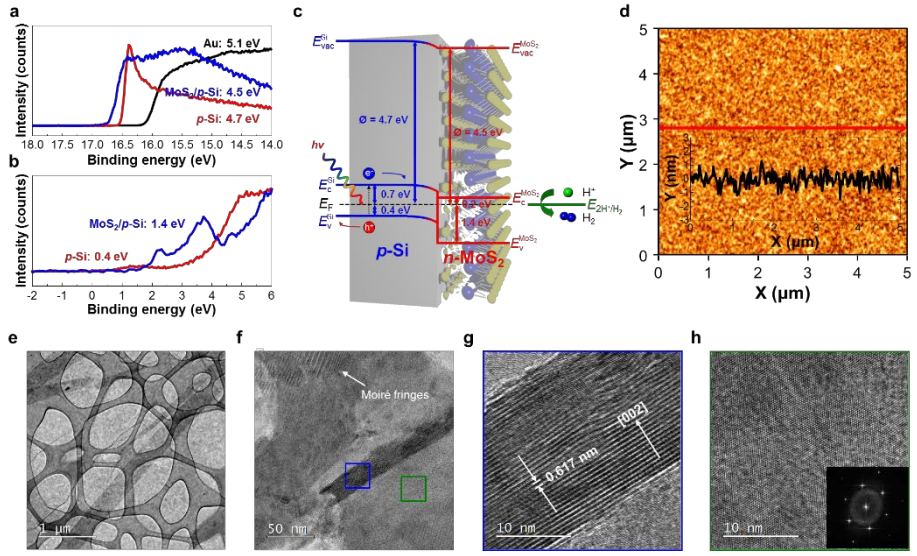

Fig. 4.16. Characterization of MoS_2 thin film (13 nm) grown by solution precursor-based thermolysis method. (a) UPS spectra of *p*-Si, 13-nm-thick MoS_2/*p*-Si, and reference Au foil. (b) XPS spectra of *p*-Si, 13-nm-thick MoS_2/*p*-Si, and reference Au foil. (c) Schematic of energy band diagram of MoS_2/*p*-Si heterojunction photocathode. (d) AFM image of MoS_2 thin film on SiO_2/Si substrate. (e) – (f) TEM images of synthesized MoS_2 thin film with different magnifications.

Because the transferred MoS_2 thin films are semitransparent, most incident light is absorbed in the underlying p-Si substrate of the MoS_2/*p*-Si heterostructured photocathodes. Thus, photogenerated electrons in *p*-Si should be efficiently transported to the MoS_2/electrolyte interface for HER. Band-bending in the MoS_2/*p*-Si heterostructures was investigated by ultraviolet photoemission spectroscopy (UPS) and XPS. The secondary electron emission (SEE) spectra of bare *p*-Si, 13-nm-thick MoS_2/*p*-Si, and reference Au foil electrodes are displayed in Fig. 4.16(a). Compared with the work function of the Au reference (5.1 eV), the work functions of the samples can be estimated from the SEE cutoffs as 4.7 eV and 4.5 eV for *p*-Si and MoS_2/*p*-Si, respectively. According to the XPS valence-band spectra displayed in Fig. 4.16(b), the energy difference

between the Fermi level and the valence band maximum (E_F - E_V) for bare *p*-Si is 0.5 eV, indicating downward band bending of ~0.3 eV. The E_F - E_V for MoS_2/*p*-Si is 1.4 eV. Because the photoelectrons escape depth of ~5 nm is less than the thickness of the MoS_2 layer, and because the MoS_2 layer with optical bandgap energy of 1.6 eV (Fig. 4.8) has negligible surface band bending, the Fermi level of MoS_2 is determined to be 0.2 eV below the conduction-band maximum (E_C). This reveals that the transferred MoS_2 thin film is an *n*-type semiconductor.[37] Based on these results, an energy band diagram for the *n*-MoS_2/*p*-Si heterojunction is illustrated in Fig. 4.16(c).

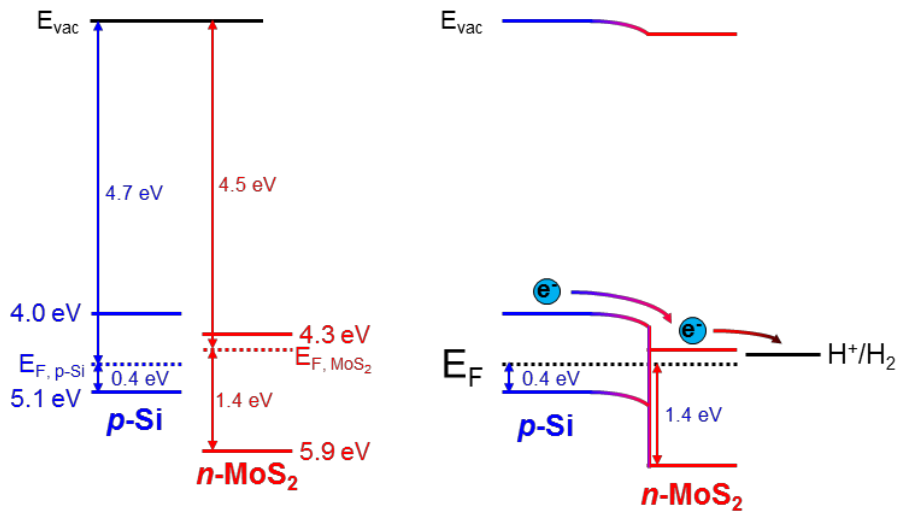

Fig. 4.17. Flat band and band bending diagram of *n*-MoS_2 thin film and *p*-Si heterojunction.

Flat band and band bending diagrams for the *n*-MoS_2/*p*-Si heterojunction are displayed in Fig. 4.17. The Fermi level should be equalized when the both *n*- and *p*- type materials make the heterojunction. By assuming that the band bending in the *p*-Si for the MoS_2/*p*-Si

heterojunction is similar to that for the bare *p*-Si, the *n*-MoS_2/*p*-Si heterojunction is found to form a type-II junction as described in Fig. 4.16(c). The band diagram clearly shows that the transport of photogenerated electrons from *p*-Si to MoS_2 is energetically favorable. Interestingly, the E_C level of the MoS_2 layer is equal to the H^+/H_2 reduction potential (4.5 eV), suggesting that electrons can be effectively transferred to the electrolyte without an electronic potential barrier.[38,39]

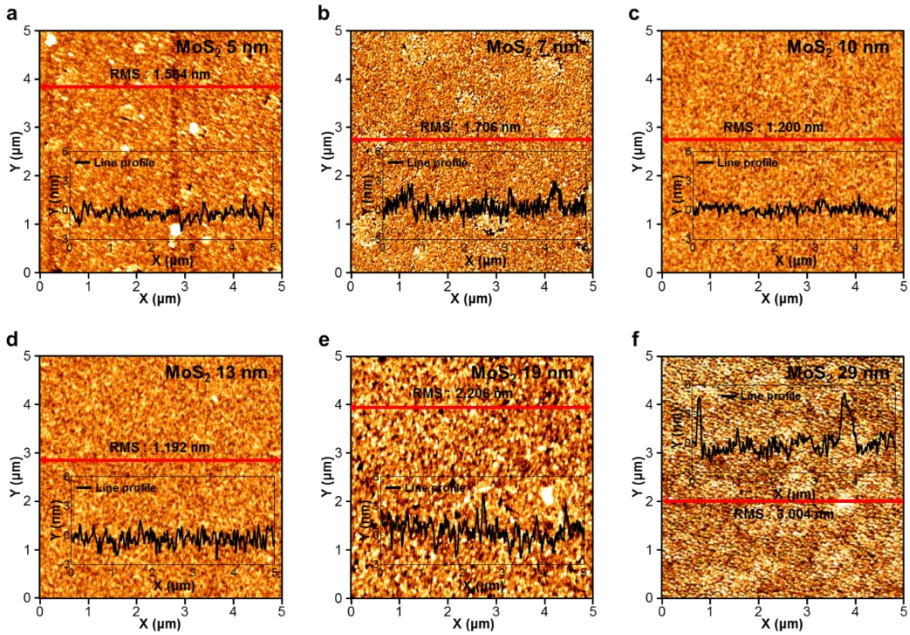

Fig. 4.18. Surface morphology analyses of synthesized MoS_2 thin films using AFM measurements. The serrated surfaces of the MoS_2 thin films have higher surface areas than atomically flat surfaces.

The overall quantum efficiency of the *n*-MoS_2/*p*-Si photocathode largely depends on the overpotential for HER at the *n*-MoS_2/electrolyte interface. The surface morphology of the transferred MoS_2 thin films was examined by AFM. All synthesized MoS_2 thin films were nano-granular (Fig. 4.18). For the 13-nm-thick MoS_2 thin film, the root-mean-square

(RMS) roughness was ~1.5 nm with a peak-to-valley depth of ~2 nm, as seen in Fig. 4.16(d). The serrated surface of the 2H-MoS_2 thin film provides a larger surface area than the atomically flat surface of a single-crystalline MoS_2 monolayer. The relatively high RMS roughness originates from the coexistence of a-domains and c-domains which have different growth rates and domain boundaries between them.

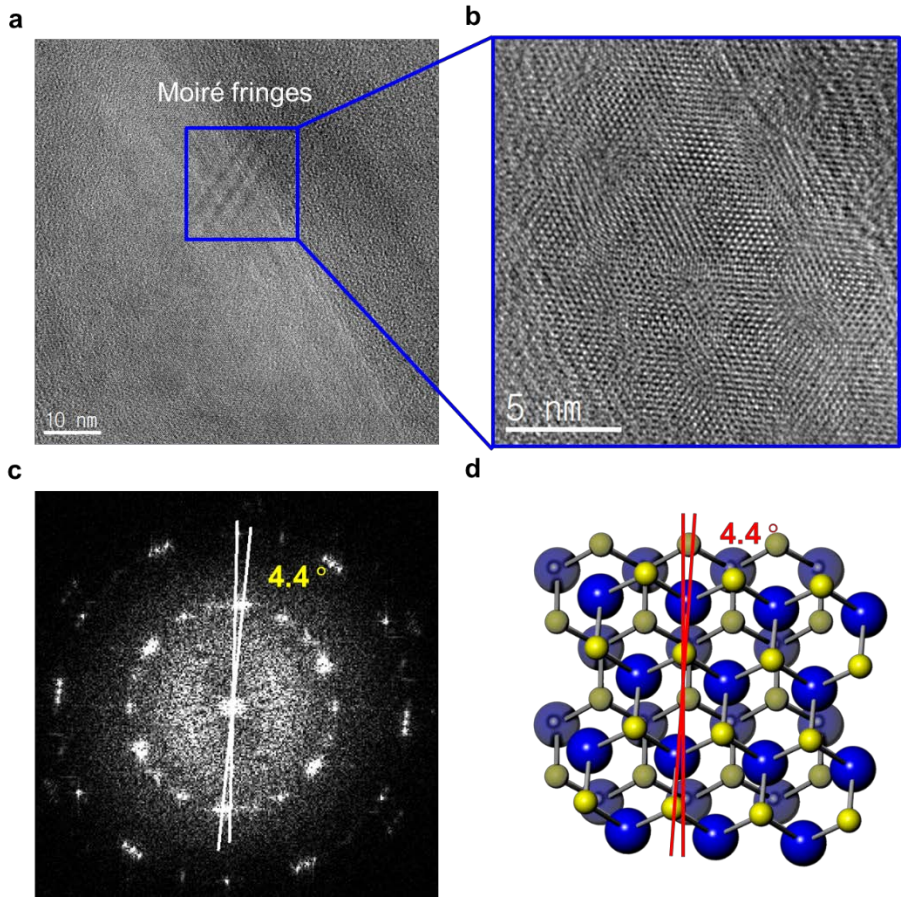

Fig. 4.19. (a), (b) High-resolution (HR) TEM images of Moiré fringes from in-plane rotation between two basal planes. (c) Selected-area electron diffraction (SAED) pattern images of in-plane rotation. (d) Schematic of structure producing Moiré fringes, corresponding to Fig. 4.19(c).

Furthermore, the partially rotated MoS_2 basal planes, Moiré fringes, roughen the surface of transferred MoS_2 thin film as observed in Fig. 4.19. The microstructure of the MoS_2 thin films was studied using transmission electron microscopy (TEM). The low-magnification TEM image in Fig. 4.16(e) shows a pinhole-free 13-nm-thick MoS_2 thin film with some wrinkles on a meshed Cu grid. High-resolution TEM images are shown in Fig. 4.16(f)–(j). Clearly, the films mainly contain a-domains with the preferred out-of-plane (001) orientation of the 2H-MoS_2 phase and c-domains with the preferred in-plane (001) orientation of the 2H-MoS_2. From some a-domain regions, Moiré fringes from in-plane rotation between two basal planes were observed (Fig. 4.19).[40]

Crystallographically, the surfaces of the a-domains are free of dangling bonds, while some dangling bonds exist at the surfaces of c-domains. Because the dangling bonds are electrochemically active sites for HER, the MoS_2 film with c-domains should act as an efficient HER catalyst, as observed in Fig. 4.10.[16] The presence of c-domains with vertically stacked (001) planes of the 2H-MoS_2 phase is the main advantage of our solution-based thermolytic method compared to CVD methods, where a-domains of the 2H-MoS_2 phase are preferentially synthesized on foreign substrates. During the thermolysis, the growth of randomly oriented nuclei in the precursor layer formed both c-domains and a-domains.

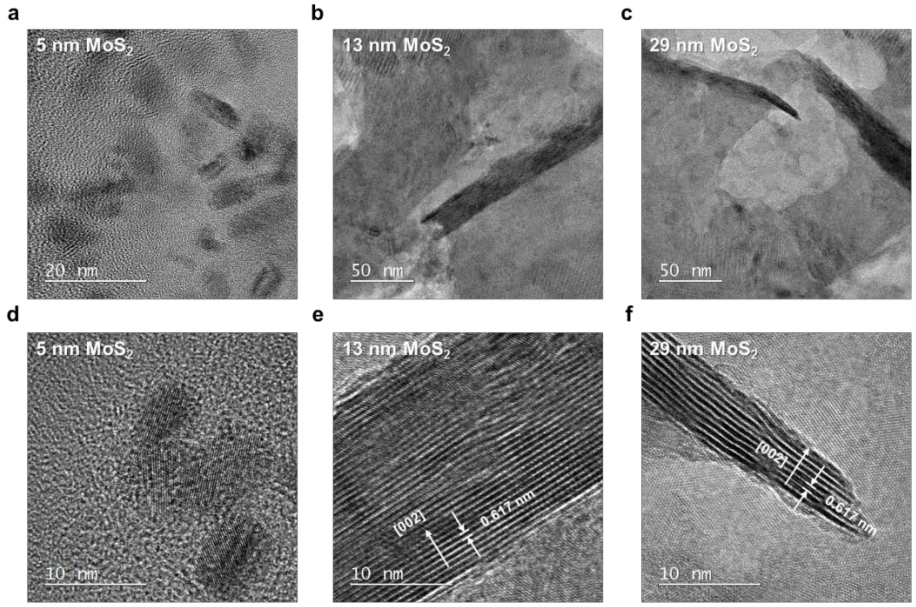

Fig. 4.20. High-resolution (HR) TEM images of synthesized MoS_2 thin films (5-nm-, 13-nm- and 29-nm-thick) with different magnifications. More c-domains and larger crystalline phases are observed in the 13-nm-thick MoS_2 thin films.

We found that thicker MoS_2 thin films had higher degrees of crystallinity and larger c-domains (Fig. 4.20), which implied that the thicker MoS_2 thin films could have higher HER activity than the thinner films, as observed in Fig. 4.10(a). Although the 29-nm-thick MoS_2 thin film would have a high HER activity, the increased attenuation of light in the MoS_2 film would reduce the light absorption in the underlying *p*-Si substrate, where the photogenerated electrons are located in energy levels higher than those in the MoS_2 film. As a result, the 29-nm-thick *n*-MoS_2/*p*-Si photocathode shows a higher overpotential than the 13-nm-thick *n*-MoS_2/*p*-Si photocathode.

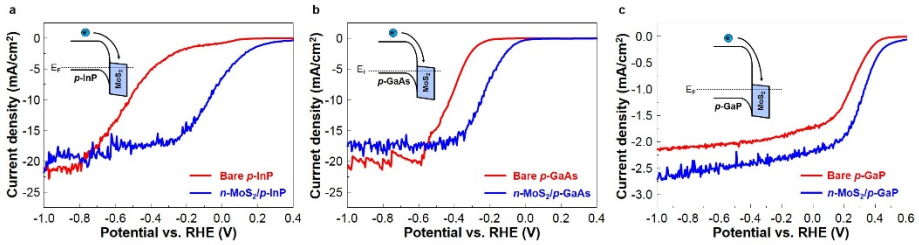

Fig. 4.21. Polarization curves of 13-nm MoS_2/*p*-type semiconductor heterojunction photocathodes. The polarization J-V curves of (a) 13-nm-thick *n*-MoS_2/*p*-InP photocathode, (b) 13-nm-thick *n*-MoS_2/*p*-GaAs photocathode, and (c) 13-nm-thick *n*-MoS_2/*p*-GaP photocathode. Insets show the energy band diagram of each heterojunction.

The novel aspect of the *n*-MoS_2 thin-film catalysts developed here is the transferability onto other substrates. To demonstrate the versatility of the thin-film catalysts, we employed various p-type III-V semiconductors as photoelectrodes. Using the same procedure for fabricating the *n*-MoS_2/*p*-Si photocathodes, 13-nm-thick MoS_2 thin films were transferred to *p*-InP, *p*-GaAs, and *p*-GaP substrates. The PEC properties of the fabricated heterojunction photocathodes are shown in Fig. 4.21. Under AM 1.5 G solar illumination, the bare *p*-type semiconductors show varied saturation photocurrents and onset potentials because of the different band gap energies (1.3 eV for InP, 1.4 for GaAs, and 2.3 eV for GaP). The onset potentials, which depend on the E_C levels and the overpotentials at the solid/liquid interfaces, also differ for the bare photocathodes. When the MoS_2 thin films are transferred to the *p*-InP, *p*-GaAs, and *p*-GaP substrates, the onset potentials are shifted toward the anodic direction without notable losses in the saturation photocurrents, indicating that the transferred MoS_2 thin films work as efficient catalysts for HER on the III-V semiconductor substrates.[41-43] Among the *n*-MoS_2/*p*-type semiconductor photocathodes, the *n*-MoS_2/*p*-Si heterojunction shows the best HER

performance. It should be noted that Si is the cheapest and most earth-abundant material among the semiconductors. Because the band bending in the *n*-MoS_2/*p*-III-V heterojunctions is large, as illustrated in the insets of Fig. 4.21, further reduction of the overpotential may be achieved by optimizing the back contacts and surface treatments for the III-V semiconductors. We believe that the transferred *n*-MoS_2 thin-film HER catalysts can be applied not only to other semiconductor photocathodes, but also to oxide-based photocathodes such as Cu_2O and SnO_x.[45,47]

4.1.4. Conclusion

We have successfully demonstrated the synthesis of MoS_2 thin films with high HER activities via solution-based thermolysis, as well as the wafer-scale fabrication of *n*-MoS_2/*p*-Si heterojunction photocathodes using a simple transfer method. The heterojunction photocathodes provide high photocurrent density (24.6 mA/cm^2 at 0 V vs. RHE), large shifts in overpotential (0.79 V at 10 mA/cm^2), and long-term stability (over 10000 s). We expanded our work to verify the efficient HER catalytic activity of *n*-MoS_2 thin films transferred to other p-type semiconductors (*p*-InP, *p*-GaAs, and *p*-GaP). Our approach can be applied to various 2D TMDs, in which the HER activity of the TMDs can be enhanced through substitutional doping and defect engineering,[46] as well as *n*-TMD/*p*-TMD heterojunctions, in which the high electric fields in the atomically thin TMD *p*-*n* junctions can further enhance the efficiency of HER.[47] Although this study focused on the enhanced catalytic activity and stability of transferable MoS_2 thin films, wafer-scale TMD thin films could be useful for various electronic and optoelectronic devices, even those using curved or flexible substrates.[19]

4.1.5. References

[1] A. J. Nozik, *Appl. Phys. Lett.*, **1976**, *29*, 150.

[2] A. J. Nozik, *Appl. Phys. Lett.*, **1977**, *30*, 567.

[3] L. Fornarini, A. J. Nozik and B. A. Parkinson, *J. Phys. Chem.*, **1984**, *88*, 3238.

[4] E. L. Warren, S. W. Boettcher, J. R. McKone and N. S. Lewis, *SPIE-Int. Soc. Optical Engineering*, **2010**, *7770*, 77701.

[5] N. C. Strandwitz, D. B. Turner-Evans, A. C. Tamboli, C. T. Chen, H. A. Atwater and N. S. Lewis, *Adv. Energy Mater.*, **2012**, *2*, 1109.

[6] D. M. Andoshe, J.-M. Jeon, S. Y. Kim and H. W. jang, *Electron. Mater. Lett.*, **2015**, *11*, 323.

[7] K. Osseo-Asare, D. Wei and K. K. Mishra, *J. Electrochem. Soc.*, **1996**, *143*, 749.

[8] M. G. Walter, E. L. Warren, J. R. McKone, S. W. Boettcher, Q. Mi, E. A. Santori and N. S. Lewis, *Chem. Rev.*, **2010**, *110*, 6446.

[9] D. Voiry, M. Salehi, R. Silva, T. Fujita, M. Chen, T. Asefa, V. B. Shenoy, G. Eda and M. Chhowalla, *Nano Lett.*, 2013, **13**, 6222.

[10] L. Cheng, W. Huang, Q. Gong, C. Liu, Z. Liu, Y. Li and H. Dai, *Angew. Chem. Int. Ed.*, **2014**, *53*, 7860.

[11] D. Voiry, H. Yamaguchi, J. Li, R. Silva, D. C. B. Alves, T. Fujita, M. Chen, T. Fujita, M. Chen, T. Asefa, V. B. Shenoy, G. Eda and M. Chhowalla, *Nature Mater.*, **2013**, *12*, 850.

[12] L. Zhang, C. Liu, A. B. Wong, J. Resasco and P. Yang, *Nano Research*, **2015**, *8*, 281.

[13] A. B. Laursen, S. Kegnæs, S. Dahl and I. Chorkendorff, *Energy Environ. Sci.*, **2012**, *5*, 5577.

[14] J. Benson, M. Li, S. Wang, P. Wang and P. Papakonstantinou, *ACS Appl. Mater. Interfaces*, **2015**, *7*, 14113.

[15] Y.-H. Lee, X.-Q. Zhang, W. Zhang, M.-T. Chang, C.-T. Lin, K.-D. Chang, Y.-C. Yu, J. T.-W. Wang, C.-S. Chang, L.-J. Li and T.-W. Lin, *Adv. Mater.*, **2012**, *24*, 2320.

[16] X. Wang, H. Feng, Y. Wu and L. Jiao, *J. Am. Chem. Soc.*, **2013**, *135*, 5304.

[17] Y. Yu, C. Li, Y. Liu, L. Su, Y. Zhang and L. Cao, *Sci. Rep.*, **2013**, *3*, 1866.

[18] T. F. Jaramillo, K. P. Jørgensen, J. Bonde, J. H. Nielsen, S. Horch and I. Chorkendorff, *Science*, **2007**, *317*, 100.

[19] Y. Yang, H. Fei, G. Ruan, C. Xiang and J. M. Tour, *Adv. Mater.*, **2014**, *26*, 8163.

[20] K. C. Kwon, C. Kim, Q. V. Le, S. Gim, J. M. Jeon, J. Y. Ham, J.-L. Lee, H. W. Jang and S. Y. Kim, *ACS nano*, **2015**, *9*, 4146.

[21] K.-K. Liu, W. Zhang, Y.-H. Lee, Y.-C. Lin, M.-T. Chang, C.-Y. Su, C.-S. Chang, H. Li, Y. Shi, H. Zhang, C.-S. Lai and L.-J. Li, *Nano Lett.*, **2012**, *12*, 1538.

[22] X. Jia, L. Yu, J. Liu, Q. Xu, M. Sickert, L. Chen and M. Lautens, *Green Chem.*, **2014**, *16*, 3444.

[23] D. E. Aspnes and J. B. Theeten, *J. Electochem. Soc.*, **1980**, *127*, 1359.

[24] M. Rubin, *Solar Energy Materials*, **1985**, *12*, 275.

[25] H. Zhang, Y. Ma, Y. Wan, X. Rong, Z. Xie, W. Wang and L. Dai, *Sci. Rep.*, **2015**, *5*, 8440.

[26] H. Li, Q. Zhang, C. C. R. Yap, B. K. Tay, T. H. T. Edwin, A. Olivier and D. Baillargeat, *Adv. Funct. Mater.*, **2012**, *22*, 1385.

[27] A. Berkdemir, H. R. Gutiérrez, A. R. B. Méndez, N. P. López, A. L. Elías, C.-I. Chia, B. Wang, V. H. Crespi, F. López-Urías, J.-C. Charlier, H. Terrones and M. Terrones, *Sci. Rep.*, **2013**, *3*, 1755.

[28] C. Yim, M. O'Brien, N. McEvoy, S. Winters, I. Mirza, J. G. Lunney and G. S. Duesberg, *Appl. Phys. Lett.*, **2014**, *104*, 103114.

[29] K. F. Mak, C. Lee, J. Hone, J. Shan and T. F. Heinz, *Phys. Rev. Lett.*, **2010**, *105*, 136805.

[30] H. S. Lee, S.-W. Min, Y.-G. Chang, M. K. Park, T. Nam, H. Kim, J. H. Kim, S. Ryu and S. Im, *Nano Lett.*, **2012**, *12*, 3695.

[31] Q. Ding, F. Meng, C. R. English, M. Cabán-Acevedo, M. J. Shearer, D. Liang, A. S. Daniel, R. J. Hamers and S. Jin, *J. Am. Chem. Soc.*, 2014, **136**, 8504.

[32] X. Guo, G. Cao, F. Ding, X. Li, S. Zhen, Y. Xue, Y. Yan, T. Liu and K. Sun, *J. Mater. Chem. A*, **2015**, *3*, 5041.

[33] J. Huang, D. Hou, Y. Zhou, W. Zhou, G. Li, Z. Tang, L. Li and S. Chen, *J. Mater. Chem. A*, **2015**, *3*, 22886.

[34] Y. Chen, P. D. Tran, P. Boix, Y. Ren, S. Y. Chiam, Z. Li, K. Fu, L. H. Wong and J. Barber, *ACS nano*, **2015**, *9*, 3829.

[35] U. Sim, T.-Y. Yang, J. Moon, J. An, J. Hwang, J.-H. Seo, J. Lee, K. Y. Kim, J. Lee, S. Han, B. H. Hong and K. T. Nam, *Energy Environ. Sci.*, **2013**, *6*, 3658.

[36] Q. Ding, J. Zhai, M. Cabán-Acevedo, M. J. Shearer, L. Li, H.-C. Chang, M.-L. Tsai, D. Ma, X. Zhang, R. J. Hamers, J.-H. He and S. Jin, *Adv. Mater.*, **2015**, *27*, 6511.

[37] M.-L. Tsai, S.-H. Su, J.-K. Chang, D.-S. Tsai, C.-H. Chen, C.-I. Wu, L.-J. Li, L.-J. Chen and J.-H. He, *ACS nano*, **2014**, *8*, 8317.

[38] L. Ji, M. D. McDaniel, S. Wang, A. B. Posadas, X. Li, H. Huang, J. C. Lee, A. A. Demkov, A. J. Bard, J. G. Ekerdt and E. T. Yu, *Nature Nanotechnol.*, **2015**, *10*, 84.

[39] K. F. Mak, C. Lee, J. Hone, J. Shan and T. F. Heinz, *Phys. Rev. Lett.*, **2010**, *105*, 136805.

[40] J. Reyes-Gasga, S. Tehuacanero and M. J. Yacamán, *Microsc. Res. Techniq.*, **1998**, *40*, 2.

[41] A. J. Ritenour, J. W. Boucher, R. DeLancey, A. L. Greenaway, S. Aloni and S. W. Boettcher, *Energy Environ. Sci.*, **2015**, *8*, 278.

[42] M. Malizia, B. Seger, I. Chorkendorff and P. C. K. Vesborg, *J. Mater. Chem. A*, **2014**, *2*, 6847.

[43] L. Gao, Y. Cui, J. Wang, A. Cavalli, A. Standing, T. T. T. Vu, M. A. Verheijen, J. E. M. Haverkort, E. P. A. M. Bakkers and P. H. L. Notten, *Nano Lett.*, **2014**, *14*, 3715.

[44] C. G. Morales-Guio, L. Liardet, M. T. Mayer, S. D. Tilley, M. Grätzel and X. Hu, *Angew. Chem. Int. Ed.*, **2015**, *54*, 664.

[45] Y. Huang, Y.-E. Miao, J. Fu, S. Mo, C. Wei and T. Liu, *J. Mater. Chem. A*, **2015**, *3*, 16263.

[46] L. Yang, K. Majumdar, H. Liu, Y. Du, H. Wu, M. Hatzistergos, P. Y. Hung, R. Tieckelmann, W. Tsai, C. Hobbs and P. D. Ye, *Nano Lett.*, **2014**, *14*, 6275.

[47] C.-H. Lee, G.-H. Lee, A. M. van der Zande, W. Chen, Y. Li, M. Han, X. Cui, G. Arefe, C. Nuckolls, T. F. Heinz, J. Guo, J. Hone and P. Kim, *Nature Nanotech.*, **2014**, *9*, 676.

4.2. Tungsten disulfide thin films

4.2.1. Introduction

Energy conversion directly from solar energy to chemical bonds is one of the most attractive ways to overcome the global energy crisis.[1-3] Recently, the hydrogen (H_2) has received tremendous attention as an alternative to fossil fuels owing to its sustainability and minimal environmental impact. In this situation, the photoelectrochemical (PEC) water splitting is a promising approach for the sustainable production of hydrogen as a fuel from the sunlight. Among the various candidate semiconductors for PEC water splitting, *p*-type silicon (*p*-Si) which has a narrow bandgap of 1.1 eV can absorb wide range of wavelengths ranging from ultraviolet to near infrared.[4,5] It also has cost-efficiency and well-organized photovoltaic technologies. However, the *p*-Si has high overpotential at the interface of *p*-Si/electrolyte because of its poor hydrogen evolution reaction (HER) kinetics originating from the high hydrogen adsorption of Gibbs free energy. Furthermore, Si is thermodynamically vulnerable to photoactive dissolution.[6-8] To overcome the overpotential issue, the noble metal catalysts such as Pt, Pd, and Rh are generally used for HER catalyst.[9-11] Although these catalysts are effective to decrease the overpotential in PEC water splitting of *p*-Si, the scarcity and high cost of noble metal catalysts are critical challenges to overcome in research of alternative energy system development. Moreover, the most of noble metal catalysts are used in the form of nanoparticles, which are not able to prevent the surface of *p*-Si photocathode from the photocorrosion. Therefore, it is highly significant to develop the efficient and earth-abundant

photocatalysts, which can protect the surface of *p*-Si, to replace the noble metal catalysts.

Recently, two-dimensional transition metal disulfides (2D TMDs) such as molybdenum disulfide (MoS_2) and tungsten disulfide (WS_2) are one of the promising candidates for replacing noble metal catalysts due to their inherently high surface-to-volume ratios and the large number of catalytically active edge sites for HER.[12-15] These materials are generally synthesized by exfoliation, solution-based method, and chemical vapor deposition (CVD). Even though the TMD nanoparticles synthesized by exfoliation or solution-based method have a lot of electrochemically active edge sites, it is difficult to obtain a uniform and dense thin film to cover the entire surface of *p*-Si. We used the CVD synthesis technique to overcome these limitations by synthesizing the homogeneous thin films which can protect the surface of *p*-Si. The synthesis of MoS_2 and WS_2 by using CVD techniques are mainly subdivided into three methods; i) thermolysis of solution precursors, ii) sulfurization of metal oxide thin films, and iii) vapor deposition of the powder precursors (sulfur and metal chlorides).[16-18] In the vapor deposition of powder precursors, it is difficult to make the uniform TMD thin films and thus the whole surface of a *p*-Si photocathode cannot be passivated by the TMD thin film. The MoS_2 thin film catalysts which were grown by simple thermolysis method have been reported that it can provide the relatively high photocurrent density and the lower overpotential compared to *p*-Si. Furthermore, it can be durably operated over 50 hours without any notable degradation.[19] However, the WS_2 thin film which is analogue of MoS_2 cannot be obtained by this method because the

coordination of ammonium tetrathiotungstate [$(NH_4)_2WS_4$] with any solvent is poor to make uniform precursor layers.[20] In this regard, the sulfurization of a WO_3 thin film is considered as the most favorable way to obtain uniform WS_2 thin film which act as the HER catalyst and passivation layer for *p*-Si photocathode. Although the sulfurization of WO_3 thin films have been demonstrated,[21-22] the application of the WS_2 thin film catalysts for the *p*-Si photocathode has not been reported to the best of our knowledge.

Here, we demonstrate that the WS_2 thin film catalysts synthesized by the simple sulfurization of WO_3 thin films can provide the low overpotential (0.18 V at 1 mA/cm^2) and high photocurrent density (8.37 mA/cm^2 at 0 V) via heterostructuring with *p*-Si photocathode. By changing the thickness of the WO_3 thin films, the thickness of the sulfurized WS_2 thin films could be controlled. Although all synthesized WS_2 thin film catalysts can improve the overpotential of *p*-Si, the 23-nm-thick WS_2 thin film catalysts (sulfurized from the WO_3 10-nm-thick film) shows the best performance among the all samples. The Faradaic efficiency of 23-nm-thick WS_2 thin film/*p*-Si heterojunction photocathode is over 90 %. The investigation of charge transport resistance by using electrochemical impedance spectroscopy (EIS) indicates that the 23-nm-thick WS_2 thin film catalysts can efficiently transport the photogenerated electrons from *p*-Si to electrolyte. These results clearly show the promising potential of WS_2 thin film catalyst synthesized by simple sulfurization of WO_3 thin films in the efficient PEC hydrogen production.

4.2.2. Experimental procedures

SiO_2 (300 nm)/Si wafers (1-10 Ω-cm, <100> plane, DASOMRMS Co., Ltd) were cleaned with a standard piranha solution (3:1 volume ratio of H_2SO_4, 95 % grade and H_2O_2, 30 % grade) with conventional cleaning procedures followed by ultrasonication in acetone, isopropyl alcohol, and deionized (DI) water. The DI water was purified by water purification system (Human Power, Human Co, Ltd., 18.3 MΩ-cm). The tungsten trioxide (WO_3, 99.995 % purity, Sigma-Aldrich, 204781) thin films with various thicknesses (5, 10, and 20 nm) were deposited by using thermal evaporator (KVE-T2000, Korea Vacuum Tech Co, Ltd). In order to synthesize the WS_2 thin films, we used the simple sulfurization process as following. The N_2 and H_2 (99.9999 %, high-purity) gases were used for the sulfurization process in a thermal chemical vapor deposition system (CVD). First, the CVD furnace temperature was raised to 700 °C and was maintained at this temperature for 50 min under flow of H_2 and N_2 at 1 Torr. The flow rate of H_2 and N_2 was set at 40 and 200 cm^3/min, respectively, by using mass flow controllers (MKS Co., Ltd, Type 1479A). Then, sublimation of sulfur power (99.998 %, Sigma-Aldrich, 213292) precursor was initiated in the other heating zone, whose temperature was set at 300 °C. This process was kept for 1 hour for the successful sulfurization of WO_3 thin films. Once the sulfurization process was completed, the [poly(methyl methacrylate)] (PMMA, GPC 10000, Sigma-Aldrich, 81497) dissolved in chlorobenzene (99.5 % purity, Sigma-Aldrich, 319996) with concentration of 2 g / 50 mL was spin-coated onto the CVD-grown thin films. The PMMA/thin films/SiO_2/Si substrates were immersed in a buffered oxide etchant to separate the thin films from the

substrate by etching away the SiO_2 layers. The obtained thin films were washed with DI water seven to nine times to remove the residual etchants and were transferred to the arbitrary substrates. After the PMMA/thin film membranes had perfectly adhered onto the substrates, the PMMA layers were removed using hot acetone bath at 50 °C for 1 hour.

The PEC measurements (Ivium Technologies, Model: Nstat) were carried out with a three-electrode system using a saturated calomel electrode as the reference electrode and a graphite rod as the counter electrode in a 0.5 M H_2SO_4 standard electrolyte solution. We used a graphite rod counter electrode (WonATech Co., Ltd) to avoid the deposition of Pt on the working electrode. The three-electrode system was set up inside a quartz vessel, which protected the samples from UV absorption. The conversion equation of potentials vs. RHE is expressed as following equation:

$$E_{RHE} = E_{SCE} + E^{\circ}_{SCE} + 0.059 \times \text{pH} \quad (E^{\circ}_{SCE} = 0.242 \text{ vs. SHE}) \qquad (1)$$

where the E_{SCE} is potential of saturated calomel electrode, the $E°_{SCE}$ is potential of the saturated calomel electrode with respect to the standard hydrogen potential (SHE), and the pH is 0.5 M H_2SO_4 is 0.27. A Xe arc lamp (Abet Technologies, LS150) was used and calibrated to an output of 100 mW/cm^2 (AM 1.5 G condition). A scan rate of 10 mV/s was used for the linear sweep with cathodic direction. The incident-photon-to-current conversion efficiency (ICPE) was measured with a light source and a monochromator (DONGWOO OPTRON, MAC150) and the efficiency was calculated by following equation:

$$\text{IPCE}\ (\lambda) = EQE\ (\lambda) = \frac{|j_{ph}(mA/cm^2)| \times 1239.8\ (V \times nm)}{P_{mono}\ (mW/cm^2) \times \lambda\ (nm)} \qquad (2)$$

where the j_{ph} is photocurrent of the sample, the λ is wavelength, and the P_{mono} is the power of monochromator. The external quantum efficiency was measured with a standard Si photodiode. EIS was conducted by applying a constant potential of 0.27 V vs. RHE near the open-circuit potential. The sweeping frequency was varied from 250 kHz to 1 Hz using a 10 mV AC dither.

4.2.3. Results and Discussion

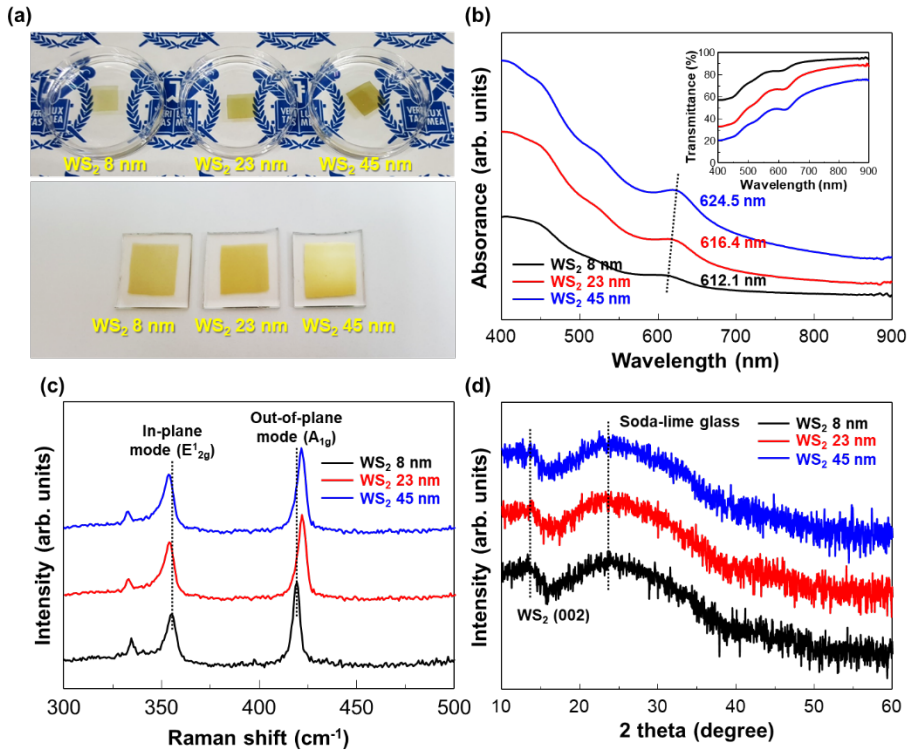

Fig. 4.22. Photographic images and characterization of synthesized WS_2 thin films. (a) The photographic images of synthesized WS_2 thin films floated onto de-ionized water bath and transferred to glass substrates. (b) Absorbance spectra and transmittance of synthesized WS_2 thin films. The inset figure shows the transmittance of WS_2 thin films. (c) Raman spectra of synthesized WS_2 thin films. (d) XRD analysis of synthesized WS_2 thin films on glass substrates.

The WS_2 thin films used in this study were synthesized by simple sulfurization of WO_3 thin films. The WO_3 thin films with various thicknesses (5, 10, and 20 nm) were deposited on cleaned SiO_2 (300 nm)/Si substrates by using thermal evaporator. To synthesize the WS_2 thin films, the simple sulfurization of WO_3 thin films was conducted by using thermal CVD system with the sublimation of sulfur power precursors. For the characterization of the synthesized thin films and their application as PEC catalyst, they had to be

transferred to substrates such as glass, *p*-Si, and SiO_2/Si wafers. The PMMA was used as the supporting polymer and was spin-coated onto the synthesized thin films for wet transfer. The photographic images of the synthesized thin films floated onto DI water bath and transferred on glass substrates are shown in Fig. 4.22(a). The yellow color of synthesized WS_2 thin films gradually changes to deep as a function of thickness of WO_3 precursor thin films. Fig. 4.22(b) shows that the absorbance spectra of WS_2 thin films prepared with different thickness of WO_3 thin films exhibit similar peak positions for each thin film. The excitonic absorption peaks attributing from the transition of direct gap at the K point of the Brillouin zone. The corresponding peaks are located at the wavelengths of 612, 616, and 624 nm for the 8-, 23-, and 45-nm-thick WS_2 thin films, respectively.[23] The optical absorption peak change originates from the variation of optical band gaps of synthesized thin films. These results are in good agreement with previously reported absorption spectra of the WS_2 thin film via other CVD methods.[23]

Raman spectroscopy is a general investigation method to detect the atomic vibrations in thin films, especially 2D layered materials. For a WS_2 thin film, the in-plane vibration (E^1_{2g}) appears near 355 cm^{-1}, while the out-of-plane vibration (A_{1g}) appears near 418 cm^{-1}.[24] The Raman spectra of the synthesized WS_2 thin films from sulfurization of WO_3 thin films with different thicknesses are shown in Fig. 4.22(c). The difference in frequencies between those two Raman modes of WS_2 thin films depends on the number of layers and can be easily used as a thickness indicator.[25] The frequency difference between E^1_{2g} and A_{1g} modes was approximately 64 cm^{-1}, indicating that the synthesized WS_2

thin film is multilayer. The peak gap between E^1_{2g} and A_{1g} gradually increased as a function of increase of WO_3 thin films precursor layer thickness. Fig. 4.22(d) shows the X-ray diffraction (XRD) patterns of the WS_2 thin films prepared with different WO_3 precursor layer thicknesses. Because the XRD measurement of synthesized thin films was conducted on soda-lime glass substrate, the broad peak near 23° was obtained in all the samples. The small peak, which is WS_2 (002) plane, near 13° appeared in the synthesized WS_2 thin films, regardless of the WO_3 precursor layer thicknesses.[26]

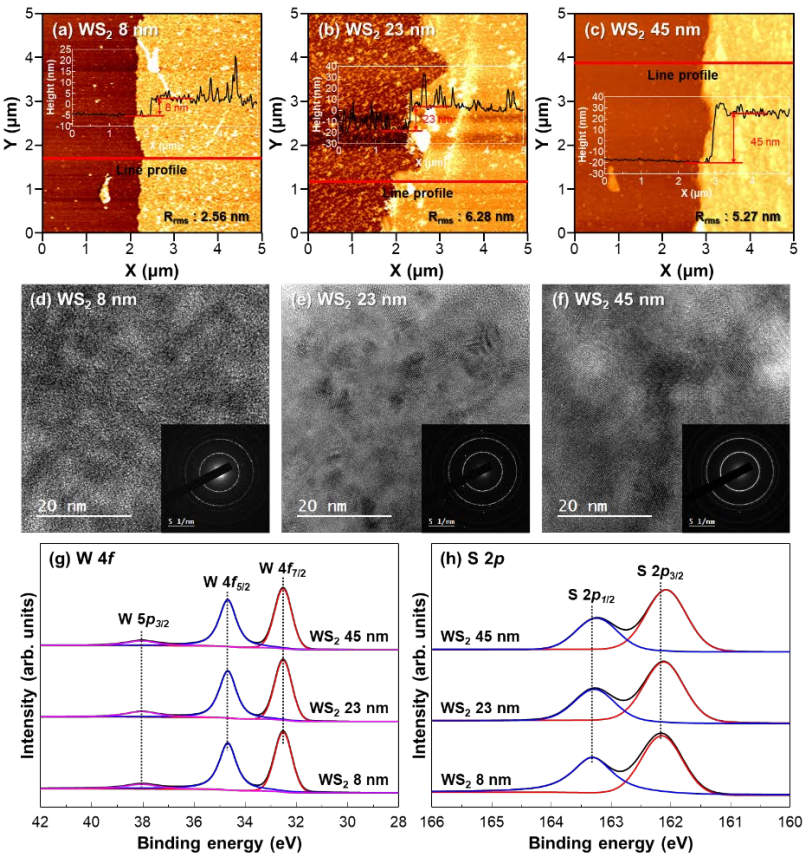

Fig. 4.23. (a)–(c) Atomic force microscopy images of synthesized WS_2 thin films by using sulfurization of different thickness of WO_3 thin films. (d)–(f) High-resolution transmission electron microscopy images of synthesized WS_2 thin films. The SAED pattern shows that the synthesized thin films were poly-crystalline. (g)–(h) The core level X-ray photoemission spectroscopy (W 4*f* and S 2*p*) analysis of synthesized WS_2 thin films.

To evaluate the thickness and surface morphology of the synthesized thin films, atomic force microscopy (AFM) was used as shown in Figs. 4.23(a)–(c). The thickness of synthesized WS_2 thin films increased from 8 to 45 nm when the thickness of WO_3 precursor thin layer increased from 5 to 20 nm. The increase of film thickness in each sample is attributed to the structure modification from 3D monoclinic WO_3 (space group of $P2_{1/n}$) to 2D hexagonal WS_2 (space group $P6_3/mmc$). The weak van der Waals bonds in the WS_2 thin films make the films thicker than the original 3D WO_3 thin films. All the synthesized thin films were nano-granular. The serrated-surface of the synthesized thin films with different thickness provides a large surface area than the atomically flat surface of a single-crystalline WS_2 layer. The root-mean-square (RMS) roughness was 2.6 nm for the 8 nm-thick WS_2 thin films fabricated with the sulfurization from 5 nm-thick WO_3 film. The RMS roughness increased from 2.6 to 6.2 nm. These increased RMS roughness values could help enhancing the catalytic activity due to the increase of surface area of synthesized 23 nm-thick WS_2 thin films. Figs. 4.23(d)–(f) shows the high-resolution transmission electron microscopy (HR-TEM) images of synthesized WS_2 thin films. The periodic atomic arrangements of the WS_2 thin films are obtained and the selected area electron diffraction (SAED) patterns reveal a hexagonal structure with poly-crystalline. Furthermore, the pin-hole free WS_2 thin films which can protect the dissolution of *p*-Si photocathode were successfully synthesized by using simple sulfurization method. These results indicate that the poly-crystalline WS_2 thin films were synthesized by sulfurization of WO_3 films. In order to investigate the chemical components

and atomic ratios of the synthesized thin films, the X-ray photoemission spectroscopy (XPS) was conducted as shown in Figs. 4.23(g) and (h). For the WS_2 thin films with different thicknesses, the atomic ratio of W to S was constant at 65 % to 35 %, regardless of the WO_3 precursor thicknesses. Five peaks appear at 32.4, 34.6, 38, 162, and 163.3 eV in the synthesized WS_2 thin films, which are assigned to W $4f_{7/2}$, W $4f_{5/2}$, W $5p_{3/2}$, S $2p_{3/2}$, and S $2p_{1/2}$, respectively. These results are well-consistent with the findings of previous reports on WS_2 crystals.[27]

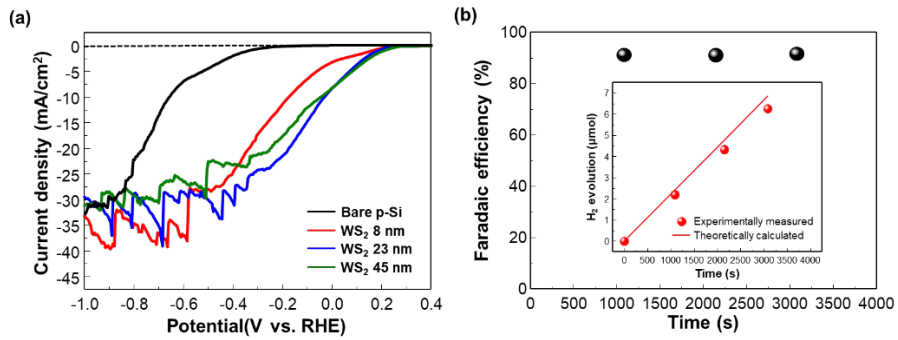

Fig. 4.24. Photoelectrochemical hydrogen evolution reaction performances of the WS_2 thin films on *p*-type Si photocathodes with different thickness. (a) Linear-sweep voltammetry curves of WS_2 thin film catalysts/*p*-Si heterojunction photocathodes. (b) Faradaic efficiency measurements for the 23-nm-thick WS_2/*p*-Si photocathode under illumination at 0 V vs. RHE with 0.5 M H_2SO_4 electrolyte. The inset graph shows the amount of H_2 evolved as a function of the calculated amount of H_2 by the passed charge.

The PEC measurement of the WS_2/*p*-Si heterostructure photocathodes was conducted using a 3-electrode cell with 0.5M sulfuric acid (H_2SO_4) as the HER electrolyte.[28] We employed a saturated-calomel electrode as reference electrode and a graphite rod as counter electrode. Fig. 4.24(a) displays linear-sweep voltammetry (LSV) measurements under a solar simulated light source (air mass 1.5G). The dashed lines show the result of LSV measurement without light. We set the potential when the photocurrent density reaches -1 mA/cm^2 as

the onset potential. The large negative onset potential of -0.35 V was observed for the bare *p*-Si photocathode. As mentioned in introduction, the bare *p*-Si requires an additional overpotential due to the carrier concentration and kinetics issue.[6-8] The 23-nm-thick WS_2/*p*-Si photocathode exhibited the lowest onset potential of 0.2 V. For the 23-nm-thick WS_2/*p*-Si photocathode, the anodic shift of the onset potential was 0.63 V with regard to that of the bare *p*-Si. The PEC performances with photocurrent density at 0 V and potential at 20 mA/cm^2 were summarized in Table 4.3.

Table 4.3. The summarized PEC performances of WS_2/*p*-Si heterojunction photocathodes.

Photocathodes	Current density (mA/cm^2) at 0 V	Potential (V) at 20 mA/cm^2
Bare *p*-Si	0.013	+ 0.685
WS_2 8 nm/*p*-Si	3.179	+ 0.176
WS_2 23 nm/*p*-Si	8.375	+ 0.024
WS_2 45 nm/*p*-Si	8.302	+ 0.045

It is well-known that the edges of 2D TMD materials could act as catalytic active sites. The nano-serrated surface of the synthesized WS_2 thin films as displayed in Figs. 4.23(a)-(c) should contain a number of active sites. The RMS roughness values of the 23- and 45-nm-thick WS_2 thin film shows the higher value (6.3 nm and 5.3 nm) than the that of 8-nm-thick WS_2 thin film (2.6 nm), indicating that the thicker WS_2 thin films have the plenty of catalytic edge sites and a large surface area. For this reason, the photocurrent densities of the 23- and 45-nm-thick WS_2/*p*-Si photocathodes at 0 V (vs. reversible hydrogen electrode (RHE)) showed the higher values of 8.3 and 8.2 mA/cm^2 than that of

the 8-nm-thick WS_2/*p*-Si photocathode (3.2 mA/cm^2). Meanwhile, the saturation photocurrent density of the 45-nm-thick WS_2 thin film/*p*-Si photocathode is lower than the other photocathodes due to its lower transmittance, as shown in the inset of Fig. 4.22(b). These results obviously display that the PEC performances of the WS_2/*p*-Si photocathodes rely on the thickness of the WS_2 thin film and that an optimum WS_2 thin-film thickness exists.

To elucidate the Faradaic efficiency for H_2 evolution of the WS_2 23 nm/*p*-Si photocathode, we conducted gas chromatography measurements at constant voltage of 0 V vs. RHE under continuous illumination. The H_2 evolution was monitored several times at intervals of 15 ~ 20 minutes. The inset graph of Fig. 4.23(b) displays the relation between the amount of evolved H_2 and the calculated amount of H_2 by the passed charge. Although the straight line does not exactly fit into the data point, but the Faradaic efficiency represents over 90 % (Fig. 4.23(b)) which suggests that most of the measured current goes toward H_2 evolution.

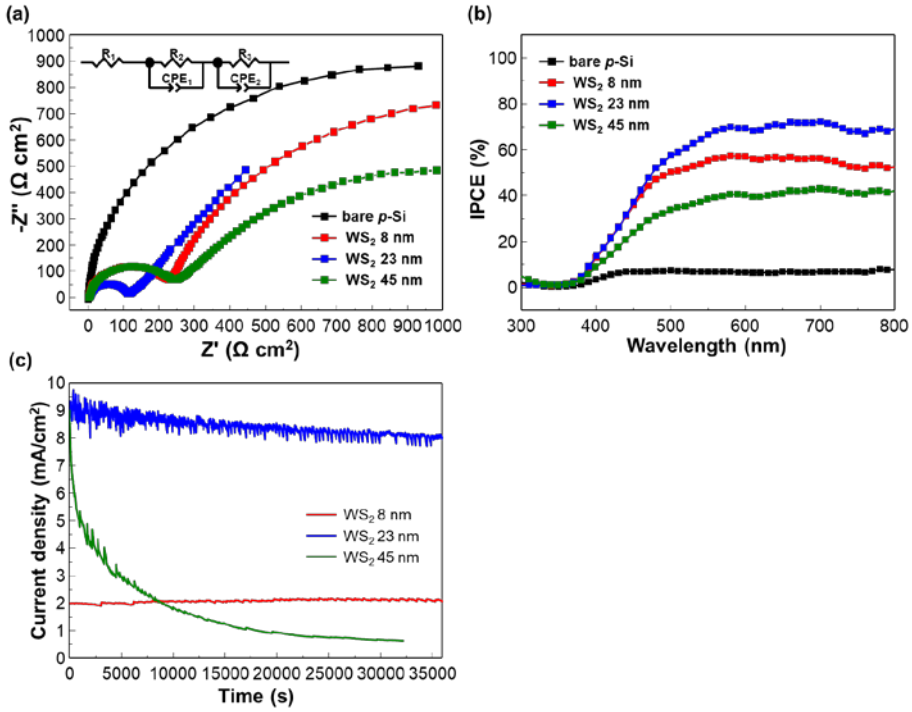

Fig. 4.25. Investigation of photoelectrochemical hydrogen evolution reaction performances for the synthesized WS_2 thin films/*p*-Si heterojunction photocathodes. (a) Electrochemical impedance spectroscopy analysis of fabricated WS_2/*p*-Si photocathodes. (b) Incident-photon-to-current-efficiency curves of fabricated WS_2/*p*-Si photocathodes. (c) Chronoamperometric curves of 8-, 23-, and 45-nm-thick WS_2 thin films/*p*-Si photocathodes for 10 hours. The 23-nm-thick WS_2 can maintain the 83 % of initial photocurrent density even after 10 hours.

Fig. 4.25(a) shows Nyquist plots of the electrochemical impedance spectroscopy (EIS). The charge transfer resistances (R_{ct}) could be determined using a simplified equivalent circuit. The low R_{ct} at each interface appears in the small semicircular arc in the Nyquist plot. The semicircular arcs which correspond to R_{ct} were considerably reduced as the thickness of WS_2 thin films increased from 8 to 23 nm. This decrease in the semicircular arc was affected by the enhancement of the thin film quality with the increase of WS_2 thin film thickness. The 23-nm-thick WS_2/*p*-Si photocathode exhibited the smallest R_{ct}

value that is smaller than one order of magnitude compared to the other WS_2/*p*-Si photocathodes, as displayed in Table 2.

Table 4.4. The summarized charge transport resistance values of various thicknesses WS_2/*p*-Si photocathodes.

Photocathodes	$R_{ct,1}$ (Ω cm^2)	$R_{ct,2}$ (Ω cm^2)	$R_{ct,3}$ (Ω cm^2)
	contact/*p*-Si	*p*-Si/TF[1]	TF/EL[2]
Bare *p*-Si	1.17	4810[3]	N/A
WS_2 8 nm/*p*-Si	3.20	1843.30	228.59
WS_2 23 nm/*p*-Si	5.07	1347.50	83.79
WS_2 45 nm/*p*-Si	3.92	1721.49	223.48

[1]TF: Thin Film, [2]EL: Electrolyte, [3]*p*-Si/electrolyte

We evaluated the incident-photon-to-current conversion efficiency spectra of the WS_2/*p*-Si photocathodes at 0 V vs. RHE as illustrated in Fig. 4.25(b). Among the WS_2/*p*-Si photocathodes, the highest efficiency over 60% was obtained by the 45-nm-thick WS_2/*p*-Si photocathode at long wavelengths (660 – 730 nm). This phenomenon originates from a decrease in the band gap of the WS_2 thin film as the thickness of the WS_2 thin film becomes thicker. Meanwhile, the areas under the IPCE curve of 23- and 45-nm-thick WS_2/*p*-Si photocathodes are almost similar, in accordance with the similar photocurrent densities at an applied bias of 0 V vs. RHE.

We investigated the long-term stability of the WS_2/*p*-Si photocathodes using chronoamperometric measurements as shown in Fig. 25(c), in order to examine whether our WS_2 thin film catalysts could carry out a role as a passivation layer of *p*-Si. For the 23-nm-thick WS_2 thin film, the degradation of the photocurrent

density at 0 V vs. RHE was significantly suppressed, maintaining 83 % of initial current for 10 hours. Even though the 8-nm-thick WS_2 thin film catalyst shows the lowest catalytic activity among the three samples, it can be maintained the initial photocurrent density at 0 V vs. RHE over 10 hours due to the relatively strong adhesion between the *p*-Si and the its bottom layer. On the other hand, the severe photocurrent degradation can be observed in the 45-nm-thick WS_2 thin film catalyst.

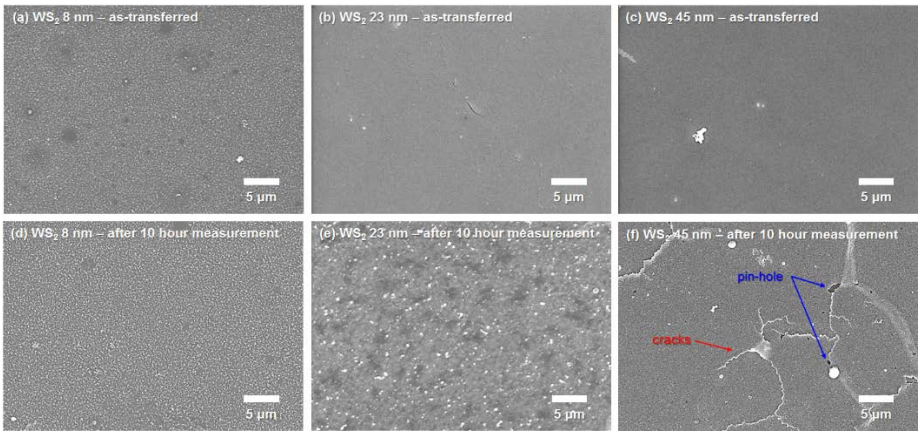

Fig. 4.26. The top-view field-emission scanning electron microscopy (FE-SEM) images of as-transferred and chronoamperometry measured (for 10 hours) samples for 8-, 23-, 45-nm-thick WS_2 thin films on *p*-Si. In the case of the 45-nm-thick WS_2 thin film catalyst, the thin film significantly degraded after 10 hour chronoamperometry measurement.

To check the surface morphologies of the as-transferred and the chronoamperometry measured samples, field-emission scanning electron microscopy (FE-SEM) was conducted for 8-, 23-, and 45-nm-thick WS_2 thin film catalysts, as shown in Fig. 26. For the as-transferred samples, the clean and flat surface without pin-holes was observed. However, the surface of the 45-nm-thick WS_2 thin film was significantly damaged by the catalytic reaction, while the 8- and 23-nm-thick WS_2 thin films maintained the flat surface without

pin-holes. This result is attributed to the fact that the thicker 2D material have the weaker van der Waals force in its top layers. In this reason, the top layers of the 45-nm-thick WS_2 thin film could be easily exfoliated or damaged by the catalytic reaction.

4.2.4. Conclusion

We have demonstrated that the WS_2 thin film HER catalyst synthesized by simple sulfurization of WO_3 thin film for efficient PEC water splitting. The synthesized WS_2 thin film successfully transferred using the simple method to the target substrate. Thickness dependent PEC performance of WS_2 thin films was studied. The 23-nm-thick WS_2/*p*-Si heterojunction photocathodes showed excellent photocurrent density of 8.3 mA/cm^2 at 0 V with 72 % of incident photon-to-current conversion efficiency. The onset potential of bare *p*-Si is shifted from -0.35 V to 0.2 V due to WS_2 thin film HER catalyst. The WS_2/*p*-Si photocathode can be stable for a longer time in the liquid electrolyte while generating hydrogen. The WS_2 thin film HER catalysts could be the one of the promising candidates for reducing the overpotential of bare *p*-Si as well as for protecting from photo-electrochemical corrosion.

4.2.5. References

[1] S. Dunn, *Int. J. Hydrog. Energy*, **2002**, *27*, 235.

[2] J. D. Holladay, J. Hu, D. L. King, and Y. Wang, *Catal. Today*, **2009**, *139*, 244.

[3] J. R. Rostrup-Nielsen and T. Rostrup-Nielsen *Cattech*, **2002**, *6*, 150.

[4] X. Chen, S. Shen, L. Guo and S. S. Mao, *Chem. Rev.*, **2010**, *110*, 6503.

[5] F. E. Osterloh and B. A. Parkinson, *MRS Bulletin*, **2011**, *36*, 17.

[6] S. Y. Reece, J. A. Hamel, K. Sung, T. D. Jarvi, A. J. Esswein, J. J. H. Pijpers and D. G Nocera, *Science*, **2011**, *334*, 345.

[7] M. G. Walter, E. L. Warren, J. R. McKone, S. W. Boettcher, Q. Mi, E. A. Santori and N. S. Lewis, *Chem. Rev.*, **2010**, *110*, 6446.

[8] N. C. Strandwitz, D. B. Turner-Evans, A. D. Tamboli, C. T. Chen, H. A. Atwater and N. S. Lewis, *Adv. Energy. Mater.*, **2012**, *2*, 1109.

[9] L. Zhu, H. Lin, Y. Li, F. Liao, Y. Lifshitz, M. Sheng, S.-T. Lee and M. Shao, *Nat. Comm.*, **2016**, *7*, 12272.

[10] M. Li, Q. Ma, W. Zi, X. Liu, X. Zhu and S. Liu, *Sci. Adv.*, **2015**, *1*, e1400268.

[11] J. Kye, M. Shin, B. Lim, J.-W. Jang, L. Oh and S. Hwang, *ACS Nano*, **2013**, *7*, 6017.

[12] D. M. Andoshe, J.-M. Jeon, S. Y. Kim and H. W. Jang, *Electron. Mater. Lett.*, **2015**, *11*, 323.

[13] K. C. Kwon, C. Kim, Q. V. Le, S. Gim, J.-M. Jeon, J. Y. Ham, J.-L. Lee, H. W. Jang and S. Y. Kim, *ACS Nano*, **2015**, *9*, 4146.

[14] Q. Ding, J. Zhai, M. Cabán-Acevedo, M. J. Shearer, L. Li, H.-C. Chang, M.-L. Tsai, D. Ma, X. Zhang, R. J. Hamers, J.-H. He, S. Jin, *Adv. Mater.*, **2015**, *27*, 6511.

[15] Q. Ding, F. Meng, C. R. English, M. Cabán-Acevedo, M. J. Shearer, D. Liang, A. S. Daniel, R. J. Hamers, S. Jin, *J. Am. Chem. Soc.*, **2014**, *136*, 8504.

[16] Q. Ding, B. Song, P. Xu, S. Jin, *Chem* **2016**, *1*, 699.

[17] R. Morrish, T. Haak and C. A. Wolden, *Chem. Mater.*, **2014**, *26*, 3986.

[18] G. V. Bianco, M. Losurdo, M. M. Giangregorio, A. Sacchetti, P. Prete, N. Lovergine, P. Caperzzuto and G. Bruno, *RSC adv.*, **2015**, *5*, 98700.

[19] K. C. Kwon, S. Choi, K. Hong, C. W. Moon, Y.-S. Shim, D. H. Kim, T. Kim, W. Sohn, J.-M. Jeon, C.-H. Lee, K. T. Nam, S. Han, S. Y. Kim and H. W. Jang, *Energy Environ. Sci.*, **2016**, *9*, 2240.

[20] P. K. Panigrahi and A. Pathak *Sci. Technol. Adv. Mater.*, **2008**, *9*, 045008.

[21] Q. Fu, W. Wang, L. Yang, J. Huang, J. Zhang and B. Xiang, *RSC adv.*, **2015**, *5*, 15795.

[22] C. Lan, C. Li and Y. Liu, *Nanoscale*, **2015**, *7*, 5974.

[23] A. K. Mishra, K. V. Lakshmi and L. Huang, *Sci. Rep.*, **2015**, *5*, 15718.

[24] A. Berkdemir, H. R. Gutiérrez, A. R. Botello-Méndez, N. Perea-López, A. L. Elías, C. Chia, B. Wang, V. H. Crespi, F. López-Urías, J.-C. Charlier, H. Terrones and M. Terrones, *Sci. Rep.*, **2013**, *3*, 1755.

[25] H. Li, Q. Zhang, C. C. R. Yap, B. K. Tay, T. H. T. Edwin, A. Olivier and D. Baillargeat, *Adv. Funct. Mater.*, **2012**, *22*, 1385.

[26] T. P. Nguyen, W. Sohn, J. H. Oh, H. W. Jang and S. Y. Kim, *J. Phys. Chem. C*, **2016**, *120*, 10078.

[27] Z.-Q. Xu, Y. Zhang, S. Lin, C. Zheng, Y. L. Zhong, X. Xia, Z. Li, P. J. Sophia, M. S. Fuhrer, Y.-B. Cheng and Q. Bao, *ACS Nano*, **2015**, *9*, 6178.

[28] T. P. Nguyen, S. Choi, J.-M. Jeon, K. C. Kwon, H. W. Jang and S. Y. Kim, *J. Phys. Chem. C*, **2016**, *120*, 3929.

4.3. Sulfur-doped molybdenum phosphide thin films

4.3.1. Introduction

The depletion of fossil fuels has raised a global concern regarding the energy crisis and environment. In recent years, hydrogen fuels have been widely investigated as sustainable and renewable alternatives to fossil fuels.[1-3] Most of the hydrogen is produced by steam reforming which generates carbon dioxide and consumes a large amount of electricity.[4-6] At present, hydrogen production through photoelectrochemical (PEC) water-splitting is being extensively studied as a potential sustainable fuel production method to meet the increasing energy demands. In the pursuit of developing efficient and durable photoelectrodes, *p*-type silicon (*p*-Si) has been widely studied as it is considered as one of the most promising candidates for photocathodes for hydrogen evolution reaction (HER) because of its absorption of wide ranges of the solar spectrum, earth abundance (low cost), and well-organized production technologies.[7-10]

However, the surface of *p*-Si has poor kinetics for absorbing protons (H^+) because of its high hydrogen adsorption Gibbs free energy (ΔG_H). This increases the overpotential between the surface of *p*-Si and electrolyte.[8-9] In addition to this overpotential issue, Si is thermodynamically vulnerable to photoactive dissolution or photocorrosion. To resolve the poor kinetics of *p*-Si surfaces, noble metals such as Pt, Ir, and Rh are widely used as HER catalysts.[11-13] Even though these catalysts are suitable for water splitting at low overpotentials, the scarcity, high cost, and maintenance of the high current density of

these materials are significant challenges in developing alternative energy systems. Furthermore, nanoparticle-shaped noble metal catalysts cannot prevent the photoactive dissolution of *p*-Si photocathodes.[14-16] As a consequence, the development of highly efficient earth abundant element-based photocatalysts has become imperative for replacing noble metal-based photocatalysts.

Two-dimensional transition metal disulfides (2D TMDs) such as MoS_2 and WS_2 are regarded as promising candidates to replace noble metal catalysts because TMD nanostructures inherently have large surface-to-volume ratios and possess high densities of catalytically active edge sites for HER.[17-21] It has been reported that the edge sites of MoS_2 could be more catalytically active than its basal plane.[22] In our previous study, MoS_2 thin film catalysts with c-domains of vertically stacked region exhibited excellent HER performances.[23] However, MoS_2 thin films mainly consist of a 2D layered structure, in which each layer is weakly bound to the adjacent layers by van der Waals forces. Although thick MoS_2 films exhibit good HER performance because of the presence of many active sites, their adhesion on *p*-Si photocathodes is poor owing to their weak van der Waals forces. Such a poor adhesion between MoS_2 layers and between the bottom MoS_2 layer and the *p*-Si substrate is not enough for the long-term stability of *p*-Si photocathodes. On the other hand, thin MoS_2 films adhere well onto *p*-Si substrates and exhibit a low catalytic activity owing to the lack of active sites.

Meanwhile, transition metal phosphides (TMPs) such as Ni_2P, CoP, MoP, and FeP also have attracted much attention as promising candidates to substitute Pt because of their high catalytic activity for HER and good stability.[24-26] Among these previously reported TMP catalysts, molybdenum phosphide (MoP) has been extensively investigated as an HER catalyst because it is a 3D hexagonal material and is a counterpart of 2D-layered MoS_2. Owing to their crystal structure, the inherent dangling bonds on the surface of thick MoP films facilitate their adhesion to *p*-Si substrates, indicating that long-term stability can be achieved even for thick MoP/*p*-Si heterojunction photocathodes. Furthermore, thick MoP films, which exhibit low ΔG_H as compared to MoS_2 basal plane and have many dangling bonds on their surface, have been reported to be good "H delivery" materials.[27] MoP catalysts have been successfully synthesized by various methods. Deng et al. synthesized 3D MoP sponges by sintering of ammonium molybdate tetrahydrate and ammonium hydrogen phosphate.[28] 3D MoP can act as both an electrode and a catalyst. Ye et al. synthesized a $MoS_{2(1-X)}P_X$ solid solution by mixing MoS_2 and red phosphorus powders.[27] An increase in the surface area of the $MoS_{2(1-X)}P_X$ solid solution led to an improvement in its HER activity. Even though 2D TMD and TMP nanoparticles show electrochemical HER catalytic activities, the photocorrosion of *p*-Si PEC catalysis cannot be prevented. Furthermore, to the best of our knowledge, the catalytic activity of phosphorus-doped MoS_2 (P:MoS_2) and sulfur-doped

molybdenum phosphide (S:MoP)-based thin film catalysts for photoelectrochemical HER has not been reported yet.

Here, we demonstrate the wafer-scale fabrication of S:MoP/*p*-Si heterojunctions by using a thin-film transfer method for highly efficient photoelectrochemical hydrogen production. By controlling the S/P powder precursor ratios, P:MoS_2 and S:MoP thin films were synthesized by simple thermolysis of an ammonium tetrathiomolybdate [$(NH_4)_2MoS_4$] solution precursor on SiO_2/Si substrates. The P:MoS_2 and S:MoP thin films layers were transferred to a *p*-Si photocathode (see the Experimental Section for details). The synthesized thin films with different S/P ratios gradually transformed from 2D-layered MoS_2 (S) to P:MoS_2 (S-rich, S/P = 3, S/P = 1) and 3D hexagonal S:MoP (P-rich, S/P = 0.33, P). At an S/P ratio of 0.33, the photocurrent density at 0 V reached the peak value of 33.13 mA/cm^2. At a photocurrent (J_{ph}) of 1 mA/cm^2, the onset potential of the film shifted by 0.65 V with respect to that of a bare *p*-Si photocathode. This is one of the highest overpotential reduction value reported till date for HER catalysts without noble metals. The energy band diagram clearly showed that metallic S:MoP thin film catalysts can efficiently transport the photogenerated electrons from *p*-Si to the electrolyte interfaces. The density-functional-theory (DFT) calculations also revealed that thermo-neutral hydrogen adsorption on the S:MoP surface may account for the efficient HER.

4.3.2. Experimental procedures

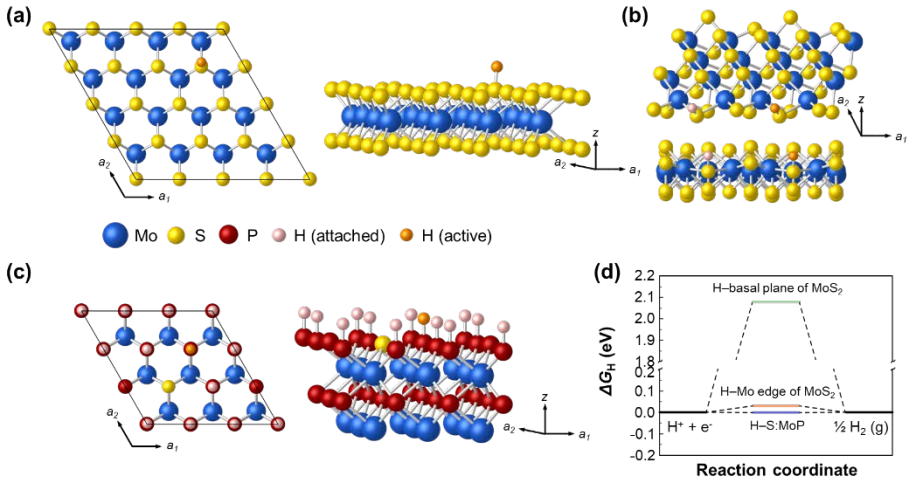

Fig. 4.27. Hydrogen adsorption energies obtained from the DFT calculation. (a) Basal plane of MoS_2, assuming θ = ~0. (b) $(10\bar{1}0)$ Mo-edge, H coverage θ = 0.5. (c) S:MoP surface, θ = 0.875. (d) Free energy diagram of H adsorption on the edge sites, i) basal plane of MoS_2, ii) Mo-edge of MoS_2, and iii) surface of S:MoP.

DFT calculations. The density functional theory (DFT) calculations using the Vienna *Ab initio* Simulation Package (VASP) code based on the projector augmented wave (PAW) pseudopotential.[44-45] The cutoff energy for the plane-wave basis set was chosen to be 400 eV, and we used k-space meshes of 4×4×1 for MoPS and MoS_2 basal plane, and 2×1×1 for MoS_2 edge for the supercells in Fig. 4.27. The ionic configurations were relaxed until the atomic forces are reduced to within 0.02 eV/Å. The zero-point energy of the H atom was included, and the entropy of H_2 gas was obtained from a thermodynamic table.

MoS_2, P:MoS_2, and S:MoP thin films synthesis. SiO_2 (300 nm)/Si wafers were cleaned with a standard piranha solution (3:1 mixture of H_2SO_4 and H_2O_2) by conventional cleaning procedures followed by

ultrasonication in acetone, isopropyl alcohol, and deionized (DI) water. To obtain hydrophilic surfaces on the SiO_2/Si wafers, O_2 plasma and UV-O_3 surface treatments were sequentially performed for 15 min, respectively. The precursor solution was prepared by dissolving $(NH_4)_2MoS_4$ powder (Sigma-Aldrich, 99.97% purity) in ethylene glycol (Sigma-Aldrich, 99.8% purity, anhydrous) at a concentration of 500 mM. The precursor solution was spin-coated onto the prepared SiO_2/Si substrate at 3500 rpm for 60 s. High-purity H_2 and N_2 gases were used for the thermolysis process in a thermal chemical vapor deposition (CVD) system. First, the CVD chamber temperature was increased to 500 °C and was maintained at this temperature for 30 min under the flow of H_2 and N_2 at 1 Torr. The flow rate of H_2 and N_2 was set at 40 and 200 cm^3/min, respectively, by mass flow controllers. The thermolysis process was started slowly under a H_2 gas atmosphere and at a relatively high temperature. Then, the temperature of the CVD furnace was increased to 950 °C and was maintained for 1 h. The sublimation of powder precursor, which have particular weight ratios (S, S/P = 3, S/P = 1, S/P = 0.33, P) of sulfur to phosphorus powder (S: Sigma-Aldrich, 99.5% purity, P: Sigma-Aldrich, 99.9%), was initiated in the other heating zone, whose temperature was set at 400 °C. Once the thermolysis was complete, PMMA was spin-coated onto the CVD-grown thin films. The edges of the synthesized thin films were scratched by a razor blade to promote the rapid separation of the synthesized thin films from the SiO_2/Si substrate. The PMMA/thin films/SiO_2/Si substrate was immersed in a buffered

oxide etch (BOE, Sigma-Aldrich, 40%) to separate the thin films from the substrate by etching away the SiO_2 layers. The obtained thin films were washed with deionized water seven to nine times to remove the residual etchants and were transferred to an arbitrary substrate (glass, SiO_2, gold, or *p*-Si substrates). After the PMMA/thin film membranes had perfectly adhered to the substrates, the PMMA layers were removed using acetone and toluene at 50 °C for 1 h.

Materials Characterization. The Raman spectra of the synthesized thin films were recorded with a Lab RAM HR (Horiba JobinYvon, Japan) at an excitation wavelength of 532 nm. The non-contact-mode AFM (XE-100, Park Systems) measurements at a scanning rate of 0.5 Hz were performed to examine the surface morphology and to determine thickness of the synthesized MoS_2 thin films. Synchrotron radiation photoelectron spectroscopy experiments were carried out in an ultra-high vacuum chamber (base pressure of ca. 10^{-10} Torr) with a 4D beam line, equipped with an electron analyzer and a heating element at the Pohang Acceleration Laboratory. The onset of photoemission corresponding to the vacuum level at the surface of the MoS_2 thin films was measured by applying an incident photon energy of 350 eV with a negative bias on the sample. The results were corrected for the charging effects using Au 4*f* as an internal reference. The bright-field and high-resolution TEM (JEOL JEM-2100F, 200 kV) images were obtained to investigate the microstructure of the synthesized thin films. The absorption spectra of the

synthesized thin films were measured by UV-Visible spectroscopy (JASCO-670).

PEC characterizations. The HER measurements (Ivium Technologies, Model: Nstat) were carried out with a three-electrode system using a saturated calomel electrode as the reference electrode and a graphite rod as the counter electrode in a 0.5 M H_2SO_4 standard electrolyte solution. The three-electrode system was set up inside a quartz vessel, which protected the samples from UV absorption. A Xe arc lamp was used and calibrated to an output of 100 mW/cm^2 (AM 1.5 G condition). For measuring the stability of each photocathode (i.e., bare *p*-Si, MoS_2 (S)/*p*-Si, and S:MoP (S/P = 0.33)/*p*-Si), we used a graphite rod counter electrode (WonATech Co., Ltd) to avoid the deposition of Pt on the working electrode. A scan rate of 10 mV/s was used for the linear sweep. The incident-photon-to-current conversion efficiency was measured with a light source and a monochromator. The quantum efficiency was measured with a standard Si photodiode. EIS was conducted by applying a constant potential of 0.27 V vs. RHE near the open-circuit potential. The sweeping frequency was varied from 250 kHz to 1 Hz using a 10 mV AC dither. The Faradaic efficiency was calculated by using a gas chromatography measurement system (FID-GC, PerkinElmer, NARL8502 Model 4003).

4.3.3. Results and Discussion

The hydrogen-evolution activity of a PEC catalyst strongly correlates with the energy required for chemisorption of atomic hydrogen at the catalytic site or the Gibbs free energy for the hydrogen binding (ΔG_H).[31,32] To evaluate the catalytic activity of S:MoP for HER, we conducted DFT calculations and obtained ΔG_H on the surface of S:MoP thin films using the following relations:

$$\Delta G_H = \Delta E_H + \Delta E_{ZPE} - T\Delta S \quad (1)$$

where ΔE_H is the internal energy of hydrogen adsorption, ΔE_{ZPE} is the zero-point energy, T is the temperature, and ΔS is the entropy change. ΔE_H is computed as follows:

$$\Delta E_H = E(*n\mathrm{H}) - E(*(n\text{-}1)\mathrm{H}) - \tfrac{1}{2}E(\mathrm{H_2}) \quad (2)$$

where $E(H_2)$ is the total energy of a hydrogen molecule and E(*nH) is the energy when n hydrogen atoms are bound at active sites. This means that ΔE_H depends on the H coverage (θ). When the hydrogen binding energy at a certain θ is negative, the equilibrium value of H coverage can be estimated from the adsorption isotherm as the upper value of the coverage.[33] That is to say, we assumed that the relevant H binding energy is at the average H coverage. The θ values for the MoS_2 basal plane, MoS_2 edge, and S:MoP surface were ~0, 0.5, and 0.875, respectively in the present models. The main results are shown in Fig. 4.27. For comparison, we also calculated ΔG_H on the basal plane and edge of MoS_2 system. According to the Sabatier's principle, a near-zero value of hydrogen binding energy is optimal for PEC catalysts so that H can be readily

attached to and detached from the catalyst surface to facilitate the reaction. From the computational results shown in Fig. 4.27(d), it is seen that S:MoP is more active than MoS_2 edges that are known to be active for HER, as well as the inert basal plane of MoS_2. The ΔG_H value (~ 0.05 eV) of the S:MoP thin film was much lower than that reported for $MoS_{(1-X)}P_X$ solid solution catalysts (~ 0.7 eV), in which a P atom is substituted into the MoS_2 lattice structure.[27] This marked change in ΔG_H can be attributed to the presence of many dangling bonds on the surface of S:MoP thin films. Our results clearly show that the 3D hexagonal P-rich S:MoP thin film could act as an efficient HER catalyst.

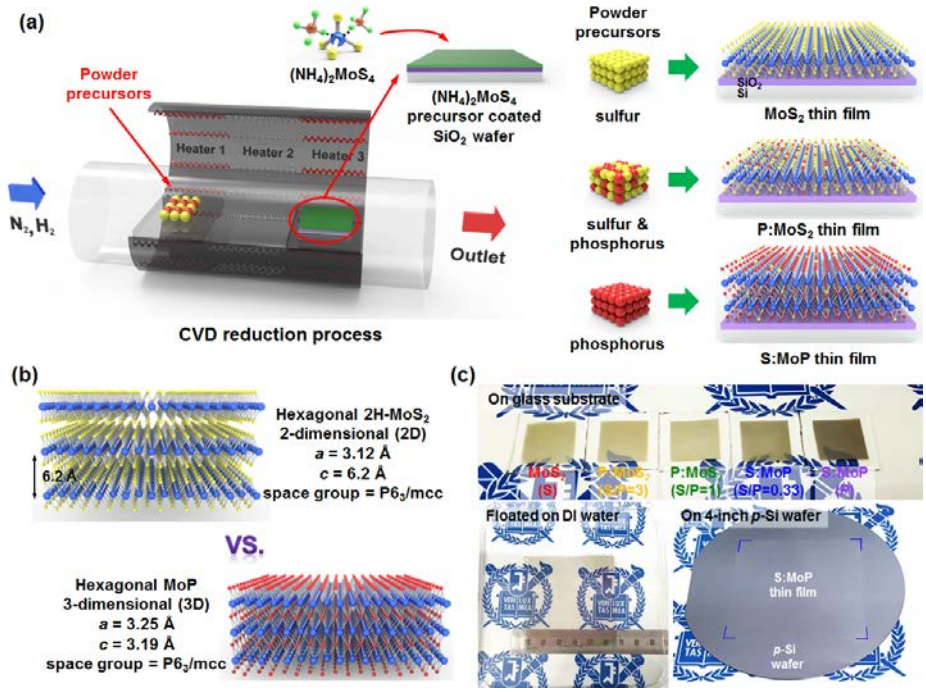

Fig. 4.28. Schematic of experimental procedures and photographic images of large-area synthesis of sulfur-doped molybdenum phosphide. (a) The synthetic procedure for sulphur-doped MoP thin film catalysts. (b) Atomic structures of MoS_2 and MoP. (c) Photographic images of the thin films transferred onto the glass substrate, floated onto a deionized water bath, and transferred onto a four-inch *p*-Si wafer.

The P:MoS_2 and S:MoP thin films used in this study were synthesized by simple thermolysis of an ethylene glycol solution of [$(NH_4)_2MoS_4$]. To elucidate the role of phosphorus substitution on the catalytic activity of MoS_2 thin film catalyst, a 500 mM [$(NH_4)_2MoS_4$] solution, which showed a moderate catalytic activity in our previous study, was used as the base precursor.[23] The schematic of the thermolysis method used in this study is shown in Fig. 4.28(a). The 500 mM [$(NH_4)_2MoS_4$] solution was spin-coated onto a SiO_2/Si substrate. By changing the S/P powder precursor ratio, the MoS_2 (S), P:MoS_2 (S-rich, S/P = 3 and S/P = 1), and S:MoP (P-rich, S/P = 0.33 and P) thin films were successfully synthesized. MoS_2 and MoP exhibit a hexagonal atomic structure ($P6_3/mmc$) in which a Mo atom is coordinated with six S and P atoms as displayed in Fig. 4.28(b). Since the lattice structures of MoS_2 and MoP are similar to each other,[34] the substitutional dopant P atoms could replace the S atoms in the [$(NH_4)_2MoS_4$] precursor layer during the growth step. Furthermore, the atomic radii of S and P are almost the same. Hence, P atoms can act as anions in hexagonal MoX_2 (X = S and P) without breaking its structure. MoS_2 surface is free of dangling bonds, while some inherent dangling bonds exist at the surface of MoP. Since dangling bonds are electrochemical active sites, MoP can act as an efficient HER catalyst. For the characterization of the synthesized thin films and their application as PEC catalysts, they had to be transferred to a substrate. Glass, *p*-Si, and SiO_2/Si are widely used as substrates for such films. Poly[methyl methacrylate] (PMMA) was used as the supporting polymer and was

spin-coated onto the synthesized thin films for wet transfer. The PMMA/thin films were separated from the SiO_2/Si substrates by immersing them in a bath of hydrogen fluoride and a buffered oxide etchant. Then, the separated films were transferred onto arbitrary substrates. The photographic images of the synthesized thin films transferred on glass substrates are shown in Fig. 4.28(c). The color of synthesized MoS_2 thin film, which was greenish-yellow, gradually turned black with an increase in the amount of phosphorus powder.

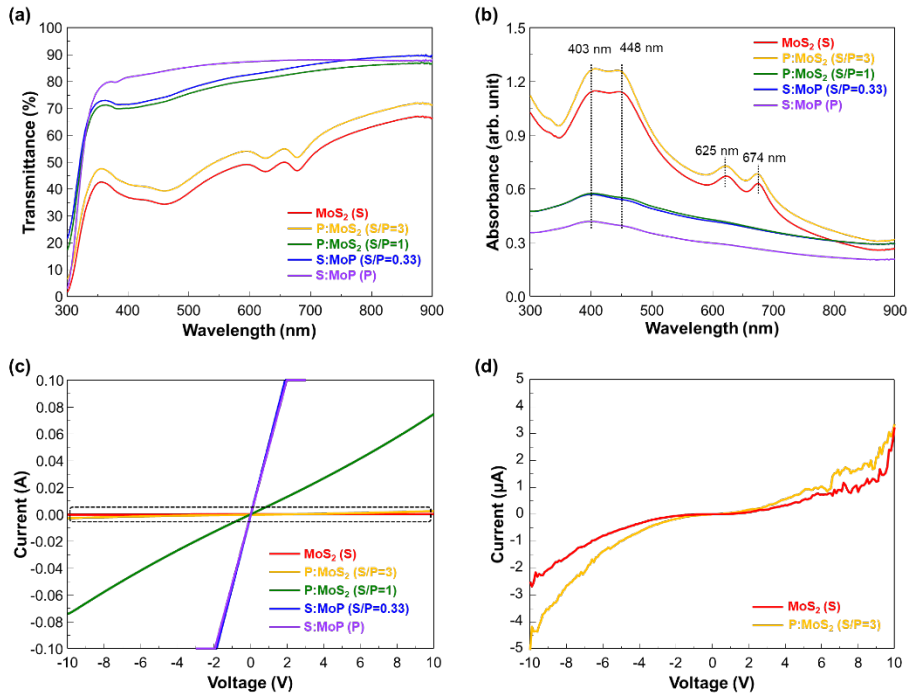

Fig. 4.29. Optical and electrical characterization of synthesized thin films. (a) Transmittance and (b) absorbance spectra of the thin films synthesized with different S/P powder precursor ratios. (c) The current-voltage (I-V) sweep data with 0.1 A compliance. (d) The magnified I-V curve of dashed region in the (c).

The transmittance of anion engineered MoS_2 thin films was gradually increased with respect to the increase of P amounts (Fig. 4.29). The absorbance and the current-voltage (*I-V*) sweep curve data clearly show that anion engineered MoS_2 thin films were drastically changed to the metallic S:MoP from the semiconducting MoS_2 (Fig. 4.29). Furthermore, the photographic images of the PMMA/S:MoP layer suspended in deionized water and a 6 cm × 6 cm S:MoP thin film suspended on a four-inch *p*-Si wafer are shown in Fig. 4.28(c).

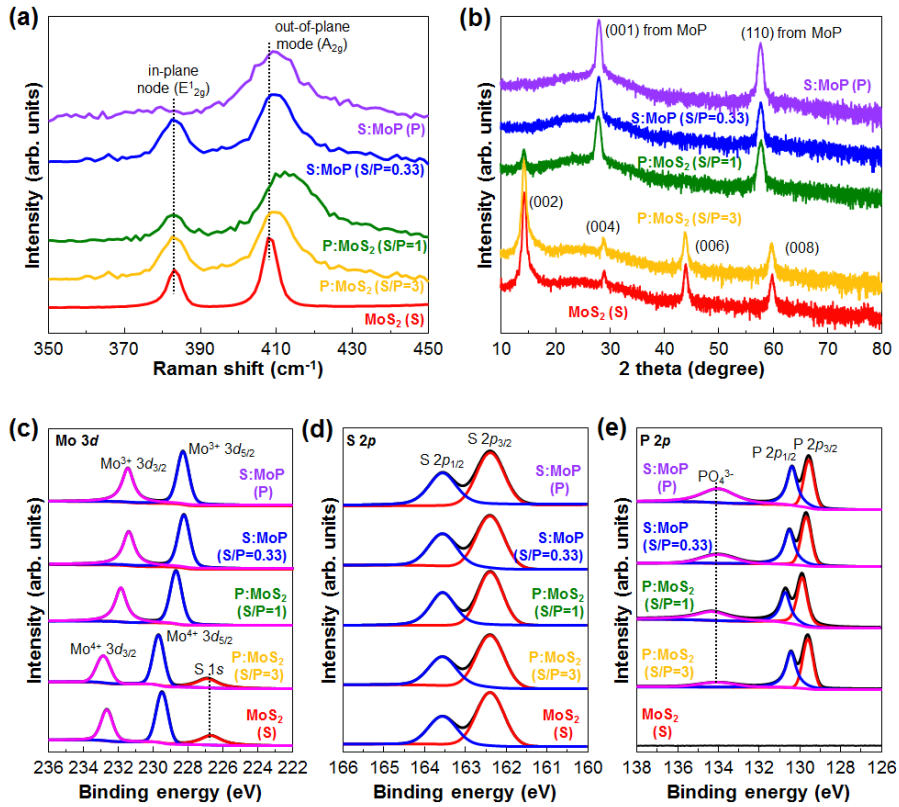

Fig. 4.30. Characterization of synthesized thin films grown by simple thermolysis method with various S/P ratios. (a) Raman spectra of the synthesized thin films. The E^1_{2g} peaks significantly reduced when the MoS_2 layer was doped with phosphorus. (b) XRD spectra of the synthesized thin films. The MoS_2 peaks disappeared at S:P = 1:1. XPS core level spectra of (c) Mo 3*d*, (d) S 2*p*, and (e) P 2*p* of the synthesized thin films.

Raman spectroscopy is a powerful tool to detect the atomic vibrations in thin films, especially 2D layered materials. For a MoS_2 layer, the in-plane vibration appears near 384 cm^{-1}, while the out-of-plane vibration appears near 410 cm^{-1}.[35] The Raman spectra of the MoS_2, P:MoS_2, and S:MoP thin films synthesized with different S/P powder precursor ratios are shown in Fig. 4.30(a). Two characteristic peaks, E^1_{2g} (in-plane vibration) and A_{1g} (out-of-plane vibration), appeared around 384 and 408 cm^{-1}, respectively. The frequency difference between these two Raman modes of MoS_2 thin films depends upon the number of layers and can be easily used as a thickness indicator.[35] The frequency difference between the E^1_{2g} and A_{1g} modes was approximately 24 cm^{-1}, indicating that the synthesized MoS_2 thin film had multilayers. With the incorporation of phosphorus into MoS_2, the A_{1g} peak slightly shifted to a higher wavenumber as a result of the softening of the A_{1g} vibrations. Furthermore, the full width at half maximum of the A_{1g} peak showed broadening in the range of 5.1–12.3 cm^{-1}. On the other hand, the E_{2g} peak disappeared when the concentration of phosphorus atoms was much larger than that of sulphur atoms in the S:MoP thin films. These observations are analogous to the results obtained in previous studies focusing on the surface charge transfer doping of MoS_2 and electrostatic doping of MoS_2 by a back-gate potential.[36,37] Fig. 4.30(b) shows the X-ray diffraction (XRD) patterns of MoS_2, P:MoS_2, and S:MoP. The XRD patterns of the thin films with S and an S/P ratio of 3 show the characteristic peaks of MoS_2. When the concentration of P was

comparable to or higher than that of S, the intensity of the MoS_2 peak decreased significantly and MoP peaks were observed, confirming the formation of simple hexagonal MoP thin films.[28,38] The chemical components and atomic ratios of the synthesized thin films were investigated using X-ray photoemission spectroscopy (XPS). The core level spectra of Mo 3*d*, S 2*p*, and P 2*p* were recorded (Figs. 4.30(c)–(e)). In the Mo 3*d* core level spectra, the Mo^{4+} $3d_{3/2}$ and Mo^{4+} $3d_{5/2}$ peaks slightly shifted to lower binding energies corresponding to the Mo^{3+} $3d_{3/2}$ and Mo^{3+} $3d_{5/2}$ peaks, confirming the successful transformation of MoS_2 into MoP structures. Furthermore, the peak intensity of S 1*s* in the Mo 3*d* core level spectra reduced significantly. The S 2*p* and P 2*p* core level spectra of each synthesized thin film were almost the same. Because the starting material i.e., $[NH_4]_2MoS_4$ contained S atoms, the S:MoP (P) thin film showed a S 2*p* peak. In the P 2*p* core level spectra, two types of peaks were observed: two sharp peaks near ~129 eV and a broad peak near ~134 eV. The broad peak near ~134 eV corresponds to PO_4^{3-} and is a characteristic peak for MoP exposed to air.[27] The intensity of the PO_4^{3-} peak gradually increased with an increase in the weight ratio of P. The atomic ratio of Mo to S was constant at 33.2 % to 67.8 %. This is consistent with previous reports (Fig. 4.31).[34]

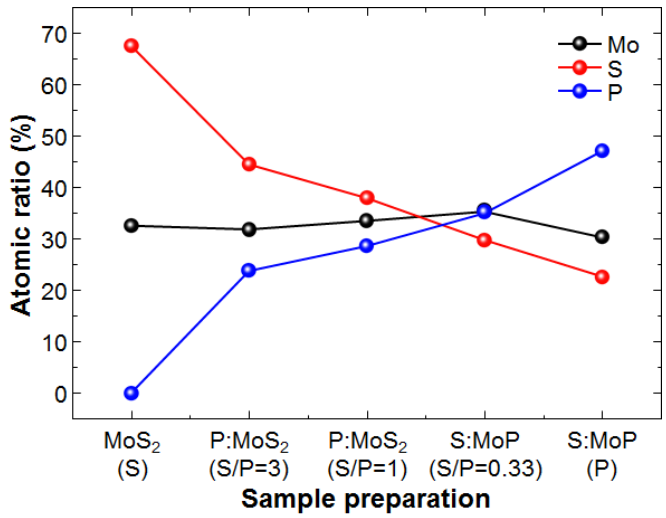

Fig. 4.31. The XPS atomic ratio of synthesized thin films as a function of the S/P powder precursor ratio.

The atomic ratio of P in the MoS_2 thin films increased gradually with the introduction of P into them. Furthermore, the atomic ratio of P became higher than that of S at S/P = 0.33, indicating that the synthesized thin film with only P powder precursor was a P-rich S-doped MoP thin film. Based on these measurements, the P-doped MoS_2 and S-doped MoP thin films were successfully synthesized by the thermolysis of the $[(NH_4)_2MoS_4]$ solution precursor and mixed power precursors with different S/P ratios.

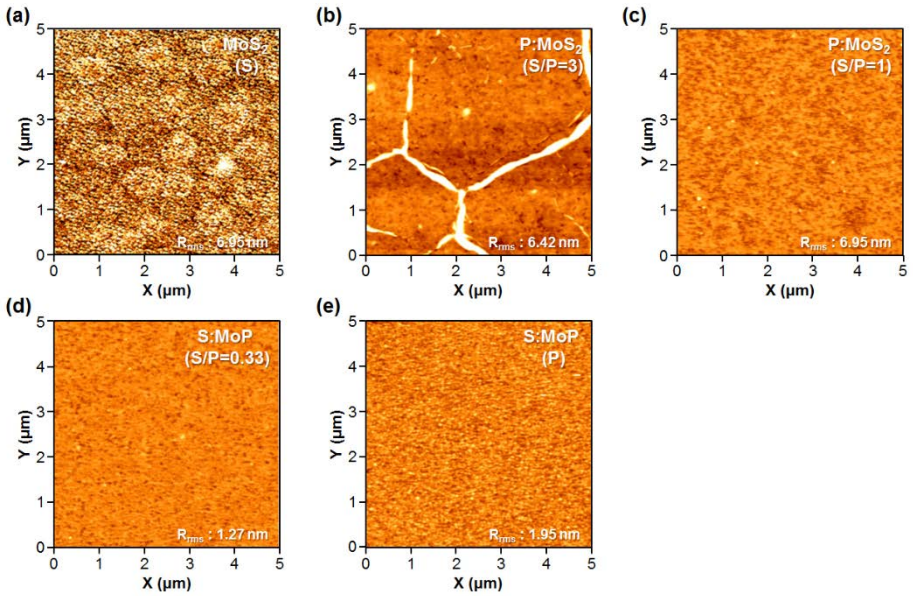

Fig. 4.32. AFM images of the thin films synthesized with different S/P powder precursor ratios. Nano-granular surfaces were observed in each thin film.

To evaluate the thickness and surface morphology of the synthesized films, atomic force microscopy (AFM) was used. All the synthesized thin films were nano-granular (Fig. 4.32). The serrated surface of the synthesized films with different powder precursors provided a larger surface area than the atomically flat surface of a single-crystalline MoS_2 layer. The root-mean-square (RMS) roughness was 3 nm for the MoS_2 thin film. The RMS roughness increased from 3 to 7 nm when the MoS_2 and MoP structures coexisted in the P:MoS_2 thin films, as shown in Figs. 4.33(a)–(c).

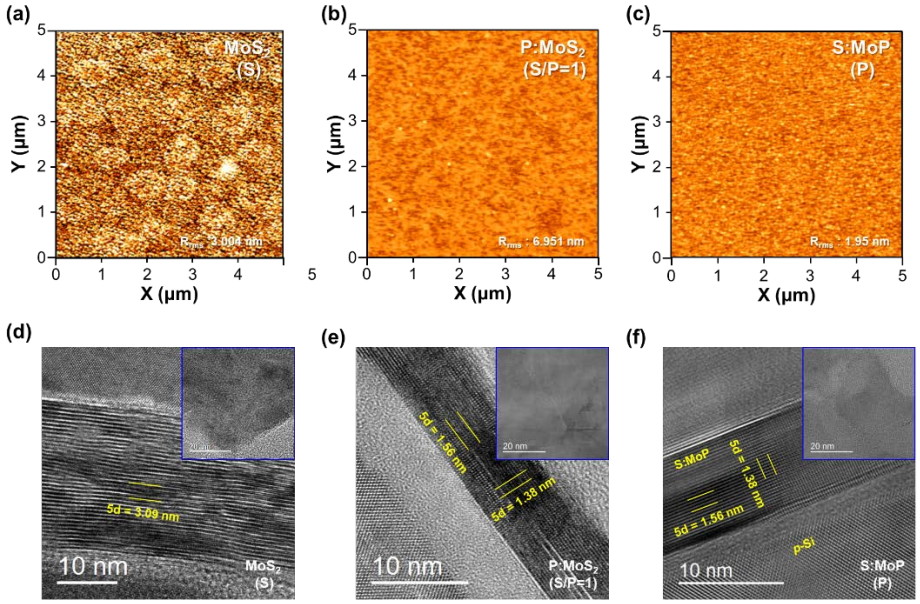

Fig. 4.33. Characterization of the MoS_2, P:MoS_2 (sulfur-rich), and S:MoP (phosphorus-rich) thin films. Topographic AFM images of the synthesized thin films: (a) MoS_2 (S), (b) P:MoS_2 (S/P = 1), and (c) S:MoP (P) on the SiO_2 substrate. Cross-sectional TEM images of the synthesized thin films: (d) MoS_2 (S), (e) P:MoS_2 (S/P = 1), and (f) S:MoP (P) on *p*-Si wafer. The inset of each figure shows the high-resolution TEM images of the thin films on Cu grid.

However, it drastically decreased from 7 nm for the P:MoS_2 thin films to 2 nm for the S:MoP thin films when P atoms were predominant in the synthesized film. Furthermore, the thickness of the synthesized films decreased significantly from 20 nm for MoS_2 to 13 nm for S:MoP (Fig. 4.34). The surface analysis of the synthesized MoS_2 and S:MoP (S/P = 0.33) with 5 different regions shows the reliability of our AFM measurement. (Fig. 4.35)

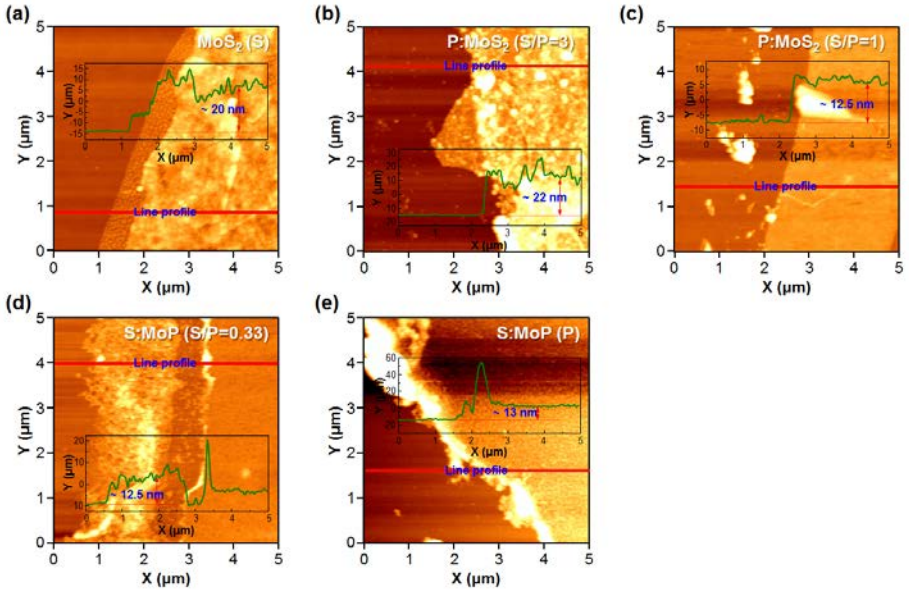

Fig. 4.34. AFM images with line profiles of the thin films synthesized with different S/P powder precursor ratios. The thickness of the synthesized thin films decreased from ~ 20 to ~ 13 nm when P atoms were completely substituted into the MoS_2 atomic structure.

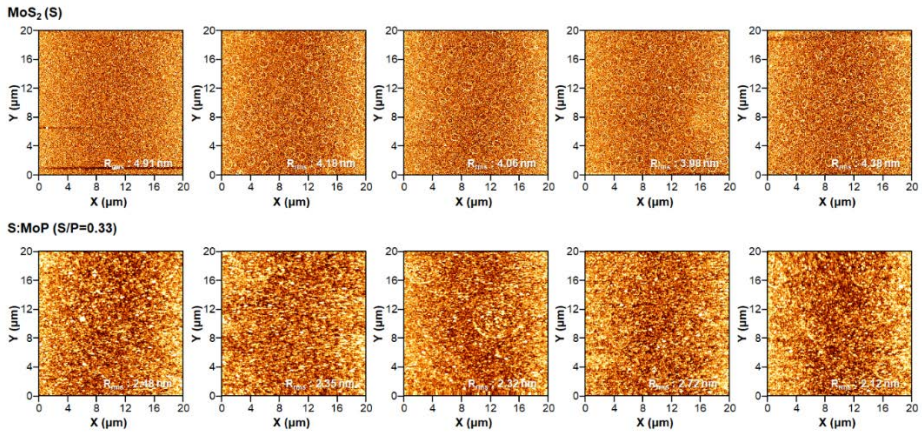

Fig. 4.35. Surface analysis of synthesized thin films with 5 different regions. The average RMS roughness values of MoS_2 and S:MoP (S/P=0.33) are 4.74 and 2.21 nm, respectively.

The 20 × 20 μm^2 AFM images and the RMS roughness values clearly show that the thermolysis of solution precursor is an effective way for synthesis of the MoS_2 and S:MoP catalysts. MoS_2 is a 2D material whose layers are bound to each other by van der Waals force (d-spacing = 0.618 nm), while MoP is a 3D material without van der Waals forces (d-spacing = 0.312 nm). This resulted in a decrease in the thicknesses of the P:MoS_2 and S:MoP thin films. The microstructures of the synthesized thin films were studied by transmission electron microscopy (TEM).

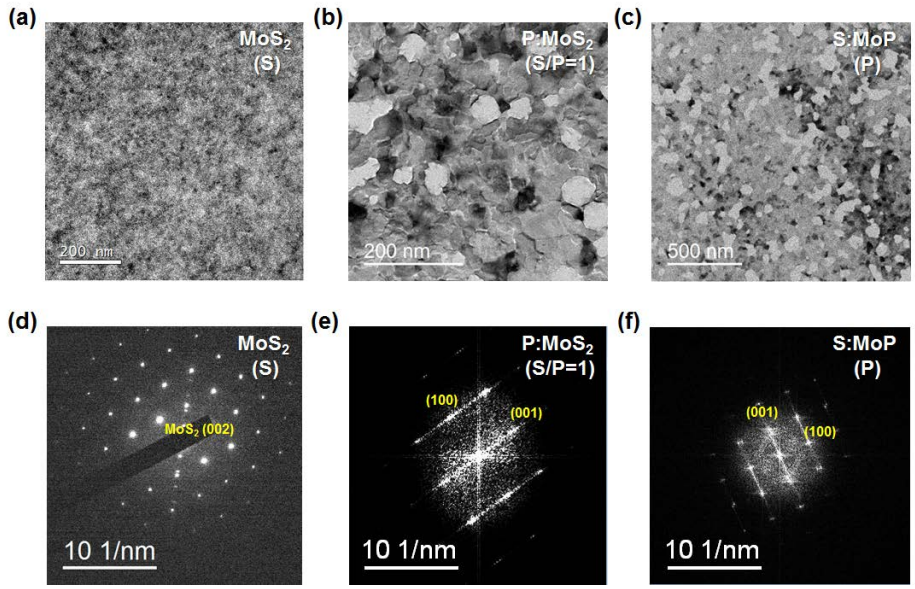

Fig. 4.36. (a)–(c) The low-magnification transmission electron microscopy (TEM) images of the thin films synthesized with different S/P powder precursor ratios. (d)–(f) The selected area electron diffraction (SAED) patterns of the thin films synthesized with different S/P powder precursor ratios. The SAED patterns of the MoS_2 thin films showed the MoS_2 (002) plane. The SAED patterns significantly changed into MoP (100) and MoP (001) planes with the introduction of phosphorus into the MoS_2 atomic structure.

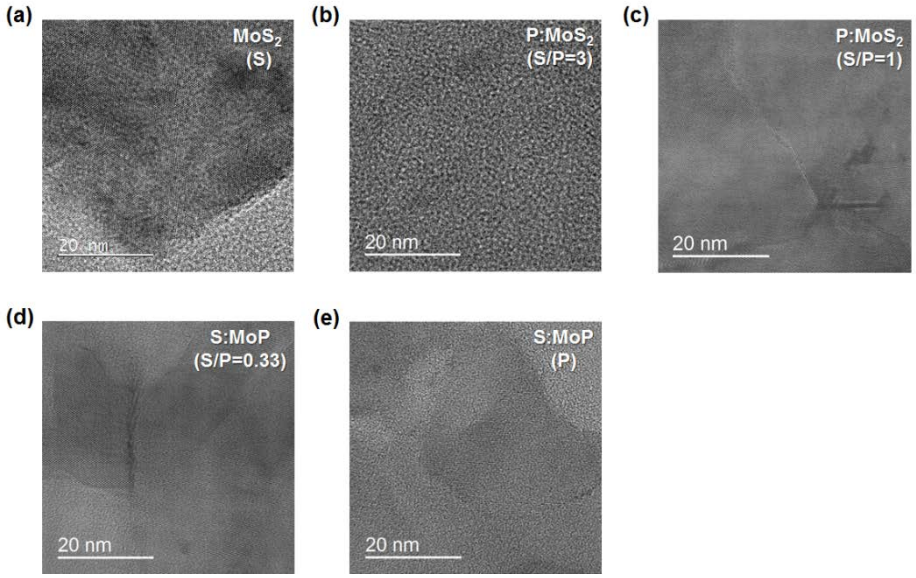

Fig. 4.37. The high-resolution TEM images of the thin films synthesized with different S/P powder precursor ratios. The surface of the thin films was gradually smoothed with an increase in the S/P powder precursor ratio.

The low magnification and high-resolution TEM images (Fig. 4.36 and Fig. 4.37) show the pinhole-free thin films on a Cu grid. The synthesized films showed the 3D to 2D structural transition after the introduction of P atoms into the MoS_2 structure. The selected area electron diffraction pattern (SAED) of each thin film clearly showed that the atomic structure significantly changed from MoS_2 to MoP. The top- and cross-sectional-view high-resolution TEM images of the thin films are shown in Figs. 4.33(d)–(f). The thin films containing only P (S:MoP) showed a nano-granular surface. Furthermore, the d-spacing of the thin film containing only S (MoS_2 (S)) was comparable to that of the films with S/P = 1 and S:MoP (P:MoS_2 (S/P = 1:1) and S:MoP (P)). The d-spacing of the P:MoS_2 and S:MoP thin films (d = 0.312 nm) is consistent with that of MoP,

indicating that P atoms were successfully substituted into the MoS_2 atomic structure by the simple thermolysis.

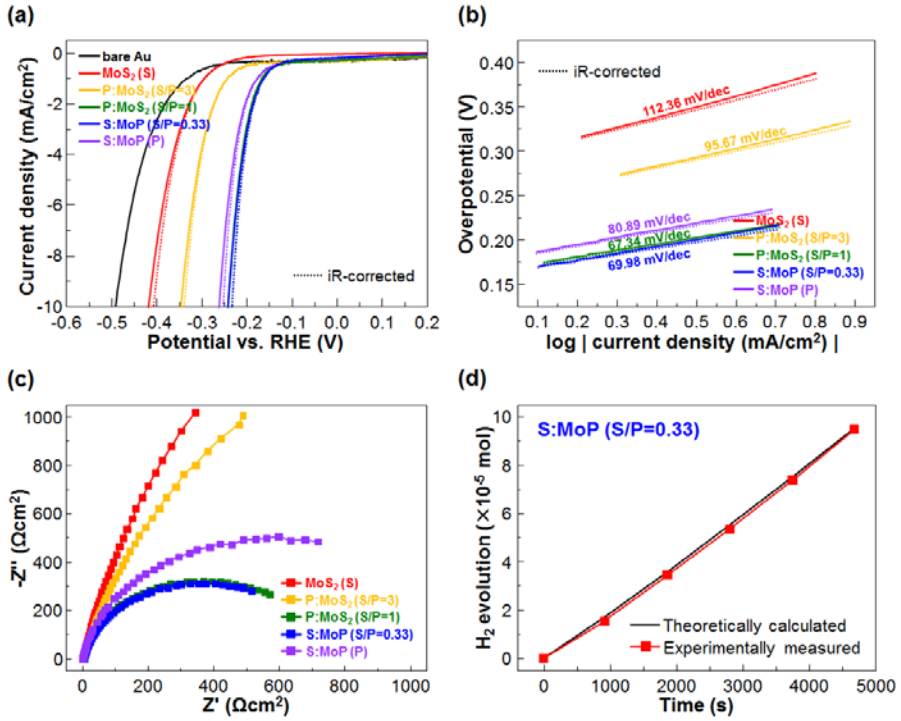

Fig. 4.38. (a) Electrochemical (EC) performances of the synthesized thin films on Au electrode. (b) Tafel plots from the linear portion of the EC measurement. (c) The electrochemical impedance spectroscopy measurements. (d) The faradaic efficiency measurements of the synthesized thin films transferred onto Au electrodes.

We have investigated the electrochemical (EC) HER performance of the thin films synthesized with different S/P powder precursor ratios on an Au substrate with iR-correction (Fig. 4.38). The HER performance of the S:MoP (S/P = 0.33) thin films is comparable to that of the previously reported MoP catalysts.[28,38-40]

Table 4.5. Electrochemical catalytic properties of the thin films synthesized on Au electrodes.

Electrodes	Potential (V) @ 10 mA/cm^2	Potential (V) @ 20 mA/cm^2	Tafel slope (mV/dec)
bare Au	- 0.492	- 0.546	157.83
MoS_2 (S)	- 0.407	- 0.450	112.36
P:MoS_2 (S/P=3)	- 0.341	- 0.375	95.67
P:MoS_2 (S/P=1)	- 0.234	- 0.255	67.34
S:MoP (S/P=0.33)	- 0.233	- 0.255	69.98
S:MoP (P)	- 0.254	- 0.276	80.89

The EC performance of the thin films synthesized on an Au electrode is summarized in Table 4.5. The reaction mechanism of HER can be explained by Tafel slopes. HER proceeds via a three-step mechanism involving a discharge step (Volmer reaction, Tafel slope of 120 mV/dec), a desorption step (Heyrovsky reaction, Tafel slope of 40 mV/dec), and a recombination step (Tafel reaction, 30 mV/dec).[41] In the EC measurements, the S:MoP (S/P = 0.33)/Au electrode showed a Tafel slope of 67.34 mV/dec, indicating that the HER in this case, proceeded probably with the Volmer-Heyrovsky reaction. Furthermore, this value of Tafel slope (67.34 mV/dec) indicates that the electrode had an outstanding catalytic activity, considering that our S:MoP catalysts were flat thin films with a much lower surface area than nanoparticles or nanostructures.

Table 4.6. Electrochemical catalytic properties of the thin films synthesized on various electrodes.

No.	Sample type	Measured Electrode	Synthesis method	η^* at 10 mA/cm^2	Tafel slope (mV/dec)
1	grain type	Ti foil	thermal CVD	117 mV	50
2	nano-particle	glassy carbon	air ambient calcination	125 mV	54 – 83
3	nano-particle	Ti foil	solution-phase synthesis	110 mV	45
	porous MoP | S	Ti foil	thermal annealing	90 mV	50
4	mirco-particle	glassy carbon	grinding	150 mV	56
5	sponge (3D)	glassy carbon	solution synthesis	105 mV	126
6	$MoS_{2(1-X)}P_X$ solid solution	glassy carbon	MoS_2 + red-P solid solution	150 mV	57
7	nanosheets	glassy carbon	hydrothermal	43 mV	34
This work	**S:MoP thin film**	**Au** ***p*-Si**	**thermal CVD (thermolysis)**	**233 mV** **- 207 mV**	**70** **32**

*Overpotential.

In order to compare the HER performance of the S:MoP (S/P = 0.33)/*p*-Si or Au electrode with that of previously reported state-of-the-art electrodes with similar material systems, their overpotentials at 10 mA/cm^2 and Tafel slope values are summarized in Table 4.6.

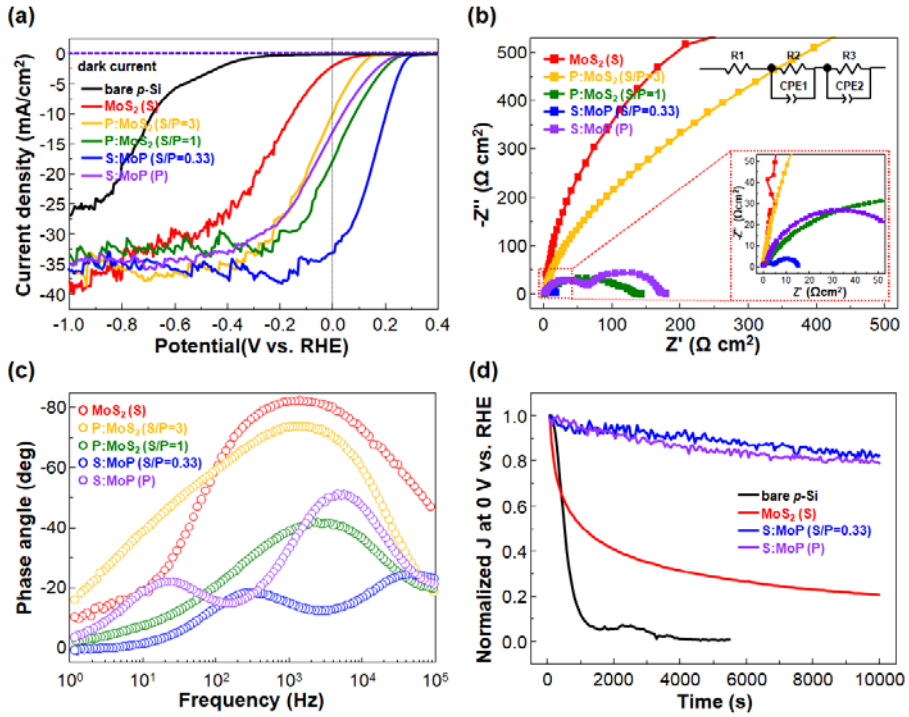

Fig. 4.39. Photoelectrochemical performance of synthesized thin films/*p*-Si heterojunction photocathodes. (a) Linear sweep voltametry curves of each thin film catalyst. The S:MoP (S/P = 0.33)/*p*-Si photocathode showed a current density of 33.13 mA/cm^2 at 0 V and a significant potential value shift at 10 mA/cm^2 from -0.69 to 0.082 V for *p*-Si. (b) Electrochemical impedance spectroscopy analysis of the synthesized thin films catalysts/*p*-Si heterojunction photocathodes. Inset graph shows the magnified 0 to 50 Ω cm^2 results for better understanding. (c) Bode plot of each thin film catalyst/*p*-Si heterojunction photocathode. (d) Stability tests over 10000 s for the bare *p*-Si, MoS_2 (S), and S:MoP (S/P = 0.33 and P) thin films at 0 V.

The PEC characterization of the S:MoP/*p*-Si photocathodes was carried out with a standard three-electrode configuration using a 0.5 M H_2SO_4 solution as the electrolyte. All the measurements were conducted with a graphite rod counter electrode. Fig. 4.39(a) shows the current density vs. potential (*J*–*V*) behavior of the S:MoP/*p*-Si photocathodes under a simulated air mass 1.5 G condition. The dashed lines indicate the dark current. We define the onset potential in *J*–*V* curve as the potential

when the photocurrent density reaches -1 mA/cm^2. The bare *p*-Si photocathode showed a large negative onset potential of -0.35 V. Even though *p*-Si is a promising candidate for photocathodes because of its narrow band gap, which enables it to absorb a wide portion of the incident solar spectrum, an additional potential must be supplied to drive HER because of the carrier concentration and kinetic overpotential issues.[9] The highest catalytic activity for HER was exhibited by the S:MoP (S/P = 0.33) thin films. The onset potentials of the synthesized thin film catalysts/*p*-Si photocathodes shifted gradually to the anodic direction at S/P = 0.33. For the S:MoP (S/P =0.33)/*p*-Si photocathode, the onset potential shifted towards the anodic direction by 0.63 V with respect to that of the bare *p*-Si. Furthermore, the photocurrent density at 0 V (vs. RHE) reached a value of 33.13 mA/cm^2. It is notable that the value is even higher than the maximum photocurrent density (24.6 mA/cm^2) of thickness controlled *n*-MoS_2/*p*-Si heterojunction photocathodes in our previous study.[23] At S/P ratios greater than 0.33, the photocurrent onset shifted slightly to the cathodic direction. Because of the transfer of the S:MoP (S/P =0.33) thin film, the potential required to reach the photocurrent of 10 mA/cm^2 decreased from 0.685 (bare *p*-Si) to -0.21 V. The applied-bias photon-to-current efficiency (ABPE) was also calculated from the *J–V* curves shown in Fig. 4.39(a). The largest anodic shift of the onset potential resulted in a maximum applied-bias photon-to-current efficiency (ABPE) of 2.8% for the S:MoP (S/P = 0.33)/*p*-Si

photocathode. This value is comparable to the ABPE obtained with noble metal-decorated Si-based photocathodes.[39]

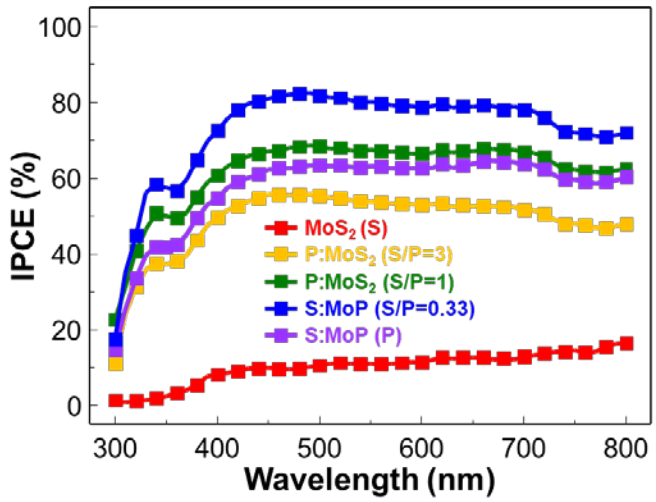

Fig. 4.40. Incident-photon-to-current conversion efficiency measurements of each thin film catalyst/p-Si photocathode.

The incident-photon-to-current conversion efficiency spectra of the S:MoP/*p*-Si were recorded at an applied potential of 0 V vs. RHE (Fig. 4.40). Among the tested photocathodes, the photocathode with a S:MoP (S/P = 0.33) layer exhibited the highest efficiency of around 80% in the wavelength range of 410–720 nm. The linear-sweep voltammetry curves show that the PEC properties of the S:MoP/*p*-Si photocathodes depended on the S/P powder precursor ratios and it was necessary to determine an optimum S/P ratio. The PEC performances of the thin films synthesized with different S/P powder precursor ratios on *p*-Si photocathodes are summarized in Table 4.7.

Table 4.7. The summarized photoelectrochemical performances of synthesized thin films/*p*-Si heterojunction photocathodes.

Photocathodes	Current density (mA/cm^2) @ 0 V	Overpotential (V) at 10 mA/cm^2
Bare *p*-Si	0.013	+ 0.685
MoS_2 (S)	2.051	+ 0.150
P:MoS_2 (S/P=3)	10.192	- 0.002
P:MoS_2 (S/P=1)	18.014	- 0.087
S:MoP (S/P=0.33)	33.132	- 0.207
S:MoP (P)	13.131	+ 0.040

We also conducted electrochemical impedance spectroscopy (EIS) measurements using a simplified equivalent circuit as shown in Fig. 4.39(b). The simplified equivalent circuit consisted of constant phase elements (CPE) and charge-transfer resistances (R_{ct}). The impedance spectra were recorded at a bias near the onset potential to avoid the possible complicated factors. The small semicircular arcs in the Nyquist plots reflect the lower charge transfer resistance at each interface. The semicircular arcs corresponding to CPE and R_{ct} decreased significantly and thus were clearly separated for the photocathodes with S:MoP (P-rich, S/P = 0.33 and P) thin film catalysts. This significant decrease in the overall impedance is attributed to the semiconductor-metal transition caused by phosphorus doping into the MoS_2 thin film. The R_{ct} values for the S:MoP (S/P = 0.33)/electrolyte interface ($R_{ct,3}$) showed the smallest value, which is two orders of magnitude smaller than the $R_{ct,3}$ value for the MoS_2 (S)/*p*-Si photocathode as summarized in Table 4.8.

Table 4.8. The charge transport resistances of the synthesized thin film/*p*-Si photocathodes.

Photocathode	$R_{ct,1}$ (Ω cm^2)	$R_{ct,2}$ (Ω cm^2)	$R_{ct,3}$ (Ω cm^2)
	contact/*p*-Si	*p*-Si/TF[1]	TF/EL[2]
Bare *p*-Si	1.17	4810[3]	-
MoS_2 (S)	1.38	1305.1	1425.7
P:MoS_2 (S/P=3)	3.04	2385.4	383.1
P:MoS_2 (S/P=1)	5.14	108.9	17.7
S:MoP (S/P=0.33)	2.15	10.0	6.6
S:MoP (P)	5.21	103.0	63.7

[1]TF: Thin films, [2]EL: Electrolyte, [3]p-Si/electrolyte.

Additional information on EIS can be obtained by the Bode plot as displayed in Fig. 4.39(c). Two peaks corresponding to the two main processes taking place can be observed. The peaks in the high and low frequency regions represent the charge transfer from *p*-Si to the catalytic thin films and the charge transfer at the catalytic thin film/electrolyte interface, respectively.[42] For the P:MoS_2 thin film/*p*-Si photocathodes, the two peaks almost overlapped, leading to a single broad peak. Meanwhile, the S:MoP thin film/*p*-Si photocathodes showed two clearly separated peaks. For the S:MoP (S/P = 0.33) thin film/*p*-Si photocathode, the peak in the high frequency region shifted towards the highest frequency range and showed a significant decrease in the phase angle, suggesting that a low-resistance ohmic contact was formed between *p*-Si and S:MoP.[43] These are in agreement with the results obtained by linear sweep voltammetry in Fig. 4.39(a).

The long-term stability of the S:MoP/thin-film catalysts was evaluated by chronoamperometric measurements. These measurements were carried out to determine whether the catalysts could play the role of a passivation layer in *p*-Si. Fig. 4.39(d) shows the choronoamperometry curves of bare *p*-Si, MoS_2 (S)/*p*-Si, S:MoP (S/P = 0.33)/*p*-Si, and S:MoP (P)/*p*-Si for 10,000 s. The bare *p*-Si photocathode suffered from severe degradation, as reported by several groups.[39,44-47] On the other hand, in the case of the S:MoP (S/P = 0.33, P) thin film, the photocurrent degradation was considerably suppressed. Among all the thin film passivation layer-loaded photocathodes, the MoS_2 (S)/*p*-Si photocathode showed a rapid degradation. Since the MoS_2 (S) thin film (22 nm) used in this study is thicker than the MoS_2 thin film with the optimum thickness (13 nm) which shows the highest PEC performance in our previous study,[23] the top layers of the MoS_2 thin film were compiled by the weak van der Waals force compared to the bottom layers of MoS_2 thin films which form the heterojunction with the surface of *p*-Si. The P-rich S:MoP thin films (S/P = 0.33 and P) are hexagonal 3D materials with no interlayer van der Waals force. The reason behind the enhanced stability of the S:MoP thin film is 2D to 3D structural transition with the introduction of P atoms, which substituted the S atomic sites. The S:MoP (S/P = 0.33)/*p*-Si photocathode maintained more than 80% of its initial photocurrent during the operation time, suggesting that the S:MoP thin film (S/P = 0.33) protected the *p*-Si photocathode from severe photocorrosion.

The main light absorber in the S:MoP (S/P = 0.33)/*p*-Si heterostructure photocathodes was the *p*-Si substrate because of the semi-transparency of the S:MoP thin films. Thus, it is important to know whether the photogenerated electrons inside *p*-Si moved efficiently toward the S:MoP/electrolyte interface for triggering HER. Ultraviolet photoemission spectroscopy (UPS) and XPS valence band spectra were used in order to explore the band-bending of the S:MoP (S/P = 0.33)/*p*-Si heterostructures.

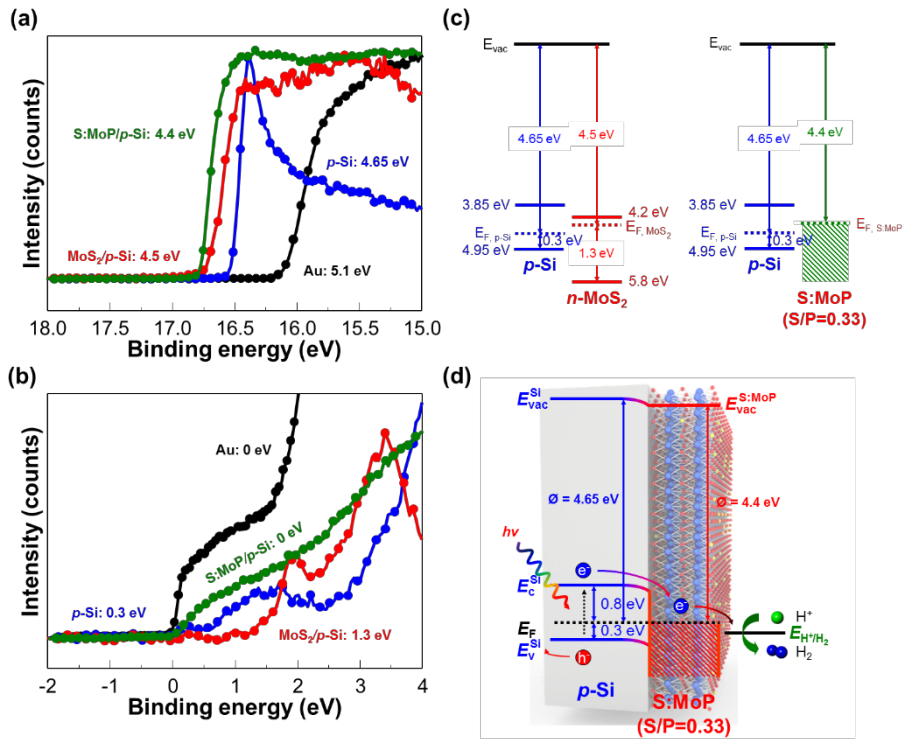

Fig. 4.41. Characterization of suggested energy band diagrams between *p*-Si and S:MoP (S/P = 0.33). (a) Ultraviolet photoemission spectroscopy (UPS) and (b) X-ray photoemission valence spectra of bare *p*-Si, MoS_2/*p*-Si, and S:MoP/*p*-Si. Each measured value was corrected with Au reference. (c) Comparison of the flat band energy diagrams of MoS_2 (S) and S:MoP (S/P = 0.33) on the *p*-Si photocathodes. (d) Energy band diagram of the S:MoP(S/P = 0.33)/*p*-Si heterojunction photocathode.

Fig. 4.41(a) shows the secondary electron emission (SEE) cutoffs of *p*-Si (4.65 eV), MoS_2 (S)/*p*-Si (4.5 eV), and S:MoP (S/P = 0.33)/*p*-Si (4.4 eV). We could determine the work functions of *p*-Si, MoS_2 (S), and S:MoP (S/P = 0.33) by comparing the SEE cutoff of each sample with the work function of the Au reference (5.1 eV). The energy differences between the Fermi level and the valence band maximum (E_F - E_V) could be obtained from the XPS valence-band spectra shown in Fig. 4.41(b). The E_F - E_V values for *p*-Si and MoS_2 (S)/*p*-Si were 0.3 and 1.3 eV, respectively. From the absorption spectra, the optical band gap of MoS_2 (S) was found to be around 1.6 eV, while S:MoP (S/P = 0.33) showed a zero gap (Fig. 4.29).

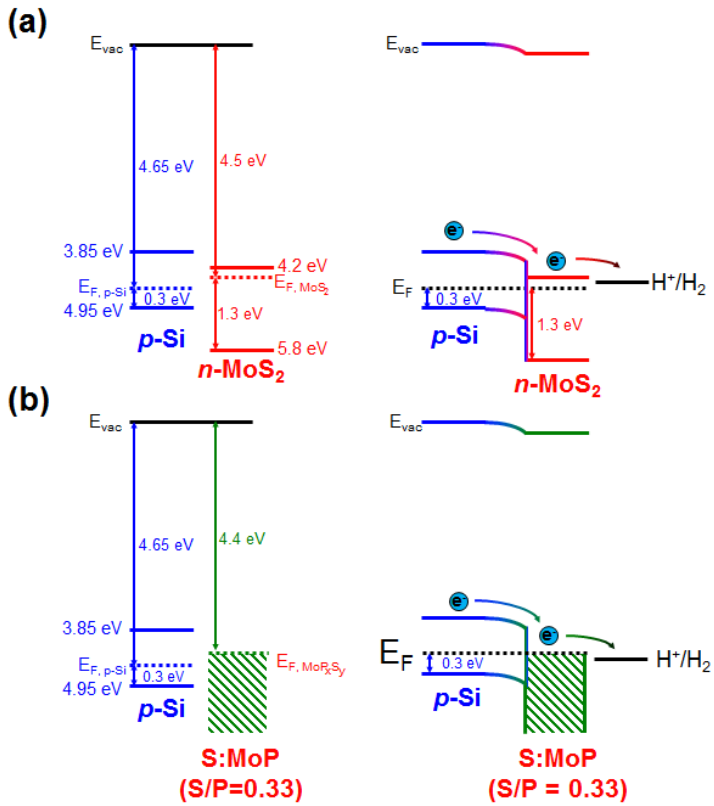

Fig. 4.42. The flat band and band-banding diagrams of (a) n-MoS_2 (S)/p-Si, and (b) S:MoP (S/P =0.33)/p-Si heterojunction photocathodes.

Based on these results, the flat band and band bending diagrams for the *n*-MoS_2 (S)/*p*-Si heterostructure were obtained (Fig. 4.41(c) and Fig. 4.42). These diagrams were consistent with those reported in our previous study.[23] Interestingly, the E_F - E_V value of the phosphorus-rich S:MoP thin film was 0 eV. The absorbance spectra revealed that the phosphorus-rich S:MoP thin film was metallic. According to the DFT calculations, the metallic S:MoP thin film of 3D hexagonal structure is more active catalyst compared to the 2H-MoS2 thin film of 2D hexagonal structure, which has a limited number of active sites for HER. On the basis of the UPS and XPS measurement results, an energy band diagram was suggested for S:MoP (S/P = 0.33)/*p*-Si (Fig. 4.41(d)). The energy band diagram revealed that the photogenerated electrons could be easily transported to the S:MoP (S/P = 0.33)/*p*-Si interface and no electronic potential barrier was observed.

4.3.4. Conclusion

We have successfully demonstrated a simple method to improve the PEC HER catalytic activity of molybdenum disulfide thin film catalysts by introducing substitutional phosphorus dopants in their atomic structure. The S:MoP/*p*-Si heterojunction photocathodes showed a high photocurrent density (33.13 mA/cm^2 at 0 V vs. RHE), large overpotential shift (0.9 V at 10 mA/cm^2), and long-term stability (over 10000 s). The characterization of the S:MoP/*p*-Si photocathodes revealed that they could act not only as surface active catalysts owing to their low hydrogen adsorption Gibbs free energy but also as passivation layers owing to their 3D tight bonding between molybdenum and sulphur or phosphorus atoms. This work highlights that the anion substitution in MoS_2 thin films is an effective way to enhance the PEC performance of the thin films.

4.3.5. References

[1] X. Chen, S. Shen, L. Guo and S. S. Mao, *Chem. Rev.*, **2010**, *110*, 6503.

[2] F. E. Osterloh and B. A. Parkinson, *MRS Bull.*, **2011**, *36*, 17.

[3] A. Kudo and Y. Miseki, *Chem. Soc. Rev.*, **2009**, *38*, 253.

[4] L. B. Braga, J. L. Silveira, M. E. Da Silva, C. E. Tuna, E. B. Machin and D. T. Pedroso, *Renewable Sustainable Energy Rev.*, **2013**, *28*, 166.

[5] D. G. Nocera, *Acc. Chem. Res.*, **2012**, *45*, 767.

[6] A. Haryanto, S. Fernando, N. Murali and S. Adhikari, *Energy & Fuels*, **2005**, *19*, 2098.

[7] M. G. Walter, E. L. Warren, J. R. McKone, S. W. Boettcher, Q. Mi, E. A. Santori and N. S. Lewis, *Chem. Rev.*, **2010**, *110*, 6446.

[8] N. C. Strandwitz, D. B. Turner-Evans, A. C. Tamboli, C. T. Chen, H. A. Atwater and N. S. Lewis, *Adv. Energy Mater.*, **2012**, *2*, 1109.

[9] D. M. Andoshe, J.-M. Jeon, S. Y. Kim and H. W. Jang, *Electron. Mater. Lett.*, **2015**, *11*, 323.

[10] K. Osseo-Asare, D. Wei and K. K. Mishra, *J. Electrochem. Soc.*, **1996**, *143*, 749.

[11] E. L. Warren, S. W. Boettcher, J. R. McKone and N. S. Lewis, *SPIE-Int. Soc. Opt. Eng.*, **2010**, *7770*, 77701F.

[12] L. Zhu, H. Lin, Y. Li, F. Liao, Y. Lifshitz, M. Sheng, S.-T. Lee and M. Shao, *Nat. Commun.*, **2016**, *7*, 12272.

[13] M. Li, Q. Ma, W. Zi, X. Liu, X. Zhu, S and F. Liu, *Sci. Adv.*, **2015**, *1*, e1400268.

[14] J. Kye, M. Shin, B. Lim, J.-W. Jang, I. Oh and S. Hwang, *ACS nano*, **2013**, *7*, 6017.

[15] S. Y. Reece, J. A. Hamel, K. Sung, T. D. Jarvi, A. J. Esswein, J. J. Pijpers and D. G. Nocera, *Science*, **2011**, *334*, 645.

[16] Y. Hou, B. L. Abrams, P. C. Vesborg, M. E. Björketun, K. Herbst, L. Bech, A. M. Setti, C. D. Damsgaard, T. Pedersen, O. Hansen, J. Rossmeisl, S. Dahl, J. K. Nørskov and I. Chorkendorff, *Nat. Mater.*, **2011**, *10*, 434.

[17] D. Voiry, H. Yamaguchi, J. Li, R. Silva, D. C. Alves, T. Fujita, M. Chen, T. Asefa, V. B. Shenoy, G. Eda and M. Chhowalla, *Nat. Mater.*, **2013**, *12*, 850.

[18] K. C. Kwon, C. Kim, Q. V. Le, S. Gim, J.-M. Jeon, J. Y. Ham, J.-L. Lee, H. W. Jang and S. Y. Kim, *ACS nano*, **2015**, *9*, 4146.

[19] A. B. Laursen, S. Kegnæs, S. Dahl, I. Chorkendorff, *Energy Environ. Sci.*, **2012**, *5*, 5577.

[20] H. Li, C. Tsai, A. L. Koh, L. Cai, A. W. Contryman, A. H. Fragapane, J. Zhao, H. S. Han, H. C. Manoharan, F. Abild-Pedersen, J. K. Nørskov and X. Zheng, *Nat. Mater.*, **2016**, *15*, 48.

[21] T. F. Jaramillo, K. P. Jørgensen, J. Bonde, J. H. Nielsen, S. Horch and I. Chorkendorff, *Science*, **2007**, *317*, 100.

[22] D. Voiry, M. Salehi, R. Silva, T. Fujita, M. Chen, T. Asefa, V. B. Shenoy, G. Eda and M. Chhowalla, *Nano Lett.*, **2013**, *13*, 6222.

[23] K. C. Kwon, S. Choi, K. Hong, C. W. Moon, Y.-S. Shim, D. H. Kim, T. Kim, W. Sohn, J.-M. Jeon, C.-H. Lee, K. T. Nam, S. Han, S. Y. Kim and H. W. Jang, *Energy Environ. Sci.*, **2016**, *9*, 2240.

[24] E. J. Popczun, J. R. McKone, C. G. Read, A. J. Biacchi, A. M. Wiltrout, N. S. Lewis and R. E. Schaak, *J. Am. Chem. Soc.*, **2013**, *135*, 9267.

[25] F. H. Saadi, A. I. Carim, E. Verlage, J. C. Hemminger, N. S. Lewis and M. P. Soriaga, *J. Phys. Chem. C*, **2014**, *118*, 29294.

[26] P. Jiang, Q. Liu, Y. Liang, J. Tian, A. M. Asiri and X. Sun, *Angew. Chem. Int. Ed.*, **2014**, *53*, 12855.

[27] R. Ye, P. del Angel-Vicente, Y. Liu, M. J. Arellano-Jimenez, Z. Peng, T. Wang, Y. Li, B. I. Yakobson, S. H. Wei, M. J. Yacaman and J. M. Tour, *Adv. Mater.*, **2015**, *28*, 1427.

[28] C. Deng, F. Ding, X. Li, Y. Guo, W. Ni, H. Yan, K. Sun, Y.-M. Yan, *J. Mater. Chem. A*, **2016**, *4*, 59.

[29] G. Kresse and J. Furthmüller, *Phys. Rev. B: Condens. Matter. Mater. Phys.*, **1996**, *54*, 11169.

[30] P. E. Blöchl, *Phys. Rev. B: Condens. Matter. Mater. Phys.*, **1994**, *50*, 17953.

[31] T. Bligaard, J. Nørskov, S. Dahl, J. Matthiesen, C. Christensen and J. Sehested, *J. Catal.*, **2004**, *224*, 206.

[32] M. Cabán-Acevedo, M. L. Stone, J. Schmidt, J. G. Thomas, Q. Ding, H.-C. Chang, M.-L. Tsai, J.-H. He and S. Jin, *Nat. Mater.*, **2015**, *14*, 1245.

[33] C. M. A. Brett and A. M. O. Brett, *Electrochemistry: Principles, Methods, and Applications*, Oxford University Press, Oxford, 1993.

[34] Z. Feng, C. Liang, W. Wu, Z. Wu, R. A. van Santen and C. Li, *J. Phys. Chem. B*, **2003**, *107*, 13698.

[35] H. Li, Q. Zhang, C. C. R. Yap, B. K. Tay, T. H. T. Edwin, A. Olivier and D. Baillargeat, *Adv. Funct. Mater.*, **2012**, *22*, 1385.

[36] J. Suh, T.-E. Park, D.-Y. Lin, D. Fu, J. Park, H. J. Jung, Y. Chen, C. Ko, C. Jang, Y. Sun, R. Sinclair, J. Chang, S. Tongay and J. Wu, *Nano Lett.*, **2014**, *14*, 6976.

[37] D. Kiriya, M. Tosun, P. Zhao, J. S. Kang and A. Javey, *J. Am. Chem. Soc.*, **2014**, *136*, 7853.

[38] Z. Xing, Q. Liu, A. M. Asiri and X. Sun, *Adv. Mater.*, **2014**, *26*, 5702.

[39] L. Ji, M. D. McDaniel, S. Wang, A. B. Posadas, X. Li, H. Huang, J. C. Lee, A. A. Demkov, A. J. Bard, J. G. Ekerdt and E. T. Yu, *Nat. Nanotechnol.*, **2015**, *10*, 84.

[40] J. Kibsgaard and T. F. Jaramillo, *Angew. Chem. Int. Ed.*, **2014**, *53*, 14433.

[41] A. J. Bard and L. R. Faulkner, *Electrochemical methods: fundamentals and applications*, John Wiley & Sons, Inc., New York, 2001.

[42] S. Hernández, D. Hidalgo, A. Sacco, A. Chiodoni, A. Lamberti, V. Cauda, E. Tresso and G. Saracco, *Phys. Chem. Chem. Phys.*, **2015**, *17*, 7775.

[43] K. Ojha, S. Saha, H. Kolev, B. Kumar and A. K. Ganguli, *Electrochim. Acta*, **2016**, *193*, 268.

[44] D. M. Andoshe, S. Choi, Y.-S. Shim, S. H. Lee, Y. Kim, C. W. Moon, D. H. Kim, S. Y. Lee, T. Kim, H. K. Park, M. G. Lee, J.-M. Jeon, K. T. Nam, M. Kim, J. K. Kim, J. Oh, H. W. Jang, *J. Mater. Chem. A*, **2016**, *4*, 9477.

[45] U. Sim, T.-Y. Yang, J. Moon, J. An, J. Hwang, J.-H. Seo, J. Lee, K. Y. Kim, J. Lee, S. Han, B. H. Hong, K. T. Nam, *Energy Environ. Sci.*, **2013**, *6*, 3658.

[46] Q. Ding, F. Meng, C. R. English, M. Cabán-Acevedo, M. J. Shearer, D. Liang, A. S. Daniel, R. J. Hamers and S. Jin, *J. Am. Chem. Soc.* **2014**, *136*, 8504.

[47] Q. Ding, B. song, P. Xu and S. Jin, *Chem*, **2016**, *1*, 699.

Chapter 5

Summary

As a new class of material, two-dimensional (2D) atomic crystals have attracted enormous research interest in the last decade that has led to a number of breakthroughs in physics owing to the confined charge, spin and heat transport within the 2D planes. The most outstanding one of these materials is graphene, as its exceptional electronic, optical and mechanical properties may hold great promise for a variety of future applications.

The chapter 3 will cover the application of 2D transition metal disulfide thin films to charge transport layers and p-n junction material with *p*-Si wafer. Transition metal disulfides (MeS_2) such as MoS_2 and WS_2 were used as charge transport layers in organic light-emitting diodes (OLEDs) and organic photovoltaic (OPV) cells in order to enhance the stability in air comparing to poly(3,4-ethylenedioxythiophene):poly(styrenesulfonate) (PEDOT:PSS). MeS_2 layers with a polycrystalline structure were synthesized by a chemical deposition method using uniformly spin-coated $(NH_4)MoS_4$ and $(NH_4)WS_4$ precursor solutions. The ultraviolet-ozone ($UV\text{-}O_3$) treatment on MeS_2 leads to the removal of the surface contaminants produced by the transfer process, resulting in a uniform surface and an increase of the work function.

Furthermore, the strong light absoption of single-layer of MoS_2 could be utilized by light absorption layer in p-type Si-based photovoltaic cells. Specifically, a single semiconducting 0.6-nm-thick MoS_2 can absorb as much sunlight as 50 nm of Si and generate photocurrents as similar as 12-nm-thick

GaAs semiconductor. The MoS_2 thin films could be the one of promising light absorption layer and have potential to make p-n heterojunction photovoltaic cells with p-Si substrate. We synthesize the wafer-scale molybdenum disulfide thin-films by thermolysis of solution precursor based method. After that, the thin films are transferred to p-Si and formed a heterojunction with p-Si. In order to maximize and fully utilize the excellent property of the n-MoS_2, Transparent Au nanomesh electrode (Sheet resistance ≈ 6 Ω/sq. at 90% transmittance) fabricated from UV-O_3 treated polymeric nanofiber templates is integrated to *n*-MoS_2/*p*-Si heterojunction**.** The *n*-MoS_2/*p*-Si heterojunction with Au nanomesh electrodes exhibit a power conversion efficiency of 4.69%. After antireflection coating, the device shows the efficiency of 5.96% at 0.44 cm^2 of the active area.

Hydrogen appears as a next-generation clean energy source to replace fossil fuels. One of the most promising ways to produce hydrogen is photoelectrochemical (PEC) water splitting. However, the existing photoelectrodes such as Si with noble metal catalysts still suffer from low efficiency and poor stability and the extremely high cost of the noble metal catalysts limits the wide use of water splitting photoelectrodes. Therefore, a novel approach is necessary to make a breakthrough for highly efficient PEC water splitting. This thesis contains that the demonstration of wafer-scale, transferable, and transparent thin-film catalysts based on MoS_2, which consists of cheap and earth abundant elements, can provide the low onset potential of 1 mA/cm^2 at 0.17 V versus a reversible hydrogen electrode and the high photocurrent density of 24.6 mA/cm^2 at 0 V for a *p*-type Si photocathode. c-

Domains with vertically stacked (100) planes in the transferable 2H-MoS_2 thin films, which are grown by a thermolysis method, act as active sites for the hydrogen evolution reaction, and photogenerated electrons are efficiently transported through the *n*-MoS_2/*p*-Si heterojunction**.**

Moreover, in chapter 4.3, the anion-engineered MoS_2 thin-films display the higher catalytic activity compared to the partially vertical-aligned MoS_2 thin films, due to its many inherent dangling bonds on their surface and the metallic nature. The transferrable and transparent anion-engineered molybdenum disulfide thin-film catalysts synthesized through simple thermolysis method by using [$(NH_4)_2MoS_4$] solution and powder precursors with different sulfur/phosphorus weight ratios. The synthesized sulfur-doped molybdenum phosphide (S:MoP) thin film changed from two-dimensional van der Waals structure to three-dimensional hexagonal structure by introduction of phosphorus atoms in the MoS_2 thin film. The S:MoP thin film catalyst, which is composed of cheap and earth abundant elements, could provide the lowest onset potential and the highest photocurrent density for planar *p*-type Si photocathode. The density functional theory calculations indicate that the surface of S:MoP thin film absorb hydrogen better than that of MoS_2 thin film. The structurally engineered thin film catalyst facilitates the easy transfer of photogenerated electrons from *p*-Si light absorber to electrolyte. Anion-engineering of MoS_2 thin film catalyst would be an efficient way to enhance the catalytic activity for photoelectrochemical water splitting.

국문초록

새로운 차원의 물질로서, 2차원 원자 결정체는 지난 10년 동안 엄청난 관심을 끌어왔으며, 2D 평면 내에서 제한된 전하, 스핀 및 열 전달로 인해 물리학에서 수많은 혁신을 이끌어왔다. 이 재료 중 가장 뛰어난 물질은 그래핀으로서, 광학 및 기계적 특성이 뛰어나 미래의 다양한 응용분야에서 큰 가능성을 제시하고 있으며 많은 연구가 진행중에 있다. 최근 5년 간 2차원 전이금속 디칼코게나이드 물질이 물 분해 촉매 및 논리회로 중 하나인 FET에서 채널로서 많은 연구가 진행중에 있다. 본 박사학위 논문은 2차원 전이금속 디칼코게나이드 물질 중 MoS_2 및 WS_2를 이용하여 태양전지의 광흡수 층 및 전하수송층으로의 응용과 p형 실리콘 웨이퍼의 낮은 광안정성과 높은 과전압 특성을 해결하고자 촉매로서의 응용에 대해 다룰 것이다.

3장에서는 유기태양전지와 유기 발광다이오드에서의 정공수송층으로의 활용과 p형 실리콘과의 p-n접합을 형성하여 안정적인 광흡수층으로서의 역할에 대해서 기술한다. MoS_2 및 WS_2와 같은 전이 금속 디설파이드는 유기 발광 다이오드 및 유기 태양전지 셀에서 전하수송층으로서 사용되어 폴리(3,4-에틸렌 디옥시티오펜):폴리(스티렌설포네이트) (PEDOT:PSS)를 대체하고자 하였다. 다결정 구조를 갖는 전이 금속 디설파이드층은 균일하게 스핀-코팅된 $(NH_4)_2MeS_4$ (Me = Mo, W) 전구체 용액을 사용하여 화학 기상 증착 법에 의해 합성하였다. 전이 금속 디설파이드에 자외선-오존 표면처리는 전사 공정에 의해서 생성된 표면 오염물을 제거하여 표면이 균일해지며, 일함수가 증가하여 광 여기된 정공이 더 잘 분리될 수 있도록 도와준다. 이러한 특성으로 인해, 자외선-오존 표면 처리된 전이 금속 디설파이드 정공 수송층은 PEDOT:PSS에 비해 95% 이상의 효율을 보일 수 있다. 또한, 공기 중에서 수분을 흡수하여 유기박막 층을 손상시킬 수 있으며 강한 산성으로 인해 투명전극이 손상이 일어날 수 있는 PEDOT:PSS층에 대비하여 200% 이상 수명이 향상되는 결과를 얻을 수 있었다.

또한, MoS_2의 단일 층의 강한 광 흡수는 p형 실리콘 계 광전지에서

광 흡수층에 의해 이용될 수 있다. 특히, 단일 층의 반도체 특성을 가지는 0.6 nm 두께의 MoS_2는 50 nm 두께의 실리콘만큼의 태양광을 흡수할 수 있으며, 12 nm 두께의 GaAs 반도체와 유사한 광전류를 생성할 수 있다. MoS_2 박막은 유망한 광 흡수층 중에 하나이며, p-n헤테로 접합 광전지를 p형 실리콘 기판으로 만들 수 있는 장점이 있다. 먼저, 용액 전구체 기반 방법의 열분해에 의해 4인치 크기의 웨이퍼 스케일로 MoS_2박막을 합성한다. 그 후, 합성된 박막을 p형 실리콘으로 전사하여 p형 실리콘과 헤테로 접합을 형성한다. n형 MoS_2의 우수한 특성을 극대화하고 최대한 활용하기 위해 자외선-오존 표면 처리된 폴리머 나노 섬유 템플릿으로 제작된 투명한 금 나노 메쉬 전극(90% 투과율에서 면저항 6Ω/□)을 활용하였다. 이렇게 제작된 소자는 4.69%의 전력 변환 효율을 나타낸다. 반사 방지 코팅 후, 소자는 0.44cm^2의 활성 영역에서 5.96%의 전력 변환 효율을 나타내었다. 이 결과는, 기 보고된 연구결과보다 우수한 성과를 나타내었다.

다음으로는, MoS_2 촉매를 이용하여 낮은 광 안정성과 높은 과전압 특성을 보이는 p형 실리콘의 물 분해 특성을 향상시키는 연구에 대해서 기술한다. 수소는 화석 연료를 대체 할 차세대 청정에너지 원으로 각광받고 있다. 수소를 생산하는 가장 유망한 방법 중 하나는 광 전기화학 (PEC) 물 분해이다. 그러나, p형 실리콘만을 물 분해에 사용했을 때, 낮은 광 안정성과 높은 과전압 특성으로 인해 플래티늄과 같은 귀금속 촉매를 사용하게 되는데, 이때, 귀금속 촉매가 두꺼우면 태양광이 반사되어 낮은 광전류가 형성되고 얇으면 실리콘 표면을 보호할 수 없어 낮은 광 안정성이 큰 문제점이 된다. 또한, 귀금속 촉매는 가격이 높아 광범위한 사용이 제한된다. 따라서, 고효율의 광 전기화학적 물 분해를 위한 획기적인 방법이 필요하다.

4장에서는, 저렴하고 풍부한 원소로 구성된 MoS_2에 기반한 웨이퍼 스케일, 전사 가능한 투명한 박막 촉매는 가역 수소 전위에 비해 0.17V에서 1mA/cm^2의 낮은 과전압 특성을 보였다. p형 실리콘과의 접합 시, 0V에서 24.6mA/cm^2의 높은 광전류 밀도를 나타내었다. 열 분해법에 의해 성장한 전사 가능한 2H상의 MoS_2박막에서 수직으로 적층된 (100)면을 갖는 도메인은 수소 발생 반응을 위한 활성 사이트로서

작용하고, 광 생성 된 전자는 n-MoS2/p형 실리콘 광전극을 통해 효율적으로 수송된다.

더욱이, 음이온-도핑된 MoS_2 박막은 부분적으로 수직으로 정렬 된 MoS_2 박막에 비해서 더 높은 촉매 활성을 나타내었는데, 이는 표면 및 금속 성질에 많은 고유의 댕글링본드가 있기 때문이다. 전사가 가능하고 투명한 음이온 도핑된 이황화 몰리브덴 박막 촉매는 $[(NH_4)_2MoS_4]$ 용액과 황/인의 중량비가 다른 분말 전구체를 사용하여 간단한 열분해 법으로 합성되었다. 합성된 황-도핑된 몰리브덴 인(S:MoP) 박막은 MoS_2 박막에 인 원자를 의도적으로 도입하여 2차원 반 데르 발스 구조에서 3 차원 육각 구조로 바뀌었다. S:MoP 박막 촉매는 값 싸고 지구의 원소가 풍부하여 평면 p형 실리콘 광음전극에 비해 가장 낮은 개시 전위와 가장 높은 광전류 밀도가 나타났다. 밀도 함수 이론 계산은 S:MoP 박막의 표면이 MoS_2 박막의 표면보다 수소를 잘 흡수함을 나타냅니다. 계산에 따르면, 수소 흡착 깁스 자유 에너지는 MoS_2박막 보다 S:MoP 박막의 표면에서 훨씬 더 낮은 값을 나타내어 수소 이온이 합성된 촉매 표면에 더 잘 흡착 될 수 있음을 보여주었다. 구조적으로 설계된 박막 촉매는 p형 실리콘 광 흡수층에서 여기된 광 생성 전자의 전해질로의 전달을 용이하게 하여 특성이 향상되었다. MoS_2 박막 촉매의 음이온–엔지니어링은 광전기 화학적 물 분해를 위한 촉매 활성을 향상시키는 효율적인 방법이 될 것이다.

List of Publications

[1] **K. C. Kwon**, C. Kim, Q. V. Le, S. Gim, J.-M. Jeon, J. Y. Ham, J.-L. Lee, H. W. Jang, S. Y. Kim, *ACS Nano*, **2015**, *9*, 4146.

[2] S. H. Lee, D. P. Singh, J. H. Sung, M.-H. Jo, **K. C. Kwon**, S. Y. Kim, H. W. Jang, J. K. Kim, *Sci. Rep.*, **2015**, *6*, 19580.

[3] D. H. Kim, D. M. Andoshe, Y. S. Shim, C. W. Moon, W. Sohn, S. Choi, T. L. Kim, M. Lee, H. K. Park, K. T. Hong, **K. C. Kwon**, J. M. Suh, J. S. Kim, J. H. Lee, and H. W. Jang, *ACS Appl. Mater. Interfaces*, **2016**, *8*, 23793.

[4] S. Kim, **K. C. Kwon**, J. Y. Park, H. W. Cho, I. Lee, S. Y. Kim, J.-L. Lee, *ACS Appl. Mater. Interfaces*, **2016**, *8*, 12932.

[5] **K. C. Kwon**, K. Hong, Q. V. Le, S. Y. Lee, J. Choi, K.-B. Kim, S. Y. Kim, H. W. Jang, *Adv. Funct. Mater.*, **2016**, *26*, 4213.

[6] **K. C. Kwon**, S. Choi, K. Hong, C. W. Moon, Y.-S. Shim, D. H. Kim, T. Kim, W. Sohn, J.-M. Jeon, C.-H. Lee, K. T. Nam, S. Han, S. Y. Kim, H. W. Jang, *Energy Environ. Sci.*, **2016**, *9*, 2240.

[7] Y. G. Kim, **K. C. Kwon**, Q. V. Le, K. Hong, H. W. Jang, S. Y. Kim, *Journal of Power Sources*, **2016**, *319*, 1.

[8] **K. C. Kwon**, H. J. Son, Y. H. Hwang, J. H. Oh, T.-W. Lee, H. W. Jang, K. Kwak, K. Park, S. Y. Kim, *J. Phys. Chem. C*, **2016**, *120*, 1309.

[9] T. P. Nguyen, S. Choi, J.-M. Jeon, **K. C. Kwon**, H. W. Jang, S. Y. Kim, *J. Phys, Chem. C*, **2016**, *120*, 3929.

[10] G. J. Choi, Q. V. Le, K. S. Choi, **K. C. Kwon**, H. W. Jang, J. S. Gwag, S. Y. Kim, *Adv. Mater.*, **2017**, *29*, 1702598.

[11] J.-M. Jeon, T. L. Kim, Y.-S. Shim, Y. R. Choi, S. Choi, S. Lee, **K. C. Kwon**, S.-H. Hong, Y.-W. Kim, S. Y. Kim, M. Kim, H. W. Jang, *Adv. Mater.*, **2017**, *28*, 1605929.

[12] J. M. Suh, Y.-S. Chim, D. H. Kim, W. Sohn, Y. Jung, S. Y. Lee, S. Choi, Y. H. Kim, J.-M. Jeon, K. Hong, **K. C. Kwon**, S. Y. Park, C. Kim, J.-H. Lee, C.-Y. Kang, H. W. Jang, *Adv. Mater. Technol.*, **2017**, *2*, 1600259.

[13] J. H. Oh, G. J. Choi, **K. C. Kwon**, S.-R. Bae, H. W. Jang, J. S. Gwag, S. Y. Kim, *Electron. Mater. Lett.*, **2017**, *13*, 277.

[14] S. Choi, **K. C. Kwon**, S. Y. Kim, H. W. Jang, *FlatChem*, **2017**, *4*, 68.

[15] **K. C. Kwon**, S. Choi, J. Lee, K. Hong, W. Sohn, D. M. Andoshe, K. S. Choi, Y. Kim, S. Han, S. Y. Kim, H. W. Jang, *J. Mater. Chem. A*, **2017**, *5*, 15534.

[16] **K. C. Kwon**, S. Choi, K. Hong, D. M. Andoshe, J. M. Suh, C. Kim, K. S. Choi, J. H. Oh, S. Y. Kim, H. W. Jang, *MRS Communications*, **2017**, *7*, 272.

[17] M. Park, **K. C. Kwon**, J. H. Oh, Y. G. Kim, H. W. Jang, S. Y. Kim, *Sci. Adv. Mater.*, **2017**, *9*, 758.

[18] J. Choi, Q. V. Le, K. Hong, C. W. Moon, J. S. Han, **K. C. Kwon**, P. R. Cha, Y. Kwon, S. Y. Kim, H. W. Jang, *ACS Appl. Mater. Interfaces*, **2017**, *9*, 30764.